NUI MAYNOOTH

Ollscoil na hÉireann Má Nuad

DESIGN AND ANALYSIS OF A QUASI-OPTICAL BEAM COMBINER FOR THE QUBIC CMB INTERFEROMETER

David G. Bennett B.Sc.

Research Supervisor: Dr. Créidhe O'Sullivan
Head of Department: Prof. J.A. Murphy

A thesis submitted for the degree of
Doctor of Philosophy

Sub-mm Optics Research Group
Department of Experimental Physics
National University of Ireland, Maynooth
Co. Kildare
Ireland

9th July 2014

Contents

Acknowledgments

There are quite simply no words that can express my gratitude to my supervisor Dr. Créidhe O'Sullivan. Also to quantify my thanks to Prof. Anthony Murphy and the NUIM Experimental Physics department will require a logarithmic scale. I am deeply grateful to my parents, brother, grandparents and my family. And finally many thanks to my friends and colleagues, both new and old. And finally a special thanks to Lee and Dave who saved the entire day at the last minute !!!

Abstract

In winter 2009 a number of physicists met in Paris to discuss the prospect of observing the CMB B-mode polarization using a novel technique called bolometric interferometry. This was the first meeting of what would later become the QUBIC collaboration. In this thesis we discuss the scientific reasons for CMB observation, we present a detailed explanation of how QUBIC will use bolometric interferometry to measure CMB polarization and in particular we discuss the author's contribution to the project. As part of the sub-mm optics research group in the National University of Ireland Maynooth the author was charged with the design and modeling of the optics that would focus the beam from the sky onto the bolometric detectors. This thesis describes various types of reflecting and refracting optics that were investigated. The results we present are useful not only for the QUBIC instrument, but for the design of imaging experiments in general.

Detection of CMB B-mode polarization is one of the supreme goals of modern cosmology. The faintness of this signal, combined with the interferometric observing technique, places extreme performance specifications on the QUBIC optics. Fortunately, as we shall show, there are types of well-known reflecting and refracting telescopes that are suitable for QUBIC. In this thesis I propose a design for the quasi-optical combiner that will perform as required.

1 The Cosmic Microwave Background

Between the idea
And the reality
Between the motion
And the act

T. S. Eliot

1.1 A signal from the early Universe

The Cosmic Microwave Background (CMB) is a highly red-shifted thermal radiation signal from the early Universe. From its initial prediction and detection to current attempts to map its polarization the CMB has profoundly deepened our understanding of the Universe. To date the CMB has the most accurately measured black body spectrum in nature. Its black body spectrum corresponds to a temperature of $T = 2.7$ K and it is responsible for a "glow" across the cosmos not associated with a stellar or galactic source. Initially thought to be spurious systemic noise, the CMB has allowed us to quantify the curvature of space time as well as ordinary and dark-matter densities. A plethora of scientific knowledge has emerged from the quantification of CMB temperature anisotropies. Detection of CMB polarization is expected to herald a new era of understanding of inflationary cosmology. In this chapter we briefly discuss the characteristics of the Microwave Background from its origin to its temperature and polarization spectrum. We also present the case for the further study of the CMB concluding with the importance of detecting the extremely faint B-mode polarization.

1.2 A brief history of CMB observations

For almost 50 years cosmologists have made remarkable attempts to observe the CMB with greater and greater sensitivity. These efforts culminated in May 2009 with the launch of ESA's Planck satellite [1]. Like many scientific milestones the initial discovery of the CMB was purely accidental. Predicted by Alpher, Gamov and Hermann in 1947 [2] as a consequence of a Freidmann-Lemaître Universe it lay undetected until 1965 when two radio astronomers (Penzias and Willson) encountered excess noise in a well calibrated horn antenna. The signal causing this noise appeared isotropic and they estimated that it corresponded to a temperature of 3.5 $\pm$ 1.0 K. Following discussions with various other researchers the noise was linked with the relic black body radiation predicted by Alpher and Herman. In 1965 two papers were published that would dramatically influence the course of far infrared astronomy over the next 50 years. The first by Penzias and Wilson detailed their observations [3]. This was complimented by Dicke, Peebles and Roll who used the Hot Bang cosmological paradigm to offer an explanation for the thermal background noise [4].

Large scale galaxy surveys have revealed that the structure of the Universe is not uniform in all directions. Cosmologists ascertain that modern structures have evolved from anisotropies within the primordial fluid. In the 1970's physicists realized that these anisotropies would have imprinted themselves onto the CMB in the form of temperature fluctuations. Over the next 20 years CMB cosmology was dominated by attempts to observe these fluctuations. In 1992 the DMR (Differential Microwave Radiometers) on NASA's COBE (Cosmic Microwave Explorer) satellite detected temperature anisotropies in the CMB at the level of $\frac{\Delta T}{T} \approx 10^{-5}$ [5]. Also the FIRAS (Far Infrared Absolute Spectrophotometer) instrument on COBE gave a definitive measurement of the CMB's power spectrum [6]. The FIRAS data gave an excellent fit to a back-body spectrum with a temperature of 2.726 K. Stephen Hawking commented that the COBE results were the "greatest scientific discovery of the century".

Fluctuations in the primordial fluid imposed a damped oscillating temperature power spectrum on the CMB. A model of the CMB power spectrum is shown in Figure 1.1. Here the various classifications of temperature anisotropies are indicated[1]. In the past two decades a number of CMB experiments have detected the primary peak of the

[1] A brief description of these temperature anisotropies will be given in section 1.3.3

temperature spectrum as well as the damped second and third peak. NASA's WMAP (Wilkinson Microwave Anisotropy Probe) observations have produced a remarkably precise power spectrum [7] [8]. This measured power spectrum is shown in Figure 1.2 and is consistent with the power spectrum resulting when one assumes a ΛCDM dominated Universe. It is predicted that the acoustic peaks in the CMB's temperature power spectrum are the result of quantum fluctuations occurring in the Universe within 10^{-35} seconds of the Big Bang. ESA's Planck satellite currently operating in an L2 orbit has been designed to measure with the minutest of precision the remaining information from the temperature anisotropies and also measure the CMB's polarization to a high degree of accuracy [9].

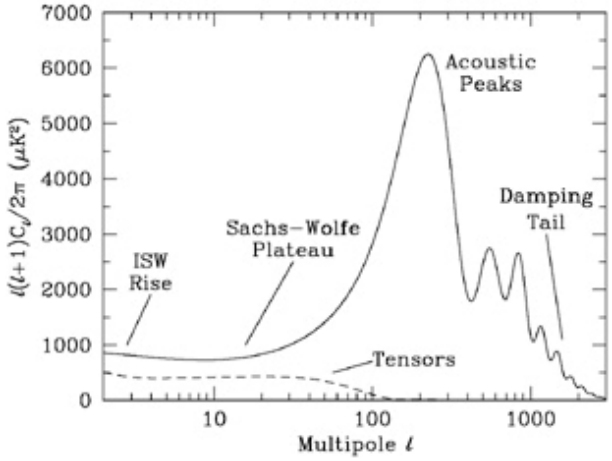

Figure 1.1: Simulated angular power spectrum of CMB primary temperature anisotropies. The levels of tensor anisotropies resulting from gravitational waves are also shown. This image is taken from `http://nedwww.ipac.caltech.edu/level5/March05/Scott/Scott4.html` and was generated using the well-known CMBFAST computer program [10]

Thompson scattering of photons off electrons in the primordial fluid led to the polarization of the CMB. In the 1970's cosmologists estimated that photons scattered during the era of recombination would have their polarization states frozen within the CMB. The detection of CMB polarization is of primary importance in modern cosmology. The degree of CMB polarization is extremely small and it wasn't until 2002 that the DASI (Degree Angular Scale Interferometer) experiment detected a definitive polarization signal in the CMB [11].

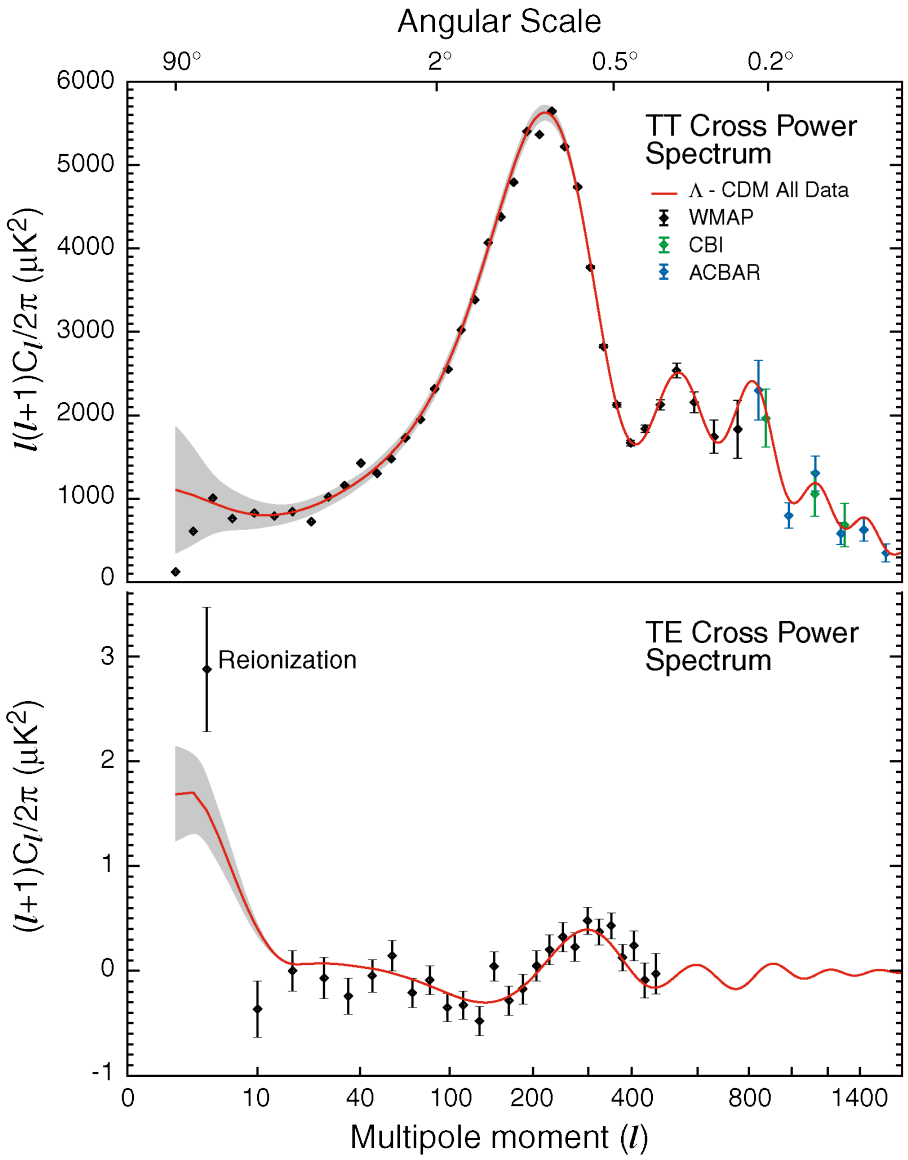

Figure 1.2: CMB power spectra measured by WMAP. *Top* : WMAP temperature power spectrum. These results are consistent with the ACBAR and CBI measurements. *Bottom* : The cross correlation of the temperature power spectrum and the E-mode polarization power spectrum. All figures taken from `http://lambda.gsfc.nasa.gov/product/map/dr4/m_images.cfm`.

The polarization signal detected by DASI is referred to as the E-mode polarization of the CMB. Another even fainter signal dubbed the B-mode polarization has been predicted by theorists and currently lies unobserved. Quantification of the CMB B-mode polarization is the *Sanctum Sanctorum* of CMB cosmology with repercussions

for inflationary models as well as Grand Unification theories.

1.3 Modern Cosmology and the CMB

1.3.1 The Big Bang and the expanding Universe

The CMB was predicted as a thermal radiation fossil of the Big Bang. The Big Bang theory is in part a result of careful consideration of the consequences of general relativity and cosmological observations. The Einstein equation

$$G_{\mu\nu} = 8\pi G T_{\mu\nu} - g_{\mu\nu}\Lambda \tag{1.3.1}$$

describes the coupling of the energy momentum tensor $T_{\mu\nu}$ of a massive object to the space time occupied by the object [12]. Here $G_{\mu\nu}$ is the Einstein tensor, Λ is the cosmological constant, G is Newton's gravitational constant and $g_{\mu\nu}$ is the metric tensor. The metric tensor quantifies the separation of events in space time. Assuming the Universe itself is homogeneous and isotropic the metric, which is dependent on the curvature of space, can be written as

$$(ds)^2 = c^2(dt)^2 - R^2(t)\Big[\frac{(dr)^2}{1-Kr^2} + r^2(d\theta)^2 + r^2 sin^2\theta(d\phi)^2\Big]. \tag{1.3.2}$$

This was derived independently in the 1930's by Friedmann, Robertson and Walker. Here $R(t)$ is the cosmological scale factor while K is a measure of the curvature of 3-dimensional space. Also r, θ and ϕ are co-moving spherical coordinates. Assuming the Friedmann Robertson Walker metric to be correct the Einstein equation reduces to

$$\Big(\frac{\dot{R}}{R}\Big)^2 + \frac{c^2K}{R^2} = \frac{8\pi G\rho}{3} + \frac{\Lambda c^2}{3} \tag{1.3.3}$$

which allows us to relate the variation of the cosmological scale factor (R) to the density (ρ), curvature (K) and the cosmological constant (Λ) of the Universe.

Equation (1.3.3) is referred to as the Friedmann equation and the quantity $\left(\frac{\dot{R}}{R}\right)$ is called the Hubble parameter $H(t)$ [13]. The Friedmann equation indicates that the scale factor R of the Universe may vary over time. This was first verified by Edwin Hubble who investigated the redshift of visible light from Cepheid stars in local galaxy clusters [14]. Hubble's results and numerous others that have followed indicate that the Universe is expanding. The value of H is currently measured to be $H = 70.5 \pm 1.3$ kms^{-1} Mpc^{-1}. This value has been derived from the WMAP 5 year data combined with distance measurements from Type Ia supernovae (SN) and the Baryon Acoustic Oscillations (BAO) in the distribution of galaxies.

For simple Friedmann models $\Lambda = K = 0$. The critical mass density required for a flat Universe ($K = 0$) is $\rho_c = \frac{3H_0^2}{8\pi G}$. Here H_0 refers to today's Hubble parameter (the Hubble constant). Equation 1.3.3 shows that three competing properties of the Universe contribute its current expansion. These are the quantity of matter within the Universe , its cosmological constant and its curvature. It is convenient to express these in terms of the critical density.

We define the mass contribution to the expansion as $\Omega_M = \rho_{M_0}/\rho_c$. Here ρ_{M_0} is the current mass density of the Universe while ρ_c is the critical mass density. Observationally ρ_{M_0} has been measured to be $\approx 10^{-28}$ kgm^{-3} while ρ_c is $\approx 10^{-26}$ kgm^{-3}. Therefore $\rho_{M_0} < \rho_c$ and so Ω_M is less than unity [15].

Analogous to Ω_M we define the contribution factor of the cosmological constant as $\Omega_\Lambda = \frac{\Lambda}{3H_0^2}$ and the curvature contribution as $\Omega_K = -\frac{K}{R_0^2 H_0^2}$. Here R_0 represents the present scale factor of the Universe. These parameters allow us to rewrite equation (1.3.3) as

$$\Omega_M + \Omega_\Lambda + \Omega_K = 1. \tag{1.3.4}$$

A full set of CMB observations will allow cosmologists to determine the values Ω_M, Ω_Λ and Ω_K in equation (1.3.4) and fully describe the expanding Universe.

Proponents of the Big Bang theory use the results of Hubble and equation (1.3.3) to argue that if the Universe is currently expanding there must be an epoch in its history when all matter and radiation were compressed into a singularity of infinite pressure

and temperature. This singularity expanded outwards in an event dubbed the Big Bang to give birth to our Universe.

In the relatively early stages of the Universe the energy density would have been significantly greater than the present value due to the Universe's more compact size. When $T > 4000K$, within 370,000 years of the Big Bang, all matter was ionized due to the thermal energy of electrons exceeding the binding energy of neutral hydrogen, helium and deuterium. Until this time the average path length of photons was restricted due to Thompson scattering from free electrons. Photons and baryons were therefore coupled together by their interactions with the free electrons into a hot ionized plasma [16].

Due to expansion approximately 370,000 years after the Big Bang the temperature of the Universe had decreased to below 4000 K. Photons no longer possessed sufficient energy to overcome the binding energy of hydrogen ($B = 13.6$ eV). The primary mechanism allowing the fluid to remain ionized ceased and neutral hydrogen began to form. This is known as the era of recombination. Photons were decoupled from the baryonic matter due to the lower Thompson scattering cross section of neutral atoms. The primordial photons began to propagate with a near infinite path length. The Universe had become transparent. These photons were red shifted by the continuing expansion of the Universe and are responsible for the signal we now call the CMB. On cosmological timescales the epoch of recombination was almost instantaneous. As such the photons we detect originate from a sphere whose radius is proportional to the time elapsed since recombination. This is referred to as the surface of last scattering. This surface is the furtherest back in time we can observe the Universe by the detection of electromagnetic waves.

1.3.2 CMB temperature power spectra

An inflationary epoch during the Universe's lifetime has been proposed to solve problems with the Big Bang theory such as the Horizon Problem. Inflation assumes that before $t < 10^{-35}$ seconds the cosmological constant dominated the Universe's dynamics. Therefore Friedmann's equation reduces to

$$\dot{R}^2 \;=\; \frac{\Lambda c^2 R^2}{3}, \tag{1.3.5}$$

whose solution is simply $R = R(0)e^{\sqrt{\frac{\Lambda}{3}}ct}$. Hence the Universe underwent a rapid exponential expansion.

Inflation solves the Horizon Problem (and explains why $K \approx 0$) but can also explain why complex structures have evolved. It is proposed that during inflation the microscopic quantum fluctuations within the Universe expanded. When this occurred these fluctuations became frozen within the space-time metric on a macroscopic scale. Therefore they became classic perturbations described readily using the theory of General Relativity and

$$g_{\mu\nu} \;=\; \overline{g_{\mu\nu}} + h_{\mu\nu}. \tag{1.3.6}$$

Here $\overline{g_{\mu\nu}}$ is the original smooth metric while $h_{\mu\nu}$ represents the perturbation to the metric [17].

Perturbations in the metric can be expressed in both scalar and tensor form. Considerations of the symmetry conditions and the equations of continuity that the perturbations must obey have led cosmologists to derive the oscillator equation [18]

$$\ddot{\Theta}+\ddot{\Psi}-\frac{R_\rho}{1+R_\rho}H\dot{\Theta}-\frac{R_\rho}{1+R_\rho}H\dot{\Phi}+\frac{k^2}{3}\Big(\frac{\Theta}{1+R_\rho}+\Psi\Big)-\frac{R_\rho}{R_\rho+1}\Big(1+3{c_s}^2\Big)\Theta \;=\; 0. \tag{1.3.7}$$

Here k is an arbitrary wave number while the gravitational potential perturbations are described by Ψ (the Newtonian potential) and Φ (the curvature fluctuation). The parameter Θ represents the temperature field while $R_\rho = (p_b + \rho_b)/(p_\gamma + \rho_\gamma) \approx 3\rho_b/4\rho_\gamma$ is the ratio of the photon to baryon density. Finally the value c_s represents the speed of acoustic waves traversing the fluid[2].

[2]The values of Ψ and Φ in the oscillator equation are referred to as Bardeen potentials. The diagonal terms of the h_{uv} tensor in equation (1.3.6) are calculated from these potentials. As a result of the selected gauge symmetry applied to the metric perturbations all other terms in h_{uv} are null. A full discussion of (1.3.7) and the variables involved is outside the scope of this thesis.

Equation (1.3.7) is analogous to the simple damped oscillator equation $\ddot{y}+2\alpha\omega\dot{y}+\omega^2 y = 0$ where ω is the angular frequency of oscillation and α is the damping ratio. It indicates that the gravitational driving force attempting to compress the primordial baryonic fluid competed with the restoring force of the fluid's pressure. These compressions and rarefactions caused sound waves to oscillate throughout the ionized plasma with a frequency

$$\omega^2 \;=\; \frac{k^2}{3(1+R_\rho)} \;=\; {c^2}_s k^2 \tag{1.3.8}$$

and are responsible for all primary anisotropies present in the CMB's power spectrum. It is the behavior of this photon and baryon super-fluid that leads to the CMB power spectrum profile shown in Figure 1.1. The amplitudes of the acoustic peaks depend solely on the initial conditions we place on the primordial Universe. For example Figure 1.3 demonstrates how the profile of the CMB temperature power spectrum varies with the four fundamental cosmological parameters. By using present day observations to measure the amplitude and the angular scale of the CMB's acoustic temperature anisotropies we can quantify the fundamental parameters whose values, as explained using equation (1.3.4), dedicate the evolution of the Universe.

The most convenient way to express the power spectrum of the CMB over the full sky is to decompose it into spherical harmonics. The temperature of the CMB can be expressed in terms of a summation of Legendre polynomials as

$$T(\theta,\phi) \;=\; \sum_{l=2}^{\infty}\sum_{m=-l}^{l} a_{lm}Y_{lm}(\theta,\phi). \tag{1.3.9}$$

where the spherical harmonic $Y_{lm}(\theta,\phi)$ is the angular portion of the solution to Laplace's equation in spherical coordinates. Here θ is taken as the polar (colatitudinal) coordinate with $\theta \in [0,\pi]$ while ϕ is the azimuthal (longitudinal) coordinate with $\phi \in [0,2\pi]$. The order l is an integer and m can equal $-l$, $-l+1$, ..., l. Current interests lie in mapping the fluctuations of the CMB's power spectrum over angular scales of $l < 100$. The $l = 0$ term in (1.3.9) is ignored as it represents the CMB's constant isotropic temperature which dominates any fluctuations by a factor of 10^5. The $l = 1$ term is

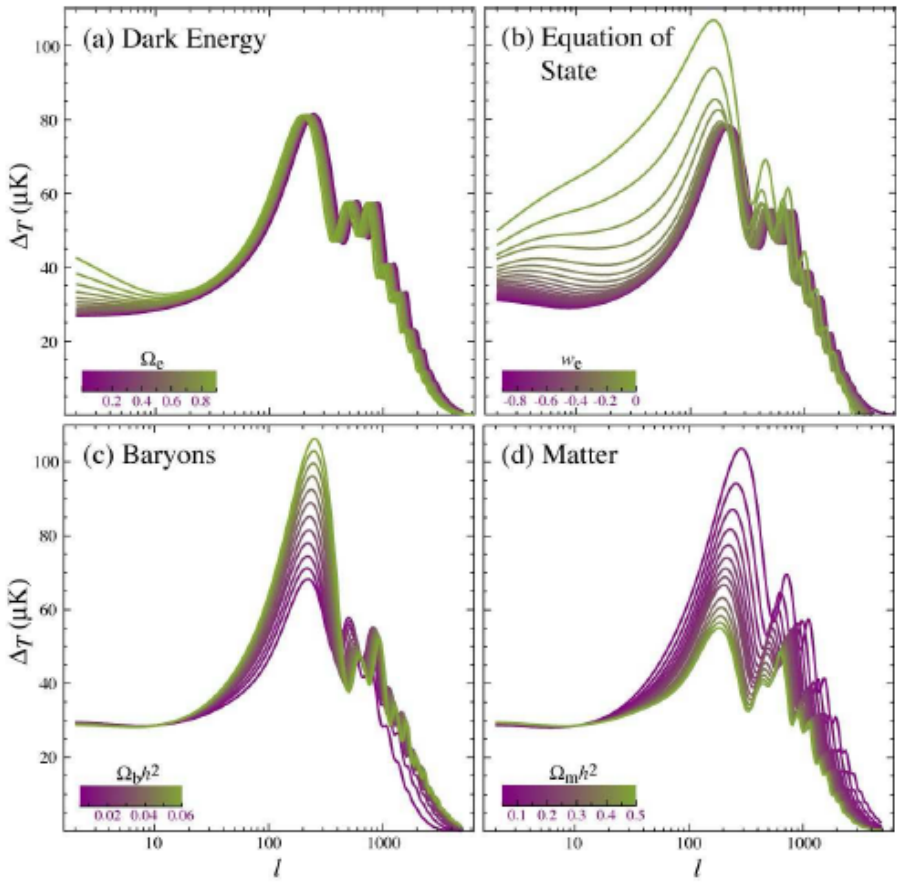

Figure 1.3: CMB tempertaure power spectra as fundamental parameters are varied. The parameters that are varied are: (a) dark energy density today Ω_e, (b) the equation of state of dark energy w_e, (c) the physical baryon density $\Omega_b h^2$ and (d) the physical matter density $\Omega_m h^2$. This image has been taken from [19].

also omitted for the reason that any intrinsic temperature fluctuation stored within this harmonic level will be obscured by the Earth's Doppler dipole anisotropy effect.

Early Universe models indicate that CMB temperature fluctuations should obey Gaussian quantum statistics. In this case

$$C_l^T = \frac{1}{2l+1} \sum_{m=-l}^{l} \mid a_{lm} \mid^2 = \left\langle \mid a_{lm} \mid^2 \right\rangle \tag{1.3.10}$$

and all the information contained within the temperature fluctuations can be obtained

by calculating the expectation values of the coefficients of (1.3.9). The temperature anisotropies of the CMB

$$(\Delta T_l)^2 = \frac{1}{2\pi} l(l+1) C_l^T. \tag{1.3.11}$$

are then readily related to the power spectrum ${C_l}^T$ [20].

Plots of the temperature anisotropy (1.3.11) versus angular scales have become ubiquitous within CMB cosmology. Figures 1.1 and 1.3 and are examples of such plots. The profiles of such graphs are directly related to dynamics of the Universe before and during recombination. Temperature fluctuations of the CMB are divided into two groups referred to as primary and secondary anisotropies and we discuss these in more detail in the following sections.

1.3.3 Primary temperature anisotropies

In Figure 1.1 the main categories of primary temperature anisotropies are labeled. A brief explanation of these anisotropies follows. The amplitude of these primary anisotropies are solely dependent on the angular scale at which one observes the CMB power spectrum.

The dominant anisotropies at $l < 100$ are referred to as the Sachs-Wolfe anisotropies [21]. This is the super-horizon region of the CMB power spectrum[3] and represents regions of the Universe outside the Hubble radius at the time of recombination[4]. The acoustic waves responsible for the acoustic peaks in the CMB's temperature spectrum did not oscillate over these scales. At $l < 100$, $\frac{\delta T}{T}$ is related to the perturbation of the gravitational potential which generates, via the Sachs Wolfe effect, a gravitational redshift and therefore intrinsic temperature fluctuations within the CMB's low scale power spectrum.

The dominant feature on the CMB temperature power spectrum is the primary peak. The oscillator equation (1.3.7) tells us that compressions and rarefactions transversed

[3] As such from regions of the Universe that are too large to have ever been in causal contact.

[4] The Hubble radius is defined by $c/H(t)$. It is roughly the size of the observable radius at time t. The value $H(t)$ indicates the Hubble parameter and was defined when dicussing equation (1.3.3).

the primordial baryonic fluid. These acoustic waves generated regions of higher and lower densities and hence temperatures fluctuations within the fluid. During recombination the temperature differences between photons propagating from these crests and troughs became imprinted onto the surface of last scattering. The first peak is due to the fundamental harmonic of the primordial acoustic waves. It is the temperature anisotropy caused by the maximal compression of the baryon fluid. Both its amplitude and position are highly dependent on the curvature of the Universe.

The higher order peaks are due to the higher harmonics of the acoustic waves within the baryon fluid. The amplitudes of these are dampened in accordance with equation (1.3.7). The second peak represents the restoring radiation pressure's response to the compression of the primary peak. The amplitude of the secondary peak is damped due to baryon loading. Essentially the increased gravitational potential of the recently compressed baryonic mater dampens the radiative pressure's restoring force. Such damping is present in at all higher order peaks on the CMB power spectrum associated with a rarefaction [22].

The third peak is due to the secondary compression of the fluid (occurring when the angular scale corresponds to the horizon over which one and a half acoustic oscillations took place). The amplitude of the third peak is magnified due to the presence of dark matter increasing the gravitational potential of the well into which the fluid was being compressed. On smaller angular scales the higher order peaks are suppressed due to photon diffusion. Also referred to as Silk damping this occurred when the photons that occupied smaller horizon scales migrated from hot dense regions to cooler ones. Due to the coupling between the photons and baryons the migrating photons would have pulled the baryons into these cooler regions. This matter diffusion led to a reduction of temperature anisotropies that were caused by the oscillating acoustic waves and thus dampened the higher order fourth and fifth peaks [23].

1.3.4 Secondary anisotropies

Whereas primary anisotropies can be accounted for by considering the equation of state of the primordial fluid during recombination, secondary CMB anisotropies are classed as changes to the power spectrum that occurred between the surface of last

scattering and an observer. Most secondary temperature fluctuations are local and due to astronomical foregrounds. Local foregrounds include objects such as the sun and the moon whose effects can be negated by observing the sky in a direction where these objects are not visible. Astrophysical foregrounds refer to sources of emission or absorption fixed within the observing reference frame. Synchrotron, free-free and thermal dust emissions are all examples of such sources. The most famous astrophysical foreground in all CMB sky maps is of course the equator region of the map indicating our own Milky Way galaxy. An example of the galactic foreground present on a CMB full sky map is shown in Figure 1.4. An entire library of methods involving multi-frequency observations exists to take account of these foregrounds and produce credible CMB observations. Descriptions of the brute force likelihood analysis that was performed on the COBE data set is outlined in [24] and [25], more recent analysis techniques are discussed in [26] and [27].

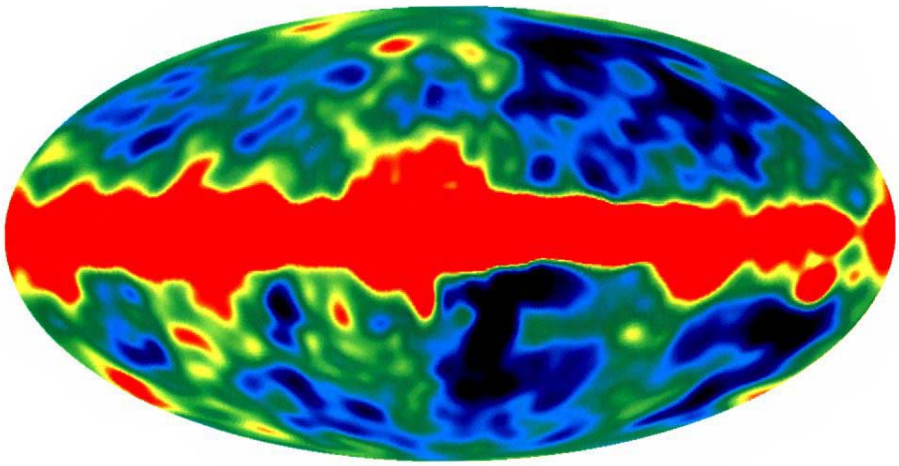

Figure 1.4: COBE 4 year full sky map. The foreground emission from the Milky Way Galaxy is the dominant feature of this map. This image has been taken from `http://www.casca.ca/lrp/vol2/firstplanck/planck.html`.

Much has been written on the subjects of primary and secondary CMB anisotropies. To approach these subjects in any detail is beyond the scope of this thesis. For an excellent and detailed discussion of the most dominant CMB secondary anisotropies the reader is referred to [28]. Here other causes of secondary anisotropies including gravitational and electromagnetic interactions are discussed in detail. Gravitational foregrounds include lensing and the Rees-Sciama (RS) effect. Gravitational lensing affects both

CMB temperature and polarization anisotropies[5]. The RS effect will cause a drop in the energy of CMB photons due to a net redshift effect when the photons enter and exit an expanding potential well. Electromagnetic foregrounds include interactions such as the Sunyaev−Zel'dovich (SZ) effect in which photons scatter off hot electrons in galaxy clusters. On average these interactions lead to a a gain in the photon's energy and therefore lead to an increase in temperature.

1.3.5 CMB Polarization

Due to photons interacting with electrons via Thompson scattering, CMB polarization anisotropies were also generated at the surface of last scattering. A full account of the origin of these CMB polarization anisotropies is provided in [29]. Here it is shown that if an electron scatters photons from an anisotropic temperature distribution the scattered plane wave may contain a polarization anisotropy. Due to the symmetry of the problem the only temperature anisotropy that can lead to such polarization effects are quadrupole temperature anisotropies. An illustration of the Thompson scattering of photons within such a quadrupole temperature anisotropy is shown in Figure 1.5.

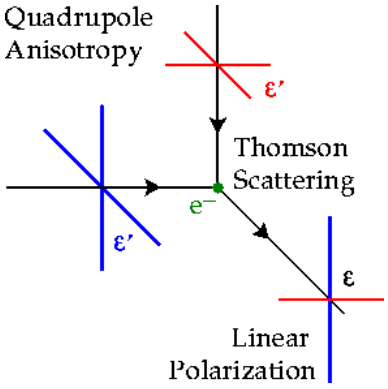

Figure 1.5: Polarization anisotropy via Thompson scattering. Here ϵ indicates the direction of polarization. Image taken from Wayne Hu's home page `http://background.uchicago.edu/~whu/physics/physics.html`.

Quadrupole temperature anisotropies are described by the $Y_{2,m}$ group of spherical harmonics. There are three distinct categories of quadrupole patterns for such temperature anisotropies. These correspond to the $m = 0, \pm 1$ and ± 2 modes of the $l = 2$

[5]We will begin a discussion of CMB polarization in section 1.3.5

harmonic. Each of these quadrupole temperature anisotropies occurred within the primordial fluid and have physically distinctive origins. Scalar, vector and tensor perturbations of the fluid give rise to $Y_{2,0}$, $Y_{2,\pm1}$, $Y_{2,\pm2}$ temperature anisotropies [6]. It has been shown that scalar perturbations of the fluid give rise to oscillating acoustic waves via (1.3.7). This in turn gives rise to $Y_{2,0}$ quadruple temperature anisotropies at the troughs and peaks of the density anisotropies generated by these acoustic waves. Meanwhile tensor perturbation that give rise to $Y_{2,\pm2}$ quadrupole temperature anisotropies are generated by primordial gravitational waves stretching and compressing the metric. During recombination Thompson scattering of photons converted the quadrupole temperature anisotropies due to scalar and tensor perturbations into a partially polarized CMB signal. These two quadrupole anisotropies are shown in Figure 1.6. In consequence it is estimated that the CMB is polarized at a level of approximately 10 % of its temperature anisotropy [30].

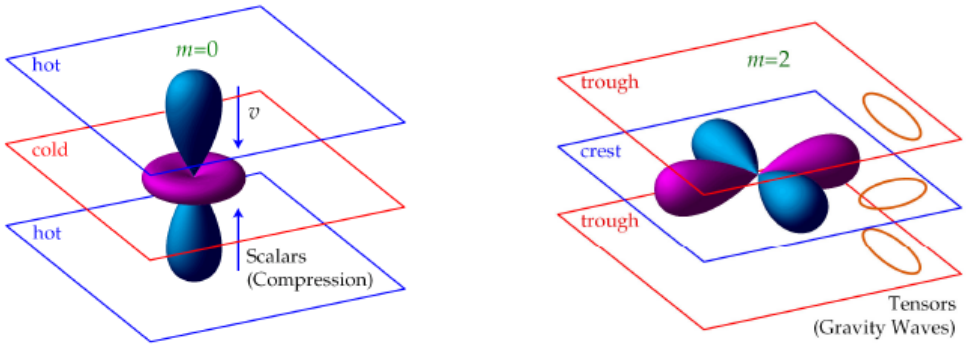

(a) A $Y_{2,0}$ temperature anisotropy arises from a scalar perturbation of the primordial fluid.

(b) A $Y_{2,\pm1}$ temperature anisotropy arises from a tensor perturbation of the primordial fluid.

Figure 1.6: Quadruple temperature anisotropies that lead to part polarization of the CMB during recombination. These images have been taken from [30].

Classically, partially polarized light is described by the Stokes parameters

$$S_0 = I = {E_x}^2 + {E_y}^2 \tag{1.3.12}$$

$$S_1 = Q = E_x^2 - E_y^2 \tag{1.3.13}$$

[6] It is expected that due to the short mean free path of photons vortical motions of the primordial fluid that generate vector temperature anisotropies would have dissipated

$$S_2 \;=\; U \;=\; 2E_xE_y\cos\delta \tag{1.3.14}$$

$$S_3 \;=\; V \;=\; 2E_xE_y\sin\delta \tag{1.3.15}$$

where the value I is the total intensity of the electric field. The values of Q and U completely describe the orientation of a linearly polarized wave while the term δ is the difference in phase between the x and y components. The value V represents the degree of circular polarization. There is no known mechanism that can generate circular polarization in the CMB (or in any other galactic signal) so we will ignore this parameter. The Stokes parameters are dependent on a fixed coordinate system. A more convenient way exists of expressing CMB polarization that removes this requirement. These are the so called E-mode and B-mode polarization states. Stokes parameters are invariant under a 180° rotation. We can therefore generate the terms $Q \pm iU$ and decompose them into the spin-2 spherical harmonic terms

$$Q \pm iU \;=\; \sum_{l=2}^{\infty}\sum_{m=-l}^{l} a_{lm\,\pm 2}^{\pm 2}Y_{lm}. \tag{1.3.16}$$

We then take the terms $e_{lm} = \frac{1}{2}(a_{lm}^{(2)} + a_{lm}^{(-2)})$ and $b_{lm} = -\frac{i}{2}(a_{lm}^{(2)} - a_{lm}^{(-2)})$. The E-mode polarization state is then defined as

$$E \;=\; \sum_{l=2}^{\infty}\sum_{m=-l}^{l} e_{lm}Y_{lm} \tag{1.3.17}$$

while the B-mode polarization is defined as

$$B \;=\; \sum_{l=2}^{\infty}\sum_{m=-l}^{l} b_{lm}Y_{lm}. \tag{1.3.18}$$

Such a decomposition of polarization anisotropies is analogous to splitting any vector field into its divergence and curl components. The E-modes represent the curl-free components of the polarization while the B-modes identify the gradient-free components. The crucial benefit of this decomposition is that E-modes are the direct result of scalar perturbations while B-modes originate from tensor perturbations.

We now define the auto- and cross-correlation functions of the CMB power spectra as:

$$\begin{aligned}
\left\langle a_{lm}^{T*} a_{lm'}^{T} \right\rangle &= C_l^{TT} \delta_{ll'} \delta_{mm'}, & \left\langle a_{lm}^{T*} a_{lm'}^{E} \right\rangle &= C_l^{TE} \delta_{ll'} \delta_{mm'} \\
\left\langle a_{lm}^{E*} a_{lm'}^{E} \right\rangle &= C_l^{EE} \delta_{ll'} \delta_{mm'}, & \left\langle a_{lm}^{T*} a_{lm'}^{B} \right\rangle &= C_l^{TB} \delta_{ll'} \delta_{mm'} \\
\left\langle a_{lm}^{E*} a_{lm'}^{B} \right\rangle &= C_l^{BB} \delta_{ll'} \delta_{mm'}, & \left\langle a_{lm}^{B*} a_{lm'}^{B} \right\rangle &= C_l^{BB} \delta_{ll'} \delta_{mm'}.
\end{aligned} \tag{1.3.19}$$

These are analogous to (1.3.10) yet offer a full description of the CMB power spectrum. Of these terms C_l^{TB} and C_l^{EB} vanish due to parity considerations. The complete measurement of the remaining four data sets is one of the main goals of modern observational cosmology.

Assuming a flat sky approximation the spin-2 harmonics representing the CMB polarization can be reduced to Fourier modes. Under this approximation the polarization of the E-modes occurs parallel or perpendicular to the wave vector. For the B-modes the polarization aligns at a 45° angle to the wave vector. An example of these polarization alignments is shown in Figure 1.7.

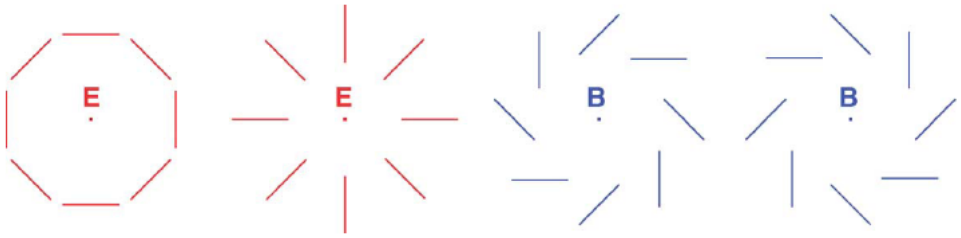

Figure 1.7: The CMB TT, TE, EE and BB power spectra. The wave vector is pointing out of the page. This image is taken from [31]

The flat sky pattern for both E and B-modes are shown in Figure 1.8. A superposition of these patterns is shown in Figure 1.9. In both patterns areas of polarization "hotspots" can be identified. In the E-mode patterns distinctive areas of divergence are observable while in the B-mode pattern areas of significant handedness are visible [32]. A succinct explanation of how CMB polarization can be decomposed into both E/B-modes is presented in [33].

Figure 1.10 shows a predicted power spectrum for all four CMB observables. These spectra have been generated by the CMBFAST program using the results of the

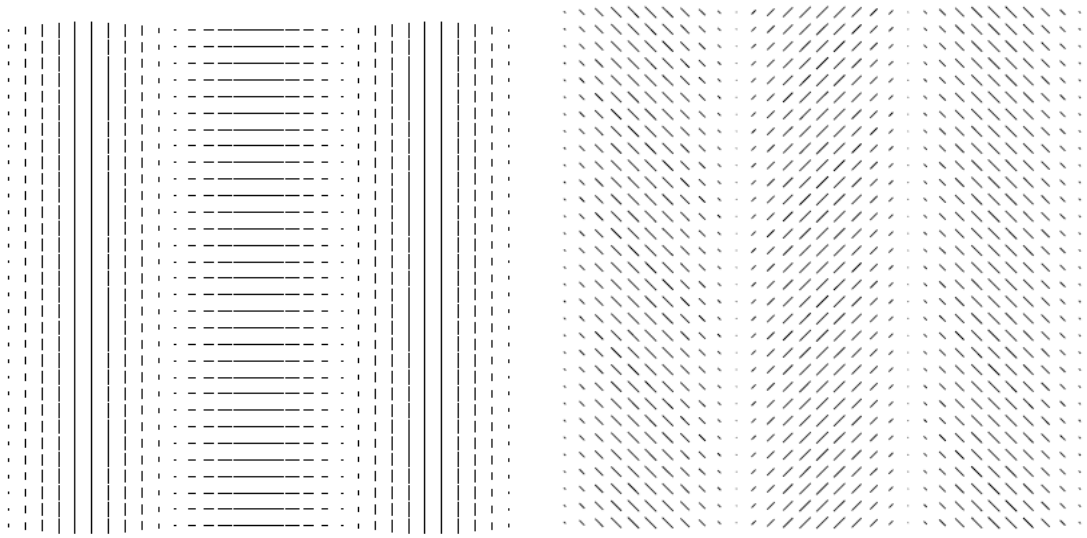

(a) E polarization Fourier modes. (b) B polarization Fourier modes.

Figure 1.8: Using a flat sky approximation plane wave Fourier modes can describe the CMB polarization. The flat sky E and B Fourier modes are shown. The wave vector runs horizontally along both graphs.

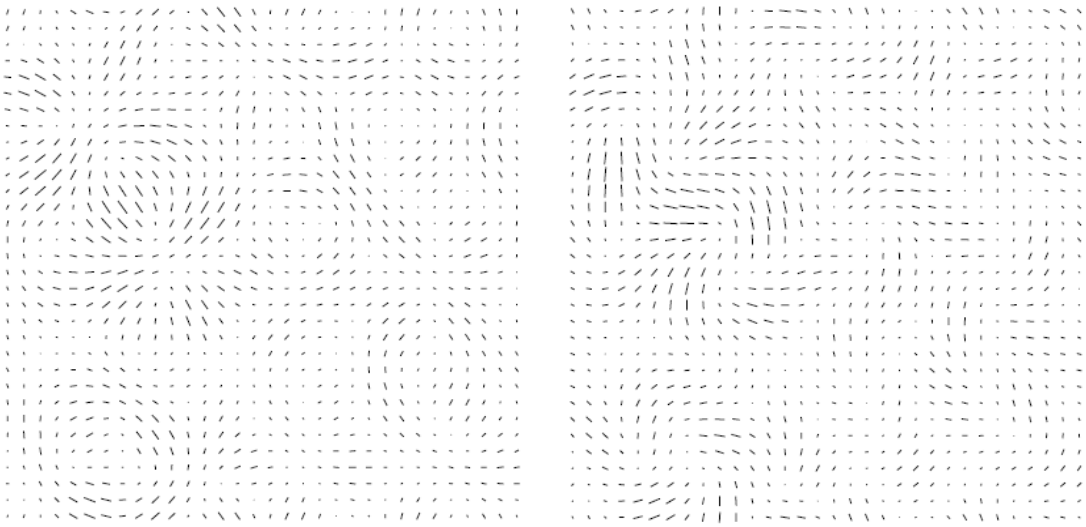

(a) Superposition of E Fourier modes. (b) Superposition of B Fourier modes.

Figure 1.9: E and B-mode polarization patterns generated from the superposition of 80 flat sky Fourier modes. Images taken from [34].

WMAP experiment [10]. We note that the level of B-mode polarization anisotrop-

ies is not yet known. Upper limits of the BB signal would have been set prior to all calculations. It is apparent that the level of temperature anisotropies dominates both the E and B-mode polarization intensities. The EE spectrum peaks on scales where the temperature anisotropy (TT spectrum) begins to undergo damping. We can see that acoustic oscillations in the primordial fluid also generate a number of peaks along the EE power spectrum. The strong correlation between the temperature anisotropies and E-mode polarizations (the TE spectrum) reinforce the prediction that both these anisotropies have a common origin, namely acoustic waves generated via (1.3.7)

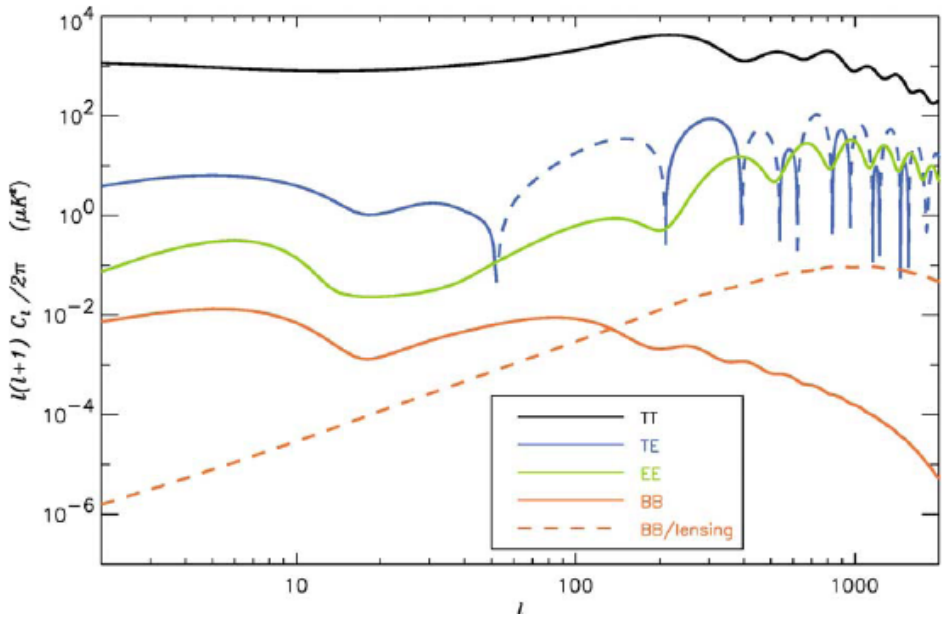

Figure 1.10: The CMB TT, TE, EE and BB power spectra. This image is taken from [31]. It has been generated by the CMBFAST program using the results of the WMAP experiment [10]. For more information visit `http://www.cmbfast.org`.

It is expected that gravitational lensing of the CMB will occur. This lensing acts to smooth out both the temperature and E-mode power spectra. This effect can occur at a level of 10 % in the damping tails of these spectra. Another result of gravitational lensing is that the CMB B-mode signal has two separate sources. The first is due to temperature quadrupole anisotropies caused by tensor perturbations of the the primordial fluid. These anisotropies are expected to be caused by relic gravitational waves propagating throughout the early Universe. The second source is

the gravitational lensing of E-mode polarization by intervening foreground structures in the Universe. This creates B-modes at the μK level. This lensing mixes some of the polarized power between E and B-modes. This source of B-modes peaks over the same scales as does the E-mode polarization. At these scales the lensed signal dominates the expected pure B-mode signal. The QUBIC experiment described in this thesis is designed to observe in the multipole range $l \approx 35 - 125$ where the primordial B-mode signal is expected to constrain current theories best. Unfortunately foregrounds from lensing place a strict limit on the detectability of the B-mode polarization signal. It is predicted that if the ratio of tensor-to-scalar perturbations of the primordial plasma is less than 6×10^{-4} B-mode polarization will not be detectable [35]. A comprehensive treatment of CMB lensing is given by [36] .

1.3.6 The CMB and Inflation

Three widely used inflationary models are referred to as small-, large- and hybrid-field models. The tensor-to-scalar ratio of the CMB power spectrum is defined as $r = C_l^T / C_l^S$. Here C_l^S represents the part of the CMB's spectrum that can be attributed to temperature anisotropies caused by scalar perturbations within the primordial fluid. Meanwhile C_l^T represents the parts of the power spectrum that can be attributed to tensor perturbations. The scalar spectral index of the CMB (n_s) is defined by assuming a power-law for the scalar perturbations in the primordial fluid. It has been shown that $n_s - 1 \sim \frac{\ln(P_R)}{\ln(k)}$ where P_R are the scalar perturbations due to fluctuations in the matter density of the Universe whose wavenumber is k [37]. As shown in Figure 1.11 the variation of the tensor-to-scalar ratio (r) to the scalar spectral index (n_s) of the the CMB is dependent on the Universe's inflationary mechanism.

Complete measurement of the TT, TE, EE and BB polarization data sets will allow us to determine both the tensor-to-scalar ratio and the scalar spectral index of CMB anisotropies. Detection of E-modes and B-modes will allow physicists to ascertain the energy scales of the Universe when inflation occurred 10^{-35} seconds after the Big Bang. Between the Big Bang and the inflationary epoch unification of the electromagnetic, weak and strong nuclear forces are predicted as well as Grand Unification via super-symmetry or super-strings. Full measurement of all CMB data sets will allow use to asses the validity of these predictions [38].

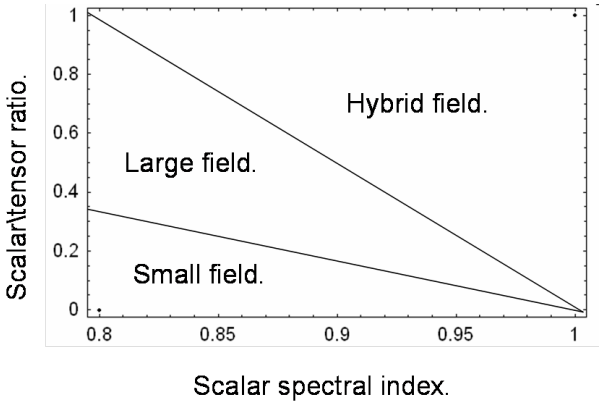

Figure 1.11: The relationship between r and n_s depends of the inflationary model. The image has been adapted from the "zoo plot" shown in [37].

1.4 Recent CMB experiments

The intricacies of the CMB's anisotropies are matched by the profusion and meticulous design of experiments designed to measure them. In the past two decades the number of CMB experiments has grown dramatically and the pace of novel discoveries about the CMB has accelerated. As we shall explain the results of these experiments have enabled many facets of the standard cosmological model to be verified. A selection of recent CMB experiments is shown below in Table 1.1. These experiments have taken measurements over a wide range of frequencies and detection devices have included transition edge sensors (TES), polarization sensitive bolometers (PSB) and high electron mobility transistors (HEMT). The list includes balloon borne (BB), ground based South Pole (SP) and satellite (Sat) missions. Many of the experiments have now been decommissioned however others are, at the time of writing, observing the CMB (Obs). Others are still in the planning stages.

As one can see a significant amount of progress has been made in recent years as regards observing CMB anisotropies. In July 2010 pictures of PLANCK's first full sky survey were released by ESA. One of these images is shown in Figure 1.12. It is expected that analysis of such maps will allow quantification of both CMB temperature and E-mode anisotropies with unprecedented accuracy.

Current efforts focus on quantifying the scalar-to-tensor ratio of the primordial perturbations. Within the past 12 months conversations about a space borne mission

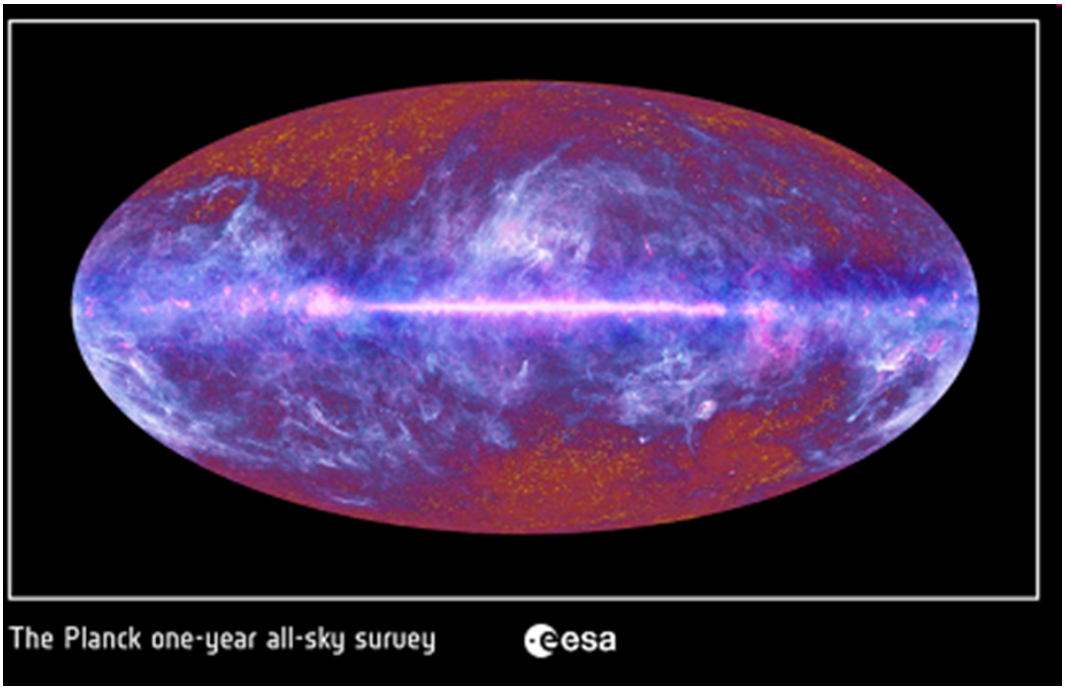

Figure 1.12: Image of the full microwave sky observed by the PLANCK satellite. Image taken from `http://sci.esa.int/science-e/www/object/index.cfm?fobjectid=47333`.

to measure B-modes have begun. Other endeavors of future CMB experiments include measuring the lensing of peaks, observing the integrated Sachs-Wolfe anisotropies due to dark energy and examining whether non Gaussianity exists within the CMB [52], [53].

1.5 The CMB and the cosmological parameters

It is expected that measurement of the polarization coefficients shown in equation (1.3.19) will allow complete and unambiguous determination of the cosmological parameters shown in equation (1.3.4). Inclusion of these values into the Einstein - Friedmann equations will allow physicists to describe the past present and future of the Universe.

Following the success of COBE, the WMAP satellite measured the amplitudes of the acoustic primary and secondary CMB temperature power spectrum peaks with ex-

quisite accuracy. Current knowledge of CMB anisotropies from a selection of CMB experiments have generated values for the cosmological constants all in agreement with the WMAP temperature power spectrum. The information pertaining to the cosmos derived form these data sets is summarized in this section. The temperature anisotropy power spectrum measured by the WMAP satellite is shown in Figure 1.2. WMAP became the first mission to report an accurate observation of the primary peak oscillation of the temperature power spectrum. Since then a number of different experiments have observed the primary and higher order peaks of the CMB temperature anisotropies. Figure 1.13 compares the WMAP power spectrum to the spectra measured by several other experiments including the ACBAR, BOOMERanG, CBI and DASI. A number of polarization sensitive experiments have also successfully measured the TE and EE CMB power spectra. Figure 1.14 compares the TE and EE power spectra obtained from the DASI and CBI interferometers to the QUAD imaging CMB telescope.

The consistency of measurements from multiple experimental sources has lead cosmologists to conclude many things about the Universe. The amplitude and angular scale of the primary peak in the TT power spectrum is highly dependent on the curvature of the Universe. The position and amplitude of the primary peak in several CMB observations has led cosmologists to the conclusion that the Universe is spatially flat ($K = 0$). Therefore $\Omega_M + \Omega_\Lambda \approx 1$. The amplitudes of the secondary and third higher order peaks are related to the quantity of ordinary and cold dark matter present within the primordial plasma. Analysis of WMAP's 5-year data sets have indicated that:

- The age of the Universe, t_0, is 13.72 ± 0.12 Gyr.
- The Hubble constant, H_0, is 70.5 ± 1.3 kms^{-1} Mpc $^{-1}$.
- The physical baryon density, $\Omega_b h^2$, is 0.02267 ± 0.0005. Here $h = H_0/(100$ kms^{-1} Mpc $^{-1})$ where H_0 is Hubble's constant.
- The physical dark matter density, $\Omega_c h^2$, is 0.1131 ± 0.0034.
- The dark energy density, Ω_Λ, is 0.726 ± 0.015
- The scalar spectral index, n_s, is 0.96 ± 0.013.

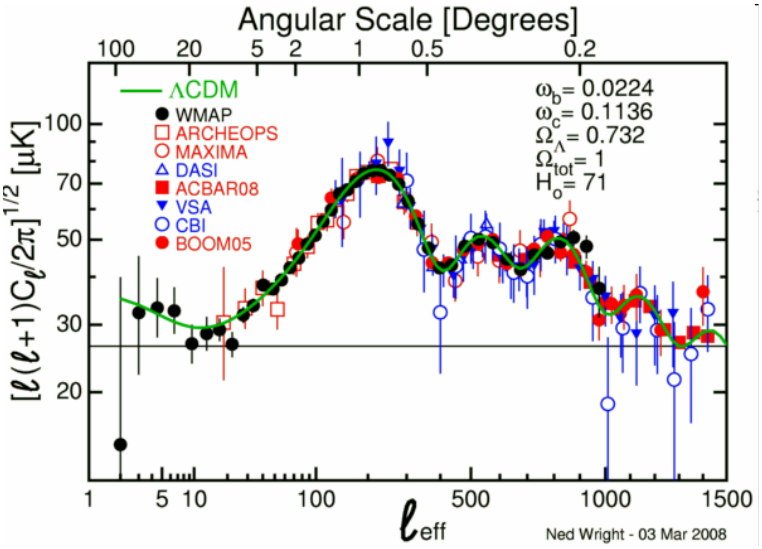

Figure 1.13: The WMAP temperature anisotropy power spectrum has been confirmed by several ground based and baloon borne instruments. Here the TT power spectra obtained from the ACBAR, BOOMerANG, CBI and DASI. CMB experiments are compared. Image taken from `http://www.astro.ucla.edu/~wright/CMB-DT.html`. The green line shows the best fit ΛCDM model to the WMAP data. A complete description of the cosmological parameters determined from WMAP observations is presented in [54] [55].

These figures have been refined from the values calculated using WMAP's data with information obtained from the observations of galaxy clusters, supernovae and quasars. The state of the art of experimental cosmology has thus generated the concordance ΛCDM theory of cosmology. This predicts that roughly only about 4% of the Universe is composed of the ordinary baryonic matter (protons and neutrons) we interact with every day. The majority of matter present in the Universe is dark matter. Neither the nature or evolution of this dark matter is understood. However the most startling conclusion of the concordance ΛCDM theory is that approximately 75% of the mass-energy density of the Universe is composed of a mysterious form of energy dubbed "dark energy". The current accelerated expansion of the Universe is attributed to this dark energy [8] [56].

It is predicted that the scalar perturbations that give rise to the quadrupole anisotropies that cause temperature and polarization anisotropies will generate a TE power

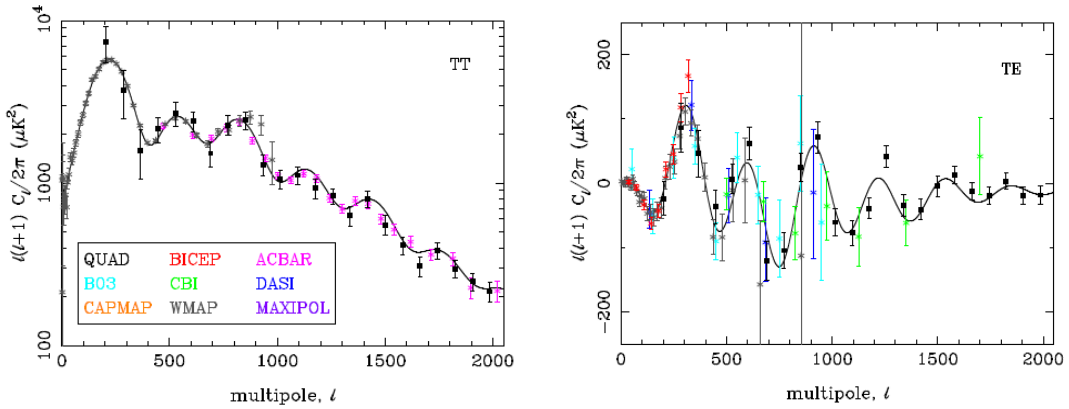

(a) TT power spectrum obtained from various CMB experiments.

(b) The TE power spectra obtained from various CMB experiments.

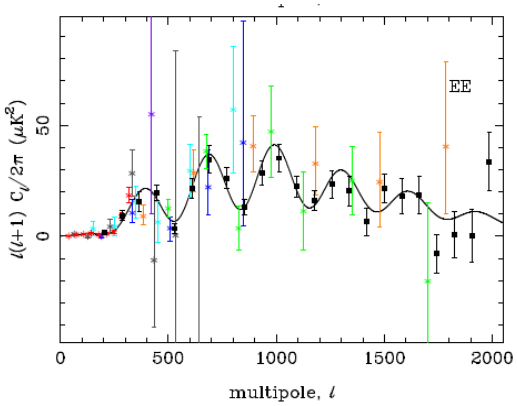

(c) The EE power spectra obtained from various CMB experiments.

Figure 1.14: CMB E-modes were first observed by the DASI interferometer. Several other experiments have verified these results. Image taken from [48]. The black lines show the power spectra expected in the best-fit ΛCDM model to the WMAP 5-year data.

spectrum out of phase with the TT spectrum. As shown in Figure 1.14 results from the several CMB polarimeters have indicated as much and therefore reinforce the current theories of the early Universe. From observation of E-mode polarization and upper limits placed on the BB power spectrum we conclude that $r = C_l^T/C_l^S < 0.27$ (95% $c.l$) [48]. Finally, a firm-detection of B-mode polarization anisotropies would provide direct evidence for inflation and the energy scale at which it occurred.

1.6 Conclusions

In this chapter we have provided a general introduction into the origin and nature of the CMB. We have provided a brief explanation of both its temperature power spectrum as well as its E/B-mode polarization. One of the most remarkable aspects of CMB cosmology research is that the countless hours of work by so many scientists and engineers over the past 40 years began on the back the two page article published by Penzias and Willson. These gentlemen would later receive the noble prize for their detection of the CMB yet in the authors opinion the most remarkable part of their submitted paper is the line "*this excess temperature is, within the limits of our observation, isotropic, unpolarized and free from seasonal variations*". We have shown how many of the cosmological parameters have been quantified by continuing to observe the CMB within the limits of modern observation techniques. These pursuits have allowed us to gain a remarkable insight into the nature and composition of the Universe. We have also outlined the reasons cosmologists now wish to measure the extremely faint B-mode signal. It is expected that detection of the CMB B-mode signal will allow us to estimate the energy levels at which inflation occurred. As such cosmologists are now beginning to vigorously pursue the detection of CMB B-modes. This thesis is concerned with the design and modeling of an optical system for the proposed QUBIC CMB mission. QUBIC will attempt to detect B-modes down to a tensor-to-scalar ratio of ~ 0.01 using a novel observation technique we call bolometric interferometry. In the next chapter we present the QUBIC mission.

Name	Year	Freq (GHz)	Location or Type	Detector Type	Measured anisotropy
ACBAR [39]	01 - 05	150, 220 & 289	SP	Bolometers	1st temperature peak.
Archeops [40]	02	150, 220 & 289	BB	PSB	Temperature peaks and polarization detection.
BICEP1/2 [41]	Obs	100 & 150	SP	PSB & TES	B-mode.
BOOMERanG/03 [42]	99-00	90-410	BB	Bolometer	Temperature peaks.
CAPMAP/ PIQUE [43]	00 -03	100	New - Jersey	HEMT mixers	Limits on polarization anisotropies.
COBE [5]	1989	31 - 90	Sat	Radiometer	Sachs Wolf anisotropies. Black body spectrum
DASI [11]	00 -03	26-36	SP	Heterodyne interferometer	Higher order temperature peak and E mode polarization.
KECK ARRAY [44]	Future	100, 150 & 220	SP	TES	Scalar-to-tensor ratio within 0.02
MAXIMA/ MAXIPOL [45]	99 - 00	140 & 420	BB	bolometers	Doppler peak of anisotropies.
MBI-4 [46]	Obs	26-36	Pine Bluff Obs	Bolometric Interferometer	Limitations on scalar-to-tensor ratio.
Polarbear [47]	Obs	150	Atacma Chile	TES	B-modes.
PLANCK [9]	Obs	26-36, 100 - 857	Sat	PSB & HEMT mixers	Higher order temperature peaks.
QUaD [48]	05-08	100 & 150	SP	PSB	E-mode polarization. Limits on B mode polarization.
QUIET [49]	Future	40 & 90	Atacma Chile		B-modes
QUBIC [50] [51]	Future	150	SP	Bolometric Interferometer	Scalar-to-tensor ratio within 0.01
WMAP [7]	01	23-94	Sat	Radiometer	1st and 2nd temperature peaks

Table 1.1: CMB Experiments

2 QUBIC: An Experiment designed to measure CMB B-mode polarization

2.1 Introducing QUBIC

QUBIC (Q and U Bolometric Interferometer for Cosmology) is a CMB polarimeter designed to measure the B-mode polarization and therefore the tensor-to-scalar ratio of the CMB anisotropies [57] [58]. The instrument will employ incoherent receivers to observe fringe patterns generated by interfering CMB sky signals. This is a novel technique of gathering information about the CMB and it is hoped to improve on heterodyne CMB interferometers such as DASI whose sensitivity was limited due to the narrow bandwidth of the coherent detectors. The goal of the QUBIC collaboration is to construct an instrument whose sensitivity is on par with a B-mode imager yet whose interferometric nature allows a high degree of systematic error control as well as extremely accurate calibration. The proposed experiment is the outcome of merging both the MBI [46] and BRAIN [59] CMB experiments. The collaboration consists of a number of institutions from France, Italy, the U.K., Ireland and the U.S.A.

2.2 Interferometry

2.2.1 Interferometers in astronomy

The development of interferometry is synonymous with the quest to investigate the heavens with greater and greater angular resolution. The angular resolution of an optical instrument is of course $\sim \frac{\lambda}{D}$ where D is the diameter of the observing instrument

and λ is the wavelength of the sky signal. The smaller this ratio the closer two celestial bodies can be to one another yet still be resolved by an instrument. For cost and weight reasons, restrictions are placed on the physical size of an antenna's diameter D. By combining two or more antennas separated by a baseline $\mathbf{B}$ astronomers can measure the intensity of the sky signal in terms of the spatial frequency $\frac{\mathbf{B}}{\lambda}$ [1]. In interferometry $|\mathbf{B}| > D$ and thus by combining two smaller antenna apertures astronomers can generate an image with the resolution that would be obtained if an antenna of diameter $|\mathbf{B}|$ was used. Depending on the baseline $\mathbf{B}$ celestial bodies can be viewed with higher and higher angular resolution.

Modern interferometry began in 1890 when Michelson published a paper detailing how to measure the profile of a star by recording the visibility of interfering signals with various baselines [60]. The fringe visibility $I_{max} - I_{min}/I_{max} + I_{min}$, where I_{max} and I_{min} are the maximum and minimum intensity in the fringe pattern, is a measure of the fringe contrast. In 1921 Michelson used such a device in the Mount Wilson Observatory in California to calculate the diameter of α Orionis [61]. In the 1950's Ryle applied the principles of stellar interferometry to radio astronomy. The first radio interferometer was constructed at the Mullard Radio Astronomy Observatory at Cambridge University UK. To date the most ambitious project in radio astronomy is the ALMA project in north Chile. It will consist of sixty four 12 m telescopes operating in ten bands between 1 cm and 0.3 mm [62].

The output of an interferometer is the mutual coherence function of the sky signal. In accordance with the *van Cittert − Zernike theorem* the mutual coherence function of a signal, and therefore the output of an interferometer, is related to the intensity of the input signal. Aperture synthesis allows us to derive the intensity $I_\nu \sim E^2$ of an incident signal from the response of an interferometer at various baselines $R(\mathbf{B})$. If an interferometer points in a direction $\mathbf{s} = \mathbf{s}_0 + \sigma$ where $\mathbf{s}_0$ is the centre of the region under observation and the sensitivity of the antenna is $A(\sigma)$ then the total response of the instrument is

$$R(\mathbf{B}) = exp\left[i\omega\left(\frac{1}{c}\mathbf{B}\cdot\mathbf{s}_0 - \tau\right)\right] d\nu \int\int_S A(\sigma)I(\sigma)exp\left(i\frac{\omega}{c}\mathbf{B}\cdot\sigma\right)d\sigma \qquad (2.2.1)$$

[1] The term baseline refers to the displacement between the centres of any two collecting antennas.

where the bandwidth ($d\nu$) is taken into account [2]. From equation (2.2.1) we can define the function

$$V(\mathbf{B}) = \int_S \int A(\sigma) I(\sigma) exp\left(i\frac{\omega}{c}\mathbf{B}\cdot\sigma\right) d\sigma \tag{2.2.2}$$

which is called the visibility function of the interferometer. The visibility determines the power response of an interferometer to any incident sky signal. From equation (2.2.2) it is apparent that $V(\mathbf{B})$ is a fringe pattern whose spatial frequency is dependent on the baseline length. We can define the coordinate system $\frac{\omega}{2\pi c}\mathbf{B} = (u, v, w)$ where u, v, and w are measured in units of wavelength. If the field being mapped is small then the visibility becomes independent of w so that $V(u, v, w) \approx V(u, v, 0)$ and

$$V(u, v) = \int_{-\infty}^{\infty}\int_{-\infty}^{\infty} A(x, y) I(x, y) e^{i2\pi(ux+vy)} dxdy \tag{2.2.3}$$

where $I(x, y) \approx I(\sigma)$ is the intensity received from a patch of sky. Equation (2.2.3) is the fundamental law of aperture synthesis. It shows that the response of an interferometer, $V(u, v)$, is the inverse Fourier transform of the spatial intensity pattern of the area of sky under observation. By observing the sky with a range of baselines the brightness distribution of an extended source can be calculated[3].

2.2.2 Radio receivers

Radio receivers are devices that measure the spectral power density of an incident signal. Incoherent radiometers are receivers in which the phase of the signal is not preserved during detection. The most common detection devices used in such instruments are bolometers. Bolometers function on the principle that any electric field falling onto a conductor will increase its resistance due to heating effects. If the bolometer

[2] The term $I(\sigma)$ is the intensity distribution of the received signal over the patch of sky. Therefore $R(\mathbf{B})$ is essentially the power response of the interferometer to a sky signal incident over a baseline $\mathbf{B}$. The exponential term outside the integral describes the phase response of the instrument at the map center. Here τ is used to account for geometrical and instrumental delays.

[3] All material in this section is discussed in detail in [63] and [64]. These two resources offer a comprehensive review of the state of the art methods for both radiometry and interferometry.

is adequately biased the change in resistance can be measured allowing calculation of the power of the incident signal. If the radiation incident on the bolometer is chopped with a modulating frequency ν_c then the change in temperature of the detector is

$$|\Delta T| = \frac{P_0}{G\sqrt{1 + (2\pi\nu_c\tau_t)^2}} \tag{2.2.4}$$

where $\tau_t = C/G$ is the thermal time constant for a heat capacitance C and an electrical conductance G. The power of the input signal P is equal to $P_0 e^{2\pi i\nu_c t}$. For a bolometer detector to be useful it must have a short thermal time constant τ_t so that chopping frequencies faster than instrumental and weather changes can be used. Sources of noise on a bolometer include Johnson noise, phonon noise and amplifier or load resistor noise. The measure used to define the quality of a bolometer is referred to as the *noise equivalent power* (NEP). This is the power required to fall on the bolometer to raise its output by an amount equal to the RMS noise. Its value is equal to

$$NEP = 2\epsilon k T_{BG}\sqrt{\Delta\nu} \tag{2.2.5}$$

where ϵ is the emissivity of the background, $\Delta\nu$ is the device's bandwidth, k is the wavenumber and T_{BG} is the background temperature. Traditionally bolometers have proven popular within CMB experiments. They have been recently employed within the PLANCK, QUaD, BICEP and CLOVER telescopic systems. By using a wire grid the bolometers used in these experiments were made polarization sensitive [65].

Traditionally heterodyne detectors are used in interferometry. However the QUBIC experiment is a novel instrument that will mix interferometry with incoherent radiometry. The purpose of these efforts is to combine the large bandwidth and therefore the sensitivity of incoherent bolometer detectors with the error control offered by interferometers. *In QUBIC bolometer detectors will be used to measure the spectral power density of visibility patterns produced by interferometry.*

2.2.3 Additive Bolometric Interferometry

The goal of QUBIC is to use bolometric interferometry in order to constrain the CMB's tensor-to-scalar ratio to within 0.01 [50]. Although the design of the instrument has evolved during the early stages of the collaboration the intended function of the experiment remains the same. A signal will be collected by a number of horn antennas. The signal is then split into orthogonally polarized beams via orthomode transducers (OMTs) and re-emitted into the cryostat using secondary horns. The combiner then focuses the beams onto an array of incoherent detectors where they interfere due to a geometrical phase shift. After being split by the OMTs the phase of each orthogonally polarized beam will be modulated. As we will briefly explain it is these controlled phase shifts that will allow recovery of the sky polarization from the final intensity pattern.

Figure 2.1 shows a schematic diagram of the QUBIC cryostat initial design. If sky signals E_1 and E_2 enter each of the receiver horns they will be separated by the OMTs into co-polar and cross-polar components $(E_{1\parallel} + E_{1\perp})$ and $(E_{2\parallel} + E_{2\perp})$ respectively. These polarized signals are then re-emitted into the optical combiner via the secondary horns. The time averaged power output from a single bolometer will be related to the modulus of total electric field incident on the detector array. Assuming unity gain and ignoring any imposed phase shifts the power response of a single bolometer (S_k) is related to the squared sum of the electric field components

$$S_k \approx (E_{1\parallel} + E_{1\perp} + E_{2\parallel} + E_{2\perp}) \times (E_{1\parallel} + E_{1\perp} + E_{2\parallel} + E_{2\perp}). \tag{2.2.6}$$

This response can be expanded into

$$\begin{aligned} S_k \approx (E_{1\parallel}{}^2 + E_{1\perp}{}^2 + E_{2\parallel}{}^2 + E_{2\perp}{}^2) + (2E_{1\parallel}E_{1\perp} + 2E_{2\parallel}E_{2\perp}) \\ +(2E_{1\parallel}E_{2\parallel} + 2E_{1\perp}E_{2\perp}) + (2E_{1\parallel}E_{2\perp} + 2E_{1\perp}E_{2\parallel}) \end{aligned} \tag{2.2.7}$$

where the terms $(2E_{1\parallel}E_{2\parallel} + 2E_{1\perp}E_{2\perp})$ and $(2E_{1\parallel}E_{2\perp} + 2E_{1\perp}E_{2\parallel})$ correspond to the Stokes I and U components of the cross correlated sky signal respectively. Assuming that the CMB contains no V component this information is sufficient to quantify the degree of CMB polarization.

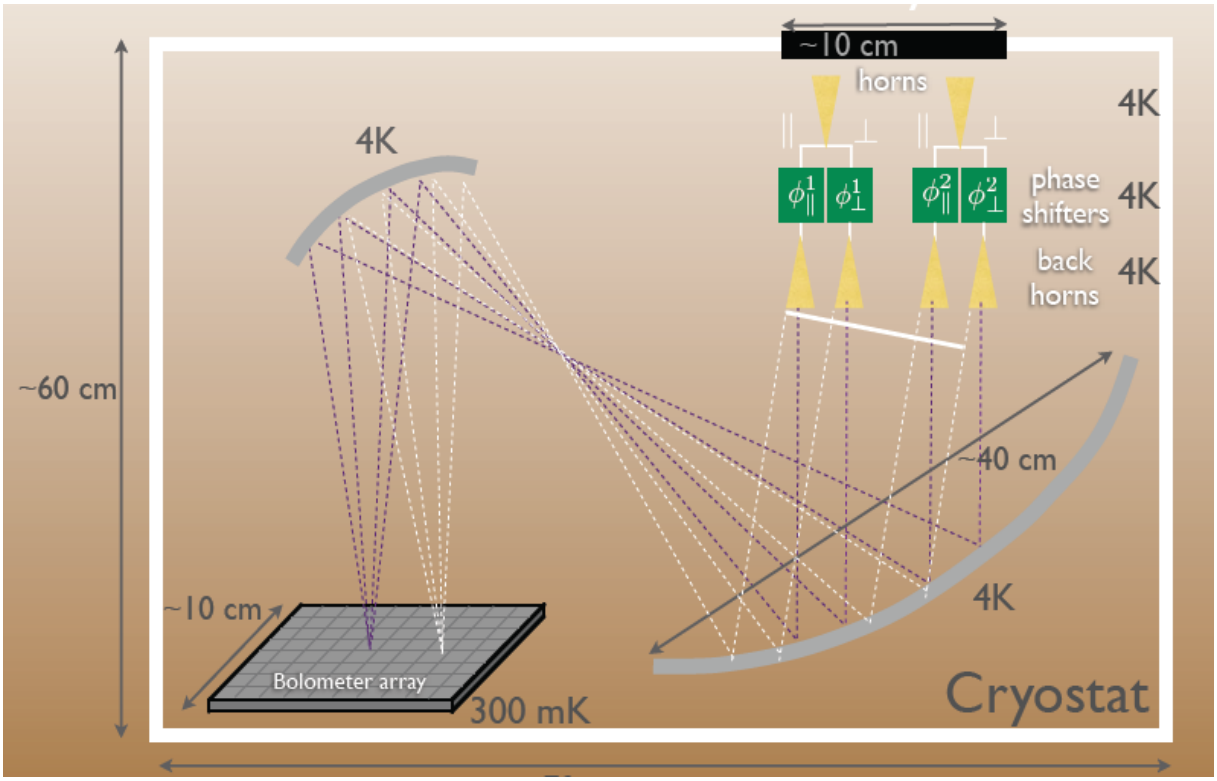

Figure 2.1: A simple bolometric additive interferometer. The initial designs for the QUBIC instrument resembled this illustration. Here the dimensions are indicative only. This image is taken from [57].

The model of Figure 2.1 is a simplification of the QUBIC instrument. It is expected that the final QUBIC design will consist of at least 144 sky horns. Equations (2.2.6) and (2.2.7) become more complicated when more than two sky horns are considered. Such matters will be discussed briefly.

Within astronomy there are two approaches to beam combination using an optical device. The first is Michelson interferometry in which beams are combined at the pupil plane of the instrument. Here the instrument combines beams from two separate yet superimposed entrance apertures. The second is Fizeau interferometry in which beams are combined at the image plane of an instrument. Here the entrance apertures are displaced from one another and so the beams from these apertures can only combine at the instrument's image plane [66]. Crucially whereas the output for a Michelson/multiplying interferometer is proportional to $E_0^2 \cos\phi$, where E_0 is the sky signal and ϕ indicates the phase shift between the interfering beams, the output

for a Fizeau/adding interferometer is proportional to $E_0^2 + E_0^2 \cos\phi$. The QUBIC instrument will therefore function as a CMB Fizeau interferometer. A simple optical Fizeau interferometer can be constructed by putting two pinholes in a mask in front of a Cassegrain telescope. The MBI collaboration was one of the first experiments to use such principles at far infrared wavelengths [46].

A visual example of the intensity pattern resulting from several apertures in a Fizeau interferometer is shown in Figure 2.2. The fringe patterns from baselines of various orientations are shown. The resulting intensity that the bolometer array detects is the furtherest image on the right hand side. The visibilities of the CMB polarization components are contained in this summed electric field. A brief outline of the QUBIC design to date and how the B-mode polarization is recovered from the imaged fringe patterns is presented below.

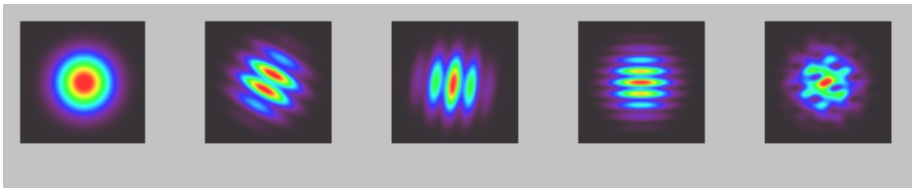

(a) (b) (c) (d) (e)

Figure 2.2: A simple bolometer additive interferometer: (a) Gaussian beam from a single entrance aperture, (b) - (d) fringe patterns from individual baselines of equal length yet various orientations and (e) the intensity pattern at the focal plane of the Fizeau interferometer resulting from all three baselines. All images taken from `http://www.qubic.org/`.

2.3 The QUBIC experiment

Heterodyne CMB interferometers and imagers such as DASI, CBI and QUaD have successfully observed E-mode polarization [67]. Although upper limits were placed on the scalar-to-tensor ratio these instruments were not sensitive enough to observe B-modes. QUBIC is a proposed advance on these experiments that implements incoherent detectors to detect the power contained in the visibility patterns from multiple baselines. QUBIC is a combination of the MBI and BRAIN collaborations both of

which were investigating the use of bolometric interferometry. These efforts were combined in 2008. BRAIN had launched three pathfinder campaigns at Dome C during the Antarctic summers of 2006, 2007 and 2009. The MBI collaboration constructed a four horn prototype Fizeau interferometer and upon implementation of a Cassegrain optical combiner made observations in 2008 and 2009.

2.3.1 QUBIC specifications

The design features of QUBIC were driven by one simple dictum. In order for additive bolometric interferometry to be a reasonable approach to observing B-modes the sensitivity of any instrument must be comparable to that of an imager. QUBIC (with all six modules, 2 at each of 3 frequencies) aims to constrain a tensor to scalar ratio of 0.01 (at the 90 % confidence level) in one year of taking data.

Every aspect of the QUBIC experiment from the number of sky horns to the size of the detector array was driven by this requirement. As one would expect inherent difficulties were encountered between the science requirements of the instrument and the engineering feasibility of any design. For example the number of sky horns and the beam size of these horns must be large enough to observe the CMB at the required angular scales yet must also fit behind an optical window that can be constructed. The QUBIC design represents a collective effort of more than 1 year to rectify such issues [4]. The study of whether an additive interferometer can be constructed with a sensitivity on par with an imager was carried out at the APC in Paris [5]. The most prominent results of this study are shown below.

The QUBIC collaboration had hoped to purchase the horn antennas used by the cancelled CLOVER experiment [68]. These horns were designed to operate at 97 GHz. Therefore an initial analysis of the sensitivity of a bolometric interferometer was carried out at frequencies from 90 to 100 GHz. There are two fundamental parameters driving the design of QUBIC. The first is the size of the primary beam of the sky horns while the second is the total number of these horns. Both these values are directly related to the tensor-to-scalar ratio we wish QUBIC to be capable of detecting. In

[4] The author of this thesis has been directly involved in these efforts.

[5] Université Paris Diderot-Paris 7,Laboratoire APC,Bâtiment Condorcet,Case 7020,75205 Paris Cedex 13. Website: `http://www.apc.univ-paris7.fr/APC_CS/en/home`

Figure 2.3 it is shown that a beam size of 15° will allow QUBIC to observe a tensor-to-scalar ratio of 0.01 if an array of 144 sky horns is implemented. If 10 observing modules are implemented and the NET of the bolometers is 200 μK Hz$^{1/2}$ $r \approx 0.01$ is achievable within 1 year of operation.

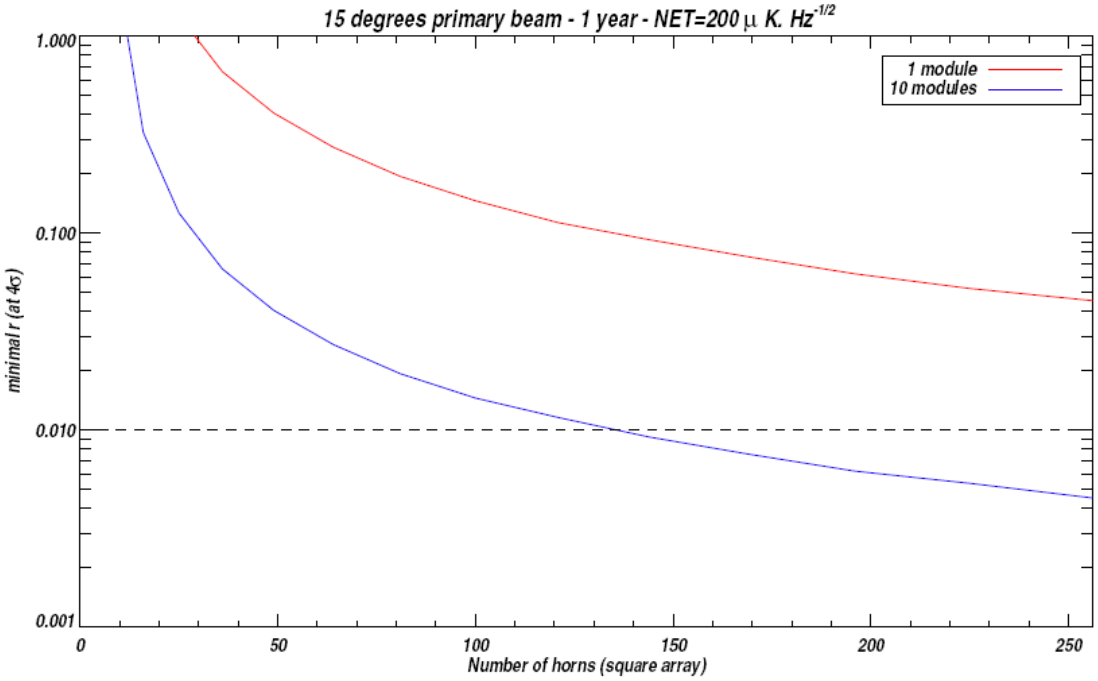

Figure 2.3: An $r \approx 0.01$ will be observable within one year of operation if 10 modules of 144 horns are implemented and each has a 15° FWHM beam on the sky. This plot was created at the APC for the QUBIC white paper using formula found in [69].

A more comprehensive plot relating the detectable tensor-to-scalar ratio, the size of the beam observing the sky and the number of back-to-back horns is displayed in Figure 2.4. Here it is shown that the minimum beam size and number of horns required to achieve a 0.01 ratio forces implementation of a 400 mm diameter optical window. It is shown once again that at least 144 horns whose primary beams are approximately 15° FWHM are required to detect $r < 0.01$[6].

[6]In Figure 2.4 the effect of bandwidth is not taken into account. A complete discussion of consequences of bandwidth in QUBIC is presented in [70].The conclusions will be discussed in a later chapter

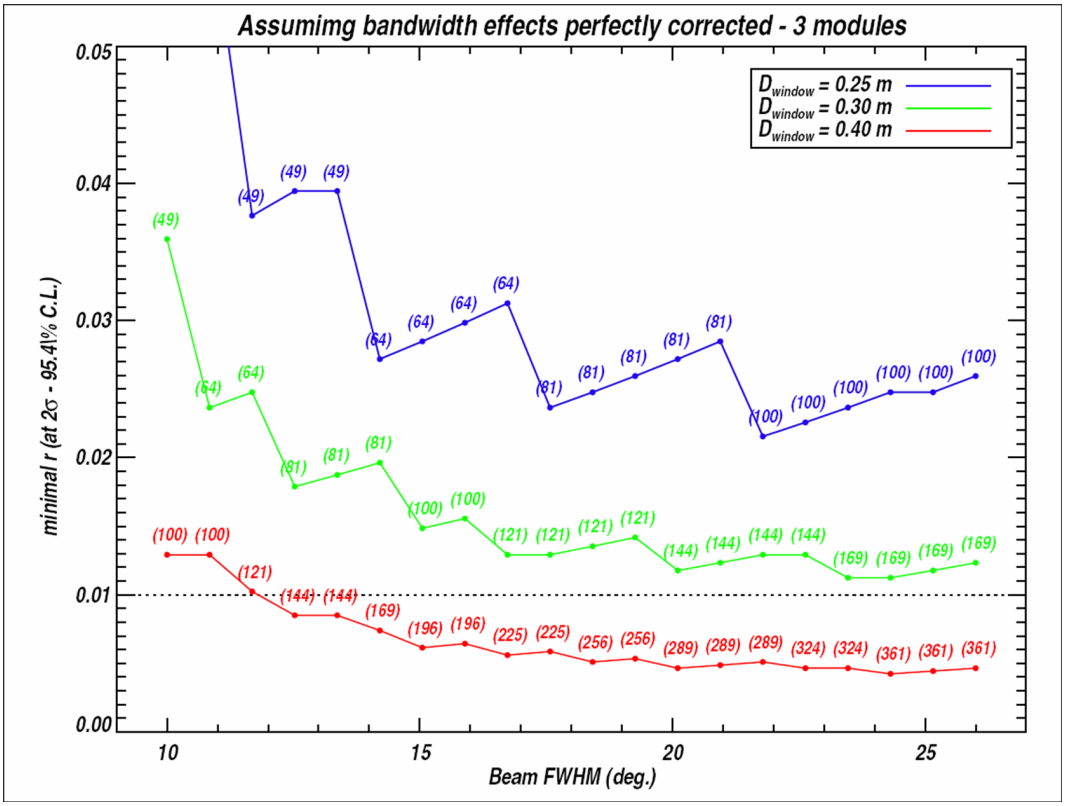

Figure 2.4: Minimal scalar-to-tensor ratio detectable versus the beam size for three observing modules. The number of sky horns are shown in parenthesis.

The angular scales at which the primordial B-mode power spectrum is most likely to be observed is between $l_{min} = 30$ and $l_{max} = 200$. Assuming a flat sky approximation $l = 2\pi \times u$ and $u = \frac{\mathbf{B}}{\lambda}$ [71]. Here $|\mathbf{B}|$ is the physical separation of the antennas of a given baseline and u is the spatial frequency of the fringe patterns. Therefore the multipoles at which we observe the sky are related to the baseline displacements by

$$l = \frac{2\pi}{\lambda} \times \mathbf{B}. \tag{2.3.1}$$

In accordance with the Nyquist sampling criteria the bolometer array must be large enough to sample the fringe patterns from each individual baseline at least twice. The locations of the fringe maxima are given by

$$n\lambda = |\mathbf{B}| \sin\theta \tag{2.3.2}$$

where θ is the angle subtended by the fringe of order n for a baseline of length $|\mathbf{B}|$. Under the paraxial approximation $\sin\theta \approx \frac{x_f}{f}$. Here x_f is the location of the first fringe maximum above the central axis and f is the focal length of the optical device that combines the two signals at its focal plane. For a given focal length the maximum size of a bolometer is determined by the Nyquist criterion for the longest baseline (smallest fringe possible). The total number of bolometers required is determined by the need to sample at least one fringe ($n = 1$) of the shortest baseline pattern. If we set $x_f = n_b \times D_b$ where n_b is the number of bolometer detectors sampling a single fringe while D_b is the size of a single bolometer, then the number of bolometers required by QUBIC is related to the baseline separation by

$$n_b = \left(\frac{f\lambda}{|\mathbf{B}|D_b}\right). \tag{2.3.3}$$

As shown in equation (2.3.3) the number of bolometers is dependent on the focal length of the combiner, the wavelength at which QUBIC will observe and the length of the baselines. As we can see small baselines require a larger number of bolometers. Assuming the smallest multipole at which B-modes are observable is $l = 30$ Table 2.1 lists the maximum number of bolometers required by QUBIC for various wavelengths and focal lengths.

Table 2.1: Parameters governing the size of the bolometer detector array and focal length of the optical combiner.

Focal length (mm)	Bolometer length (mm)	Wavelength (mm)	$\mathbf{B}_{min}$ (mm)	Number of bolometers	Area of detector plane (mm^2)	First long baseline fringe location (mm)	First short baseline fringe location (mm)
100	3	2	10	289	51	3.1	20
100	5	2	10	100	51	3.1	20
300	3	2	10	2500	150	9.4	60
300	5	2	10	900	150	9.4	60
200	3	3	15	1156	100	6.3	40
200	5	3	15	400	100	6.3	40
400	3	3	15	4356	200	12.6	80
400	5	3	15	1600	200	12.6	80

Table 2.1 lists the number of bolometers required for designs operating at different wavelengths and focal lengths. The off-axis locations of the first fringe generated by the smallest and longest baselines are also listed. The number of bolometers required in order to capture at least 95 % of the power re-emitted from the secondary horns is also shown. This figure has been calculated using simple quasi optical methods that we will discuss shortly. With the exception of a 100 mm focal length combiner and 5 mm bolometers all these systems will adequately sample the fringe patterns according to the Nyquist criterion. Ultimately the limitations on the size of the bolometer detectors and the maximum number of detectors that can be manufactured will decide the maximum focal length permissible for the combiner. The value of 2500 shown in Table 2.1 is the absolute upper limit of the number of transition edge sensors (TES) bolometers that can be multiplexed together without the electronic overhead involved (e.g. power consumption) becoming too cumbersome. The TES bolometer detectors that are being developed for QUBIC are composed of a Niobium Silicon (NbSi) compound. This technology allows the critical temperature of the bolometer to be adjusted by varying the Nb concentration. TES bolometers are well suited to multiplexing by SQUID devices and can operate at low temperatures. These detectors can be constructed to be between 3 mm and 5 mm in diameter [72]. During a meeting of collaborators in Paris at the end of July 2009 the various instrument designs listed in Table 2.1 as well as the requirements inferred from Figure 2.4 were all considered. The following blue print design for QUBIC was then agreed upon.

- The sky signal will be collected by 2×3 modules of 144 back-to-back horns operating at 90, 150, and 220 GHz. The bandwidth of these single-moded horns will be approximately 25%. The signal received by the horns will propagate through phase shifters [7]. The horns will produce beams of high Gaussicity of at least a 14° FWHM [8]. The horns will be arranged in a square grid and will be capable of observing the sky over the $l = 30 - 200$ multipoles .

- Phase shifting sequences will be carried out by inserting a combination of strip-line delays at the back end of the sky horns. Also the back end of the sky horns will

[7] Phase shifters in QUBIC are implemented to modulate the polarized beams generated by the OMTs. As we shall later discuss its is this phase shifting process that allows us to recover the Stokes visibilities from the final intensity pattern.

[8] A beam size of 14° FWHM rather than the value of 15° FWHM previously stated was eventually agreed upon.

require polarized switches which will be used during calibration.

- Orthomode transducers (OMTs) will be used to split the incident sky signal into two orthogonally polarized beams. The OMTs are placed at the back end of the sky horns. These polarized beams then propagate into the optical combiner via separate secondary horns. This model therefore requires twice as many secondary as sky horns.

- The optical window must be large enough to ensure a very low edge taper of the beam from the sky facing horn antennas. The window will be constructed from either HDPE as in the QUaD experiment or zotefoam as in BICEP. QUBIC's optical window will have to be larger ($\approx$ 400 mm) than both these examples. Based on the QUaD and BICEP examples the window thickness is expected to be at least 100 mm.

- The detectors will be superconducting TESs. The focal plane in each module will consist of at least 900 of these sensors. The maximum number of these is limited by multiplexing complexities. The space available for wiring on the substrate ultimately limits the number of sensors that can be multiplexed. The signal from the sensors will be amplified by SQUID circuits. All detectors will be laid out with an $\approx$ 100% filling factor. The number of elements should be enough to ensure that at least 95% of the power incident on the focal plane is captured. We consider a bare array (no coupling optics). For the optical simulations in this thesis we usually consider all power falling on the detector sensitive area as being captured. The target noise equivalent power (NEP) of the TES devices is 5-10$\times 10^{-18} W/\sqrt{Hz}$ with a time constant shorter than 10 ms.

- The cryogenics will consist of a 4K pulse tube cooler for each module combined with a 100 - 300 mK dilution unit for the focal plane. A maximum upper limit of 1 m^3 has been placed on the dimensions of the 4 K units.

- A high level of redundancy (the number of baseline pairs that exist with equal separation and direction) exists in the number of baselines. In an ideal instrument the fringe patterns generated from each equivalent baseline should be identical to one another. This will not be the case in a practical instrument due to wavefront aberrations imposed on the beams by the optical combiner. However a period of calibration is proposed for QUBIC in which every baseline is examined individually.

The discrepancies between each baseline can be used to calibrate the gain, phase and polarization mismatches between all channels. Thus systematic errors that introduce uncertainties into the Stokes visibilities can be minimized.

The optical combiner is responsible for producing the summed signal from all possible baselines over the detector array. Originally the prototype MBI experiment attempted to implement a Bulter combiner to sum all incident signals. Later a Cassegrain telescope was used to combine the baselines and MBI observed fringes. The vast increase in the number of baselines from MBI to QUBIC essentially rules out the use of a Bulter combiner due to the complexity involved in adding all signals. For this reason an optical combiner will also be used in QUBIC. The fringes observed by MBI demonstrate the applicability of an optical combiner to bolometric interferometry [73]. The design and modeling of the optical combiner are the subject of this thesis.

A diagram illustrating the diameter of the primary and secondary horns as well as the size of the necessary optical window is shown in Figure 2.5. It is estimated that if the above specifications are followed QUBIC will be able to observe a scalar-to-tensor ratio of 0.01 within 2 years of operation [69]. A plot showing this conclusion is shown in Figure 2.6.

2.4 Phase Shifting and equivalent baselines

Phase shifters are implemented in the QUBIC experiment in order to modulate the re-transmitted signal from the secondary horns. The fields are phase shifted in order to assist the recovery of the polarization components of the sky signal. We will now briefly discuss the theory behind this phase shifting scheme. As we shall see a natural consequence of data sampling in this manner leads to the notion of "equivalent baselines". We suppose our interferometer has $N_h = N_l \times N_l$ sky horns and the signal entering the j^{th} horn is written as $E_j e^{2\pi i \nu t}$ where ν represents a single frequency. For the moment we will not consider the polarization of the signal. A time dependent phase shift $\Phi_j(t)$ is applied to this signal and it then propagates through the optical combiner to the bolometer detector k where a geometrical phase shift Δ_{jk} results. The power measured by a single bolometer detector S_k is the auto and cross-correlation of all beams from the secondary horns

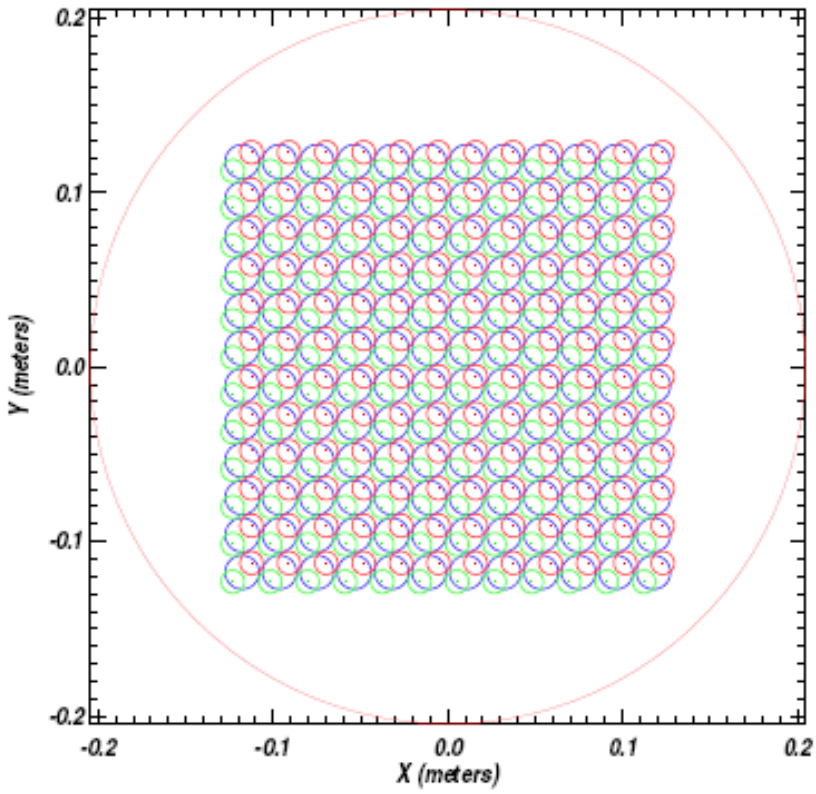

Figure 2.5: Diameter of front end optics. Here the secondary horns are shown green and red indicating orthogonal polarization states. The sky horns are shown in blue while the diameter of the optical window is shown in red. This is the smallest window required to ensure at least a 99% of the power from the most extreme horns enters the combiner. Figure taken from `http://www.qubic.org/`.

$$S_k(t) \propto \left| \sum_{j=1}^{N_h} E_j e^{i(\Delta_{jk}+\Phi_j(t))} \right|^2 = \sum_{j,m=1}^{N_l} E_j E_m^* e^{(\Delta_{jk}-\Delta_{mk}+\Phi_j(t)-\Phi_m(t))}. \tag{2.4.1}$$

In a similar manner to equations (2.2.6) and (2.2.7) when this equation is expanded the cross terms will contain the Stokes parameters of the incident signal. We rewrite equation (2.4.1) as

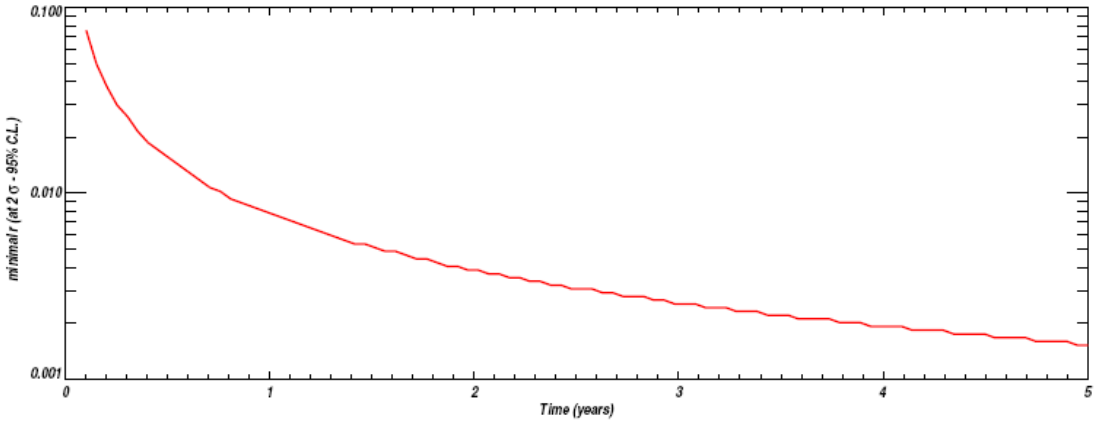

Figure 2.6: Implementation of a 144 array of sky horns with a 14° beam size will allow QUBIC to obtain a scalar-to-tensor ratio of 0.01 over an operation period of 1 to 2 years. This plot was created at the APC for the QUBIC white paper using methods found in [69]

$$S_k(t) \propto \sum_{j,m=1}^{N_l} E_j E_m^* e^{(\Phi_j(t)-\Phi_m(t))} = V_{jm} e^{i(\Phi_j(t)-\Phi_k(t))} \tag{2.4.2}$$

where the V_{jm} represents the visibilities we wish to recover. We have suppressed the time independent geometric phase shifts ($\Delta_{(j/m)k}$) as they do not affect the problem of visibility recovery [74].

In order to recover the visibilities we apply known phase shifts to the incident beams. When one includes a full description of the polarization using the Stokes parameters and the definition of visibility introduced in equation (2.2.2) the RHS of equation (2.4.2) can be expanded to give the response of a single bolometer as [75]

$$S_k(t) \;=\; N_h \int I(n)A(\mathbf{n})d\mathbf{n} \;+\; \int U(n)A(\mathbf{n})d\mathbf{n} \sum_{j=1}^{N_h} \cos(\Phi^{\parallel}_{k,i} - \Phi^{\perp}_{k,i})$$

$$+ \int V(n)A(\mathbf{n})d\mathbf{n} \sum_{j=1}^{N_h} \sin(\Phi^{\parallel}_{k,i} - \Phi^{\perp}_{k,i}) +$$

$$\sum_{b=1}^{N_b} Re[V_I(u_b)](\cos(\Delta\Phi^{\parallel\parallel}_{k,b}) + \cos(\Delta\Phi^{\perp\perp}_{k,b})) \;-\; \sum_{b=1}^{N_b} Im[V_I(u_b)](\sin(\Delta\Phi^{\parallel\parallel}_{k,b}) + \sin(\Delta\Phi^{\perp\perp}_{k,b}))+$$

$$\sum_{b=1}^{N_b} Re[V_Q(u_b)](\cos(\Delta\Phi^{\parallel\parallel}_{k,b}) - \cos(\Delta\Phi^{\perp\perp}_{k,b})) \;-\; \sum_{b=1}^{N_b} Im[V_Q(u_b)](\sin(\Delta\Phi^{\parallel\parallel}_{k,b}) - \sin(\Delta\Phi^{\perp\perp}_{k,b}))+$$

$$\sum_{b=1}^{N_b} Re[V_U(u_b)](\cos(\Delta\Phi^{\parallel\perp}_{k,b}) + \cos(\Delta\Phi^{\perp\parallel}_{k,b})) \;-\; \sum_{b=1}^{N_b} Im[V_U(u_b)](\sin(\Delta\Phi^{\parallel\perp}_{k,b}) + \sin(\Delta\Phi^{\perp\parallel}_{k,b}))+$$

$$\sum_{b=1}^{N_b} Re[V_V(u_b)](\cos(\Delta\Phi^{\parallel\perp}_{k,b}) - \cos(\Delta\Phi^{\perp\parallel}_{k,b})) \;-\; \sum_{b=1}^{N_b} Im[V_V(u_b)](\sin(\Delta\Phi^{\parallel\perp}_{k,b}) - \sin(\Delta\Phi^{\perp\parallel}_{k,b}))$$
$$+n_k \tag{2.4.3}$$

where the Stokes visibilities are defined as $V_s(\mathbf{u_B}) \;=\; \int S(\mathbf{n})A(\mathbf{n})e^{2i\pi\mathbf{u_B}\cdot\mathbf{n}}d\mathbf{n}$ where $\mathbf{n}$ is the direction the instrument is pointing and $\mathbf{u_B}$ is the displacement of a baseline b in units of wavelength. Also n_k is the noise on a bolometer k. The letter S stands for the I, Q, U or V Stokes parameter. Once again the value $A(\mathbf{n})$ is the antenna's sensitivity and N_b is the number of baselines. The term $\Delta\Phi^{\parallel\parallel}_{k,b} = \Phi^{\parallel\parallel}_{k,i} - \Phi^{\parallel\parallel}_{k,j}$ is the total phase shift difference at detector k between the i^{th} and j^{th} horns that make the b baseline (likewise for the $\Delta\Phi^{\perp\perp}_{k,b}$, $\Delta\Phi^{\parallel\perp}_{k,b}$ and $\Delta\Phi^{\perp\parallel}_{k,b}$ terms).

Although seemingly complex the signal over all bolometers shown in equation (2.4.3) can be grouped into the simple linear expression

$$S = A \cdot X + n. \tag{2.4.4}$$

Here the phase shifting sequences are known coefficients contained in the matrix A while $N = n \cdot n^T$ is the noise covariance matrix. We can then solve this signal for the unknown Stokes visibility terms

$$X = (A^t \cdot N^{-1} \cdot A)^{-1} \cdot A^t \cdot N^{-1} \cdot S. \tag{2.4.5}$$

Equation (2.4.5) is summed over all possible baselines (N_b). However such a conventional approach causes problems. The length (D) of the matrix X is equal to $3+8\times N_b$ where $N_b = N_h(N_h-1)/2$. Here N_h is the number of sky horn antennas. It is clear for a large horn array that this number is excessively large. For example a 10×10 array will produce a matrix whose length is 39603. As many data samples as unknowns are required and so a large amount of data retrieval from the sky must be followed by manipulation of large matrices. It is too cumbersome to proceed this way.

For QUBIC it has been suggested that all horns separated by equivalent baselines can be treated as a single unit during the phase shifting sequences. Therefore equation (2.4.4) can be re-expressed to consider the phase shifting sequences applied to all equivalent baselines only. The number of possible equivalent baselines (N_{eq}) is equal to $2(N_h - \sqrt{N_h})$. The value D is thus reduced to 180 for a 10×10 array [75] [9].

We define the noise covariance matrix (N) for the recovered visibilities as $\sigma^2(A^TA)^{-1}$ where σ^2 is the variance of the white noise that contaminates the received signals. It has been shown that this noise is minimized by ensuring that the orthogonal relationship

$$\sum_t A^*_{tm} A_{tm'} \; = \; 0 \, for \, m \neq m' \tag{2.4.6}$$

exists between the phase shifting sequences [74]. This means that the Stokes visibilities are recovered with minimal noise when the phase shifts between varying equivalent base lines are orthogonal[10]. This process of inducing orthogonal phase shift sequences over the various equivalent baselines is referred to as the *coherent summation of equivalent baselines*. This ensures that the recovered visibilities are maximally independent of one another. Due to the orthogonal phase shifting sequences the diagonal elements of the noise covariance matrix are then $\frac{\sigma^2 N_h}{N_t}\frac{1}{N_{eq}^2}$ while all other elements are zero. Here N_t is the number of time samples. When a bolometer detector array is considered the noise becomes dependent on the beam size of the sky horns (Ω) and the noise

[9] The concept of equivalent baselines was introduced by Romain Charlassier of the APC Paris in [75]. In this section we are summarizing the conclusions of this document.

[10] It is not necessary for the subject of this thesis to explain how orthogonal phase shift sequences can be calculated. An excellent discussion regarding possible phase shifting sequences is given in [74] and [75].

equivalent temperature (NET) of the individual bolometers. The diagonal elements of the covariance matrix become

$$N_{ij} = \delta_{ij} \frac{4(NET^2)\Omega^2 N_h}{N_t} \frac{1}{N_{eq}^2}. \tag{2.4.7}$$

when we only consider a monochromatic instrument. As shown the signal noise received by each bolometer is inversely proportional to the number of equivalent baselines implemented. Equation (2.4.7) is fully derived and discussed in [69]. The minimum number of equivalent baselines required to reduce the noise sufficiently to observe B-modes has been calculated using equation (2.4.7). It has been shown that when the FWHM of the sky horns is greater than 10° and the number of horns is greater than 144 the noise incident on each bolometer will be low enough so that the sensitivity of a bolometric interferometer is comparable with that of a bolometric imager.

The implementation of identical phase shifting schemes for equivalent baselines places practical constraints on the performance of the optical combiner. If equation (2.4.7) is summed over equivalent baselines in order for a full noise reduction proportional $\frac{1}{N_{eq}^2}$ the fringe patterns generated by each baseline in a redundant group must be as similar as possible. In effect each bolometer must image multiple redundant fringes with minimized variance due to wavefront aberrations. Thus any optical combiner implemented in QUBIC must possess an aberration free field-of-view that extends over as much as the detector array as possible. During the design phase of QUBIC there was a significant amount of work done to assess what level of aberration would be acceptable. As discussed later in Section 6.4 the effect of the aberrations is to reduce the overall sensitivity of the instrument. It was decided that a certain level of aberration would be tolerable so long as they did not reduce the overall sensitivity of the instrument by more than 10 %. As shown in Table 2.1 limitations on the number of bolometer detectors that can be implemented restrict the focal length to a maximum value of 300 mm at 150 GHz or 400 mm at 100 GHz. These focal lengths are extremely small when one considers the large entrance diameter created by the back-to-back horn array. A pupil size of at least 140 mm^2 is required for a 12×12 back-to-back horn array of 14° beams. A low focal ratio optical combiner will therefore be required that produces unaberrated fringe patterns while combining beams over a large field of view. These are extremely difficult criteria to meet. The requirement of aberration

free fringe patterns may be relaxed if an efficient calibration method is developed to take account of the wavefront aberrations in the combing beams. At time of writing such issues are under investigation. However from the point of view of prudence this thesis is concerned with designing Fizeau combiners as diffraction limited as possible over the entire horn array.

2.5 Quasi optical analysis techniques

2.5.1 Methods for the optical modeling of CMB experiments

We have introduced the QUBIC experiment that is currently being designed in order to detect a CMB tensor-to-scalar ratio of 0.01. In order to achieve this QUBIC will require an extremely well designed and characterized optical combiner to induce geometrical phase shifts in the combining beams. The author's role in QUBIC has been to design and model such an optical combiner in light of the requirements and restrictions placed on the cryostat, detectors etc. We will conclude this chapter by briefly discussing the optical design and analysis techniques we have implemented in order to achieve this task.

This thesis concerns best practice for implementation of a quasi optical combiner within a bolometric CMB interferometer. From considerations presented in the previous sections the combiner implemented in QUBIC must be a fast, blockage-free system that has a large diffraction-limited field-of-view. As a starting point for designing such a device geometrical optics (GO), also known as ray-tracing, was used.

To fully model the behavior of any system designed using GO methods, analysis techniques that treat light as a wave phenomenon must next be implemented. This is especially true for QUBIC and all CMB experiments where the millimeter wavelengths and component sizes involved will generate a large degree of diffraction. Also if we wish to model the fringes generated by equivalent baselines, modeling techniques that can account for interference must be employed.

The basis for understanding the behavior electromagnetic signals propagating through various components is Maxwell's equations. Figure 2.7 indicates the various methods

available to model the electromagnetic behavior of an optical system. These methods are based on various analytical solutions and approximations to Maxwell's linear differential equations. The variety of methods is produced by imposing certain assumptions onto the three dimensional Maxwell equations. For example forcing a beam of light to travel in a region in which no source of charge is available produces the Helmholtz equation which is solvable using Fourier transform techniques. The methods we have used to model the fringe patterns produced by the QUBIC optical combiner are quasi optics (modal analysis), Fourier and physical optics.

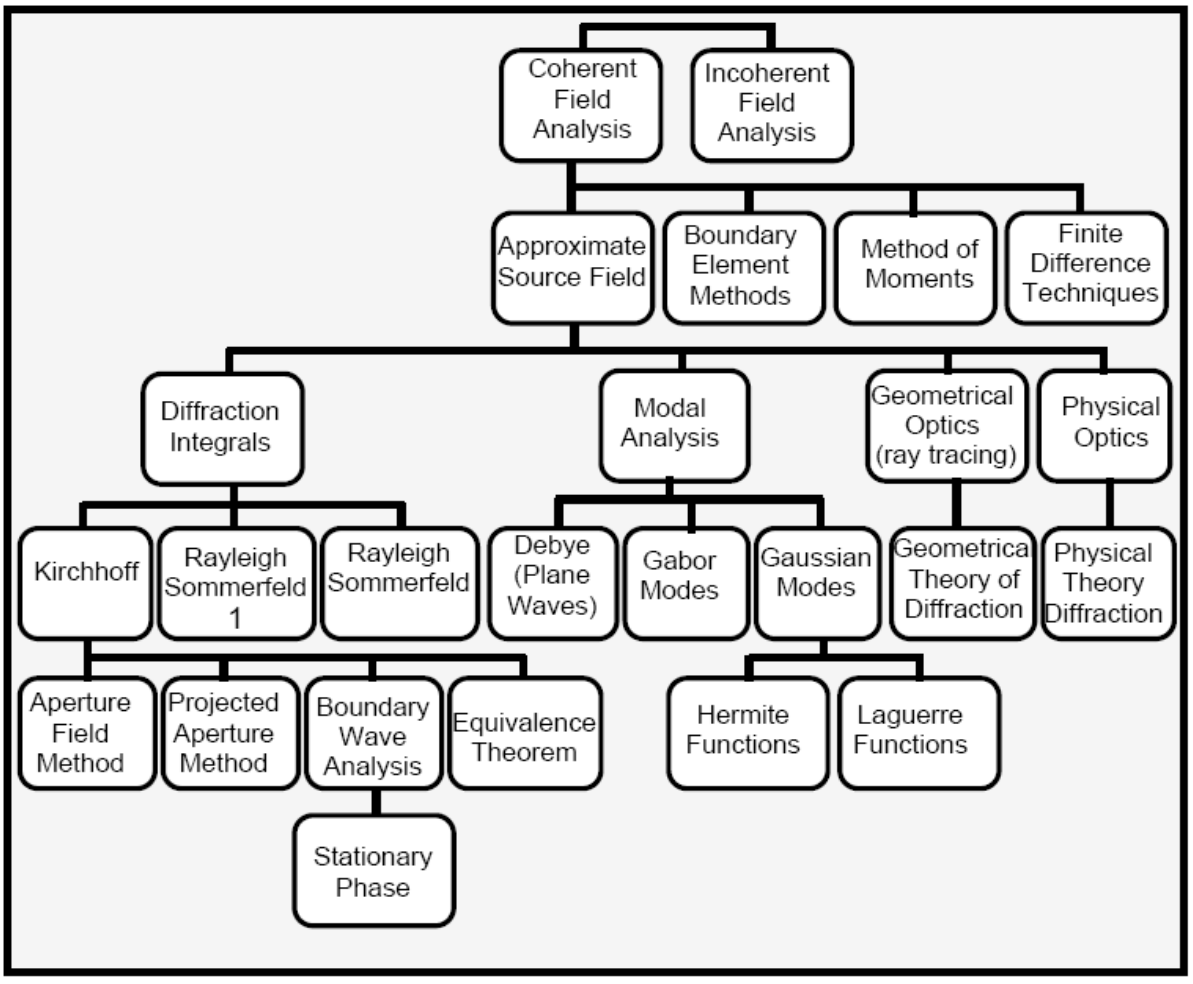

Figure 2.7: Analysis methods for optical modeling. This image is taken from [76].

Figure 2.7 indicates the various methods available to model the electromagnetic behavior of an optical system. Approximate source field methods essentially adopt the Huygens principal of secondary wavelets to solve Maxwell's equations. In these meth-

ods a source electric field generates an envelope of wavelets. The field created by these wavelets interact with the various optical components becoming redirected and refocused. All techniques use propagator functions to transfer the wavelet envelopes from one optical component to the next. The choice of propagator functions and how the electric fields interact with the optical components differentiates the diffraction integral, modal analysis and physical optics techniques from one another.

The diffraction integral approach utilizes Fourier transforms to propagate the electric field through the optical system. The optical components are phase transformers that refocus the electric field by reshaping its phase front[11]. The Gaussian mode techniques, referred to as quasi-optics from this point onwards, employs sets of closed Gaussian polynomials to describe the propagation of diffracting electric fields. Physical optics uses Green function solutions to Maxwell's equations to propagate the electric field from one component to another. The incident electric field induces a distribution of time varying electric and magnetic currents across a reflector surface. The field re-emitted by these currents is then calculated and propagated to the next reflector. The varying currents re-emit the electric field with a wavefront curvature equal to the reflector formation.

Physical optics is a full vector analysis of a reflecting optical system. As such the electric field can be independently calculated in all three spatial dimensions over a range of distances. A full treatment of polarization and concerns such as spillover is possible. Fourier and quasi optics are both scalar optical analysis techniques. Here the various components of the electric field all satisfy a single scalar wave equation. As such scalar optics will not provide an adequate analysis of polarization of an electric field. Also because scalar optics assume paraxial fields the accuracy of the techniques decreases rapidly when one moves outside the paraxial region. Paraxial restrictions simply mean we only consider or attempt to model the behaviour of the propagating field at small ($< 30^{\circ}$) angles relative to the propagation axis.

[11]The diffraction integral analysis technique will be referred to as Fourier optics from this point onwards.

2.5.2 Geometrical optics

Geometrical optics (GO) concerns the design and analysis of an optical system when the wavelength of light is negligible when compared with the optical component size and pencils of rays are assumed. The design of all refractive optical systems generally begins by considering Snell's law and the behavior of a ray at any surface boundary. By combining a pencil of rays at equi-phase locations a wavefront can be considered. Essentially all astronomical optical instruments involve transforming a plane wavefront from the sky into a spherical wavefront converging on a camera device. This of course is an ideal situation. In reality all transformed wavefronts will vary from a spherical approximation. In GO the Hamilton characteristic function is a powerful tool that allows us to quantify the variance of a given wavefront from a required planar or spherical wavefront [77] :

$$W(\sigma, \rho, \phi) = \sum_{l} \sum_{m} \sum_{n} {}_{l+n}k_{m+n,n} \sigma^{l+n} \rho^{m+n} \cos^{n} \phi \tag{2.5.1}$$

where ρ is the normalized aperture radius, σ is the field radius and ϕ is the azimuthal angle at the aperture. The value k is a coefficient that quantifies the contribution of each term in the expanded function. The characteristic function is a polynomial representation of the separation of a point on a given wavefront from an ideal reference front. Each term in the extended polynomial describes a particular classical phase aberration and gives the magnitude of their contribution to wavefront error. For example the classic coma aberration can be written as ${}_{3}k_{11}\sigma^{3}\rho\cos\phi$ while astigmatism is described by ${}_{2}k_{22}\sigma^{2}\rho^{2}\cos^{2}\phi$. The reduction of these aberrations is the fundamental goal of all optical design. A multitude of high performance systems can be designed from geometrical aspects. This is because consideration of the Hamilton function allows us to describe the wavefront aberration in terms of the surface properties of the optical devices. For example the wavefront coefficients ${}_{3}k_{11}$ and ${}_{2}k_{22}$ are equal to $\frac{1}{2}S_{11}$ and $\frac{1}{2}S_{111}$ respectively. Here S_{11} and S_{111} are called the Seidel coefficients. It has been shown that under paraxial approximations $S_{11} = -\frac{L}{2}y^{2}\left(\frac{1}{f}\right)^{2}\left(\frac{1+M}{1-M}\right)$ and $S_{111} = L^{2}\left(\frac{1}{f}\right)$ for a spherical mirror. Here f is the focal length of the mirror, L is the Lagrange invariant of the system, M is the magnification and y is the incident height of the marginal ray. Therefore the characteristic function allows us to calculate the

appropriate surface properties to minimize wavefront aberrations. The most elementary example of this is that the wavefront reflected from a parabolic mirror will not contain spherical aberration [78].

The initial design of the optical combiner was carried out using geometrical optics to derive dual reflector combiners with minimum wavefront aberrations. The Zemax software package was used to examine the propagation of rays through these possible combiners[12]. Zemax is a geometrical software package that will graphically illustrate the path of rays through an optical system. It also uses the characteristics of the defined optical surfaces to calculate the aberrations induced on a propagating wavefront. Zemax is a robust software package that can provide a fast initial assessment of a possible combiner.

In reality (and especially for CMB observations) the wavelength of light is not negligible as assumed in GO. Although Zemax offers some methods to model interference and diffraction they are highly reliant on ray optics as propagating functions for the electric field. Although the initial design of QUBIC was done in Zemax accurate fringe pattern simulations were done using the techniques of physical optics.

2.5.3 Physical optics (PO)

The behavior of electromagnetic fields in any region of space is described by Maxwell's equations

$$\begin{aligned} j\omega\epsilon\mathbf{E} - \nabla \times \mathbf{H} &= -\mathbf{J_E} \\ j\omega\mu\mathbf{H} - \nabla \times \mathbf{E} &= -\mathbf{J_M} \end{aligned} \quad . \tag{2.5.2}$$

Here $\mathbf{J_E}$ and $\mathbf{J_M}$ represent electric and magnetic source currents. These equations represent a linear system. Therefore the entire electromagnetic field through a region can be obtained by the superposition of fields produced by individual source currents. The radiated field produced by an entire volume of source distributions is obtained by integrating the system's impulse response to each source current. A physical optics

[12]Zemax is an industry standard software package that allows the user to design and analyze optical systems. For more information visit `http://www.zemax.com`.

analysis can only be implemented where the variables ϵ and μ are fully quantifiable. Here ϵ and μ are the electric permittivity and magnetic permeability constants of the medium respectively. It is clear from the curl and gradient operators that physical optics considers contributions in all dimensions around source currents. This means that physical optics is a vector analysis technique where the components of the electric and magnetic field must be calculated separately in all directions. This and the fact that the current contributions are recalculated at each optical surface means that physical optics is the most involved and time consuming technique for modeling reflector systems that we will use.

Maxwell's equations can be solved using dyadic Green functions to obtain the electric field and magnetic field generated by a distribution of source currents [13]. The dyadic Green functions are 3×3 dimensional matrices and serve as propagator functions within physical optics. The excited electric field radiated by a current distributed over a surface S is

$$\begin{aligned}\mathbf{E}(\mathbf{r}) = \tfrac{k^2 Z}{4\pi} \int_S \Bigg[\mathbf{J}_E \left(-\tfrac{j}{kR} - \tfrac{1}{k^2R^2} + \tfrac{j}{k^3R^3} \right) \\ + (\mathbf{J}_E \cdot \hat{\mathbf{R}}) \hat{\mathbf{R}} \left(\tfrac{j}{kR} + \tfrac{3}{k^2R^2} - \tfrac{3j}{k^3R^3} \right) \Bigg] e^{-jkR} ds \\ - \tfrac{k^2}{4\pi} \int_S (\mathbf{J}_M \times \hat{R}) \tfrac{1+jkR}{k^2R^2} e^{-jkR} ds\end{aligned} \tag{2.5.3}$$

while the magnetic field is

$$\begin{aligned}\mathbf{H}(\mathbf{r}) = \tfrac{k^2}{4\pi Z} \int_S \Bigg[\mathbf{J}_M \left(-\tfrac{j}{kR} - \tfrac{1}{k^2R^2} + \tfrac{j}{k^3R^3} \right) \\ + (\mathbf{J}_M \cdot \hat{\mathbf{R}}) \hat{\mathbf{R}} \left(\tfrac{j}{kR} + \tfrac{3}{k^2R^2} - \tfrac{3j}{k^3R^3} \right) \Bigg] e^{-jkR} ds \\ - \tfrac{k^2}{4\pi} \int_S (\mathbf{J}_E \times \hat{R}) \tfrac{1+jkR}{k^2R^2} e^{-jkR} ds.\end{aligned} \tag{2.5.4}$$

[13] A full description of how equation (2.5.2) can be solved to find the generated electric and magnetic field is beyond the scope of our discussion. An excellent treatment of such matters as well as some practical modeling examples is presented in [79].

Equations (2.5.3) and (2.5.4) are given in the TICRA GRASP technical manual for the electric and magnetic fields radiated by a current distribution over a surface S [14]. Here $\mathbf{r}$ is the point at which the fields are calculated, $\mathbf{R} = \mathbf{r} - \mathbf{s}$ is a vector from a source point $\mathbf{s}$ on the surface S to $\mathbf{r}$, $R = |\mathbf{R}|$ and $\hat{\mathbf{R}} = \mathbf{R}/R$. The value Z is simply the impedance of free space.

When these fields interact with a reflector they will generate source currents over its surface. Using the PO approximation (discussed next) the currents induced on a reflector's surface can be readily calculated from incident electric and magnetic fields by

$$\begin{aligned} \mathbf{J}_E &= 2\hat{\mathbf{n}} \times H^i \\ \mathbf{J}_M &= 2\hat{\mathbf{n}} \times E^i \end{aligned} \tag{2.5.5}$$

where $\hat{\mathbf{n}}$ is the surface normal of the reflector. The electric and magnetic field re-emitted by this surface can then in turn be calculated using equations (2.5.3) and (2.5.4). In this manner the electric field on a incident beam can be propagated through any number of sequential reflectors using physical optics.

Throughout this thesis the TICRA GRASP9 software (General reflector and antenna farm analysis software package) is the work horse we have employed to accurately perform a PO analysis of possible optical combiners. The above mentioned PO approximation assumes that the surface currents on a curved finite scatterer are the same as those on an infinite planar surface that is tangent to the curved surface at any considered location. GRASP9 calculates the electric field reflected by from a surface by

$$\mathbf{E}^s \approx \mathbf{E}^{PO} \tag{2.5.6}$$

where $\mathbf{E}^s$ is the scattered field and $\mathbf{E}^{PO}$ is the field calculated using the PO approximation and equation (2.5.3). This approximation breaks down at the edge of any reflector where the source current distributions display special behavior that cannot be accounted for by the PO approximation. In order to model diffraction at the edge

[14] GRASP9 is an industry standard PO software package used to model antennas at long wavelengths. For more information visit `http://www.ticra.com`

of reflectors GRASP9 uses a method referred to as the physical theory of diffraction (PTD). The scattered field is therefore described by

$$\mathbf{E}^s \approx \mathbf{E}^{PO} + \mathbf{E}^{PTD}. \tag{2.5.7}$$

A full discussion of the calculation of the scattered field contribution $\mathbf{E}^{PTD}$ is presented in [80]. In order to achieve sufficient sensitivity the QUBIC optical combiner must focus as much power as possible onto the bolometer detectors. Therefore in the designs considered the edge taper at each reflector is extremely low. We expect that the contribution from $\mathbf{E}^{PTD}$ to be minor and the PO approximation will offer an adequate analysis of the fringe patterns generated by the optical combiner. GRASP9 is the final tool implemented in the optical design. It offers no optimization techniques or wavefront error analysis however quantification of spillover and blockage are possible. GRASP9 has been used in this thesis to calculate the fringe patterns generated by various competing designs for the optical combiner.

2.5.4 Quasi optics

Quasi optics (QO) can be loosely defined as the study of optical systems that span the middle ground between the two limiting cases of ray-tracing at optical wavelengths and performing physical optics at long wavelengths. In such systems the diameter of the optical components are moderate compared to the wavelength. The electromagnetic wave is initially highly collimated however begins to spread outward during propagation. When we assume the field is scalar and confine the propagating beam to the paraxial region we find that one of the most efficient method of analysis is carried out using Gaussian beam modes. Here the electric field is described using Gaussian functions that are essentially eigenvectors to a reduced wave equation. As the beam propagates certain parameters that describe the beam's profile (e.g. width) will vary however the electric field can always be described by Gaussian functions. By understanding these varying parameters the resultant electric field can be predicted after interaction with various lenses and reflectors. All theory discussed in this section is covered in detail in [81] and [82].

When an electromagnetic field is propagating through a linear, isotropic, homogeneous and non-dispersive medium the electric and magnetic fields described by Maxwell's equations can be decoupled and written as a propagating wave. A single scalar wave equation can now describe the behavior of all components of the electric and magnetic vectors. When the scalar electric field for a monochromatic wave is substituted into the scalar wave equation we obtain the time independent Helmholtz equation

$$(\nabla^2 + k^2)\Psi = 0. \tag{2.5.8}$$

We will use $E(x, y, z) = u(x, y, z)e^{(-jkz)}$ to describe the distribution of such fields. Here $u(x, y, z)$ is a complex scalar function that indicates that the amplitude of the field we are considering differs from that of a plane wave. If we substitute this field into the Helmholtz equation we obtain a reduced version of the wave equation. As the field propagates along the optical axis diffraction occurs and the field diverges. To ensure the conservation of energy the on-axis amplitude must fall as the field expands off-axis. In the quasi optical (paraxial) region the degree of collimation of the field is greater than the amount the field spreads off-axis and therefore $\Delta(\partial u/\partial z)/\Delta z \ll \partial u/\partial z$. Under such circumstances the the reduced Helmholtz wave equation simplifies to the paraxial wave equation

$$\frac{\partial^2 u}{\partial x^2} + \frac{\partial^2 u}{\partial y^2} + \frac{\partial^2 u}{\partial z^2} - 2jk\frac{\partial u}{\partial z} = 0. \tag{2.5.9}$$

The most rudimentary solutions to (2.5.9) are Gaussian beam modes. If we wish to describe the behavior of complex diffracting fields solutions to (2.5.9) in which the fundamental Gaussian is multiplied by a set of closed form polynomials are readily derived. In practice the set of polynomials used is dictated by the choice of coordinate system. In rectangular coordinates the electric field is described by the product of the fundamental Gaussian beam and Hermite polynomials expanding along the x and y axes (assuming the optical axis is along the z axis):

$$E_{mn}(x,y,z) = \left(\frac{1}{\pi w_x w_y 2^{m+n-1} m!n!}\right)^{0.5} H_m\left(\frac{\sqrt{2}x}{w_x}\right) H_n\left(\frac{\sqrt{2}y}{w_y}\right) \cdot exp\Bigg[-\frac{x^2}{w_x^2} - \frac{y^2}{w_y^2} - jkz - \frac{j\pi x^2}{\lambda R_x} - \frac{j\pi y^2}{\lambda R_y} + \frac{j(2m+1)\varphi_{0x}}{2} + \frac{j(2n+1)\varphi_{0y}}{2}\Bigg]. \tag{2.5.10}$$

In cylindrical coordinates higher order solutions are obtained by multiplying the fundamental Gaussian beam by Laguerre polynomials:

$$E_{pm}(r,\varphi,z) = \left[\frac{2p!}{\pi(p+m)!}\right]^{0.5} \frac{1}{w(z)} \left[\frac{\sqrt{2}r}{w(z)}\right]^m L_{pm}\left(\frac{2r^2}{w^2(z)}\right) \cdot exp\left[\frac{-r^2}{w^2(z)} - jkz - \frac{j\pi r^2}{\lambda R(z)} + j(2p+m+1)\phi_0 z\right] \cdot exp(jm\varphi). \tag{2.5.11}$$

If the electric field is radially symmetric these polynomials are independent of the azimuthal angle around the bore sight φ. As a Gaussian beam propagates according to equations (2.5.10) and (2.5.11) the profile describing the beam is maintained but its height and width are altered. This alteration is dependent on the propagation distance and is described in equations (2.5.10) and (2.5.11) by parameters known as the beam radius

$$w(z) = w_0\left[1 + \left(\frac{\lambda z}{\pi w_0^2}\right)^2\right]^{0.5}, \tag{2.5.12}$$

the phase radius of curvature (ROC)

$$R(z) = z + \frac{(\pi w_0^2/\lambda)^2}{z} \tag{2.5.13}$$

and the phase slippage

$$\phi_0(z) = \tan^{-1}\left(\frac{\lambda z}{\pi w_0^2}\right). \tag{2.5.14}$$

where the value z indicates the propagation distance. Finally the values m,n and p in equations (2.5.10) and (2.5.11) indicate the order of polynomial being selected.

The beam radius (2.5.12) represents the off-axis distance at which the electric field falls to $1/e$ of its on-axis value and equals the beam waist (w_0) at $z = 0$. Rather than perceiving the electric field as propagating from a dimensionless point source the field emerges from a finite region of space that is multiple wavelengths in diameter. This is called the waist radius of the beam, w_0. The beam waist and radius of curvature are best understood by considering a Gaussian beam in the context of a diffraction integral. When a Huygens-Fresnel diffraction integral is manipulated and paraxial quasi optical conditions are assumed a solution equal to the fundamental Laguerre Gaussian solution is obtained. The beam waist becomes a finite source of Huygens wavelets. As the beam propagates the envelope of these wavelets creates a phase front with a radius of curvature described by (2.5.13). This phase front is a parabolic approximation to the spherical phase fronts classically associated with a Huygens treatment of diffraction.

The paraxial ray tracing equations and the ABCD matrix format into which these equations can be transferred are well documented in all modern optical design text books. Traditionally the ABCD matrix is a device that allows Snell's law to be implemented over numerous sequential optical components. Therefore once the focal length of these components are known the orientations and locations of all rays propagating through the system can be calculated. A useful aspect of Gaussian beam mode analysis is that by describing a Gaussian beam by its complex beam parameter q_z where

$$\frac{1}{q_z} = \frac{1}{R_z} - \frac{j\lambda}{\pi {w_z}^2}, \tag{2.5.15}$$

ABCD matrices can used to manipulate the beam parameter as follows

$$q_{out} = \frac{A \cdot q_{in} + B}{C \cdot q_{in} + D}, \tag{2.5.16}$$

and therefore describe the propagation of the electric field through an optical system in a straight-forward manner. The beam radius and phase radius of curvature can be recovered from the complex beam parameter using

$$w = \left[\frac{\lambda}{\pi Im(-1/q_{out})}\right]^{0.5} \tag{2.5.17}$$

and

$$R = \left[Re\left(\frac{1}{q_{out}} \right) \right]^{-1}. \tag{2.5.18}$$

Also the phase slippage in an optical system can be calculated by

$$\phi_{0out} - \phi_{0in} = \tan^{-1} \left(\frac{B \times (\frac{1}{q_{in}})}{A} \right) \tag{2.5.19}$$

where A and B are of course entries in the ABCD matrix describing the system.

ABCD matrices allow us to model a partially diffracting beam at any location in an optical system. This analysis technique is the simplest method that allows us to account for the behavior of an electric field without detailed mathematics. The optical system can be as complicated as one wishes so long as each component can by described by a ABCD matrix. The process of propagating a beam through such a system is iterative. The input beam radius and radius of curvature at one component is simply the output beam radius and radius of curvatures of the previous component. Matters can be simplified even further if we chose to cascaded the individual components matrices into one complete expression ($M = M_n \cdot M_{n-1} \cdot ... M_1$ for n optical components).

Two excellent summaries of recent developments in quasi-optical analysis for long wavelength systems are presented in [83] and [84]. A quasi-optical analysis of the MBI adding interferometer is presented in [73] while an analysis of the ALMA band 9 front-end is presented in [85].

2.5.5 Fourier optics

As its name suggests Fourier optics employs Fourier transforms to propagate an electric field through an optical system. Fourier optics emerges from a Huygen's consideration of the solutions of the scalar Helmholtz equation (2.5.8) as follows. The spherical wavelets discussed in Huygen's principle must obey the Helmholtz equation and can therefore be described by $e^{\pm ikr}/r$ [86]. The electric field $\psi'(x, y)$ at any displacement

from a given distribution $\psi(x, y)$ is the integral sum of spherical wavelets propagating from the distribution

$$\psi'(x, y) = K \int \psi(\xi, \eta) \frac{e^{ikr(x,\xi,y,\eta)}}{r(x, \xi, y, \eta)} d\xi d\eta. \tag{2.5.20}$$

We again assume that the field is collimated and thus not diffracting to a significant extent. This allows a binomial expansion of the phase radius of the spherical wavefront such that $r(x, \xi) \approx R + \frac{\xi^2+\eta^2}{2R} - \frac{\xi x+\eta y}{R}$. If the source and field distributions are separated by a distance that is much greater than the wave number k the term $\frac{\xi^2+\eta^2}{2R}$ can be neglected. This is called the far field approximation. The field distribution becomes the Fourier transform of the source distribution

$$\psi'(x, y) = \frac{Ke^{-ikz}}{z} \int \int \psi(\xi, \eta) exp\Big[- \frac{2\pi i}{\lambda z}(\xi x + \eta y)\Big] d\xi d\eta \tag{2.5.21}$$

where the terms x and y are the Cartesian coordinates of the source distribution and ξ and η are the Cartesian coordinates of the field distribution. The bore sight is along the z axis around which the geometry of the system is orientated. The value z is the straight line distance between the planes (x, y) and (ξ, η) and $R = \sqrt{(x^2+y^2+z^2)}$. The value K is a constant that reduces the amplitude in order to conserve energy as the field diffracts. Equation (2.5.21) is the Fraunhofer diffraction integral [87]. Within this thesis Fourier optical modeling (both near- and far- field) of possible optical combiners was carried out using the Zemax software package. Zemax's defines the far field of a source distribution of Huygens wavelets as $< A^2/\lambda z$ where A is the aperture diameter of the source distribution and z is the propagation distance. The value $F_n = A^2/\lambda z$ is referred to as the Fresnel number. If $F_n > 1$ we say that the field is within the Rayleigh range and Zemax calculates the near field diffraction pattern of a source distribution by

$$\psi'(x, y) = \frac{Ke^{-ikz}}{i\lambda z} e^{(i\pi r^2)/(\lambda z)} \int \int \psi(\xi, \eta) e^{(i\pi r^2)/(\lambda z)} exp\Big[- \frac{2\pi i}{\lambda z}(\xi x + \eta y)\Big] d\xi d\eta. \tag{2.5.22}$$

This is the Fresnel near field diffraction integral where the term $e^{(i\pi r^2)/(\lambda z)}$ is used to account for the fact that the near field diffraction patterns of an electric field are

more complex then the far field patterns. It is apparent that as z approaches infinity this value nears unity and equation (2.5.22) is equal to (2.5.21). Because (2.5.22) is a Fourier transform, Fourier optical techniques can also be used to describe the near field diffraction of a electric field.

Zemax examines diffraction within an optical system using a class called the "POP" operand. Within this operand variations of equations (2.5.20), (2.5.21) and (2.5.22) are used to propagate the electric field from a focusing device or throughout free space. There are 4 operations Zemax must perform in order to provide a full analysis of any possible optical system. The first is propagation within the Rayleigh range dubbed PTP propagation. Here Zemax multiplies the collection of spherical wavelets shown in equation (2.5.20) by a phase term e^{ikRz} where R indicates the displacements between the two planes at which the fields are calculated. The second operation is propagation of a field from inside the Rayleigh range into the far field. Zemax carries out this propagation using a combination of PTP propagation and both the Fraunhofer and Fresnel integrals shown in equations (2.5.21) and (2.5.22) respectively. The third type of propagation from the far field into the Rayleigh range is simply the reverse of this method. Finally the fourth type of propagation from outside the Rayleigh range to outside the Rayleigh range is carried out using a combination of equations (2.5.21) and (2.5.22).

The scalar nature of the POP operand immediately implies that modeled fringes will be less accurate than fringes produced by GRASP. Although fringe patterns calculated by the Zemax POP analysis will be presented in the following chapters all final conclusions concerning an optical combiner will be checked with GRASP simulations.

2.5.6 Modeling lenses

As we shall see in the forthcoming chapters where possible we will attempt to design a reflector combiner for QUBIC. Although there are many applicable lens systems for QUBIC there is currently no industrial verified software packages that will accurately model lenses. Physical optics is the most accurate technique available to model the electric fields generated from currents distributed across a material surface. We note that equations (2.5.3) and (2.5.4) do not prevent a physical optics analysis of

a dielectric. As we can see once the value $Z = \sqrt{\frac{\mu}{\epsilon}}$ is fully quantified for a surface a full calculation of the induced currents and the re-emitted electric fields is theoretically possible. However in practice numerous problems are encountered when one tries to perform a physical-optical analysis of dielectric lenses. It has proven difficult to write accurate algorithms that will calculate the currents and the electric fields on the dielectric surface and also throughout the material. An in-house optical software system called MODAL is currently under development at NUIM that can perform limited physical optics analysis of thick lenses.

MODAL essentially treats a single lens as two separate "sheets" of dielectric. When an electric field is incident over the first surface MODAL decomposes the field into its reflected and transmitted components via the Fresnel coefficients. The transmitted field is then propagated onto the back dielectric sheet using the usual physical optics approach. At the back surface the reflected and transmitted components of the incident field are once again calculated. These components are then transmitted out of the lens or propagated back into the dielectric where a new set of reflected and transmitted components are calculated. This process is repeated until the power in the electric field focused by the lens converges on a constant value. A full and elegant introduction to MODAL and its potential to provide an industry standard software package that offers optical design and analysis tools that cater for the frequency ranges between those of GRASP and Zemax is presented in [88].

Fourier and quasi-optics provide some limited options with which we can model on-axis lens systems. Both these methods allow us to define the initial amplitude and phase front of an electric field. These fields can then be propagated through an optical system. In both analysis techniques the curvature of any optical surface is used to calculate the field amplitude and also the shape of the final wavefront. In Zemax the electric field distribution is recalculated at every optical surface. We see that the displacement between the apertures at which fields are calculated will vary from point to point depending on the curvatures we set for each surface. Meanwhile values of the $ABCD$ matrices in quasi optics are defined directly from the curvature of an optical surface. These matrices are then used to recalculate the beam radius and radius of curvature after propagation through the optical surface.

In Fourier and quasi optics the interaction of the electric field with each optical com-

ponent is not directly calculated. Such techniques will not provide a full account of the polarization in an optical system or any edge effects that occur at a low focal ratio surface. Both Fourier and quasi-optics are paraxial limited and from the authors experience their results become unreliable when off-axis electric fields are considered. It is apparent that in order for our instrument to achieve sufficient sensitivity to observe a tensor-to-scalar ratio of 0.01 our optical system must be completely characterized. Unfortunately neither Fourier nor quasi-optical analysis will offer an accurate description of errors such as cross polarization, edge effects, spillover or blockage. Since these methods are the only techniques currently available to us with which the model lenses we are reluctant to implement lens combiners in QUBIC. Meanwhile research into the accurate modeling of lenses is on-going.

2.6 Thesis outline

In Chapter 1 we discussed the importance to modern cosmology of detecting CMB B-mode polarization. This thesis details the authors contribution to the QUBIC CMB mission, the primary goal of which is to measure the B-mode polarization of the CMB. In this chapter we have discussed the various components of the QUBIC instrument and have outlined how an optical combiner will be used to focus beams onto the detector plane. The author has been the one of the principal architects of the QUBIC optical combiner. The initial considerations for the optical combiner are discussed in Chapter 3 while in Chapter 4 some refined suggestions for the combiner are presented. Chapter 5 discusses a possible updated version of the QUBIC mission entitled QUBIC2.0. Once again an optical combiner is required for this mission and we discuss several plausible designs. It is currently hoped that the QUBIC instrument will be in place in Antarctica in late 2012.

2.7 Conclusions

The QUBIC instrument will use bolometer radiometers to measure the visibilities produced by a Fizeau combiner. This approach to CMB observation is completely novel and has been dubbed “bolometric interferometry”. As we have discussed there

is an inverse proportional relationship between the number of baselines with which QUBIC will observe the sky and the noise in the recovered visibilities. It has been shown that if the number of horns used to observe the sky is greater than 144 QUBIC's sensitivity will be equivalent to that of a CMB imaging telescope. It is expected that the recovery of the Stokes visibilities with QUBIC will allow us to detect a tensor-to-scalar ratio ~ 0.01. As discussed in Chapter 1 quantifying the CMB scalar-to-tensor ratio is expected to deeply broaden our understanding of the early Universe. This thesis concerns the design and modeling of a Fizeau combiner applicable to QUBIC and bolometric interferometry in general. Geometrical, physical, quasi and Fourier optics have been used to design and model several possible combiners. The details of these various optical design and modeling techniques have been discussed in this chapter. Due to the interferometric nature of QUBIC it is vital that we are capable of simulating any fringe patterns produced by our various designs over various baselines. Fortunately through the use of PO the GRASP9 software package offers a highly accurate approach to modeling any fringe patterns produced by a reflector combiner.

3 Dual reflectors for bolometric Fizeau interferometers

3.1 The Optical Combiner for QUBIC

In Spring 2009 the first meeting of what now is called the QUBIC collaboration took place in Paris. At this meeting it was decided that an optical combiner that imposes geometric phase shifts on multiple Gaussian beams should be implemented in QUBIC. The persons attending this meeting from NUIM were charged with designing such a combiner. We initially decided to implement an off-axis dual reflector. In this chapter we discuss why such a decision was taken.

In the initial stages parameters such as the combiner focal length and bolometer size were not fully determined for QUBIC. Although topics dealt with in this chapter are ultimately aimed at the design of the QUBIC optical beam combiner, we first present a general review of off-axis dual reflectors that could be implemented in a Fizeau bolometric interferometer.

From the discussions in Chapter 2 it is clear that the optical combiner will have to be extremely well characterized and transfer as much power as possible to the detector array in order for QUBIC to achieve the sensitivity level required to observe CMB B-modes. Therefore our initial intentions for QUBIC involved the designing an off-axis dual reflector. An off-axis geometry was chosen to prevent the shadowing of the array of back-to-back horns by the secondary reflector. This will ensure as much power as possible is collected by the primary mirror. We chose to explore the implementation of

reflectors first rather than on-axis lenses due to the fact that the behavior of reflectors can be accurately modeled using physical optics. An off-axis dual reflector consists of a combination of mirrors whose optical axes are not aligned. These systems are inherently difficult to design due to the large number of free parameters required for describing the positioning of the mirrors.

This chapter will then address the off-axis dual reflector designs that were considered for QUBIC. The optical combiner required for QUBIC is equivalent to a classical focusing system. As such before proceeding directly to the design of the reflectors we will briefly model the fringe patterns we expect a classic focal system to produce.

3.1.1 Focal Systems

We define a focal system as any optical device that focuses rays traveling parallel in the system's object space onto a single location in the image space. The location to which the rays converge in the image space is referred to as a focal point. Under such conditions both a simple convex lens imaging an object at infinity or more complicated instruments such as Newtonian reflectors are classed as focal systems [1]. QUBIC requires a focal device that will combine beams propagating from the back-to-back horn array. This device will simultaneously focus beams from a patch of sky onto the detector array while also providing the geometric phase shifts necessary to generate the visibility patterns. In this section we will assume the optical combiner required for QUBIC is an ideal on-axis thin lens. This will allow us investigate the anticipated behavior of a perfect optical combiner using quasi optics. A concise introduction into definition and conventions used to describe optical systems can be found in the opening three chapters of [89].

Using quasi optics we can model the behavior of the optical combiner. As it is the simplest focal system applicable to the QUBIC combiner we will consider a paraxial lens. Such a device is an ideal optical component possessing no thickness and perfect focusing capabilities. By implementing a paraxial lens we are only considering the ideal geometric change to the incident phase front.

[1] Assuming we discard the ocular within a Newtonian of course.

We let the separation between the paraxial lens and the bolometer array equal the focal length (f) of the lens. The field at the back focal point of such an arrangement is a Gaussian beam whose beam radius is readily calculated using $ABCD$ matrices as $w_{out} = \frac{\lambda f}{\pi w_{in}}$. Here λ, is the wavelength and w_{in} is the beam waist at the input horn [2]. If the incident beam is propagating from an off-axis horn the phase front at the focal plane will be tilted. Such a scenario is shown in Figure 3.1

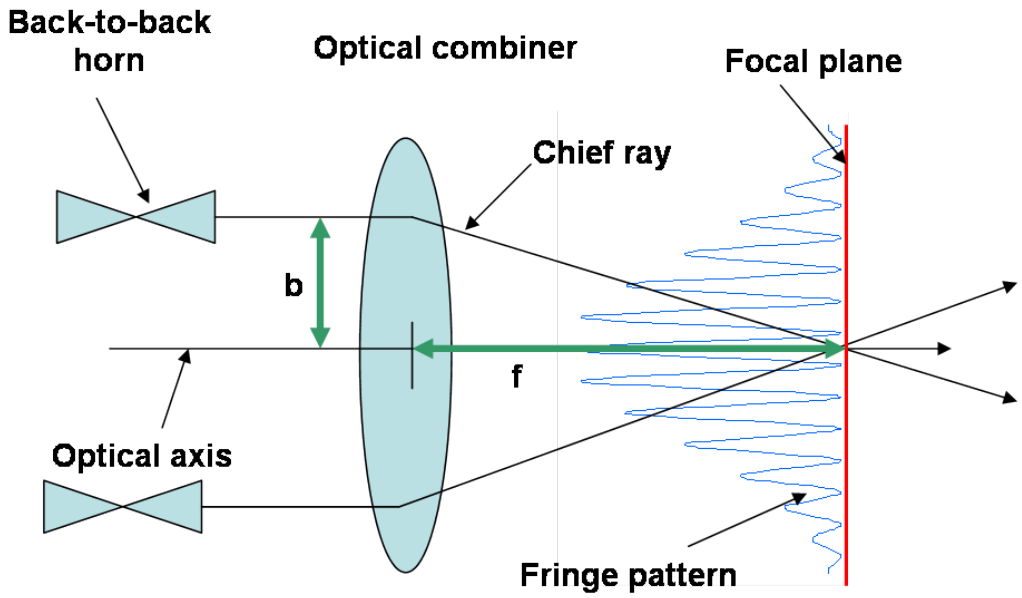

Figure 3.1: A paraxial lens combining beams from a single baseline. Here **b** is the displacement of a single horn from the optical axis and **f** is the focal length of the combiner. These values have been denoted as b and f respectively in the accompanying text.

In order to tilt a beam we multiply the field by the exponential term $e^{(-jkx\theta)}$ where θ is the angle between the incident wavefront and the focal plane [81]. The term k is of course the wave number. The value of θ can be readily calculated from the combiner geometry as $\theta \approx \frac{b}{f}$ where once again b is the displacement of the horn from the optical axis. The resulting electric field generated by a baseline of length $2b$ will be $exp(-\frac{x^2}{{w_{out}}^2})(exp(-jkx\theta) + exp(jkx\theta))$. Using trigonometry we can reduce this to

[2] It is this formula we use to calculate the size of the bolometer array in Table 2.1. From the incident beam size we can compute the beam radius at the focal plane. To ensure at least 95% is integrated the size of detector array must be at least $2 \times w_{out} \times 1.2$ mm^2.

the cosine expression[3],

$$I(x) = \left(exp(-\frac{x^2}{{w_{out}}^2}) \cos\left(\frac{kbx}{f}\right)\right)^2. \tag{3.1.1}$$

Therefore the field on the focal plane will have a periodically varying amplitude with a Gaussian envelope. The field described by equation (3.1.1) is a simplified version of equation (2.2.2). Hence the generated field will be the type of fringe pattern we wish to sample. Some examples of fringe patterns calculated using equation (3.1.1) are shown in Figure 3.2. A 4 mm input waist radius was used to generate the fringes shown in Figure 3.2. This value is consistent with the waist radius of 14° FWHM Gaussian beams expected to propagate through the QUBIC combiner. Also we set the wavelength equal to 2 mm and chose a 300 mm focal length for the paraxial lens.

In summary quasi optics confirms that using a classical focal system to combine beams from off-axis back-to-back horns will produce the fringe patterns we require to sample the sky visibilities. In reality the above assumptions we made about the nature of the combiner are not realistic. Currently it is not possible to manufacture an optical combiner that will focus light as flawlessly as a thin paraxial lens. Because of such limitations to the optical combiner's design there have been certain specifications placed on it's performance. Such performance specifications will be discussed later.

3.1.2 Performance of a Telescopic Combiner

The goal of the optical combiner is to generate equivalent fringe patterns from equivalent baselines. We have shown a focal device will generate a fringe pattern whose field is the additive sum of separate geometrically shifted beams. The question remains to be answered as to how can we design such a device.

There is a wealth of literature pertaining to the geometric design of telescopes. These methods are applicable to the design of QUBIC's optical combiner. Consider the visibility of an interferometer defined by Michelson $V = \frac{I_{max}-I_{min}}{I_{max}+I_{min}}$. When the incident signal has a high degree of coherency V is close to unity. The response signal of the

[3]We remind ourselves that $\cos x = \frac{e^{ix}+e^{-ix}}{2}$. Also by showing the absolute value we are now describing the intensity of the electric field.

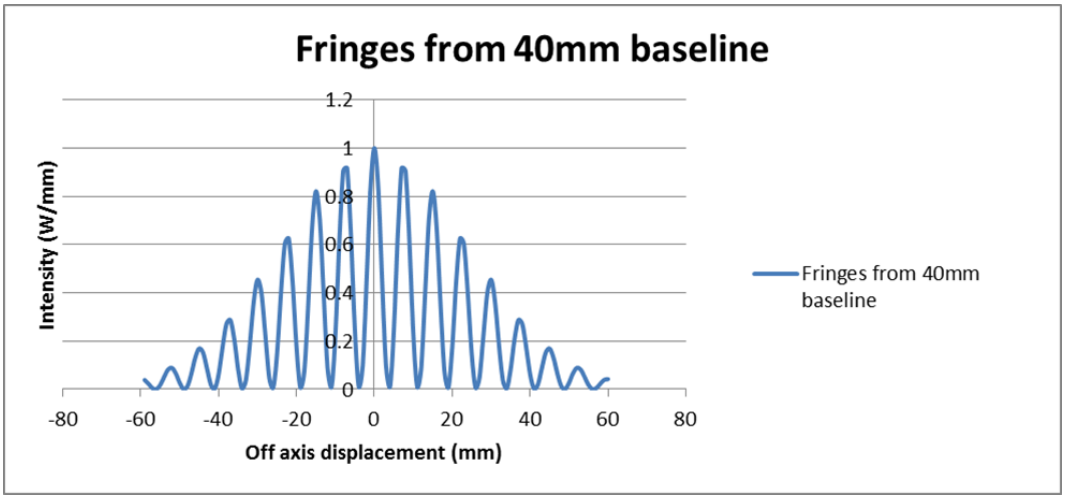

(a) Fringe pattern generated by a 40 mm baseline.

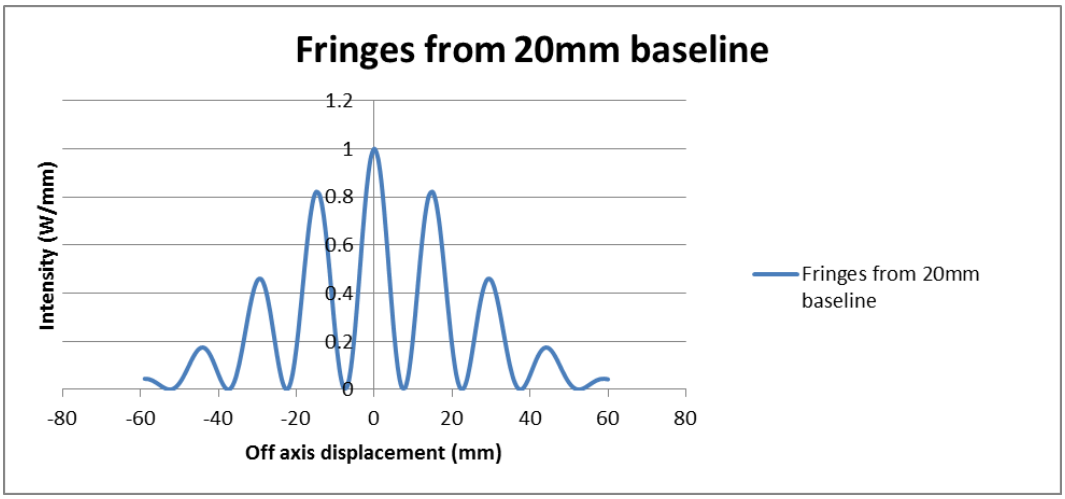

(b) Fringe pattern generated by a 20 mm baseline.

Figure 3.2: Fringe patterns predicted using Fourier and quasi optics calculations. A 300 mm focal combiner at 150 GHz has been assumed.

interferometer is strongest when this occurs. If we consider this value in the context of a telescopic optical combiner we can consider V analogous to the contrast/modulation ratio of an imager. It has been clearly documented that the presence of aberrations in an optical system will reduce the contrast in the images produced by that system [86]. This conclusion is applicable to QUBIC (we are after all "imaging" the fringe patterns). Classical phase aberrations present within the combining wavefronts will reduce the visibility of the fringe patterns, thus reducing their "quality". Also aberrations will alter the phase transfer function of an optical system. This means it is possible the

fringes will undergo a lateral shift along the focal plane. Since the magnitude of aberrations is dependent on the location of the baselines from the optical axis the fringes from various equivalent baselines will not focus at the same locations along the detector array. Therefore bolometers will not see the same regions of each fringe pattern. Such lateral shifts can cause errors during visibility recovery. Our colleagues in Milano have investigated figures-of-merit that could be used to describe the QUBIC optical combiner[4]. Using the optical transfer function they have derived an efficiency criterion for the QUBIC optical combiner. This criterion requires the use of Zemax to calculate the geometric transfer function of a given combiner. Since this does not take full account of the wave nature of the incident beams a physical optics analysis of any combiner system is still necessary.

The QUBIC optical combiner will be a classic telescopic device designed to minimize phase aberrations. The lower the phase aberration the more successful the combiner will be at producing equivalent fringe patterns from equivalent baselines. The fundamentals of geometrical optics concern designing systems that induce little or no phase aberrations on focusing wavefronts[5]. We thus proceed to follow the literature concerning best practices for geometrical optical design to construct QUBIC's optical combiner. Such methods have been used to design the optical combiner because due to the ease and speed of the calculations geometrical optics permits fast and effective optimizations of any initial system. Also such techniques are well developed in commercial software packages such as Zemax. Later we will analyze the systems using a full physical optics analysis.

3.1.3 Disadvantages of lenses of QUBIC

In the above examples we used an on-axis single lens to represent the QUBIC beam combiner. Lens antennas have been used, for example, in the HIFI instrument (Bands 5,6,7) for the Herschel Space Observatory [90] and in the DASI CMB interferometer. Their primary function was to shape the incident beam in such a manner as to allow

[4]Universitá di Milano Bicocca, P.za della Scienza 3, 20126 Milan, Italy. Website `http://www.unimib.it`

[5]If phase aberrations are produced it seems unlikely that they would be the same for equivalent baselines.

a higher coupling efficiency between the incident electric field and the horn antenna. A number of different approaches exist that are capable of accurately modeling small lenses. These include finite-difference and finite-elements techniques. However these methods are limited to lenses whose diameter is less than 10 wavelengths [91]. The QUBIC optical system, on the other hand, is a large scale quasi optical combiner. Therefore the techniques that can be used to model small lens antennas cannot be used in such a scenario.

Large dielectric lenses have been used in the QUaD and BICEP CMB imaging experiments. Although it is possible to accurately model the bending effects that these lenses have on incident waves using ray tracing techniques, such an approach does not offer a complete description of the behavior of the lenses at GHz frequencies. This is because the wavelength of the incident beams is large enough to allow diffraction to dominate the beams propagation. This diffraction cannot be modeled using ray tracing. However as discussed in the previous chapter there are currently no methods available commercially that accurately model the scattering and diffraction behavior of electric fields incident on dielectric materials whose diameter is 10λ - 100λ. Experiments such as QUaD and BICEP highlight the unpredictable behavior of the polycarbonate materials used to create GHz lenses. It is currently suspected that some of the dielectric focusing elements or optical windows within these experiments were birefringent and caused beam squint errors to occur. Because the theory of electric fields scattering from perfect conductors has been vigorously studied and explained such occurrences are not experienced when we implement reflectors. For these reasons we first concentrated on reflector designs for the QUBIC optical beam combiner.

3.1.4 Disadvantages of on-axis reflector designs for QUBIC.

Optical-wavelength Fizeau interferometers that implement on-axis reflectors and are dedicated to astronomy have been discussed in [92]. Here the instrument discussed is a typical on-axis telescope with a mask placed in front of its aperture. Pin holes have been placed in the mask to generate baselines. For an instrument such as QUBIC on-axis designs are particularly attractive due to low magnitude wave front aberrations. Several authors have demonstrated how on-axis aplanats can be adjusted to cancel out a third Seidel aberration [93], [94]. The well known Couder design is a classic on-axis

Cassegrain with a concave secondary mirror. This arrangement leads to zero spherical aberration, coma and astigmatism. Construction of flat field aplanats as well as zero distortion aplanats have also been discussed in these sources. Perhaps the most famous on-axis dual reflector telescope is the Hubble space observatory. The main design of the Hubble optics is referred to as a Ritchey-Chrétien Cassegrain variation. Here the primary mirror in a classical Cassegrain is manufactured to be slightly hyperbolic. This enables a greater reduction of coma compared to traditional systems [6]. ESA's recently launched Herschel Space Observatory is also a Ritchey-Chrétien Cassegrain [7].

Another well known on-axis design is the special Schwarzchild aplanat [95]. This arrangement cancels out spherical aberration, coma, astigmatism and field curvature. On-axis designs are thus more suitable to systems requiring low aberrations than off-axis designs. On-axis systems that cancel 3 to 4 Seidel aberrations (coma, astigmatism, field curvature and distortion) can be implemented using standard conic surfaces. For off-axis systems however it has only been demonstrated how to minimize at most two wavefront aberrations whilst using conic sections [96].

Previous CMB interferometry experiments such as MBI have implemented on-axis designs. Unfortunately on-axis systems are simply not practical for QUBIC. In MBI the minimum baselines were separated by a distance greater than the diameter of the secondary reflector. Thus the minimum baselines were not in the shadow of the secondary reflector. QUBIC will use a 250 mm^2 grid of at least 12×12 back-to-back horns to re-transmit the signal from the sky. Therefore if an on-axis design were chosen many of the centre horns of this grid would lie in the shadow of the secondary mirror regardless of its diameter. It is clear that a high degree of blockage would be present within our optical system. Therefore neither reflecting or refracting on-axis designs are applicable to QUBIC. For these reasons the only practical combiner to implement in QUBIC is an off-axis dual reflector.

We are aware we are limiting our choices to off-axis dual reflectors. Although off-axis reflector designs consisting of three and four elements can be found within the literature most of these designs include at least two aligned components [97]. Effectively at least

[6] More information on the Hubble Space Telescope can be found at `http://hubblesite.org/`.

[7] With a 3.5 m primary mirror the Herschel Space Observatory is the largest telescope ever launched into space. For more information visit `http://herschel.esac.esa.int/`

two of the reflectors will shadow one another preventing the maximum power reaching the focal plane. Also the designs that are completely unblocked are too large for the QUBIC cryostat or are simply not realistic at the low focal ratios encountered in QUBIC [98]. As such in the following sections we discuss off-axis dual reflectors only.

3.1.5 Cassegrain versus Gregorian

Two types of telescopes dominate the field of astronomy. These are the Cassegrain and Gregorian dual reflectors. Both these systems consist of a parabolic primary mirror combined with a secondary mirror. In traditional systems the secondary mirror essentially magnifies the focal length of the primary. The location of the secondary mirror dictates the title and defines the characteristics of a dual reflector. If a convex hyperbolic secondary is inserted before the primary's focal point the system is referred to as a Cassegrain telescope. If a concave elliptical secondary is inserted after the primary's focal point the telescope is a Gregorian. For equal parameters (for example focal ratio and field of view) the Cassegrain is a better performing system. It will induce marginally lower phase aberrations on propagating wavefronts and the design itself is more compact than the Gregorian [77].

3.2 Dual reflectors

The following sections present an analysis of possible dual reflector arrangements to be considered for the QUBIC experiment. The design of all these reflectors occurred bearing in mind the parameters of QUBIC that were detailed in Chapter 2. An array of 144 sky horns laid out in a 12×12 grid was considered to be the entrance pupil. These horns observe the sky using 14° FWHM primary beams. The diameter of a single horn is therefore approximately 11.6 mm (including a 2 mm rim diameter). The size of the entrance diameter is therefore 140 mm at 150 GHz while at 100 GHz it increases to 200 mm. Unfortunately the low focal ratios of QUBIC will automatically exclude some reflectors from consideration. In order to present a fair review of currently available reflectors we have allowed for future developments in multiplexing and

detector technologies that will permit a filled focal plane much larger than the one proposed for QUBIC. We have assumed a 400 mm^2 detector plane filled with 6400 5 mm bolometers. This has allowed us to consider up to 800 mm focal length systems.

3.2.1 The geometry off-axis dual reflectors

Figure 3.3 demonstrates the geometry of off-axis Gregorian and Cassegrain reflectors. In these diagrams we have only shown incoming rays that are aligned with the primary axis (indicated by the blue lines). These lines emerge parallel from the back-to-back sky horns[8]. The labeling convention used in this section will remain constant throughout the rest of this chapter when we discuss off-axis systems.

In all following diagrams the size of the back-to-back horn array is 140×140 mm^2. These are the dimensions required to house a 12×12 horn array that generates 14° FWHM Gaussian beams. In all dual reflectors we present the chief ray propagates at an angle normal to the centre of the horn array. The chief ray demonstrates the line-of-sight of the back-to-back array. The angle θ_u is the angle of throw of the primary reflector. The angle β is the tilt between the primary and secondary axes. Finally the angle α is the tilt between the chief ray and the secondary axis while **F1** and **F2** are the combiners foci[9].

3.2.2 Designing off-axis dual reflectors

An off-axis dual reflector system is required for the QUBIC optical combiner. In general the parameters of these systems lack the versatility of their on-axis counterparts to remove Seidel aberrations. However in recent years a number of publications have discussed how these systems can be optimized for low astigmatism, cross polarization and spillover [96]. Like their on-axis counterparts off-axis systems can also be manipulated to form Ritchey-Chrétien variations. Such systems will have their primary mirrors reshaped from a paraboloid into a hyperbolic or elliptical structure. Altering

[8] In later diagrams these will be accompanied by fans of rays covering the full width of the Gaussian beams propagating from the back-to-back horns. The approximate edge of the field of view will be indicated by green and red lines

[9] This notation also applies to Figure 3.3

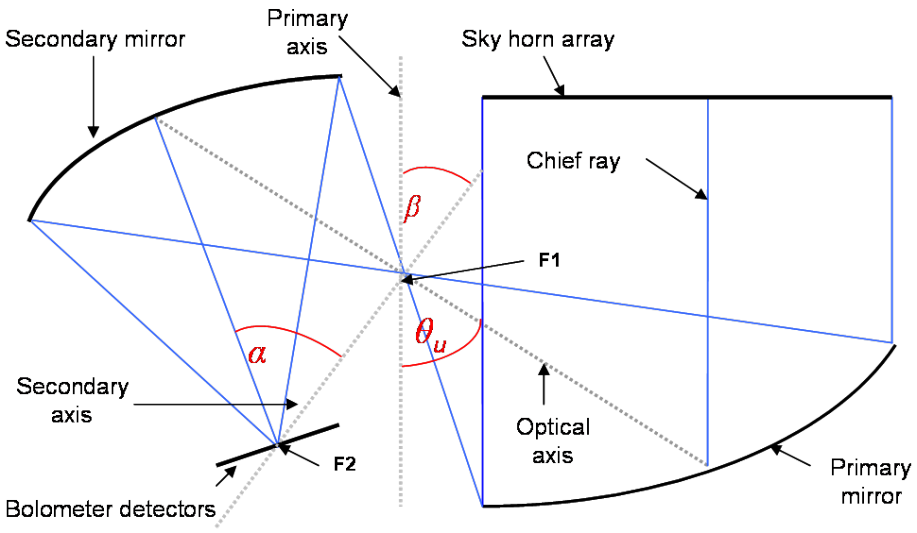

(a) Geometry of off-axis Gregorian reflector.

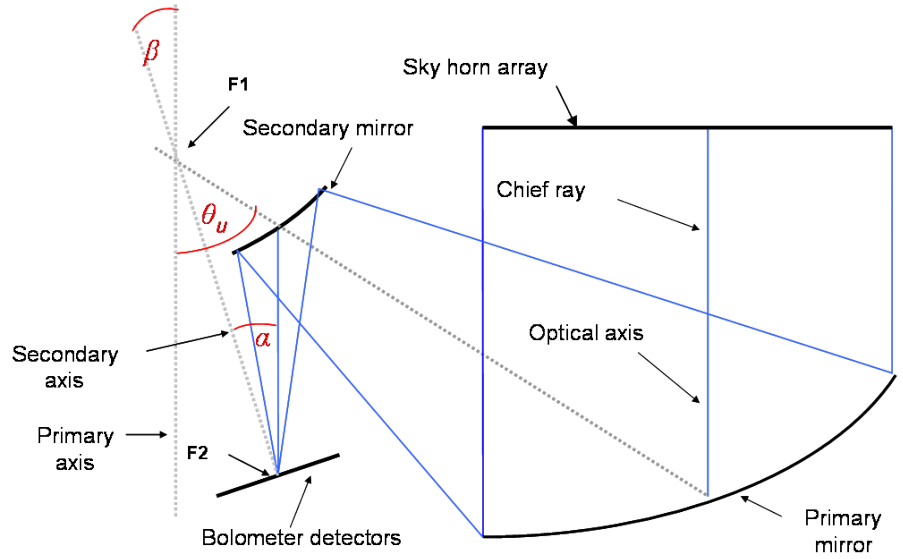

(b) Geometry of off-axis Cassegrain reflector.

Figure 3.3: Geometrical layout of off-axis dual reflectors.

the primary mirror in such a fashion leads to negligible amounts of spherical aberration and coma.

There are two conditions that describe how to align the mirrors within an off-axis dual reflector in order to achieve minimal spherical aberration, astigmatism, spillover and cross polarization. These are the Rusch condition [99] and the Mizuguchi-Dragone

criteria [100]. The Rusch condition for dual reflectors is

$$\tan\left(\frac{\beta}{2}\right) = \frac{(e-1)^2}{(e+1)^2}\tan\left(\frac{\beta-\theta_u}{2}\right). \tag{3.2.1}$$

As previously explained the angle β is the tilt between the reflectors' axes. The value θ_u is the angle of throw of the primary parabola and e is the eccentricity of the secondary reflector. Similar to on-axis systems, off-axis reflectors can be resolved into a single off-axis equivalent paraboloid. If the system parameters are chosen according to the Rusch criterion the line-of-sight of the off-axis equivalent paraboloid will align with the centre of the sub-reflector. This will create minimum spillover[10].

The Mizuguchi-Dragone condition :

$$\tan\left(\frac{\alpha}{2}\right) = \frac{(e+1)}{(e-1)}\tan\left(\frac{\beta}{2}\right) \tag{3.2.2}$$

allows one to design a dual reflector in which the offset angle of the equivalent paraboloid is zero. Here α is the angle between the chief ray and the secondary axis[11]. In effect a system that obeys this condition can be resolved into an on-axis paraboloid. Due to this central symmetry such a system will induce minimal spherical aberration, astigmatism and geometrical cross polarization. It has been shown that off-axis Gregorian reflectors designed using the Mizuguchi-Dragone condition possess a higher diffraction-limited field-of-view than off-axis aplanatic Gregorians [101].

Systems that obey the Rusch and Mizuguch-Dragone conditions are referred to as compensated dual reflectors. Such systems represent the state-of-the-art of off-axis dual reflector designs. We investigate traditional compensated Cassegrain and Gregorian reflectors as well as the more exotic side-fed and front-end-fed Cassegrain. We also investigated a relatively unknown crossed inverse Cassegrain design. Each of the systems are been optimized using the Rusch and Mizuguchi-Dragone conditions and therefore should all be suitable for QUBIC. However since both equation (3.2.1) and (3.2.2) are derived using ray-tracing techniques this assumption is solely based geometrical optics considerations that do not take account of the finite wavelength of light. As we shall

[10] All angles are shown in 3.3

[11] This angle is also shown in 3.3

show in this chapter at GHz frequencies certain dual reflectors are more applicable to CMB bolometric interferometry than others. Also the low focal ratios of QUBIC will automatically exclude some reflectors from implementation.

3.2.3 Beam distortion in dual reflectors

There is an optical aberration separate from the traditional third order Seidel phase aberrations (spherical aberration, coma, astigmatism, field curvature and distortion) referred to as amplitude or beam distortion. Unlike the Seidel aberrations that describe geometric shifts in the wavefront of a propagating field, beam distortion refers to the amplitude profile of a propagating electromagnetic field.

In this section we describe how an off-axis system causes amplitude distortion of the beams from the back-to-back horns. When a Gaussian beam spreads over the primary reflector different regions of the electric field experience a different equivalent focal length. This introduces an asymmetry into the reflected beam causing power to be transferred into higher order beam modes. The result of this power spillage is that the peak of the reflected beam no longer occurs along the propagation axis.

The fraction of incident power that spills into the higher order modes is quantified by

$$U = \frac{w_m \tan(\theta_i)}{2\sqrt{2} f_p} \tag{3.2.3}$$

where f_p is the effective focal length of the paraboloid reflector [102]. This value depends on the focal length of the paraboloid and the height above the vertex that an incident beam hits the mirror surface. The value w_m is the beam radius at the mirror surface and θ_i is the angle of incidence. The fraction U will differ for each beam striking the paraboloidal mirror at a different height. It has been calculated that after reflection from a paraboloid mirror a Gaussian beam can be described by

$$E_r = E_{00} + \frac{1}{2} U \left(\sqrt{3} E_{30} + E_{12} \right) \tag{3.2.4}$$

where E_r represent the reflected field and E_{00} is a fundamental Hermite Gaussian beam. The terms E_{30} and E_{12} are the higher order Hermite modes into which the fraction of power denoted by U becomes transfered. The presence of the terms E_{30} and E_{12} signifies that the peak amplitude of the reflected beam, E_r, will no longer occur along the propagation axis. Hence the beam's amplitude has become distorted. Also it is apparent when various beams strike the primary mirror at various heights each beam will encounter a separate value for the equivalent focal length f_p. Therefore the value U for each beam will differ and the various reflected beams will undergo different levels of distortion. An example of this is shown in Figure 3.4.

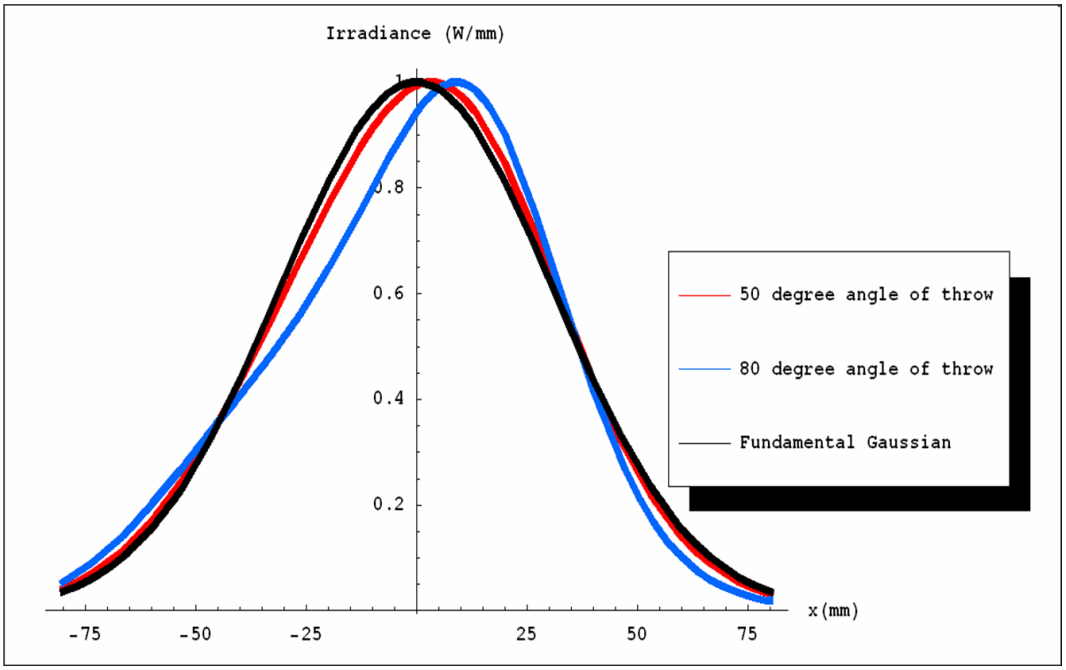

Figure 3.4: Beam distortion in the intensity profile of a Gaussian beam reflected from an off-axis paraboloid at various heights. The focal length of the reflector is 300 mm. Here the wavelength is 2 mm while the input waist radius of 3 mm. As before these values are consistent with the QUBIC parameters discussed in the previous chapter.

In Figure 3.4 we have calculated the amplitude distortion experienced by two 10° FWHM Gaussian beams intersecting a 300 mm focal length paraboloid at different heights above the vertex. The black line indicates a reflected Gaussian beam containing no amplitude distortion. The red and blue lines indicate the reflected distorted beams. We can clearly see that the peak intensities of both beams are displaced from the

propagation axis. However more importantly for QUBIC is that the peak intensities are also displaced from one another. For QUBIC this means that since each the beam from the back-to-back horns will strike the primary parabola at different distances from the axis, each beam will contain a different amount of amplitude distortion. This distortion will affect the profile of the final fringe patterns.

The total beam distortion generated by a combination of two reflectors can be calculated by

$$E_r = E_{00} + (U_2 \pm U_1 exp(-j\Delta_{12}))\frac{1}{2}\left(\sqrt{3}E_{30} + E_{12}\right) \tag{3.2.5}$$

where E_r is the profile of the final Gaussian beam and E_{00} represents an undistorted fundamental Hermite Gaussian beam. As detailed in equation (3.2.3) the terms U_1 and U_2 represent the fraction of power spilled from the fundamental beam into the higher order E_{30} and E_{12} modes after reflection from the primary and secondary reflector respectively. The term $U_2 \pm U_1$ indicates that the final fraction of power transfered into the higher order beams depends on the orientation of the coordinate system of the primary reflector with respect to that of the secondary reflector.

Equation (3.2.5) reveals that if the correct arrangement of dual reflectors is chosen the secondary mirror can compensate for the amplitude distortion induced by the primary [103]. The term Δ_{12} represents the change of the Gaussian beam phase slippage as it travels between the primary and secondary reflectors. It is well documented that after a propagation distance greater than the confocal distance the phase slippage of a Gaussian beam approaches $\frac{\pi}{2}$ radians. If the Gaussian beam does not pass through a waist between the reflectors, the beam will remain in the far field region after propagation from the feed horn. Therefore the change in phase slippage as the beam travels between two the reflectors should be negligible. The term $exp(-j\Delta_{12})$ becomes unity and the distortion induced by the primary reflector can be reduced by inserting a secondary reflector of opposite power to that of the primary. Quite simply if $f_{p1} = -f_{p2}$ where f_{p1} is the equivalent focal length of the primary mirror and f_{p2} is the equivalent focal length of the secondary mirror then $U_1 = -U_2$[12]. Also if

[12]We shall explain using 3.3.1 how the definition of equivalent focal length also includes the angle of throw.

$exp(-j\Delta_{12}) = 1$ then E_r in equation (3.2.5) simply reduces to E_{00}. This is of course an undistorted fundamental Gaussian beam [13]. As we shall now discuss some dual reflectors act to almost cancel out induced amplitude distortion within the generated fringe patterns. Unfortunately some others increase the distortion. Categorization of this particular property is crucial for any additive interferometric QUBIC mission.

Amplitude distortion of single Gaussian beams has been well documented in various combinations of reflectors. For example it has been shown that implementing a pair of equal yet oppositely orientated ellipsoids will minimize amplitude distortion in a central Gaussian beam [103]. For QUBIC we are more concerned with the effect of amplitude distortion on the fringe patterns generated by combining off-axis beams propagating through an off-axis focal systems. We have used the PO techniques of GRASP9 to combine beams from several equivalent baselines propagated through the various dual reflector arrangements we have designed. The layout of these fringe patterns will reveal whether or not the compensated off-axis Cassegrains and Gregorians we have designed induce amplitude distortion in the propagating beams.

The ability to arrange dual reflectors in order to compensate for beam distortion is an example of the insights gained from examining long wavelength systems with more rigorous tools than ray tracing. Although the following systems were designed using the best practices proposed by geometrical optics (ray tracing) these methods are not enough to distinguish precisely which system will induce or reduce amplitude distortion. In order to confirm which systems are better quasi-optical combiners at least a QO analysis or preferably a PO analysis of the systems are required. We have elected for a PO analysis of the various systems. Meanwhile the diffraction limited field of view (DLFOV) given for the various dual reflectors we have investigated will allow us to distinguish which optical systems are better imagers but not necessarily which are better quasi-optical combiners.

We note that as well as deriving conditions for eliminating astigmatism within off-axis dual reflector arrangements Dragone has explained how to significantly reduce coma over small fields of view without incurring spherical aberrations [104]. In order to

[13] This assumes that the waist radius of the Gaussian beam is similar at the secondary mirror to that which occurs at the primary. Once again provided the beam does not travel through a waist radius and the beam remains well collimated between the reflector this assumption is valid.

do so we must deform the surface of the mirrors. For the moment we have forgone this process as well as any attempt to alter the primary mirror in order to create any Ritchey-Chrétien variations. This is because, to date, no matter how complicated a final CMB optical system has emerged the design commenced by considering simple standard second order polynomial reflectors. This includes the off-axis Gregorian constructed for the Planck CMB mission [105]. Therefore the consideration of phase and beam distortion induced by various categories of dual reflectors consisting of standard conic surfaces is useful for any future bolometric interferometry, ground based or satellite mission. Once a promising basic design is found, mirror surfaces can then be deformed to improve phase aberration.

In the PO analysis we have examined the fringe patterns produced by 2 sets of 5 equivalent baselines occurring along orthogonal axes of the sky horn array. The layout of these baselines is shown in Figure 3.5. Here circles indicate the position of the back-to-back sky horns. The length of the individual baselines is 40 mm. This value represents the mid-point between the maximum and minimum baselines over which QUBIC will observe at 150 GHz. The blue lines indicate the baselines occurring along what I have called the x-axis of the horn array. Similarly the green lines indicate the baselines along the y-axis of the array. Therefore each group of blue and green lines represents two 40 mm equivalent sets of baselines. The 5 baseline pairs have been designated CEN, UPL, UPR, LOWL and LOWR according to their position in the back-to-back array.

The size of the horn array is 140 mm^2. This is the minimum number of horns QUBIC is requires in order to detect B-modes. We have chosen to examine the fringes generated by the outermost horns along this grid. Therefore the coordinates of the corner horn (X,Y) in Figure 3.5 are **(70 mm, 70mm)**. The remaining corner horns are placed at ($\pm$ 70 mm,$\pm$ 70mm) in accordance with their position relative to the origin.

In the following section we will show the fringe patterns generated by each of the individual baselines over an area of 225 $\times$ 225 mm^2. Recall that in order for QUBIC to successfully recover Stokes visibilities the fringe patterns from equivalent baselines must be as similar as possible. Part of the work carried out by the author was to determine how similar the fringe patterns produced by equivalent baselines combined using various combiners are to one another. It is through the comparison of these

baselines that the applicability of the various dual reflectors to QUBIC can be assessed. This work will be discussed in the next chapter.

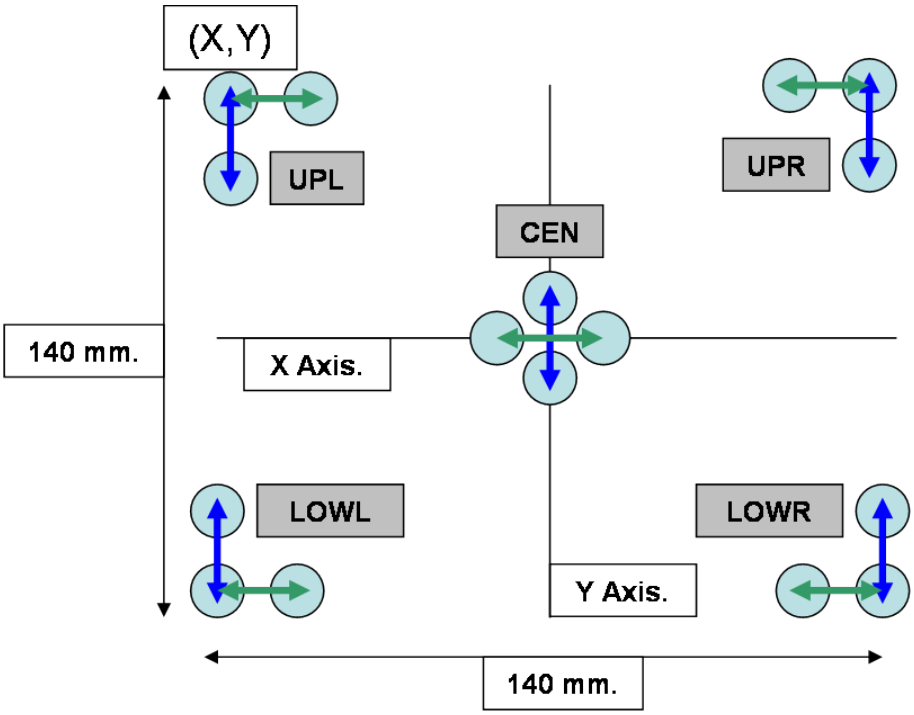

Figure 3.5: Layout of 40 mm equivalent baselines the beams from which are propagated through the various optical combiners.

3.3 Compensated dual reflectors

In the past decade a wealth of literature has emerged discussing how to design compensated dual reflectors that obey both the Rusch and Dragone conditions. At least five of the parameters shown in Figure 3.3 are required to fully design an off-axis compensated dual reflector. The various different ways these characteristics can be related to one another and the number of 5-parameter combinations possible that will describe a compensated reflector means that a large collection of approaches are available with which we can design the QUBIC combiner. For example the most authoritative paper discussing the design techniques for optical combiners lists no fewer than 21 free parameters and 39 separate formulae that can be used in 12 separate ways to design

a single compensated system [106]. The majority of the systems below were designed using some variation of the following technique.

The most comprehensive formula that describes an off-axis dual reflector is shown in equation (3.3.1)[14]. Here

The equivalent focal length f_e of an off-axis dual reflector is related to the focal length of the primary paraboloid f_p, the eccentricity e of the secondary reflector and the tilt between the reflector axes β by

$$f_e = f_p\left(\frac{e+1}{e-1}\right)\frac{1+\tan^2\left(\frac{\beta}{2}\right)}{1+\left(\frac{e+1}{e-1}\right)^2\tan^2\left(\frac{\beta}{2}\right)}. \tag{3.3.1}$$

In the systems below we have set the equivalent focal length to 800 mm and rearranged equation (3.3.1) to write the primary focal length in terms of the eccentricity and the tilt between the reflectors. From trial and error we then chose a value for the primary focal length. Then values for the tilt, the angle of throw and the eccentricity were found by solving equations (3.2.1), (3.2.2) and (3.3.1) simultaneously. Finally the distance between the two foci were set to create the smallest possible secondary mirror that will capture all rays reflected from the primary [15].

A difficulty in designing the off-axis systems presented in this chapter concerned the number of undisclosed free parameters we had to establish in order to fully quantify the systems. As stated a general rule of thumb is that at least five individual parameters are required when designing a compensated dual reflector [106]. However in QUBIC the only definitive information we have concerning the combiner is that its equivalent focal length should be $200 \sim 400$ mm.

The design procedure for these systems was as follows. As stated above, we begun by setting the equivalent focal length to 800 mm[16]. Increasing the focal length has

[14]Equation 3.3.1 has be taken from the GRASP9 Technical Description Manual. For more information visit `http://www.ticra.com/`

[15]Equation (3.3.1) has be taken from the GRASP9 Technical Description Manual. For more information visit `http://www.ticra.com/.`

[16]Such short focal lengths of $200 \sim 400$ mm will automatically exclude many dual reflectors from implementation due to the large entrance aperture needed by an array of 12×12 sky horns.

permitted us to study a variety of designs. We then set other values such as the angle of throw or the tilt between the reflectors and solved for the remaining variables using the methods described in the reference literature. The values for all predetermined parameters were chosen in order to create what we judged to be the most functional (for example the most compact) that produced the lowest magnitude wavefront aberrations. Therefore we are confident that each of the systems described below is the best performing 800 mm focal length system of its category that can be implemented to combine 14° FWHM beams emerging from a 140 mm^2 entrance aperture.

We must now elaborate on some technical terms. In this thesis we use the word imager to describe any system functioning as as telescope. This is any optical device that focuses rays traveling parallel from infinity to a single point. All dual reflectors discussed below were originally studied within the literature solely as imagers. The QUBIC combiner will function as a telescope however with some distinct differences. In most telescopes the entrance diameter is placed at the primary mirror. Therefore the size of the entrance aperture simply equals the size of the primary mirror and is unblocked. In QUBIC the entrance aperture is at the location and is the size of the back-to-back horn array. Because this entrance aperture is blocked by the horn array QUBIC functions as a Fizeau interferometer. In telescopes, the field of view (FOV) is defined as the maximum angle that light incident on the entrance diameter can be brought to a focal point. It is apparent that QUBIC's FOV will equal the FWHM of the Gaussian beams propagating from the back-to-back horns. Therefore by investigating whether or not a dual reflector can adequately focus incident rays over a 14° FOV we can find out if the same system can adequately combine 14° FWHM Gaussian beams.

Therefore we have designed dual reflectors with an 800 mm equivalent focal length. This value is in fact a reasonable upper limit when one considers the uncertainty regarding many of QUBIC's initial design specifications. We recall that the size of the focal plane and therefore the focal length is restricted by the number of bolometers that can be currently multiplexed together. However considering the constant improvement in modern lithography and edging techniques used to construct the detectors it is highly likely this number will increase within a matter of years. Therefore it is prudent that we investigate all possible dual reflectors that many be employed as off-axis beam combiners. Such an investigation is also extremely important in the context of possible future satellite CMB missions where it is likely a completely new generation of technologies will be implemented.

We have used Zemax to calculate the extent of the DLFOV of the dual reflectors discussed below. In order to demonstrate the DFLOV Zemax calculates the Strehl ratio of the systems. The Strehl ratio is defined as the ratio $S = \frac{I_{ab}}{I_{unab}}$ where I_{ab} is the intensity in the aberrated Airy pattern generated by an optical system and I_{unab} is the intensity in an unaberrated pattern. The Strehl ratio can be calculated from the wavefront variance σ by $S = exp\Big[(-k\sigma)^2\Big]$ where k is the wave number. The wavefront variance is defined as

$$\sigma^2 =< W^2 > - < W >^2 \tag{3.3.2}$$

where W is the aberrated wavefront. Zemax uses a ray tracing algorithm to calculate the magnitude of Seidel aberrations in the focusing wavefronts. Zemax then computes $W = W_{040} + W_{131} + W_{222} + W_{220} + W_{311}...$ up to any higher order polynomial terms required [17].The magnitude of aberrations increases with the field of view therefore the Strehl ratio will decrease. Plots showing the decrease of the Strehl ratio versus the FOV for various dual reflectors are shown in the next section. When the ratio drops below 0.8 the system is said to be no longer considered diffraction limited. This means that the presence of wavefront aberrations will now affect the performance of the system.

Except where stated otherwise all optimizations performed in the thesis use the Zemax *default merit function*. Zemax defines a general merit function as the sum of a number of values

$$MF = \big(\sum_i \big(V_i - T_i\big) / \sum_i W_i\big)^{\frac{1}{2}} \tag{3.3.3}$$

where MF is the merit function, W_i is the weight placed on a given value, T_i is the target value and V_i is the current value of the parameter we wish to optimize. When the Zemax *default merit function* is selected Zemax traces n number of rays from each field position through the optical system. The (x_i, y_i) location where each ray intersects the focal plane is calculated. Zemax then calculates an appropriate value W_i

[17]The terms W_{040}, W_{131}, W_{222}, W_{220} and W_{311} are the familiar third order spherical aberration, coma, astigmatism, field curvature and phase distortion.

for each ray using the RMS spot radius for all the points of intersection of the traced rays. This is defined as:

$$RMS = \Big(\sum_i \big((x_i - x_c)^2 + (y_i - y_c)^2\big)/n\Big)^{\frac{1}{2}}. \tag{3.3.4}$$

Here value (x_c, y_c) represents the centre point and can be nominated as either the chief ray pierce or the centroid value of all intersecting rays. Zemax attempts to improve the performance of a system by altering certain aspects of the system (set by the user) such as the radii of curvature or the thickness between surfaces. Upon each alteration of such values the merit function is recalculated and the optimization proceeds until the system that produces the lowest obtainable RMS has been found.

By attempting to drive RMS value to zero the system that produces the highest quality images is found. Essentially the lower the RMS of an optical system the better that system is at combining parallel rays in the object space to a single point in the image space. The closer rays from a single field all converge to a single point the closer the focusing wavefront approximates a prefect spherical wave. Recall that aberrations such a coma, astigmatism field curvature and distortion quantify how much a focusing wavefront differs from a perfect spherical reference wavefront. By optimizing the optical combiners using the $default\ merit\ function$ to reduce the above RMS value the wavefront aberrations will also be minimized.

Compensated Gregorian vs compensated Cassegrain

A geometrical optical analysis of both an 800 mm focal length off-axis compensated Gregorian and Cassegrain reflector is shown in Figure 3.6 and 3.7 respectively. These systems have been designed using equations (3.2.1), (3.2.2) and (3.3.1) in accordance with the methods discussed in [106]. Immediately it can be seen that the compensated Gregorian offers a larger DLFOV than its counterpart. This is the primary reason the compensated Gregorian has come to dominate CMB observations. The compensated Gregorian accommodates the wide field of view necessary to generate full sky maps but also allows a large entrance diameter to ensure the necessary sensitivity. Also it was found to be difficult to design an 800 mm Cassegrain that would capture all of the

power of beams over 14° FWHM.[18] We therefore expect that the Cassegrain reflector will truncate the majority of 14° FWHM beams propagating from the horn array. The amount of power loss due to spillover is greater in the compensated Cassegrain than in the Gregorian reflector. Geometrical optics thus predicts that the compensated Cassegrain is significantly more restricted by a low focal ratio than the compensated Gregorian.[19]

Figures 3.8, 3.9, 3.10 and 3.11 display the fringe patterns generated by the five 40 mm equivalent baselines combined by the compensated Gregorian and Cassegrain reflectors. The fringe patterns were produced using the software package GRASP and for a frequency of 150 GHz. The effect of a 25% bandwidth is considered later in Section 6.4.

At this stage fringe patterns were assessed qualitatively only, later in Section 4.3 I describe how the quality of combiners considered as possibilities for QUBIC were measured by comparing fringe pattern from equivalent baselines. The distortion present in the fringes generated by the baselines orientated along the x-axis of the horn array as shown in Figure 3.5 is clearly visible. We note that the same beam distortion is not present in the fringe patterns generated by baselines displaced along the y-axis of the horn array. This is because due to system geometry beams from each of the horns strike the primary mirror at the same height above the paraboloid vertex. Therefore the value of f_p in equation (3.2.3) is equal for baseline pairs at equal heights along the primary reflector. As explained above this will minimize beam distortion for these baselines.

In Figures 3.8 and 3.10 we see that both the compensated Gregorian and Cassegrain systems will produce beam distortion in the fringe patterns generated by baselines displaced along the x-axis of the horn array. The curved appearance of the fringe patterns in Figures 3.8 and 3.10 is indicative of two distorted Gaussian beams combining with one another.

[18] In all DFLOV plots shown in this chapter the x-axis representing the field of view ranges from 0 to 14°.

[19] In all lens diagrams shown we have displayed a slice of the primary parabola. In order to display the tilted nature of the two mirrors we have displayed a symmetric portion of the secondary reflector. The axis of symmetry of the secondary reflector is clearly visible as well as its tilt in relation to the primary mirror.

Also from the large DLFOV shown in Figure 3.6 it is apparent that the fringes formed by combining 14° FWHM beams using the compensated Gregorian will be less affected by the presence of classical Seidel aberrations than the fringes produced by the compensated Cassegrain. As shown in Figure 3.7 the presence of aberrations dominate the imaging properties of the 800 mm compensated Cassegrain when the field of view exceeds 10°. Therefore we expect that the fringe patterns in Figure 3.10 are not only deformed by amplitude distortion but also by the effects of truncation by the secondary reflector and the presence of large magnitude Seidel aberrations.

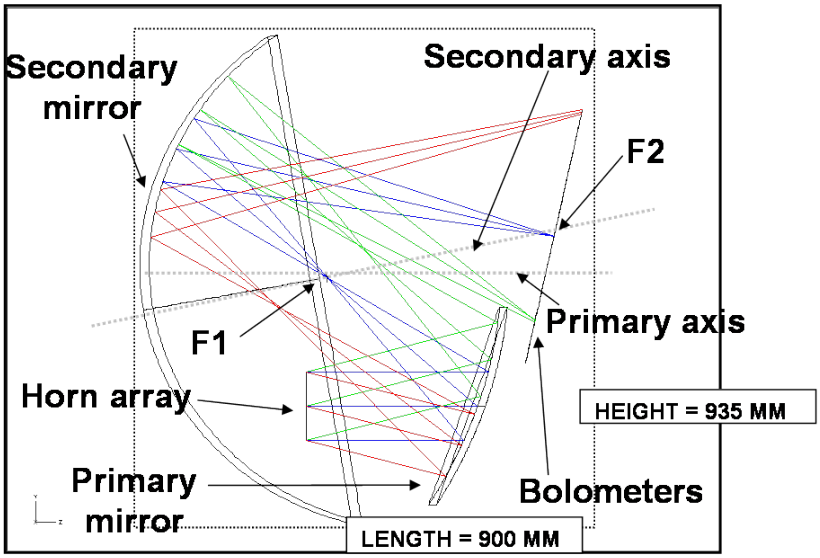

(a) Off-axis compensated Gregorian reflector. The tilt between the reflector axes is 10°. The eccentricity of the secondary ellipsoid is 0.3955. The size of any box containing this system is at least $900 \times 985 \times 700$ mm^3.

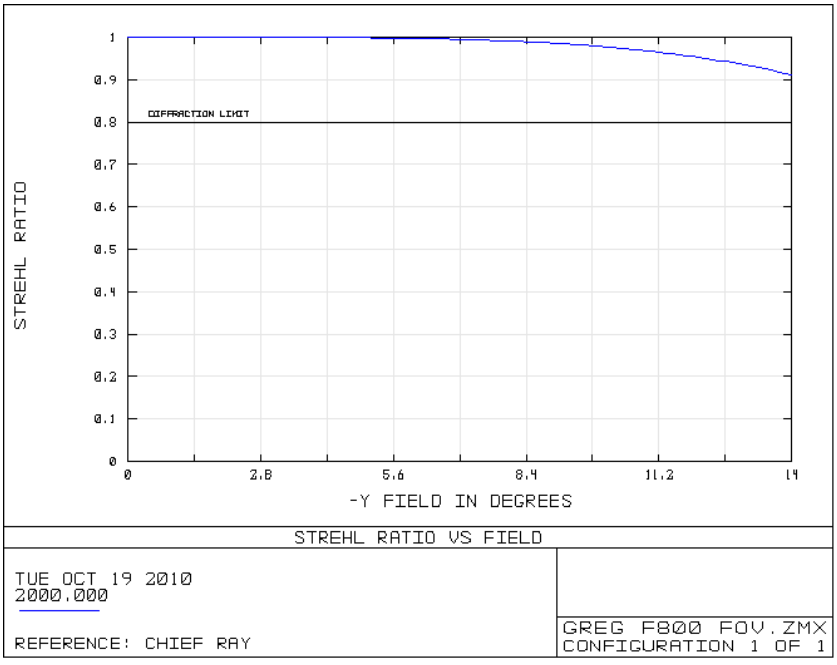

(b) The DLFOV of the compensated Gregorian is greater than 14° for a 140 mm entrance aperture.

Figure 3.6: Off-axis compensated Gregorian reflector. The focal length of this system is 800 mm.

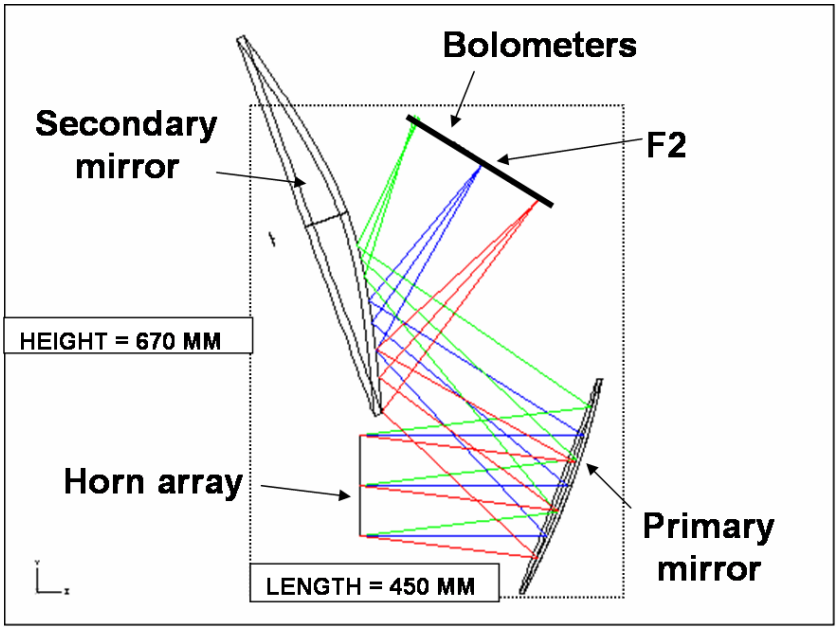

(a) Off-axis compensated Cassegrain reflector. The tilt between the reflector axes is 20°. The eccentricity of the secondary ellipsoid is 3.47. The size of any box containing this system is at least $670 \times 450 \times 700$ mm^3.

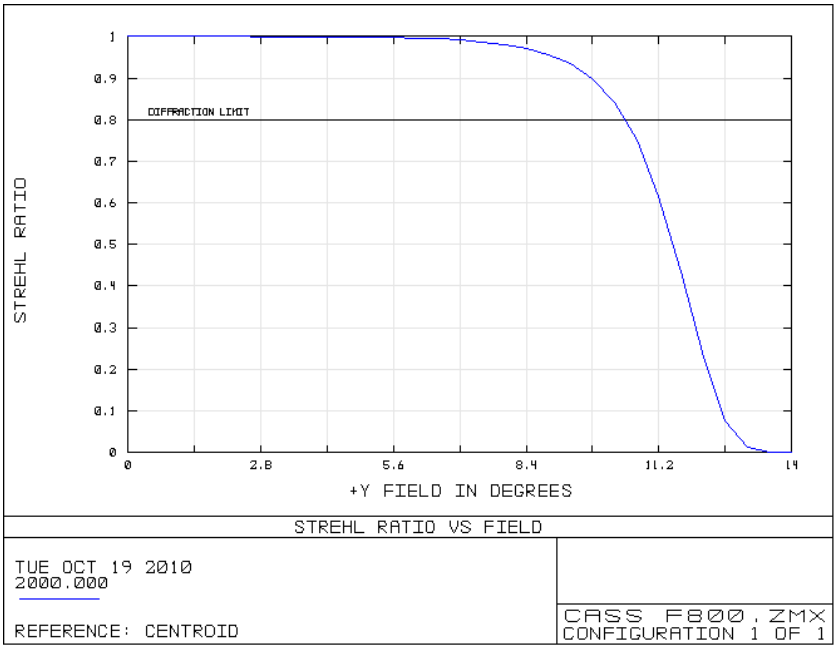

(b) The DLFOV of the compensated Cassegrain is less than 11° for a 140 mm entrance aperture.

Figure 3.7: Off-axis compensated Cassegrain reflector. The focal length of this system is 800 mm.

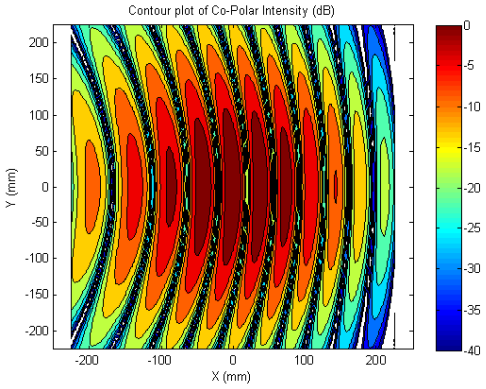

(a) CEN baseline.

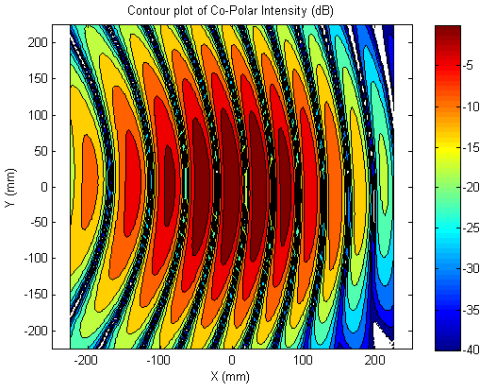

(b) LOWL baseline.

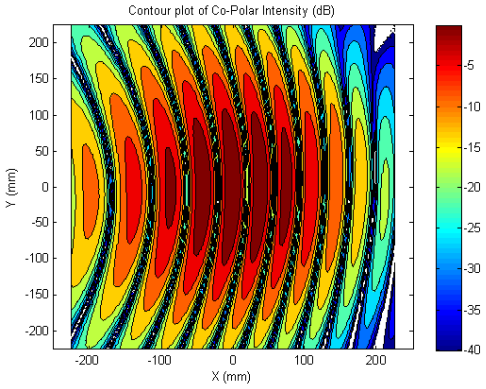

(c) LOWR baseline.

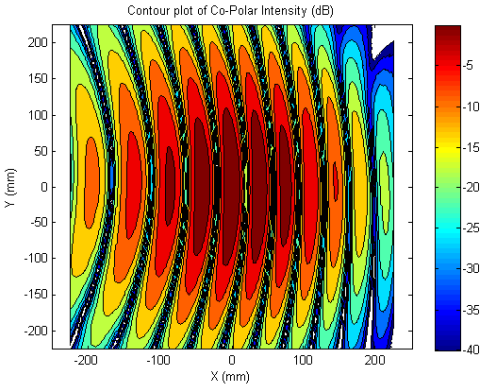

(d) UPL baseline.

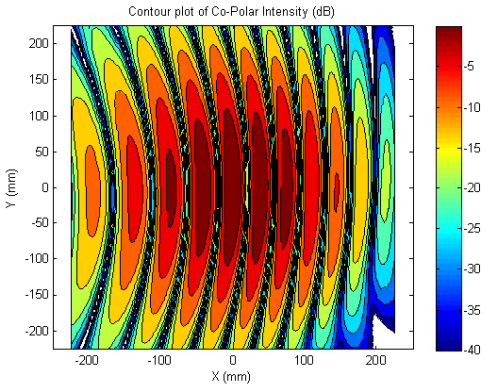

(e) UPR baseline.

Figure 3.8: Fringe patterns produced by the compensated Gregorian. These fringe patters were produced using the GRASP software package for a frequency of 150 GHz. The baselines generating these fringes occurred horizontally along the horn array's x-axis. The fringes have been formed using 14° FWHM Gaussian beams and 40 mm baselines.

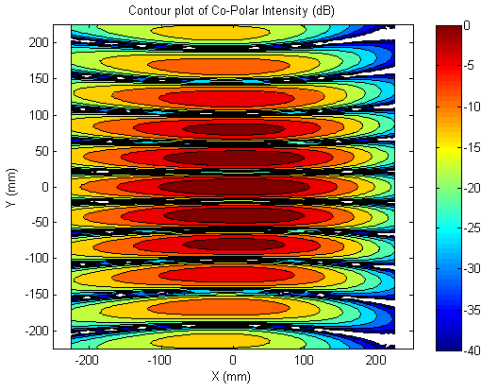

(a) CEN baseline.

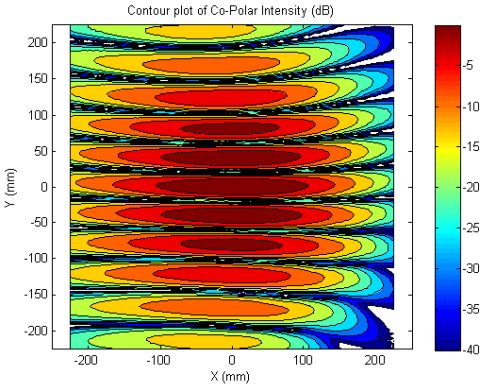

(b) LOWL baseline.

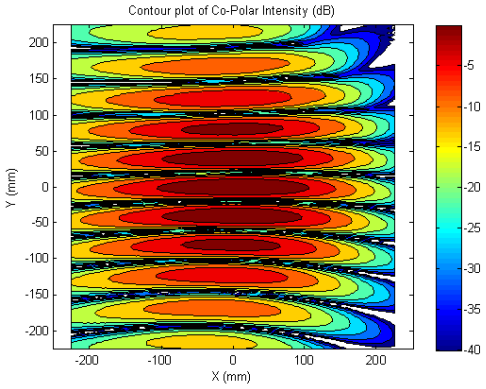

(c) LOWR baseline.

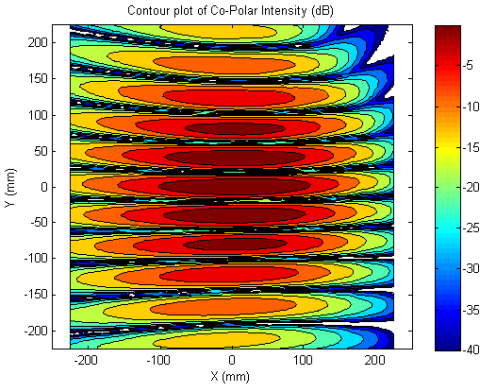

(d) UPL baseline.

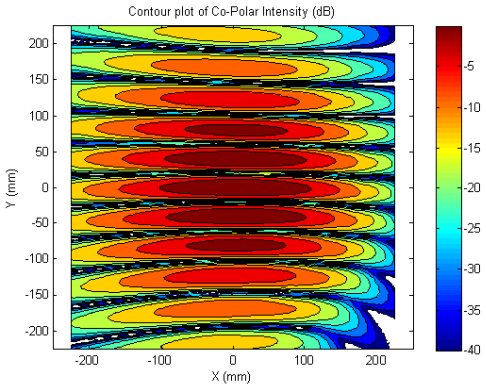

(e) UPR baseline.

Figure 3.9: Fringe patterns produced by the compensated Gregorian. These fringe patters were produced using the GRASP software package for a frequency of 150 GHz. The baselines generating these fringes occurred horizontally along the horn array's y-axis. The fringes have been formed using 14° FWHM Gaussian beams and 40 mm baselines.

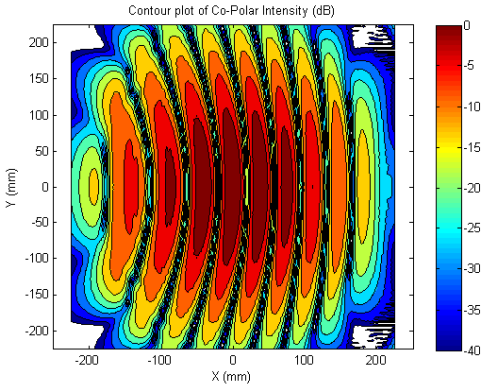

(a) CEN baseline.

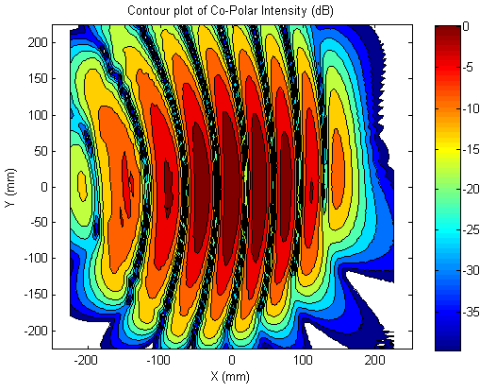

(b) LOWL baseline.

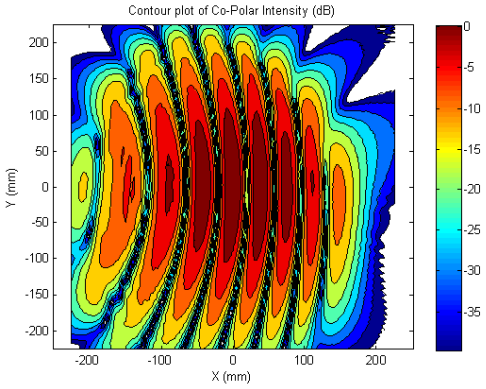

(c) LOWR baseline.

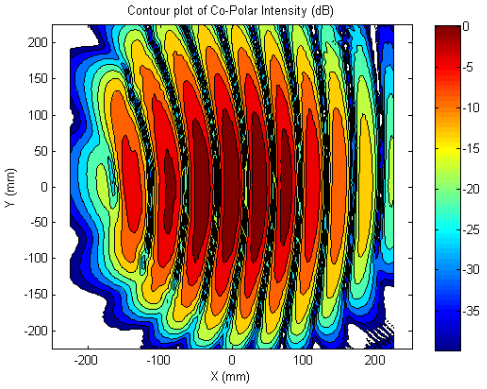

(d) UPL baseline.

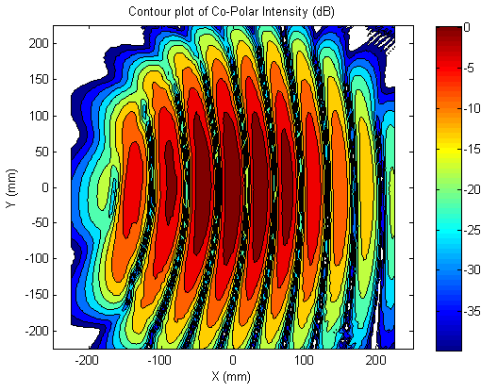

(e) UPR baseline.

Figure 3.10: Fringe patterns produced by the compensated Cassegrain. These fringe patters were produced using the GRASP software package for a frequency of 150 GHz. The baselines generating these fringes occurred horizontally along the horn array's x-axis. The fringes have been formed using 14° FWHM Gaussian beams and 40 mm baselines.

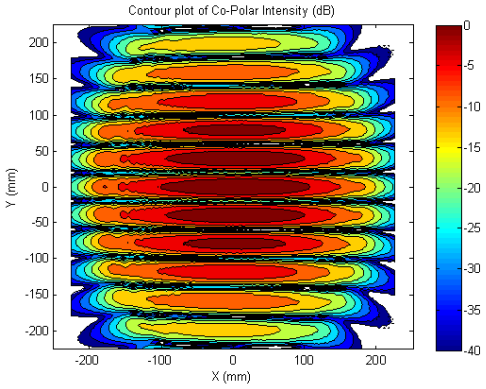

(a) CEN baseline.

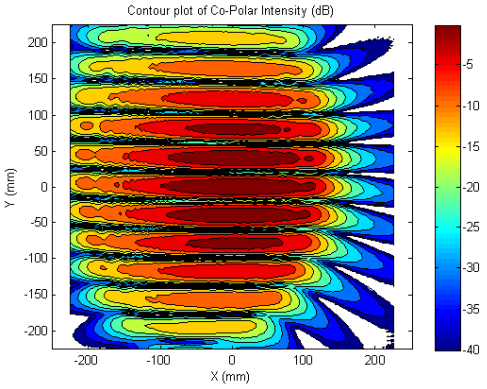

(b) LOWL baseline.

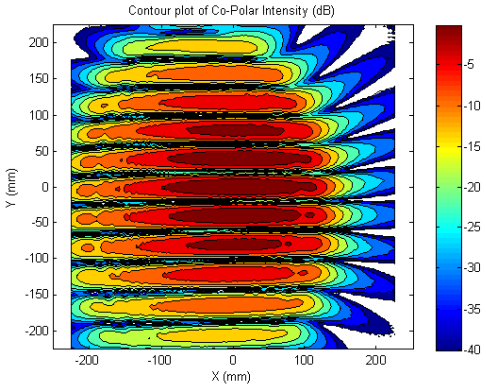

(c) LOWR baseline.

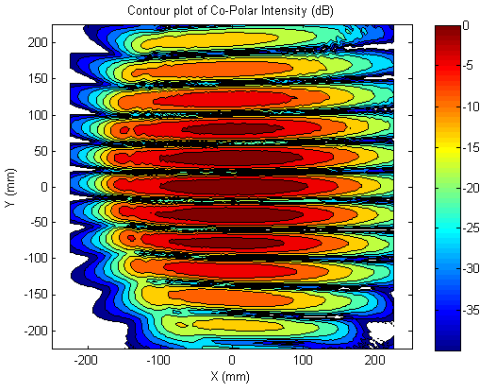

(d) UPL baseline.

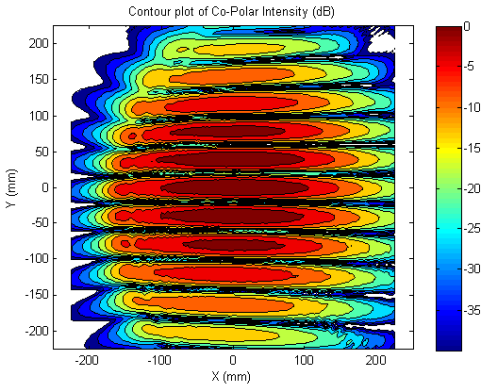

(e) UPR baseline.

Figure 3.11: Fringe patterns produced by the compensated Cassegrain. These fringe patters were produced using the GRASP software package for a frequency of 150 GHz. The baselines generating these fringes occurred horizontally along the horn array's y-axis. The fringes have been formed using 14° FWHM Gaussian beams and 40 mm baselines.

Compact antenna test range (CATR) vs an inverted-crossed Cassegrain

There are categories of compensated dual reflectors in which the rays reflected from the secondary mirror cross the rays incident on the primary. Such a reflector is referred to as a crossed system. The compact antenna test range (CATR) is a special case of a crossed reflector in which the chief ray reflected from the secondary crosses the incident chief ray on the primary at a right angle.

A geometrical optics analysis of an 800 mm focal length compact antenna test range (CATR) and an inverted-crossed Cassegrain is shown in Figures 3.12 and 3.13 respectively [20]. These crossed designs are attractive for CMB observations due to the fact that the incident and reflected chief ray are perpendicular. This means that a required optical window, or as in the case of QUBIC a back-to-back horn array, can can be placed at right angles to the detector plane. This makes the cryostat construction somewhat more simple due to the fact that the optical system can essentially be placed within a box in which the detector array and back-to-back horns can be placed on orthogonal sides. These systems have been designed by following the methods discussed in [107] and [108]. Here it has been shown that in order to ensure a crossed reflector the sum of angles $\alpha + \beta$ discussed in Section 3.2.1 must equal 90°. Once this condition is established we set the equivalent focal length and the tilt (β) between the reflectors, we then solve equations (3.2.1), (3.2.2) and (3.3.1) to find the primary focal length, secondary eccentricity and angle of throw. In these designs the secondary eccentricity in the CATR and the primary focal length in the inverted-crossed Cassegrain are both less than zero.

It is apparent from Figure 3.12 that according to geometrical optics the CATR completely surpasses all the other types of compensated dual reflectors in terms of performance. The DFLOV is significantly greater than that offered by the compensated Gregorian which is the closest rival in terms of performance. Also a Zemax comparison of these systems shows that the field curvature of wavefronts focused using the CATR is less than the curvature of the focusing wavefronts produced by the compensated Gregorian. This is shown in Figure 3.14. This means that the wavefronts of beams propagating through the CATR are more planar when compared to the wavefronts of

[20] Within this thesis we refer to any system that implements a convex primary mirror as inverted. This is following the standard convention found in the reference literature.

the beams propagating through the compensated Gregorian. Therefore the addition of secondary optics such as lenses in order to produce maximum coupling efficiency to a flat focal plane would be simpler in the CATR. All major CMB experiments such as WMAP and PLANCK have made use of a compensated Gregorian however recently for reasons mentioned above the CATR has emerged as a viable option for both CMB telescopes and interferometers.

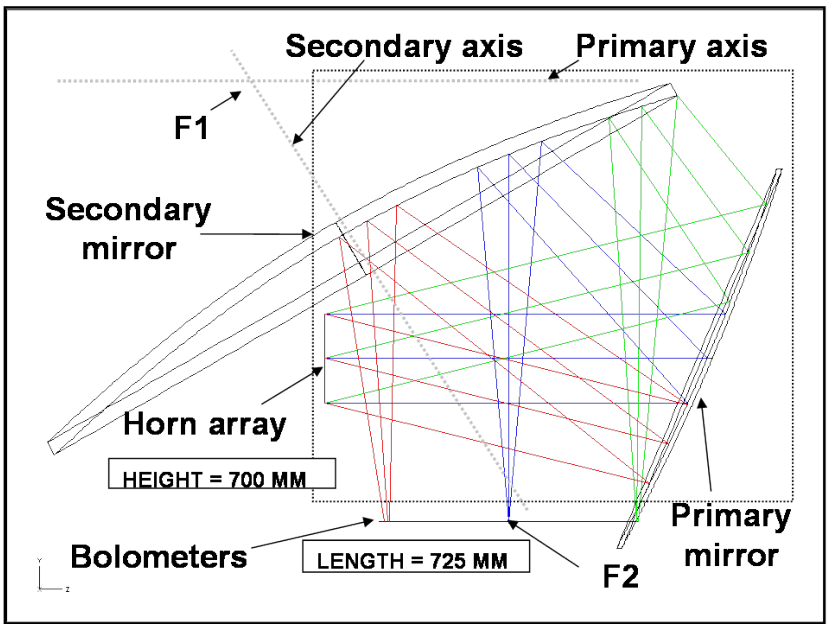

(a) CATR dual reflector. The tilt between the reflector axes is 60°. The eccentricity of the secondary ellipsoid is 2.732. The size of any box containing this system is at least $725 \times 700 \times 550$ mm^3.

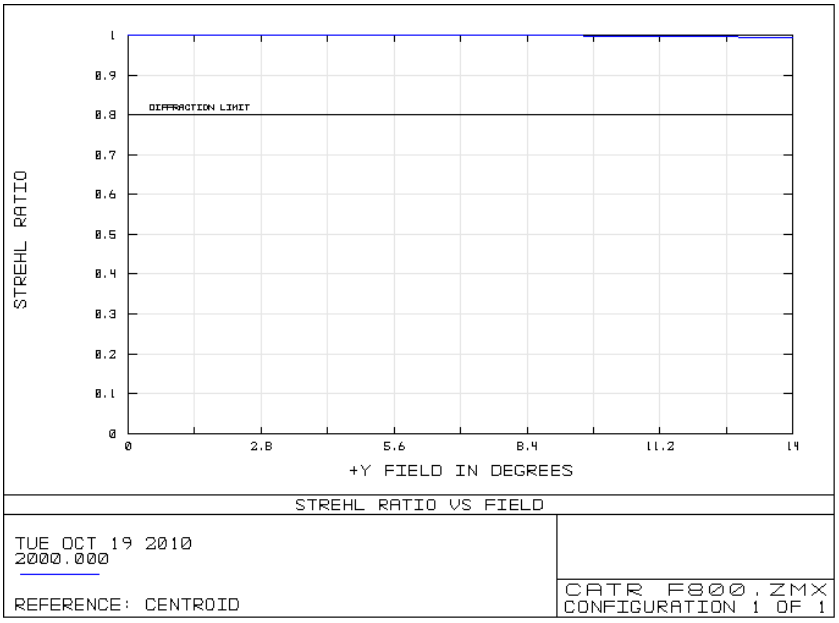

(b) The DLFOV of the CATR exceeds 14° for a 140 mm entrance aperture.

Figure 3.12: CATR dual reflector. The focal length of this system is 800 mm.

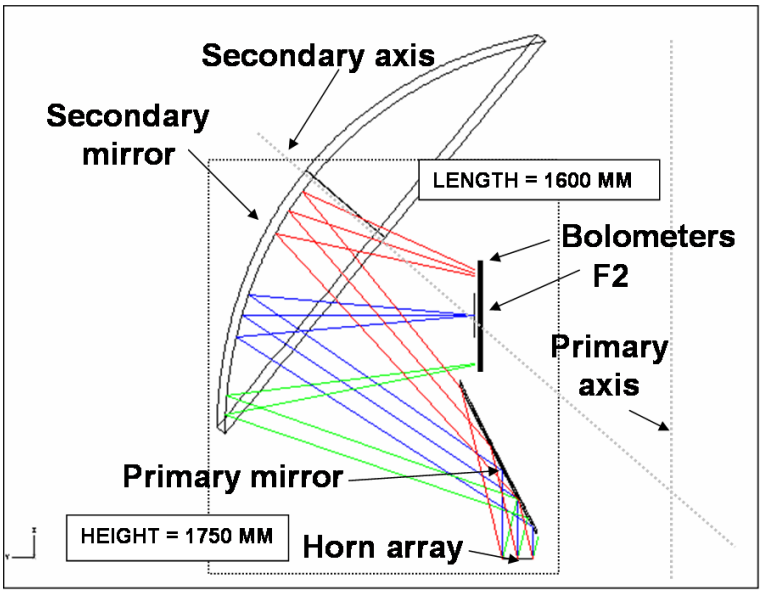

(a) Inverted-crossed Cassegrain dual reflector. The tilt between the reflector axes is 50°. The eccentricity of the secondary ellipsoid is 0.71. The size of any box containing this system is at least 1600 × 1750 × 600 mm^3.

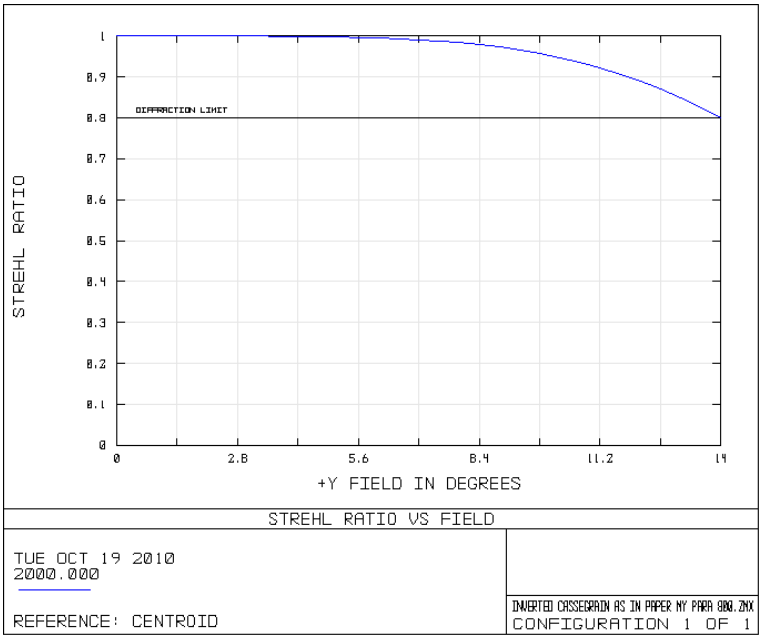

(b) The DLFOV of the inverted-crossed Cassegrain just falls short of 15° for a 140 mm entrance aperture.

Figure 3.13: Inverted-crossed Cassegrain dual reflector. The focal length of this system is 800 mm.

The inverted-crossed Cassegrain has received much less attention than the CATR. In fact to the author's knowledge there is no current sub-mm or mm observing mission implementing such a reflector. It is mainly due to the usual use of a convex primary reflector that the design has not become more prevalent. It can be seen that the DFLOV is comparable with that of the compensated Gregorian. Also although it is larger than the CATR the geometry of the inverted-crossed Cassegrain allows the primary reflector to shadow the detector field from the back-to-back horn array.

Figures 3.15, 3.16, 3.17 and 3.18 display the fringe patterns generated by the 5 equivalent baselines combined by the CATR and the inverted-crossed Cassegrain. The immediate significance of Figure 3.15 is that it illustrates that the fringe patterns generated by the CATR are all very close to straight. This means that the CATR induces minimal amplitude and phase distortion within the Gaussian beams which it combines. The reason for this concerns the system geometry and will be discussed later.

Despite the benefits of its crossed design (and the fact that spillover from the horn array onto the detector plane can be prevented by the position of the primary mirror) Figure 3.17 shows that the fringe patterns generated by baselines occurring along the x-axis of the horn array in the inverted-crossed Cassegrain are curved. Once again this deformation of the fringes suggests that the beams combining to generate the patterns contain significant levels of amplitude distortion.

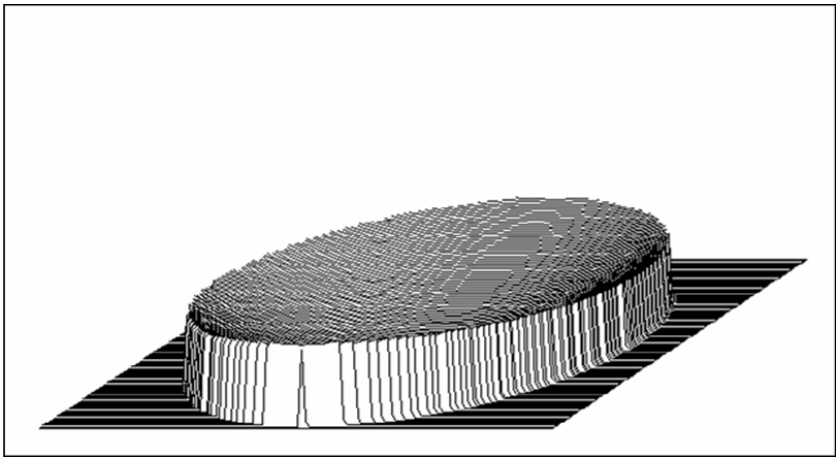

(a) Wavefront produced the CATR. This wavefront is almost planar at the focal plane.

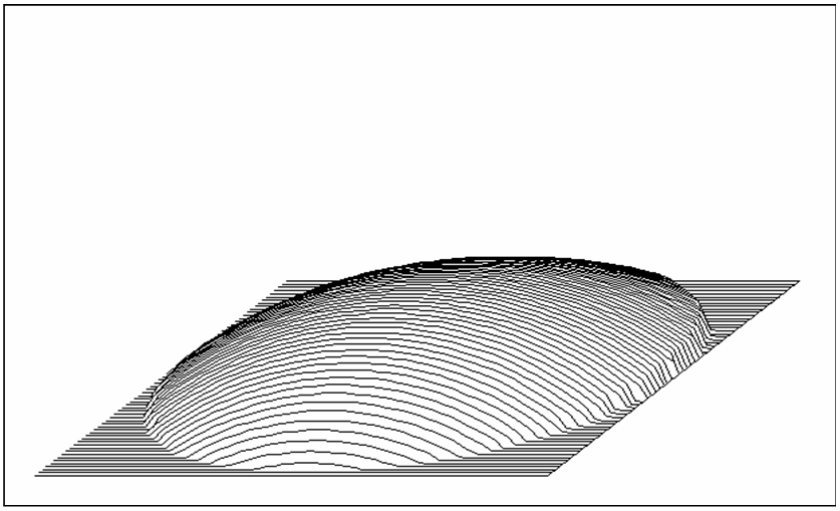

(b) Wavefront produced the compensated Gregorian. The dome shape of this wavefront suggests the this system will induce field curvature into propagating beams.

Figure 3.14: Wavefronts generated from both the CATR and compensated Gregorian reflectors using Zemax. These wavefronts were constructed by joining rays at equal optical path lengths when the chief ray crosses the system's focal plane. The rays emerge from a point representing the centre of the horn array and diverge with a 14° FOV. Both images are compiled by sampling within the radius the systems' Airy disks at the focal plane. These radii are 3.9 mm and 5.4 mm at 150 GHz for the CATR and compensated Gregorian respectively. The difference of these values is due to the different widths of the primary mirrors as listed in Table 3.1.

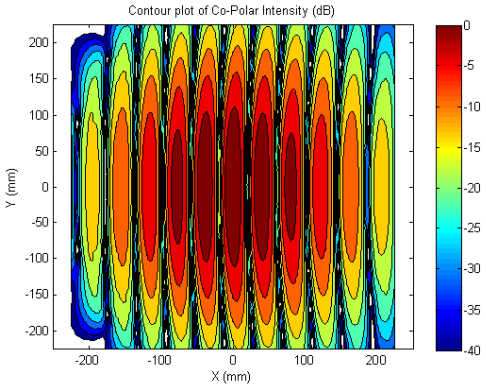

(a) CEN baseline.

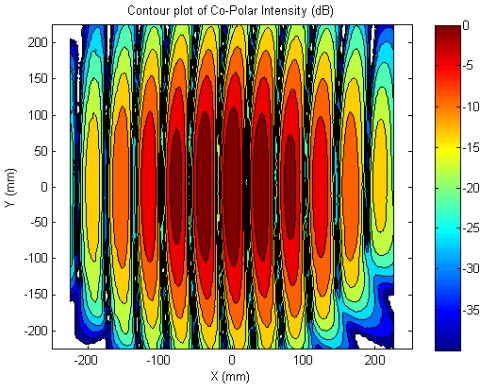

(b) LOWL baseline.

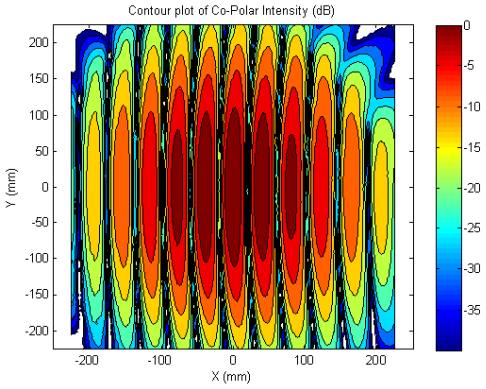

(c) LOWR baseline.

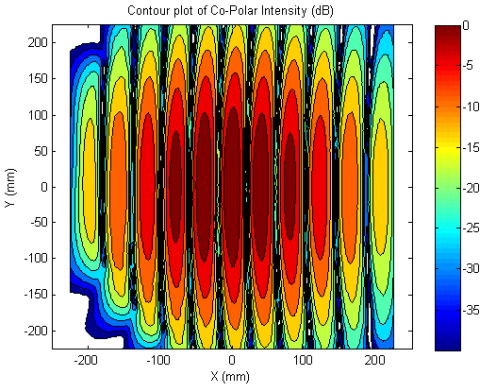

(d) UPL baseline.

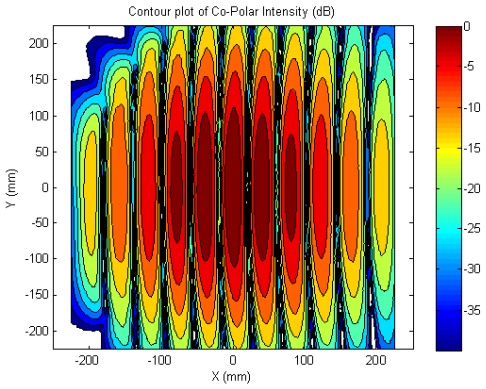

(e) UPR baseline.

Figure 3.15: Fringe patterns produced by the CATR. The baselines generating these fringes occurred horizontally along the horn array's x-axis. The fringes have been formed using 14° FWHM Gaussian beams and 40 mm baselines.

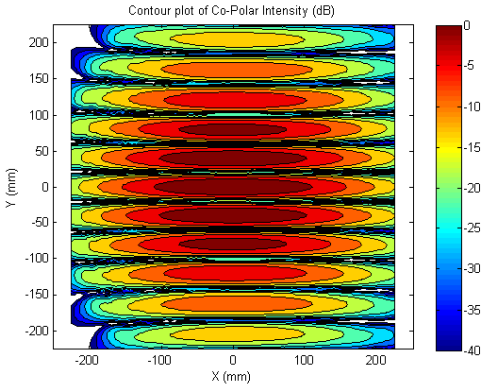

(a) CEN baseline.

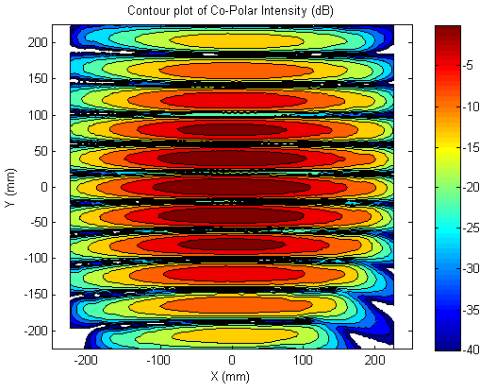

(b) LOWL baseline.

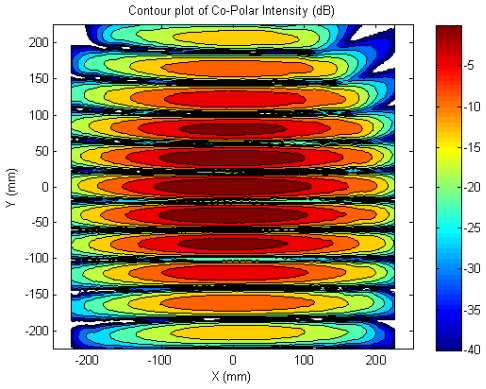

(c) LOWR baseline.

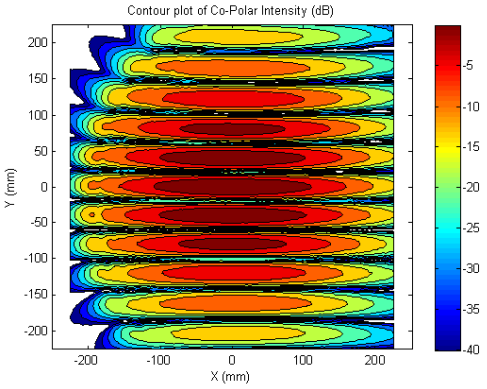

(d) UPL baseline.

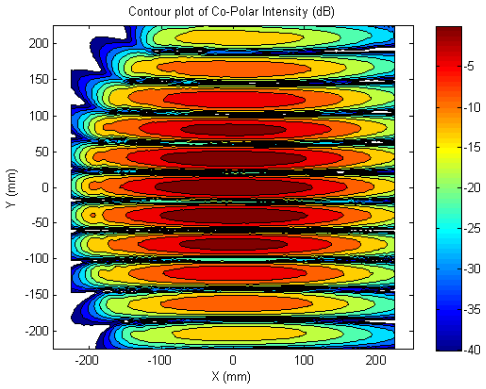

(e) UPR baseline.

Figure 3.16: Fringe patterns produced by the CATR. The baselines generating these fringes occurred horizontally along the horn array's y-axis. The fringes have been formed using 14° FWHM Gaussian beams and 40 mm baselines.

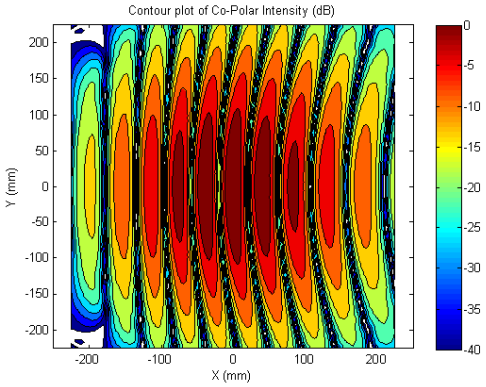

(a) CEN baseline.

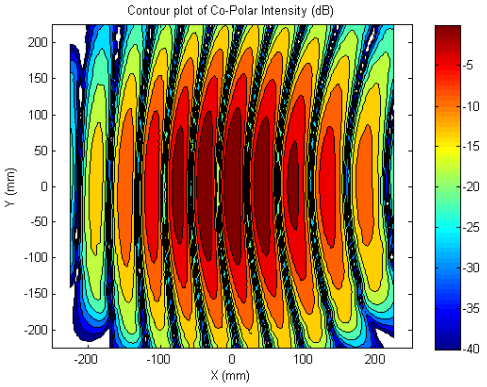

(b) LOWL baseline.

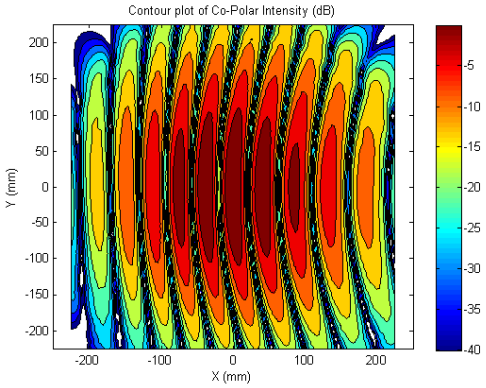

(c) LOWR baseline.

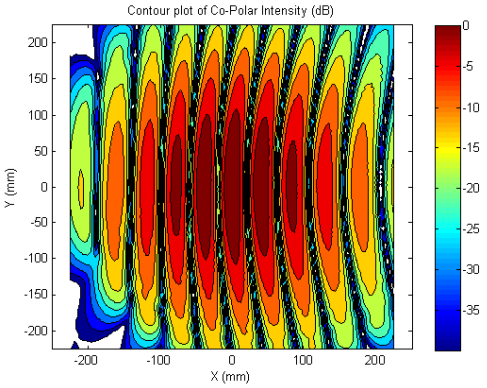

(d) UPL baseline.

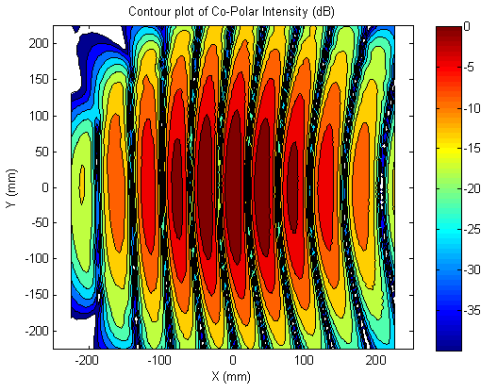

(e) UPR baseline.

Figure 3.17: Fringe patterns produced by the inverted-crossed Cassegrain. The baselines generating these fringes occurred horizontally along the horn array's x-axis. The fringes have been formed using 14° FWHM Gaussian beams and 40 mm baselines.

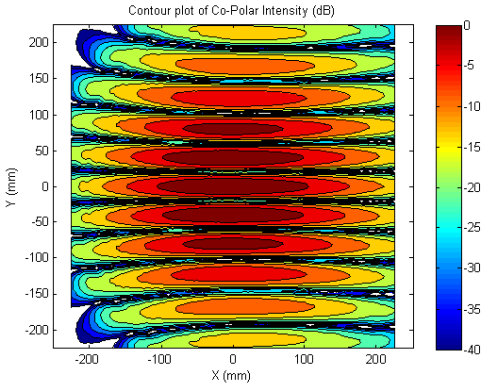

(a) CEN baseline.

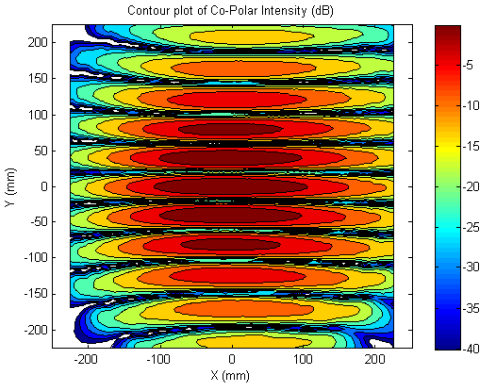

(b) LOWL baseline.

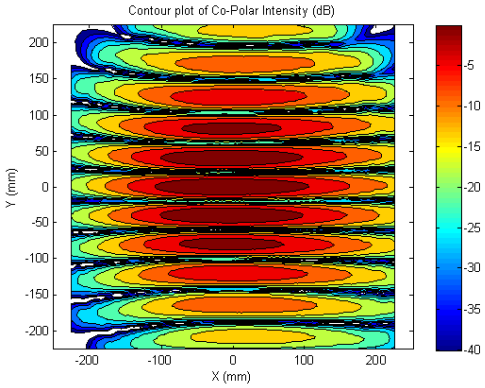

(c) LOWR baseline.

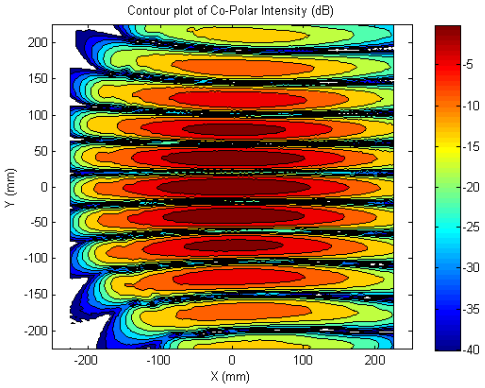

(d) UPL baseline.

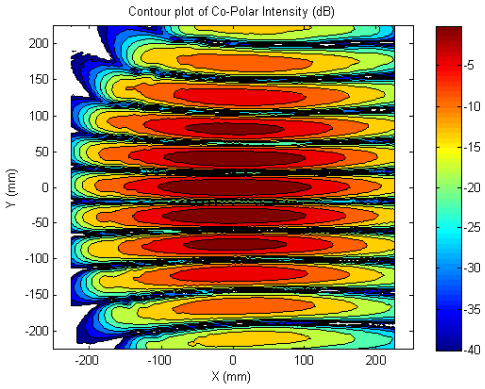

(e) UPR baseline.

Figure 3.18: Fringe patterns produced by the inverted-crossed Cassegrain. The baselines generating these fringes occurred horizontally along the horn array's y-axis. The fringes have been formed using 14° FWHM Gaussian beams and 40 mm baselines.

Front-end-fed Compensated Cassegrain vs back-end-fed Gregorian

We now consider two more systems that also allow for simple cryostat construction. The first is a front-end-fed compensated Cassegrain. Such a system is shown in Figure 3.19. Here the incident chief ray is anti-parallel to the reflected chief ray. This means that the detector array and the back-to-back sky horns can be placed parallel to one another. The removal of any tilt between these components is expected to reduce the complication of any cryostat construction. This system has been designed following the procedure outlined in [109]. Here it has been shown that in order to ensure a front-end-fed design the sum of the angles $\alpha + \beta$ discussed in Section 3.2.1 must equal 180°. Once this condition is established we set the equivalent focal length and the tilt (β) between the reflectors, we then solve equations (3.2.1), (3.2.2) and (3.3.1) to find the primary focal length, secondary eccentricity and angle of throw. The presence of a concave secondary hyperbola means that the eccentricity parameter in these equations must be less than zero. Also in order to achieve the back-fed design the tilt between the two reflectors must be set greater than 90°.

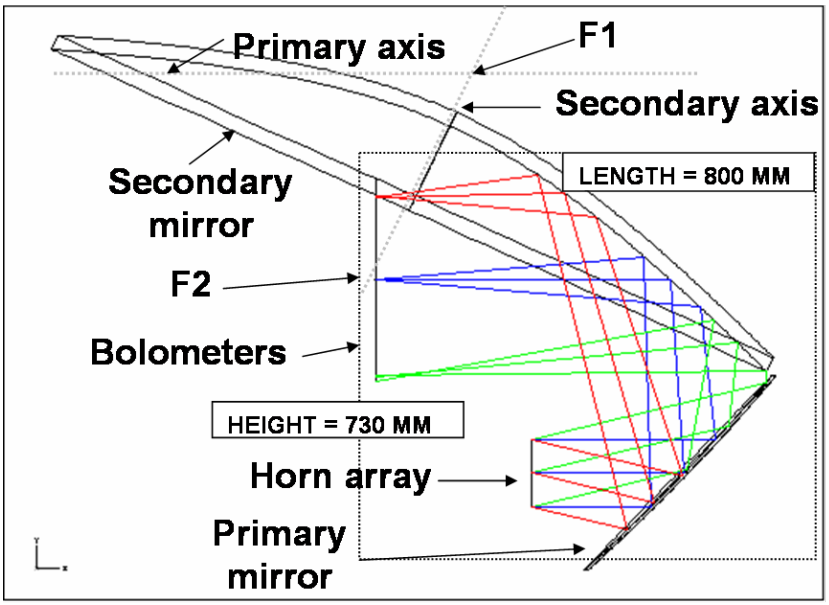

(a) Front-end-fed compensated Cassegrain reflector. The tilt between the reflector axes is 115°. The eccentricity of the secondary ellipsoid is 2.366. The size of any box containing this system is at least $800 \times 730 \times 360$ mm^3.

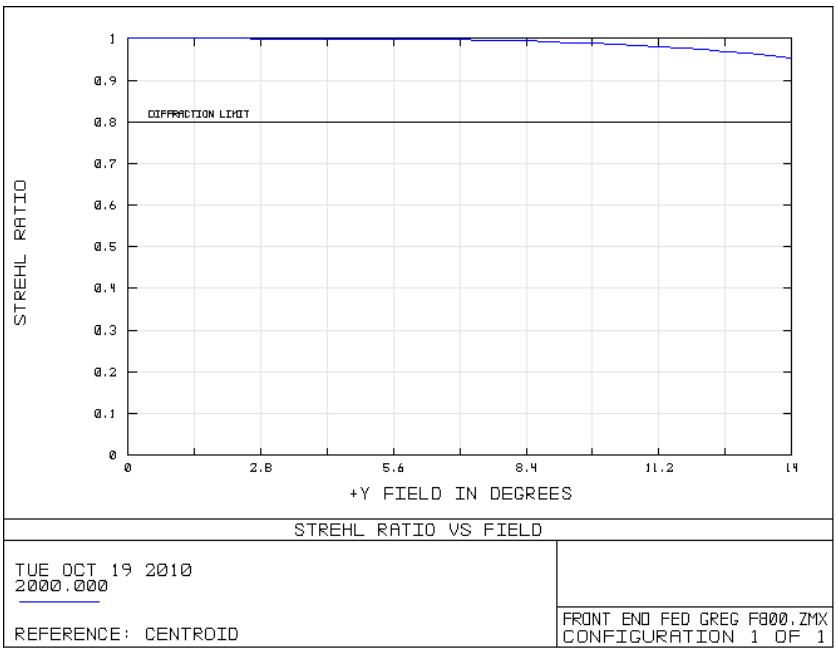

(b) The DLFOV of the front-end-fed compensated Cassegrain greatly exceeds a 14° for a 140 mm entrance aperture.

Figure 3.19: Front-end-fed compensated Cassegrain reflector. The focal length of this system is 800 mm.

The second system is a back-end-fed Gregorian whose geometry has been suggested by our colleges in Milano. Here the incident chief is parallel to the reflected ray. It is not possible to design a compensated system that obeys such geometry. Therefore this system will provide a good analysis of whether enforcing symmetry via the Dragone condition onto previous reflectors is necessary when considering systems as long-wavelength combiners rather than visible imagers. The geometry of the back-fed Gregorian is shown in Figure 3.20.

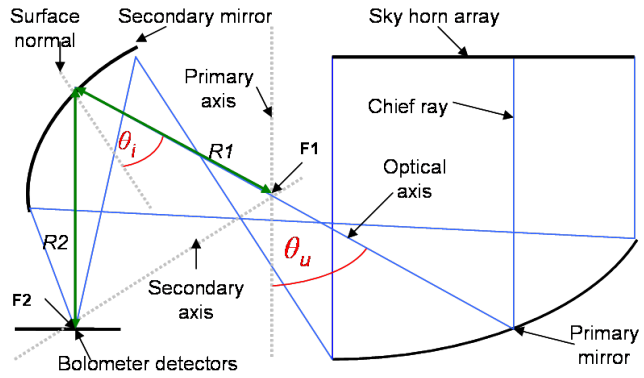

Figure 3.20: Layout of a back-fed Gregorian. Most of the parameters in this diagram have been explained in Figure 3.3. In addition $R1$ and $R2$ are the separation of the of intersection of the chief ray at the secondary and the foci. Also θ_i is the angle between the chief ray and the secondary normal.

It has been shown that when $R1$ equals $R2$ the Gaussian beam amplitude distortion after reflection from an ellipsoid reflector is minimized. When this is the case the eccentricity of the secondary reflector equals $\sin(\theta_i)$ [81]. We imposed the $R1 = R2 = R$ condition on the ellipsoid reflector. This means that the magnification of the secondary is unity so essentially the parameters of the system are decided solely by the primary focus f_p and angle of throw θ_u. These are related by

$$f_e = \frac{f_p}{\cos(\frac{\theta_u}{2})} \tag{3.3.5}$$

where f_e is the equivalent focal length of the off-axis paraboloid [81]. It is also apparent from Figure 3.20 that θ_u equals $2 \times \theta_i$. Therefore we set f_e in equation (3.3.5) equal to

800 mm and chose an appropriate value for f_p. We then solve for θ_u and calculate the angle of throw and the eccentricity of the secondary reflector. We then set the value R to a value large enough to allow the secondary mirror to capture all light reflected from the primary. From Figure 3.20 it is clear that once both R and θ_i are calculated the distance between the foci and therefore the radius of curvature of the secondary reflector can be found. Using this method we have reduced the number of parameters required to design this off-axis system when compared to the previous examples. Also the secondary reflector has been aligned in such a manner as to minimize the Gaussian beam distortion. It is hoped that this arrangement will compensate somewhat for the lack of symmetry present within the system.

Figures 3.22, 3.23, 3.24 and 3.25 display the fringe patterns generated by the above reflectors. We note from Figure 3.22 that the beam distortion induced by the front-fed compensated Cassegrain is relatively small when compared to the compensated Gregorian. From Figures 3.19 and 3.21 we also see that the front-fed Cassegrain has a significantly wider DLFOV then the compensated Gregorian. Hence the degradation of the recovered visibilities due to wavefront aberrations will be lower. Unfortunately from Figures 3.24 and 3.25 we see that the lack of symmetry within the back-fed Gregorian has drastic consequences on the fringe patterns. For the first time fringes from both orientations have become deformed. As shown in Figure 3.7 the Strehl ratio of the back-fed Gregorian drops to less than 0.8 when the field of view exceeds 4°. This means that the presence of wavefront aberrations will severely reduce the imaging ability of the back-fed Gregorian when the field of view exceeds 4°. Therefore we expect that the fringe patterns in Figures 3.24 and 3.25 generated by 14° FWHM Gaussian beams have not only been deformed by amplitude distortion but also by the presence of large magnitude Seidel aberrations. This example clearly illustrates the need for careful design of the long-wavelength combiner for QUBIC.

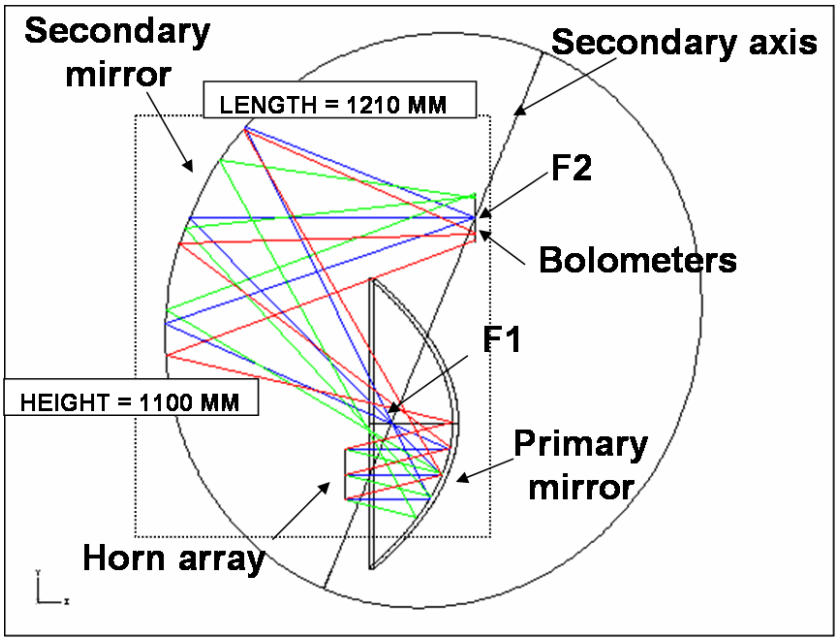

(a) Back-end-fed Gregorian reflector. The tilt between the reflector axes is 67.5°. The eccentricity of the secondary ellipsoid is 0.382. The size of any box containing this system is at least $1210 \times 1100 \times 600$ mm^3.

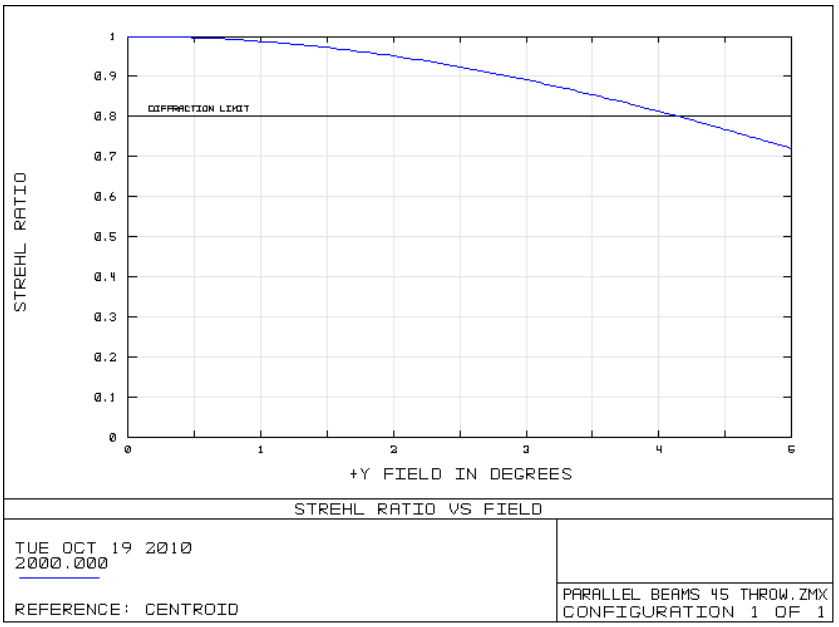

(b) The DLFOV of the back-end-fed Gregorian is 4° for a 140 mm entrance aperture.

Figure 3.21: Back-end-fed Gregorian reflector. The focal length of this system is 800 mm.

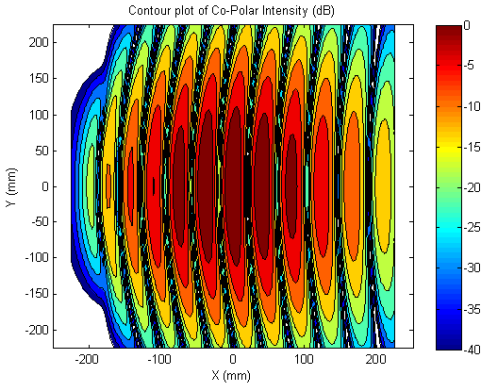

(a) CEN baseline.

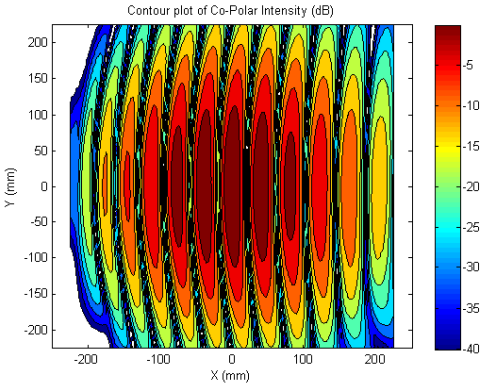

(b) LOWL baseline.

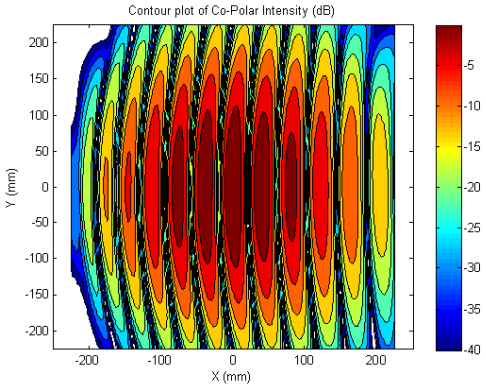

(c) LOWR baseline.

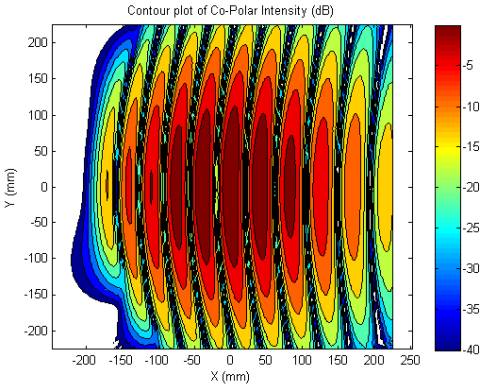

(d) UPL baseline.

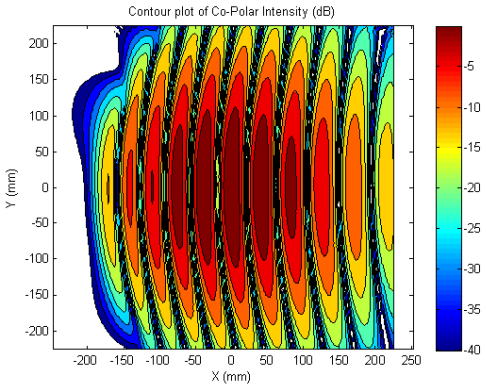

(e) UPR baseline.

Figure 3.22: Fringe patterns produced by the front-end-fed compensated Cassegrain. The baselines generating these fringes occurred horizontally along the horn array's x-axis. The fringes have been formed using 14° FWHM Gaussian beams and 40 mm baselines.

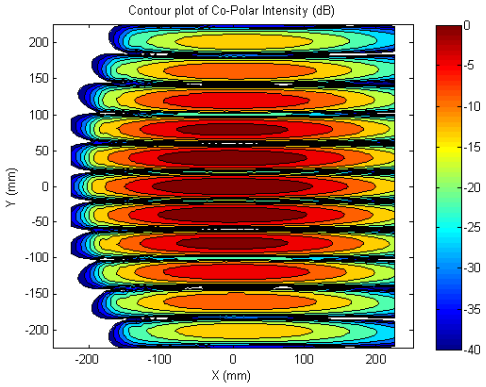

(a) CEN baseline.

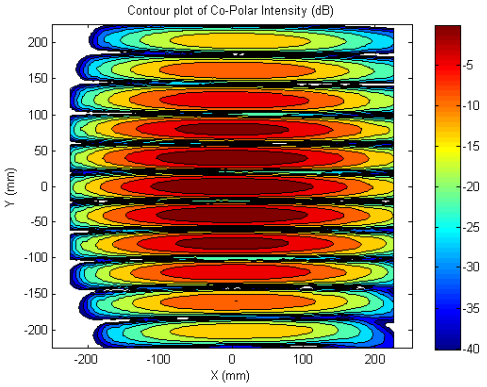

(b) LOWL baseline.

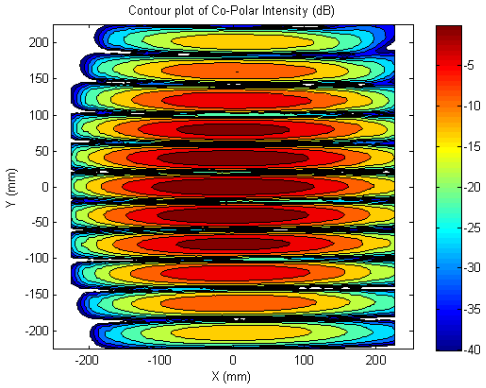

(c) LOWR baseline.

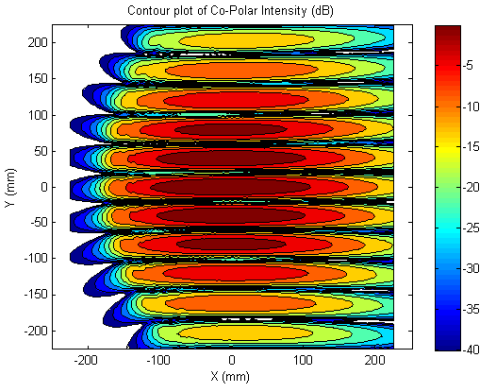

(d) UPL baseline.

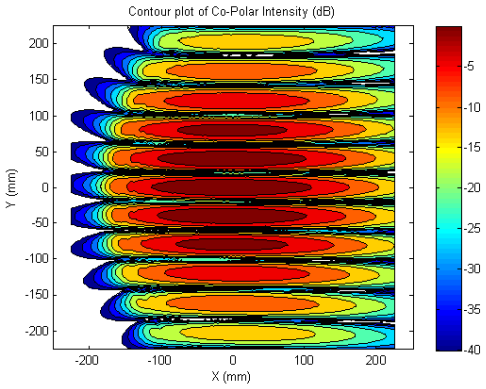

(e) UPR baseline.

Figure 3.23: Fringe patterns produced by the front-end-fed compensated Cassegrain. The baselines generating these fringes occurred horizontally along the horn array's y-axis. The fringes have been formed using 14° FWHM Gaussian beams and 40 mm baselines.

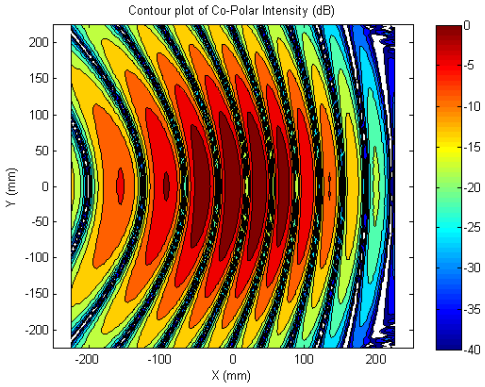

(a) CEN baseline.

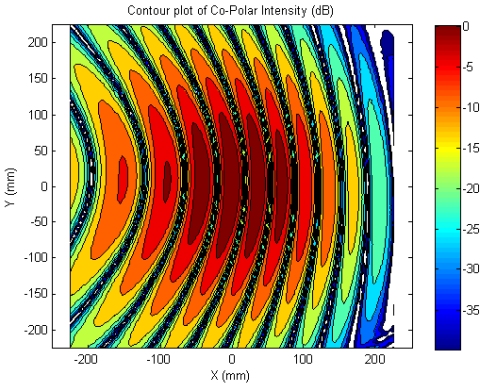

(b) LOWL baseline.

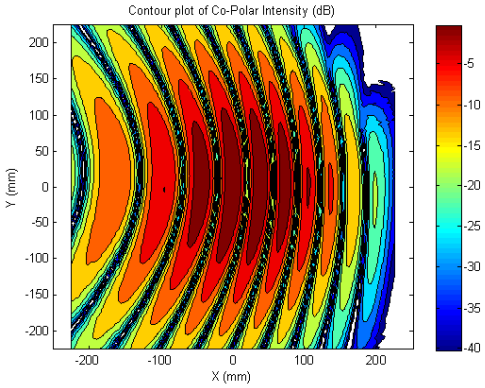

(c) LOWR baseline.

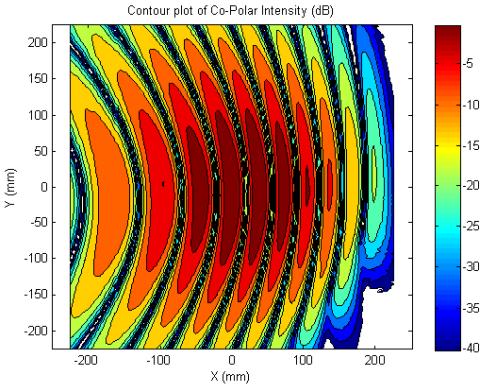

(d) UPL baseline.

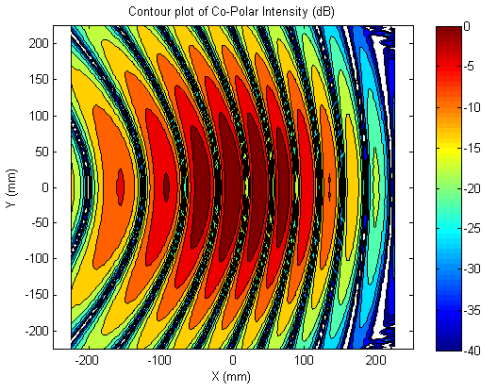

(e) UPR baseline.

Figure 3.24: Fringe patterns produced by the back-end-fed Gregorian. The baselines generating these fringes occurred horizontally along the horn array's x-axis. The fringes have been formed using 14° FWHM Gaussian beams and 40 mm baselines.

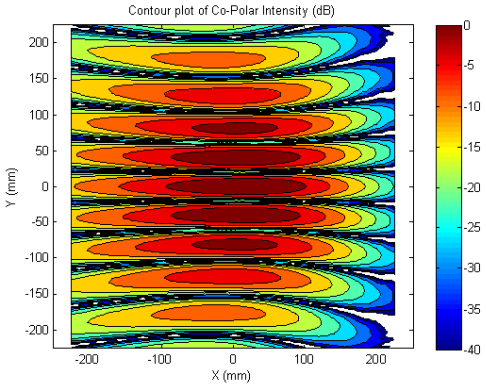

(a) CEN baseline.

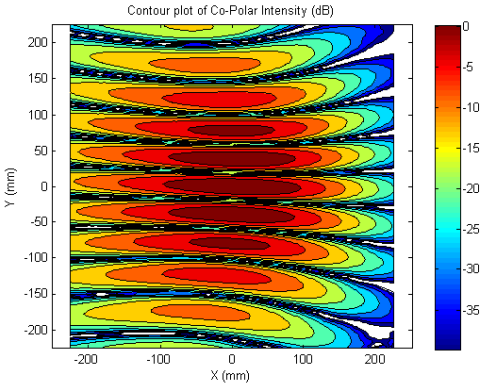

(b) LOWL baseline.

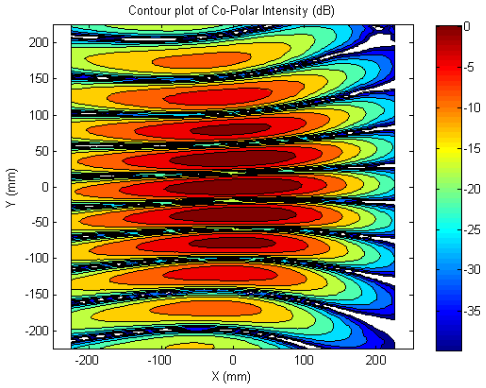

(c) LOWR baseline.

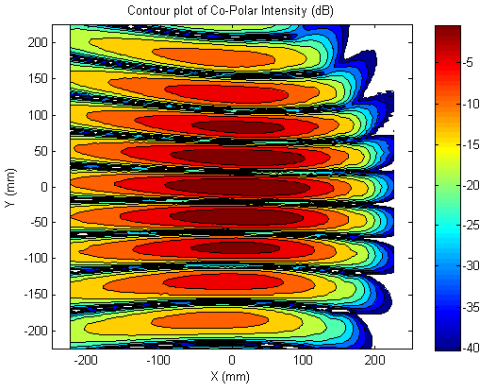

(d) UPL baseline.

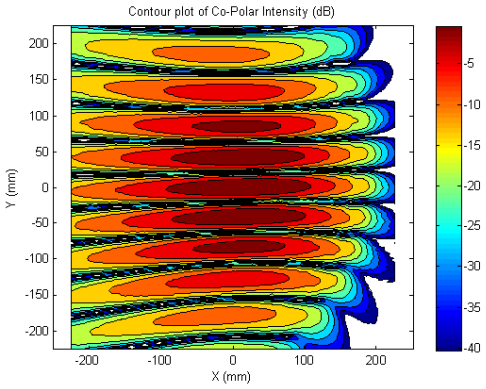

(e) UPR baseline.

Figure 3.25: Fringe patterns produced by the back-end-fed Gregorian. The baselines generating these fringes occurred horizontally along the horn array's y-axis. The fringes have been formed using 14° FWHM Gaussian beams and 40 mm baselines.

Dragone reflector

The Dragone reflector is a special category of an off-axis Cassegrain. This reflector obeys three geometrical conditions designed to minimize aberrations [104]. As can be seen from Figure 3.26 this system also implements a concave secondary reflector. The geometry of this system is unpractical for QUBIC due to the fact that the detector chamber may block beams emerging from the secondary horns. However we have included an analysis of this reflector due to the fact that it represents some of the most advanced thinking concerning off-axis dual reflector design. Unlike systems designed using only the Dragone and Rusch conditions the separation of the reflectors within a Dragone reflector is proportional to the secondary magnification. This allows a futher reduction in wavefront aberrations. The first condition this system obeys is the Dragone condition which effectively eliminates astigmatism. In the context of this reflector the Dragone condition is rewritten as

$$\tan(i_2) = \frac{M-1}{M} \times \tan(i_1) \tag{3.3.6}$$

where M is the secondary magnification, i_1 is the chief ray angle of incidence at the primary and i_2 is the chief ray angle of incidence at the secondary. To design the system shown in Figure 3.26 we scaled down the system presented by Dragone to an equivalent focal length of 800 mm [104]. Following [104] we set $M = 0.75$ and $i_1 = 25°$ where $M = \frac{e+1}{e-1}$ and e is the secondary eccentricity. The second condition removes residual astigmatism by setting the separation of the reflectors to $2 \times M\left(1 + \frac{\tan(i_1)}{\tan(i_2)}\right)$. The third conditions removes coma by deforming the mirrors into higher order polynomial surfaces. The remaining parameters can be calculated from equations (3.2.1), (3.2.2) and (3.3.1).

It is possible to calculate the coefficients required to deform the mirrors into higher order polynomials surface using equations listed in [104]. However we have determined the coefficients of Figure 3.26 using Zemax optimizations. These mirrors have therefore been deformed in the most optimal manner to reduce third order Seidel aberrations. As shown in Figure 3.26 the implementation of these conditions leads to a DFLOV greater than 14°. As such we expect this reflector to be a high performing telescope. However as shown in Figures 3.27 and 3.28 a PO analysis of this systems reveals

that the fringes it produces are unacceptable for QUBIC requirements. Once again the presence of amplitude distortion in the combining beams has deformed the fringe patterns generated by baselines orientated along the x-axis of the horn array.

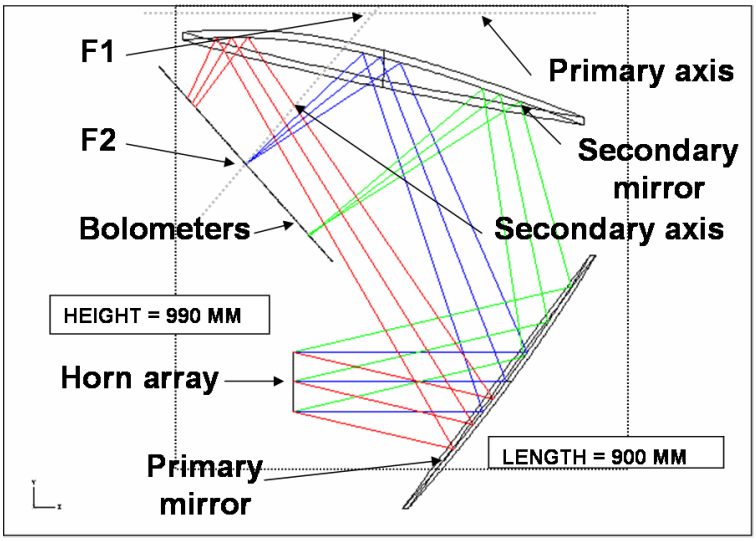

(a) Compensated Dragone reflector. The tilt between the reflector axes is 91.86°. The eccentricity of the secondary ellipsoid is 2.52. The size of any box containing this system is at least $900 \times 990 \times 400$ mm^3.

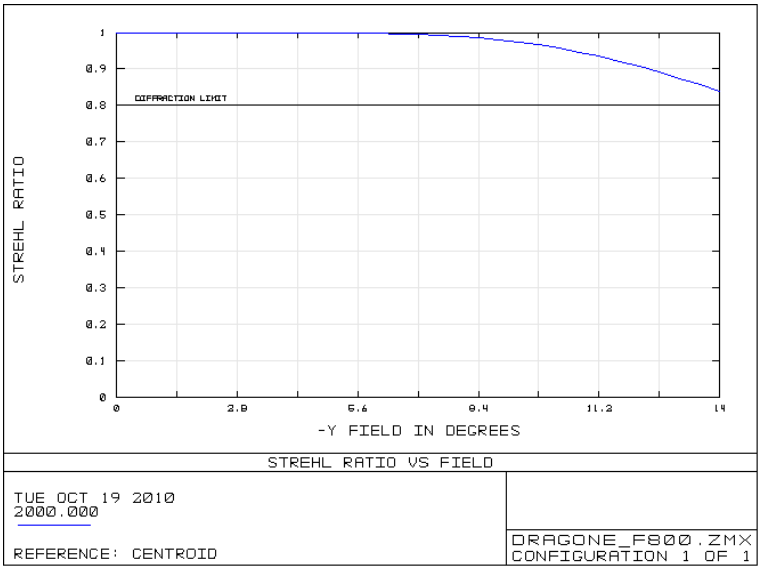

(b) The DLFOV of the Dragone reflector is 14° for a 140 mm entrance aperture.

Figure 3.26: Compensated Dragone reflector. The focal length of this system is 800 mm.

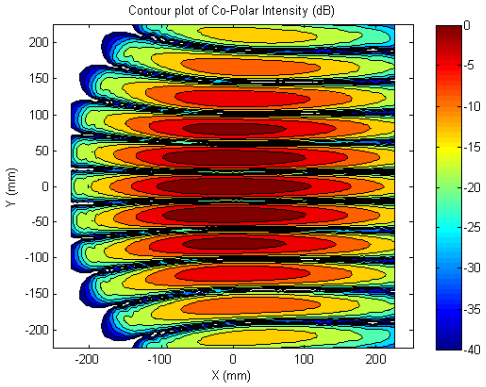

(a) CEN baseline.

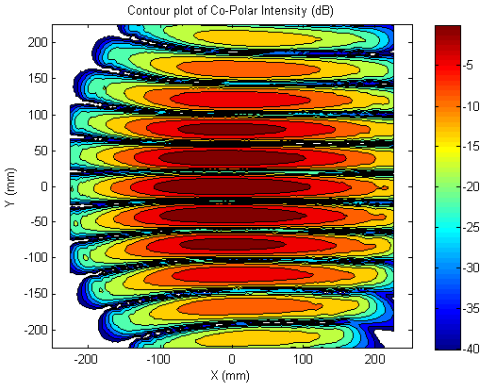

(b) LOWL baseline.

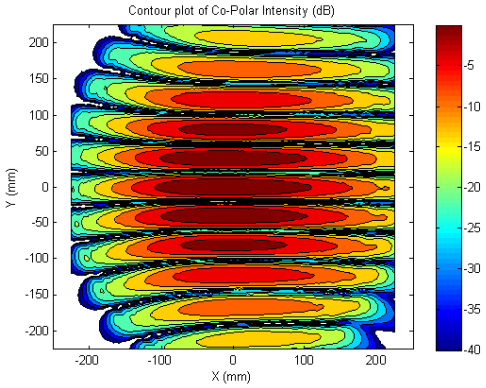

(c) LOWR baseline.

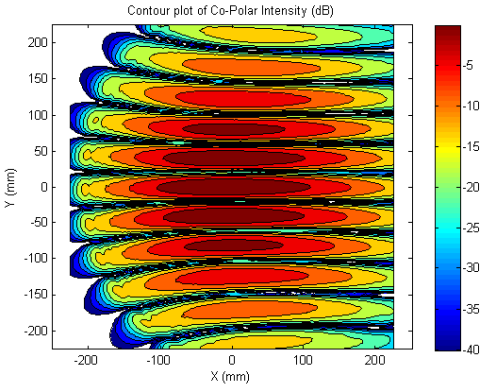

(d) UPL baseline.

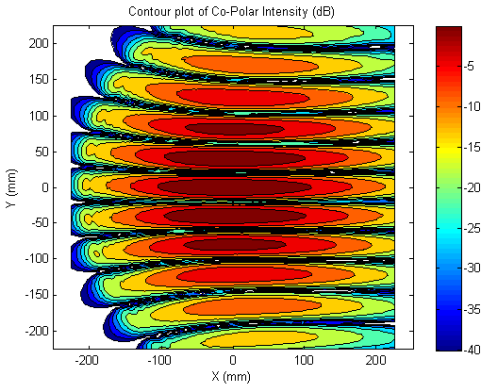

(e) UPR baseline.

Figure 3.27: Fringe patterns produced by the Dragone reflector. The baselines generating these fringes occurred horizontally along the horn array's x-axis. The fringes have been formed using 14° FWHM Gaussian beams and 40 mm baselines.

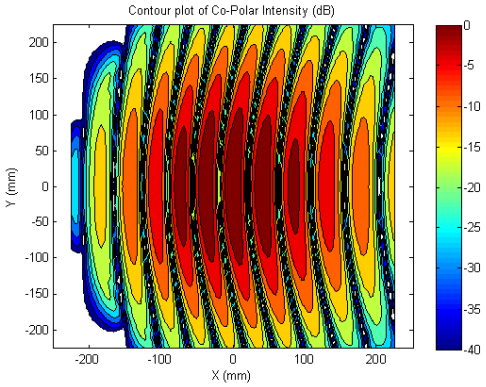

(a) CEN baseline.

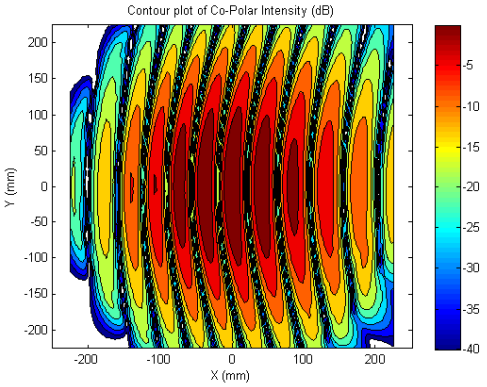

(b) LOWL baseline.

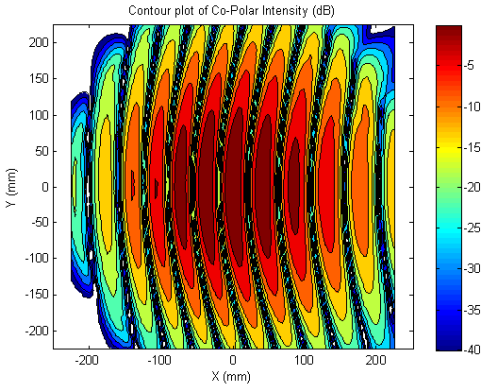

(c) LOWR baseline.

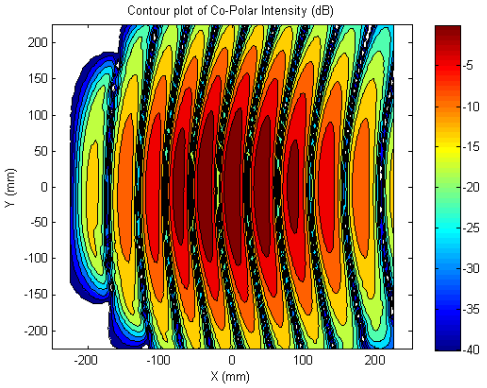

(d) UPL baseline.

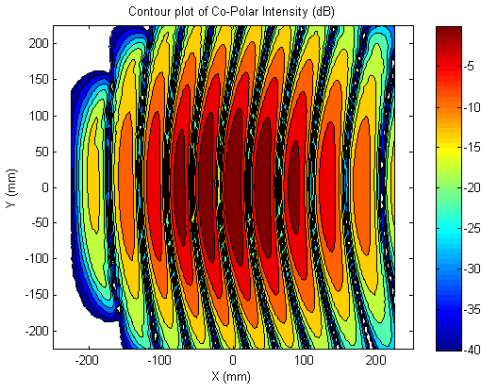

(e) UPR baseline.

Figure 3.28: Fringe patterns produced by the Dragone reflector. The baselines generating these fringes occurred horizontally along the horn array's y-axis. The fringes have been formed using 14° FWHM Gaussian beams and 40 mm baselines.

3.3.1 Summary of off-axis dual reflectors for implementation in a CMB Fizeau interferometer

The above work reviews the suitability of various dual reflector designs for the use as Fizeau optical combiners. We have compared several varieties of 800 mm focal length dual reflectors all with 140 mm entrance pupil diameters. From a visual examination of the fringe patterns this study concludes that the most suitable dual reflector for a bolometric interferometric ground based or satellite mission is a CATR. We note that the front-end-fed Cassegrain could also be used however this system many not be as suitable if a lot of read-out electronics is required. The fact that the detector plane and sky horn array are in proximity to one another in this design means there is the possibility that a large detector unit many obscure the field-of-view of the sky horns. The above study has allowed us to narrow down the choices of dual reflectors for QUBIC. We have not concerned ourselves with issues such as spillover and blockage although later when we discuss specific recommendations for QUBIC we will include these details.

We conclude this section by presenting the details of the reflectors from which the above systems are constructed in Table 3.1. The performance of different designs are quantified later for the particular case of QUBIC, at this stage the relative advantages and disadvantage of the designs can be seen in Figure 3.29 which summarises the main features of the compensated dual reflectors studied. The un-compensated back-end-fed Gregorian is not included as its performance fell below the compensated systems, as expected. As discussed in the next section, not all these layouts are suitable for low-F telescopes. Here it is apparent that the cost of the high quality fringes produced by the CATR and front-fed Cassegrain is the requirement for relatively large mirrors. However the cryostat volume would be smaller then that required for the compensated Gregorian.

Table 3.1: Details of the geometry of the 800 mm effective focal length dual reflectors investigated in this chapter. Here **CG** is the compensated Gregorian, **CC** is the compensated Cassegrain, **INVC** is the inverted-crossed Cassegrain, **FC** is the front-fed compensated Cassegrain, **BG** the back-fed Gregorian and **DR** is the Dragone reflector. The term **PF** is the primary focal length, k is the secondary conic constant, **ROCS** is the radius of curvature of the secondary mirror, β_T is the tilt between the reflectors, **PD** is the diameter of the primary mirror and **SD** is the diameter of the secondary mirror.

	PF (mm)	k	**ROCS** (mm)	β_T	**PD** (mm)	**SD** (mm)
CG	357.91	-0.15	506.13	10	360	300
CC	472.42	-12.04	497.04	20	320	320
CATR	1385.64	-7.46	1951.97	60	500	600
INVC	953.40	-0.50	1693.16	50	600	1300
FC	800.00	-5.59	1172.14	115	400	600
BG	170.71	-0.14	682.843	67.5	300	800
DR	1074.66	-6.36	1053.8	91.8	500	800

Summary of Compensated Dual Reflectors (f = 800 mm, F/# ≈ 5.7)				
Compensated Gregorian (GC)	large field-of-view, can accommodate large entrance aperture	fringe aberration present		
Compensated Cassegrain (CC)	small field-of-view, especially at lower F/#	fringe aberration present (more than GC)		
Compact Antenna Test Range (CATR)	excellent (largest) field-of-view	very low fringe aberration	input array at 90° to focal plane	large mirrors required
Inverted Crossed Cassegrain (INVC)	large field-of-view, comparable to GC	fringe aberration present	input array at 90° to focal plane	large mirrors required, more difficult geometry than CATR
Front-End Fed Cassegrain (FC)	large field-of-view, second only to CATR	some fringe aberration (next lowest after CATR)	input array parallel to focal plane	large mirrors required
Dragone Reflector (DR)	quite large field-of-view	fringe aberration present		large mirrors required

Figure 3.29: A summary of the main features of the compensated dual reflectors studies in this section.

3.3.2 Comparison of crossed reflectors for short focal length systems

We will consider for a moment short 200 mm focal-length systems. An unavoidable consequence of bolometric interferometry as intended for QUBIC is that short focal length systems are necessary if one wishes to avoid complex multiplexing of a large number of detectors. At such low focal lengths options as to what dual reflector to implement are very limited. The compensated Gregorian is a general workhorse that is functional at 200 mm, there are also two crossed reflector options which we discuss next, however they will not permit a large grid of back-to-back horns such as that required for QUBIC [21]. However these crossed systems would be suitable for use in an MBI type experiment in which a small number of horns observe the sky. The surface details of the crossed reflectors are shown in Table 3.2.

Short focal length system with short baselines observing a large field of view

The combination of short baselines with marginally large fields of view can be accommodated by implementing a CATR design. A 200 mm focal length CATR is shown in Figure 3.30. Here the maximum baselines are 40 mm and the largest possible Gaussian beams are 10° FWHM. This entire system is remarkably compact and thus favorable for cryostat construction. This dual reflector would be suitable for a simple bolometric interferometry path finder mission, for example. The off-axis design means a greater amount of power from the sky signal would fall onto the detector plane compared to the on-axis MBI experiment. If we assume such a 200 mm path finder mission observes the CMB at $\sim$ 100 GHz, similar to MBI, a square focal plane of 80 mm^2 will integrate 99 % of the received power. If 5 mm bolometers are employed the total number required is 256. Under such circumstances SQUID amplification and multiplexing of the detected signal should pose little difficulty.

[21] From over investigations we have concluded that if the focal length of the optical combiner is required to be less than 300 mm the compensated Gregorian is the only viable option.

Short focal length system with long baselines observing a small field of view

The reflector shown in Figure 3.31 is the author's own design. It is a direct application of studying the previously discussed inverted-crossed Cassegrain design. Here the axis of symmetry of both the primary and secondary mirror are aligned. In effect we are using a portion of an on-axis system. Due to the fact that the primary and secondary axes are aligned the design of such a system is significantly less complicated than the designs of the compensated dual reflectors introduced in the above section. Any on-axis optical system is described by the formula

$$\frac{1}{f_e} = \frac{1}{f_p} + \frac{1}{f_s} - \frac{t}{f_p f_s} \tag{3.3.7}$$

where f_e is the equivalent focal length of the system, f_p is the primary focal length, f_s is the secondary focal length and t is the separation of the two mirrors [78]. We let f_e equal 200 mm and set values for f_p and t in order to find f_s. A crossed design can be creating by ensuring the condition $R2\tan(\theta_u) = 2c$ where $2c$ is the distance between the foci. The terms θ_u and $R2$ have been explained in Figures 3.3 and 3.20 respectively.

In Figure 3.31 we have implemented a 160 mm baseline consisting of 5° FWHM Gaussian beams[22]. Despite an the small $f/\# \sim 1.25$ there is little spillover or blockage occurring between the reflectors. This demonstrates the remarkable ability of an inverted-crossed Cassegrain to handle low focal ratio optical arrangements. The immediate drawback is that this arrangement is considerably larger than the CATR. The size of the secondary mirror must be larger than the primary in order to capture the diverging beams reflected from the primary.

The inverted-crossed Cassegrain suffers from a severe amount of beam distortion as indicated by the curved profile of the fringe patterns in Figures 3.32(c) and 3.32(d). However examining Figures 3.32(a) and 3.32(b) we see that the CATR produces remarkably high quality fringe patterns for short baselines. From the distorted fringes shown in Figures 3.24, 3.32(c) and 3.32(d) it is reasonable to assume that, despite their

[22]This system could not be designed for the 14° beams required by QUBIC

ability to operate at low focal ratios, reflectors employing convex primary mirrors are unsuitable for off-axis Fizeau interferometers.

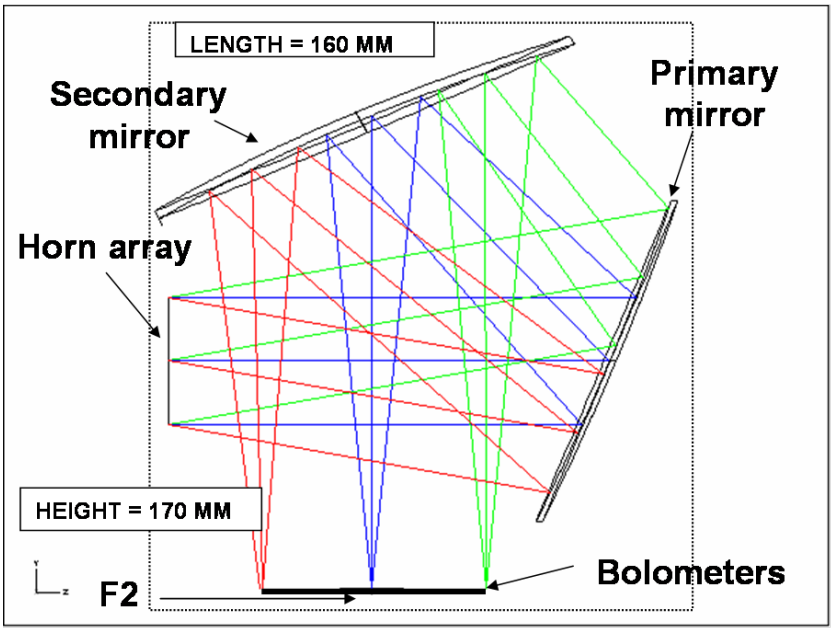

(a) CATR reflector. The tilt between the reflector axes is 60°. The eccentricity of the secondary ellipsoid is 2.73. The size of any box containing this system is at least $160 \times 170 \times 120$ mm^3.

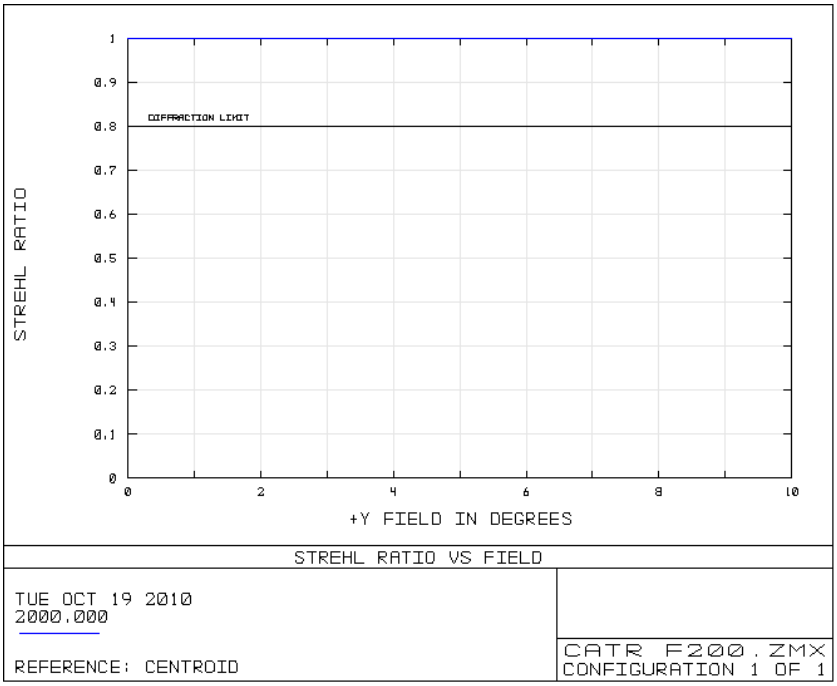

(b) The DLFOV of the CATR greatly exceeds 10° for a 40 mm entrance aperture.

Figure 3.30: CATR reflector. The focal length of this system is 200 mm.

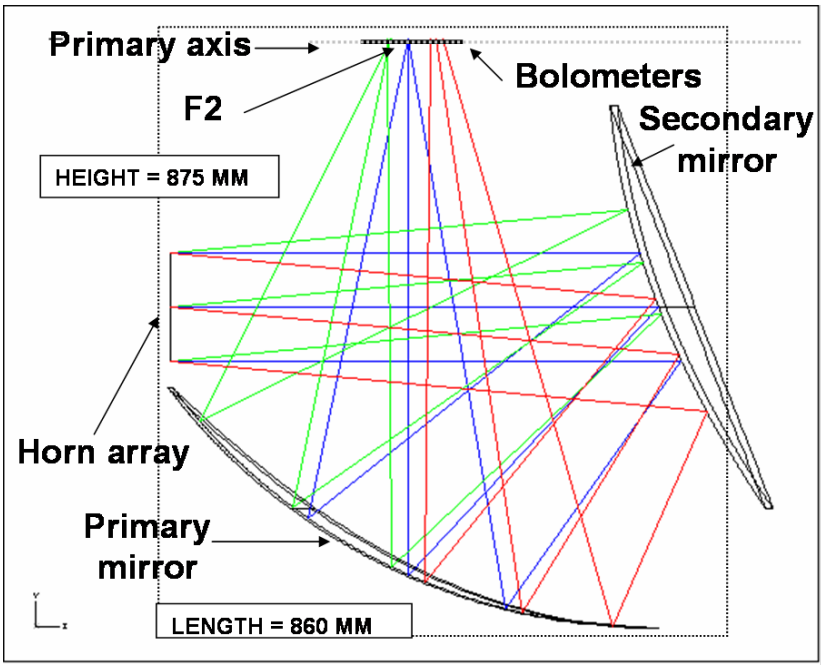

(a) On-axis inverted-crossed Cassegrain reflector. The tilt between the reflector axes is 60°. The eccentricity of the secondary ellipsoid is 0.414. The size of any box containing this system is at least $860 \times 875 \times 340$ mm^3.

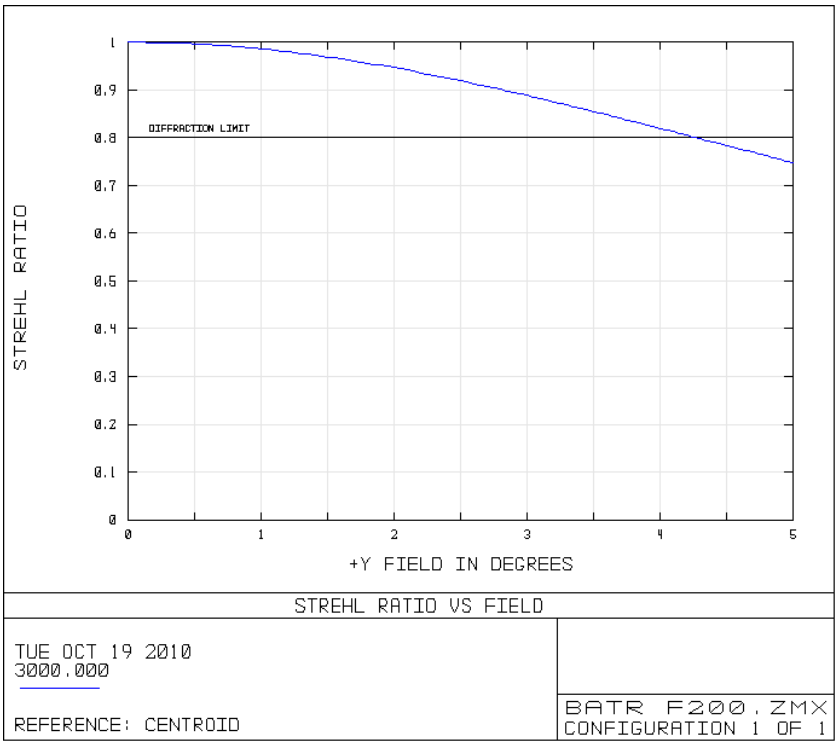

(b) The DLFOV of the on-axis inverted Cassegrain is less than 5° for a 160 mm entrance aperture.

Figure 3.31: Crossed reflector formed from a section of an on-axis inverted Cassegrain. The focal length of this system is 200 mm.

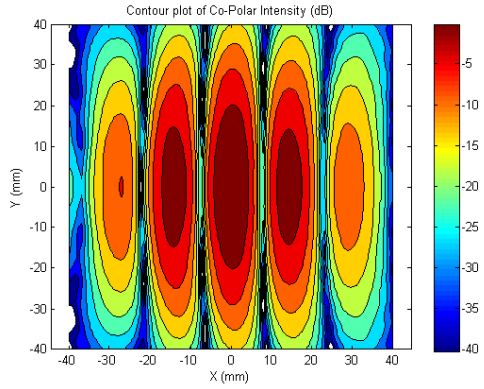

(a) A vertical 40 mm baseline about the systems line-of-sight of the combiner in Figure 3.30 is implemented. Here two 10° FWHM Gaussian beams are used. These fringes are formed by the CATR.

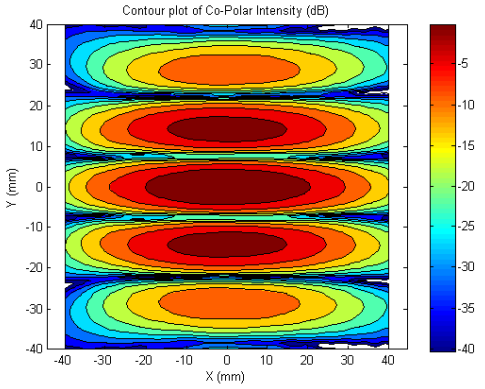

(b) A horizontal 40 mm baseline about the systems line-of-sight of the combiner in Figure 3.30 is implemented. Here two 10° FWHM Gaussian beams are used. These fringes are formed by the CATR.

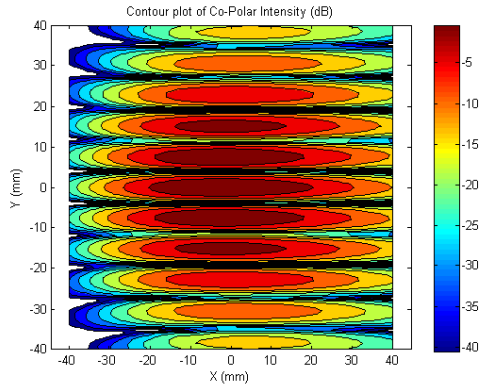

(c) A vertical 160 mm baseline about the systems line-of-sight of the combiner in Figure 3.31 is implemented. Here two 5° FWHM Gaussian beams are used. These fringes are formed by the on-axis inverted-crossed Cassegrain reflector.

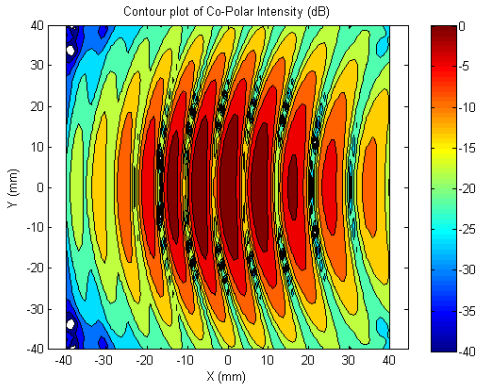

(d) A horizontal 160 mm baseline about the systems line-of-sight of the combiner in Figure 3.31 is implemented. Here two 5° FWHM Gaussian beams are used. These fringes are formed by the on-axis inverted-crossed Cassegrain reflector.

Figure 3.32: Fringe patterns produced by 200 mm focal length off-axis combiners. As previously explained different baselines and beam sizes are used in accordance to what the individual systems' geometries will allow.

Table 3.2: Details of the geometry of the 200 mm effective focal length dual reflectors investigated in this chapter. Here **CATR** is the compact antenna test range and **INVC** is the on-axis inverted-crossed Cassegrain. The term **PF** is the primary focal length, k is the secondary conic constant, **ROCS** is the radius of curvature of the secondary mirror, β_T is the tilt between the reflectors, **PD** is the diameter of the primary mirror and **SD** is the diameter of the secondary mirror.

	PF (mm)	k	**ROCS** (mm)	β_T	**PD** (mm)	**SD** (mm)
CATR	346.41	-7.46	496.87	60	120	140
INVC	482.92	-0.17	800	0	340	400

3.4 Alternative geometries for the combiner in a QUBIC-type experiment

3.4.1 Fold mirror and a crossed Cassegrain dual reflector

In the context of this thesis, the term compact antenna test range (CATR) solely refers to a Cassegrain system in which the sum of the angles $\alpha + \beta$ discussed in Section 3.2.1 equals 90°. We will now begin to discuss Cassegrain systems where the angles $\alpha+\beta = \eta$ where η can vary. We will refer to such systems as general crossed Cassegrains (GCC). In order to design these types of reflectors we set values for η, as well as values for the equivalent focal length of the system and the tilt between the reflector axes. Equations (3.2.1), (3.2.2) and (3.3.1) can then be solved to calculate the remaining parameters required to completely describe the reflector. We note that because these systems are designed using equations (3.2.1) and (3.2.2) they are also compensated systems. We recall that the term compensated refers to any dual reflector that obeys both the Rusch and Dragone conditions shown in equations (3.2.1) and (3.2.2) respectively. As such when we refer to a system compensated we simply mean that both equations (3.2.1) and (3.2.2) were used to design the system.

We have shown that a CATR reflector is the most suitable dual reflector for implementation in a QUBIC type optical system. However there is a concern that if such a reflector is used spillover of power from the back-to-back horn array may affect the sensitivity of the bolometer detectors. As such we have examined different types of CCGs that could be implemented in order to separate the back-to-back horn array and the detector plane[23]

The simplest way we have found to separate the horn array and detector plane is to include a flat plane mirror in a CCG system. There are two possible positions into which a flat mirror can be placed in combination with a CCG. The first is in the vicinity of the back-to-back horns. The second is in the far-field of the back-to-back horn array.

[23] In later chapters we will present an analysis of power spillover in a GCC system. Presently we are only concerned with whether it is possible to design reflector systems in which the horn array and detector plane are not adjacent and also generate good quality fringes.

Because of the location of the fold mirror both of these systems require different design specifications. For example there is a large distance over which the propagating beams may diverge when the fold mirror is placed in the far-field of the horn array. Therefore in order to prevent an excessive amount of spillover at the fold mirror it is advisable that narrow beams are produced by the back-to-back horns. Figure 3.33 displays the geometry of the two systems we have considered. Here the systems are shown in telescopic mode. It can be seen that rays propagating from the horn array at equal angles are combined at the same locations along the focal plane. The characteristics of these systems relevant to bolometric interferometry are listed in Table 3.3.

We have used GRASP9 to generate the fringe patterns from 70 mm baselines centred about the line of sight of the horn array[24]. Simulations were carried out at 150 GHz (bandwidth effects in general are considered later in Section 6.4). The results of our analysis are shown in Figure 3.34. These figures indicate that there will be little difference between the fringes produced whether the fold mirror is placed adjacent to the horn array or in it's far-field. We note however that because wider Gaussian beams propagate through Figure 3.33(a) more power is focused into the higher order fringes. This requires the detector plane to be larger in Figures 3.34(a) and Figure 3.34(b)

[24]For the systems below we have varied the length of the baselines in order to keep the separation of the fringe maxima equal to ~ 40 mm. Such separations are in accordance with the fringe patterns produced by the 800 mm focal length systems presented previously in this chapter.

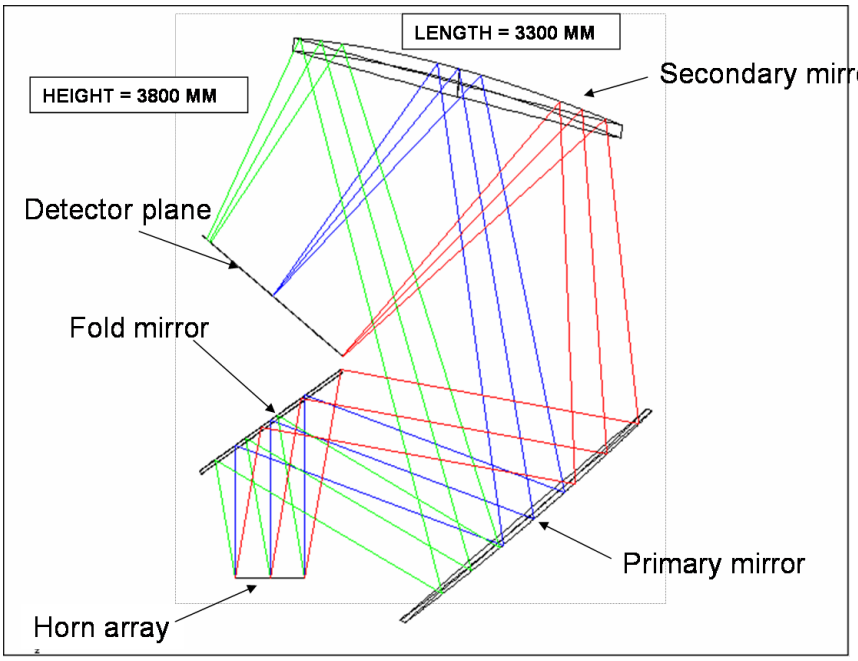

(a) Crossed Cassegrain reflector with fold mirror adjacent to horn array. The size of any box containing this system is at least $3300 \times 3800 \times 1600$ mm^3.

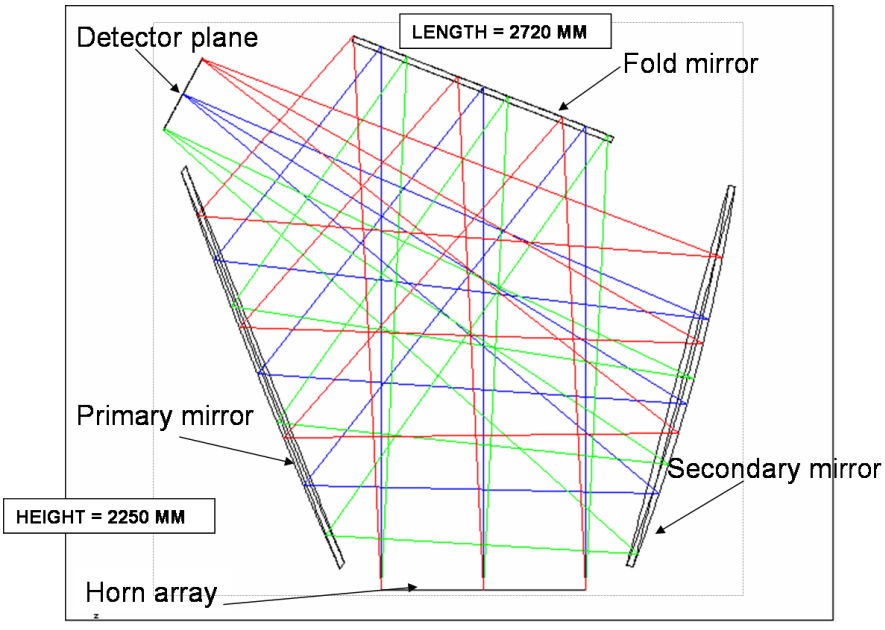

(b) Crossed Cassegrain reflector with a fold mirror in the far field of the horn array. The size of any box containing this system is at least $2250 \times 2720 \times 2400$ mm^3.

Figure 3.33: Crossed Cassegrain reflectors and a fold mirror. The focal length of these systems is 3500 mm.

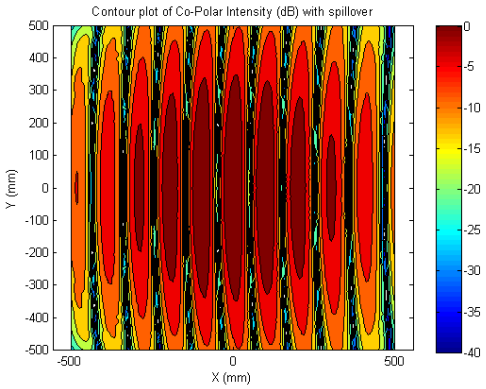

(a) Horizontal 70 mm baseline with fold mirror adjacent to horn array. The GCC shown in Figure 3.33(a) was used to generate these fringes.

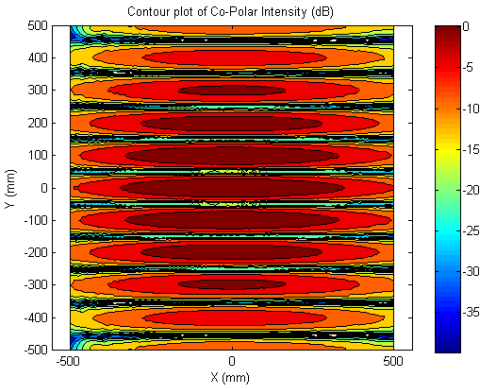

(b) Vertical 70 mm baseline with fold mirror adjacent to horn array. The GCC shown in Figure 3.33(a) was used to generate these fringes.

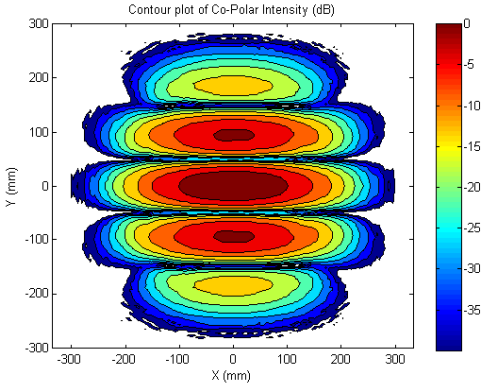

(c) Horizontal 70 mm baseline with fold mirror in the far field of the horn array. The GCC shown in Figure 3.33(b) was used to generate these fringes. Note the smaller detector plane required to integrate most of the power contained in the fringes.

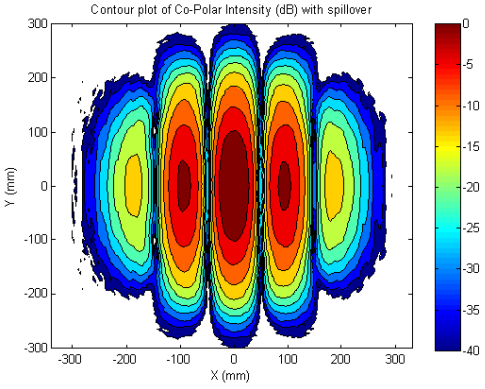

(d) Vertical 70 mm baseline with fold mirror in the far field of the horn array. The GCC shown in Figure 3.33(b) was used to generate these fringes. Note the smaller detector plane required to integrate most of the power contained in the fringes.

Figure 3.34: Fringes generated by a 3500 mm GCC reflectors combined with a fold mirror. Simulations were carried out at 150 GHz.

Table 3.3: Characteristics of two 3500 mm equivalent focal length combiners. Here **CNF** indicates the system in which the fold mirror is placed adjacent to the horn array while **CFF** indicates the system in which the mirror is placed in the far field.

	Beam FWHM (degress)	Number of horns	Size of detector plane (mm^2)	3 mm bolometers	5 mm bolometers
CNF	10	400	1320	193600	69696
CFF	3	400	380	16384	5776

3.4.2 Fold mirror and a GCC examined using equivalent baselines

For a QUBIC type experiment we require the shortest possible focal length in order to reduce the number of detectors required at the focal plane. Also the entrance aperture and beam size must be as large as possible in order to permit a sufficient amount of power from the sky enter the instrument. From our investigations we conclude that in order to maintain a low focal length, and thus reduce the number of detectors while focusing large beams, the fold mirror must be placed adjacent to the back-to-back array.

A 1000 mm focal length GCC is shown in Figure 3.35. Here beams of 10° FWHM are propagating from a 200 by 200 mm back-to-back horn array. These are the largest beams the 1000 mm focal length system can combine without a large amount of spillover occurring at the mirror edges. The characteristics of this system are listed in Table 3.4.

We have generated fringe patterns using 10 baselines from a grid of 12×12 10° FWHM back-to-back horns[25]. The beams from the various baselines have been combined using the GCC shown in Figure 3.35. These fringe patterns are shown in Figures 3.36 and

[25] All fringe patterns were produced by GRASP. Zemax was only used in the design stages and to show schematic plots of the systems.

3.37. The baselines were 40 mm in length and organized in a fashion similar to Figure 3.5[26].

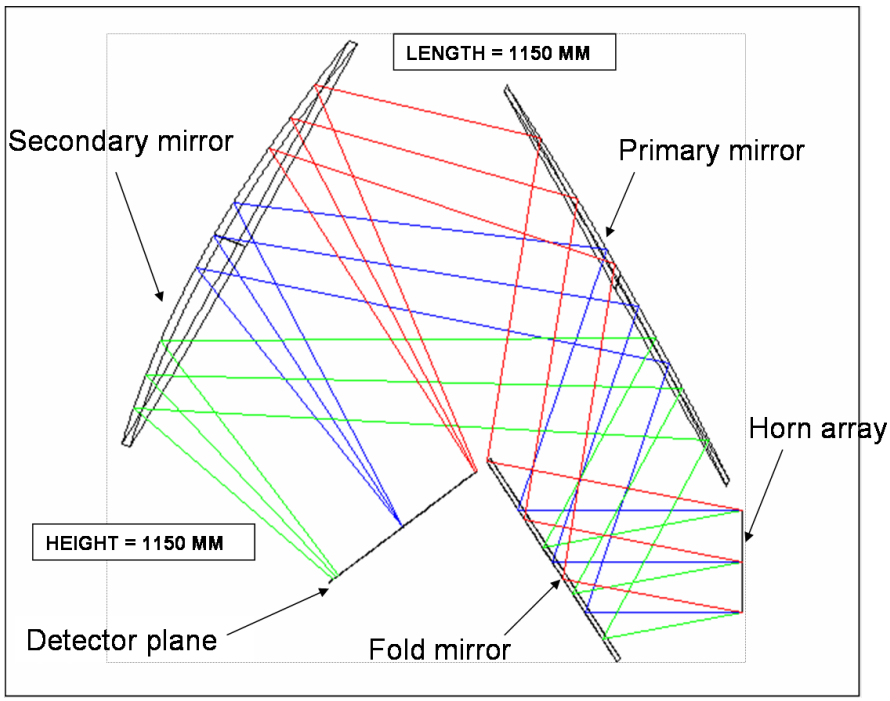

Figure 3.35: A 1000 mm focal length GCC. The size of any box containing this system is at least $1150 \times 1150 \times 1000$ mm^3..

[26]In order to accommodate the larger horns, that produce the smaller Gaussian beams, the corners of Figure 3.5 must be extended to $\pm$ 100 mm.

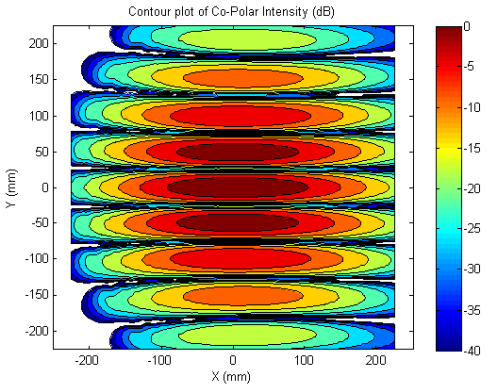

(a) CEN baseline.

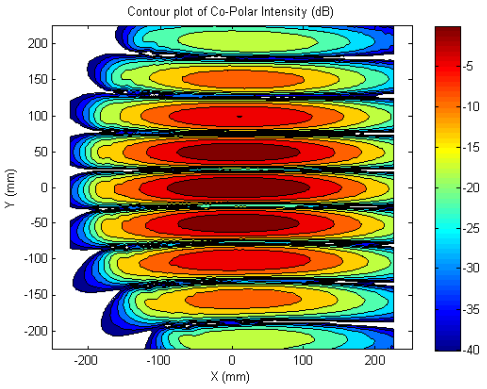

(b) UPL baseline.

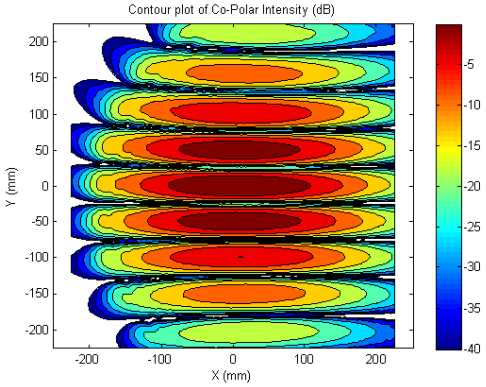

(c) UPR baseline.

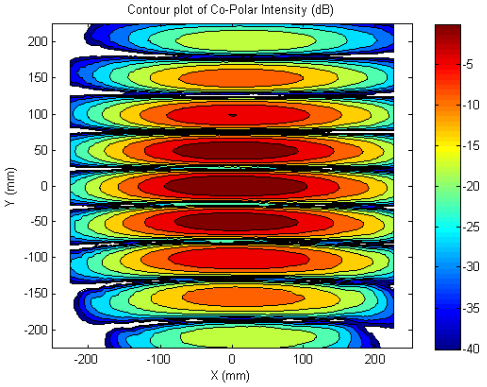

(d) LOWL baseline.

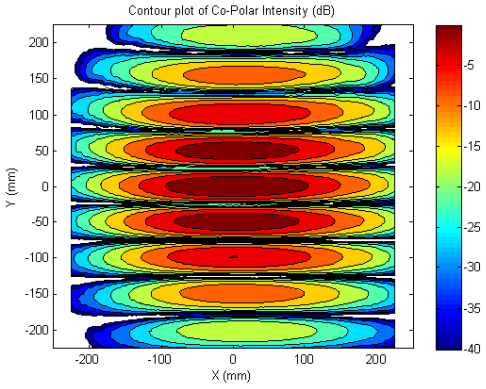

(e) LOWR baseline.

Figure 3.36: GRASP fringe patterns produced by the 1000 mm focal length GCC reflector. The baselines generating these fringes occurred vertically along the systems line-of-sight. The fringes have been formed using 10° FWHM Gaussian beams and 40 mm baselines.

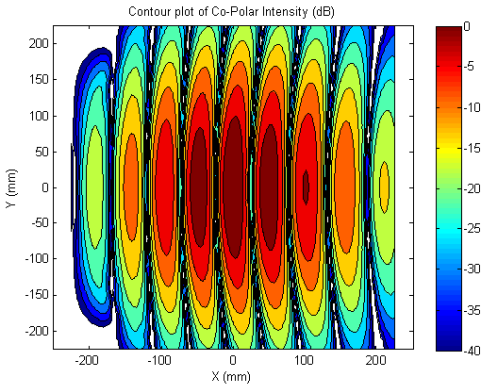

(a) CEN baseline.

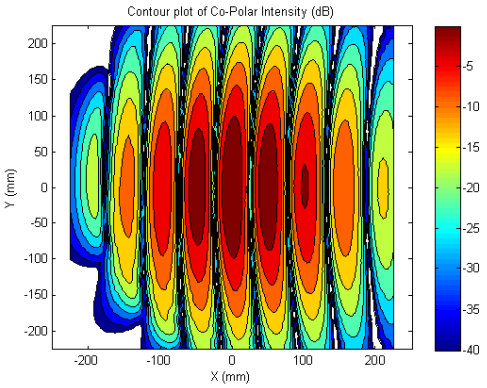

(b) UPL baseline.

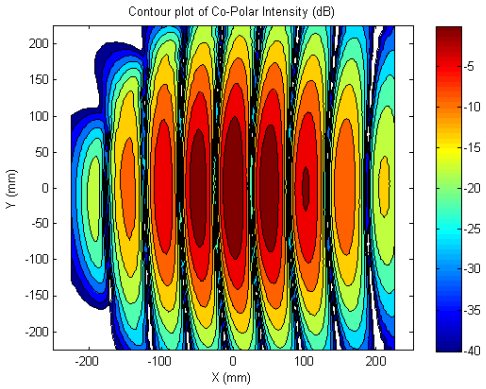

(c) UPR baseline.

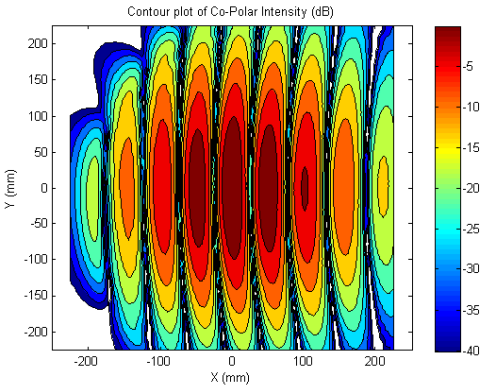

(d) LOWL baseline.

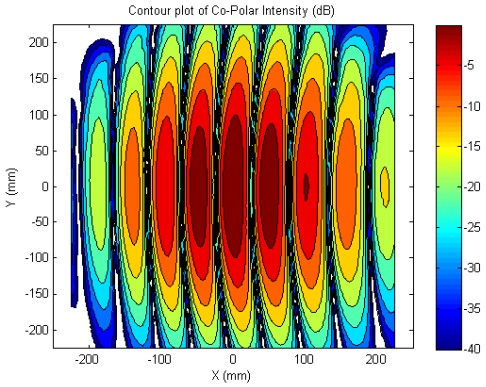

(e) LOWR baseline.

Figure 3.37: Fringe patterns produced by the 1000 mm focal length GCC reflector. The baselines generating these fringes occurred horizontally along the systems line-of-sight. The fringes have been formed using 10° FWHM Gaussian beams and 40 mm baselines.

Table 3.4: Characteristics of the 1000 mm equivalent focal length GCC reflector. Here **LCC** indicates the GCC.

	Beam FWHM (degress)	Number of horns	Size of detector plane (mm^2)	3 mm bolometers	5 mm bolometers
LCC	10	144	380	16384	5776

3.4.3 GCC dual reflector and a concave hyperboloid

There is another option we can avail of in order to separate the detector plane and the back-to-back horn array. This involves using a concave hyperboloid to refocus the beams after they pass through a GCC. This method is advantageous due to the fact the eccentricity a hyperboloid in less than -1. The magnification of a hyperboloid reflector is defined as

$$M = \frac{e+1}{e-1} \tag{3.4.1}$$

where M is the magnification and e is the eccentricity. Therefore, as we can see from Figure 3.38, placing a concave hyperboloid after the dual reflector will demagnify the beams focused onto the detector plane. This will reduce the size of the detector plane and the number of bolometers required for implementation. The geometry of such a system is shown in Figure 3.39 while its details are listed in Table 3.6. The eccentricity of the concave hyperboloid is -4 and the distance between the foci for this reflector is 1600 mm. Meanwhile its diameter is 1000 mm. We have calculated the fringes generated by baselines displaced along the line-of-sight of the horn array. These are shown in Figure 3.40. Due to restrictions arising from the GCC's we can only implement narrow beams. We have propagated 3° FWHM beams from 70 mm baselines. We note the reduction of the size of the focal plane required to capture the entire fringe patterns compared to Figures 3.34(c) and 3.34(d). This is of course due to the demagnification of the concave hyperboloid. The characteristics of this system are listed in Table 3.5. Finally the geometry details of all systems discussed in Section 3.4 are listed in Table 3.6.

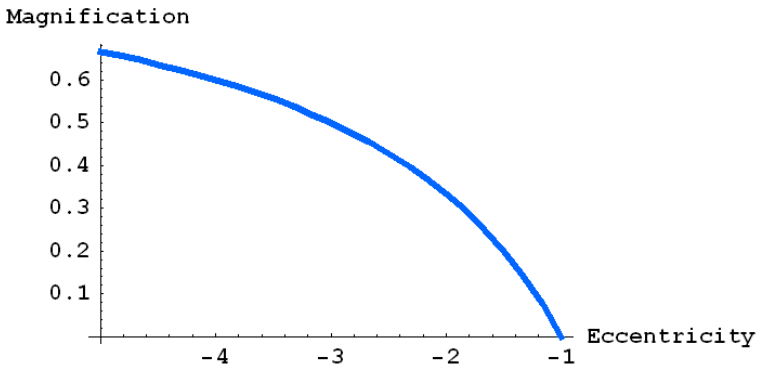

Figure 3.38: Magnification of concave hyperboloid with eccentricity less than -1.

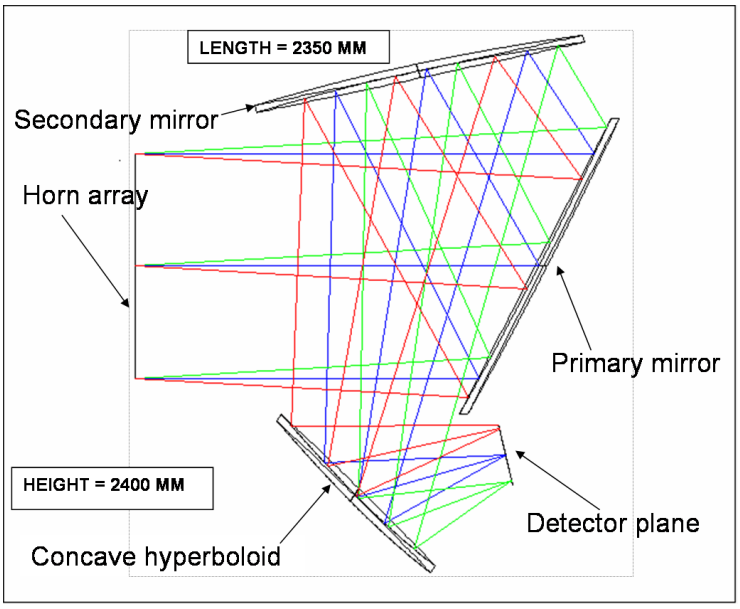

Figure 3.39: GCC reflector with concave hyperboloid. The final focal length is 2020 mm.

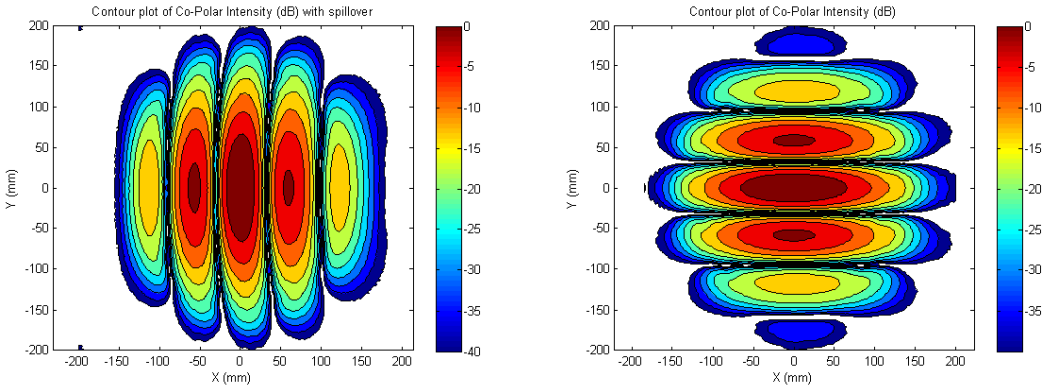

(a) Fringes generated using a 70 mm baseline occurring vertically along the systems line-of-sight.

(b) Fringes generated using a 70 mm baseline occurring horizontally along the systems line-of-sight.

Figure 3.40: Fringes generated by a 3500 mm GCC reflector combined with a concave hyperboloid.

Table 3.5: Characteristics of a GCC. Here **TMC** indicates the 3500 mm focal length GCC that has been combined with a concave hyperboloid reflector.

	Beam FWHM (degress)	Number of horns	Size of detector plane (mm^2)	3 mm bolometers	5 mm bolometers
TMC	3	400	280	8839	3136

3.5 Conclusions

In recent years CMB telescope design has been dominated by the implementation of off-axis compensated Gregorian reflectors. For example the two most prominent milestone experiments in CMB observation WMAP and PLANCK both employed such reflectors. In this chapter we have presented results that indicate that other viable options exist for the choice of reflectors in the QUBIC experiment or future CMB missions. From the perspective of a B-mode telescope both the CATR reflector and the front-fed Cassegrain offer a wider DLFOV then the compensated Gregorian. More relevant to our discussion is that from the perspective of a Fizeau combiner both these systems significantly out-perform the compensated Gregorian. The front-fed

Table 3.6: Details of the geometry of the 3500 mm effective focal length general crossed Cassegrains (GCCs). Here **CNF** indicates the system in which the fold mirror is placed adjacent to the horn array while **CFF** indicates the system in which the mirror is placed in the far field. Also **LCC** indicates the 1000 mm focal length general crossed Cassegrain and **TMC** indicates the 3500 mm focal length general crossed Cassegrain that has been combined with a concave hyperboloid reflector. The term **PF** is the primary focal length, k is the primary conic constant, **ROCS** is the radius of curvature of the secondary mirror, β_T is the tilt between the reflectors, **PD** is the diameter of the primary mirror and **SD** is the diameter of the secondary mirror. Also the term **EQ** indicates the final equivalent focal length.

	PF (mm)	k	**ROCS** (mm)	β_T	**PD** (mm)	**SD** (mm)	**EQ** (mm)
CNF	8862.3	-3.53	7857.27	60	1600	1640	3500
CFF	5894.15	-5.73	7076.75	75	2400	2300	3500
LCC	1743.445	-3.69	1778.53	90	700	900	1000
TMC	6577.85	-5.01	9056.11	70	1320	1600	2200

Cassegrain induces less amplitude distortion in the fringe patterns then the Gregorian while the CATR effectively removes any distortion. The compact geometry of these systems also has significant repercussions when one considers issues such as payload size for satellite space launch. In the next chapter we will show how complications with these systems arise when we consider QUBIC's low 300 mm focal length. However based on our initial premise of an improvement in detector and read out technologies we recommend these systems for implementation within any bolometric interferometer mission.

Figure 3.38 explains why the CATR and GCC reflectors do not produce the same levels of beam distortion as other dual reflectors. Because their eccentricity is < 1 these are the only type of dual reflectors that demagnify the image formed by the primary mirror. Therefore one can implement a large-focal-length primary mirror that reflects large-size Gaussian beams. These reflected beams remain in their far-field as they continue to propagate through the rest of the instrument. As such there is no change in the phase slippage between beams as they propagate and so beam distortion, as

explained using equation (3.2.5), is minimized. This causes the resulting fringes to appear straight. We will explore this topic further in the next chapter.

In this chapter we have presented a brief geometrical and physical optics analysis of various state-of-the-art dual reflectors. We concentrated on long ($f >= 800$) focal length systems. All results presented are of use for CMB telescopes in general. However, for practical reasons, the current design for QUBIC requires a somewhat extreme short focal length. By convention the above systems can all be classed as high performing imagers. These systems successfully capture an incident wavefront and focus it onto a detector plane with low aberrations. Such a conventional criterion, that requires our instrument produces low wavefront aberrations, is of course desirable for QUBIC. However we must also insist that amplitude distortion, arising due to the long wavelength of the beams relative to the reflector size, is also kept to a minimum. In the next chapter we shall discuss a category of optical devices referred to as telecentric systems. We will show how that systems obey these two criteria can be designed.

Finally the results of this chapter exemplify why geometrical optics alone is insufficient to model long-wavelength optical systems such as QUBIC. As we have seen although geometrical optics is a powerful design tool, it does note provide an in-depth analysis of long-wavelength optical systems in which the diffraction of propagating electric fields must be considered. The systems presented in this chapter were designed using geometrical optics and modeled using physical optics. Also the presence of amplitude distortion some fringe patterns was explained using quasi-optics. The inherent challenges of designing long-wavelength optical systems such as QUBIC is highlighted by the fact that three separate techniques were required to fully understand the above systems. The fact the that the QUBIC combiner is a long wavelength system that must produce high quality fringe patterns while possessing a low focal ratio has required some innovative thinking to produce a plausible design. In the next chapters the basic designs we proposed for QUBIC will be discussed in detail.

4 Optical Combiners for QUBIC

4.1 Possible optical combiners for QUBIC

4.1.1 Introduction

Possible off-axis dual reflector combiners for QUBIC were investigated at NUIM and University of Milano-Bicocca[1]. In the previous chapter I looked at a range of dual reflector designs with no upper-limit on focal lengths. Designs with focal lengths down to 800 mm were developed. QUBIC, however requires fast (short focal length) optics and so not all designs may be achievable. In this chapter I concentrate on short focal length designs. The QUBIC collaboration originally intended to purchase the 100 GHz band horns implemented by CLOVER [68]. At this frequency, limitations to the number of 5 mm bolometers that can be multiplexed, placed a 200 mm upper limit on the combiner's focal length. As will be explained in the next chapter later investigations at the APC Paris recommended a 3 mm maximum bolometer size. This allowed the frequency of the combiner to be increased to 150 GHz which would allow QUBIC to be more sensitive. It was calculated that at 150 GHz the maximum focal length of the combiner could be increased to 300 mm. At NUIM we designed 300 mm focal length systems to combine 150 GHz Gaussian beams propagating from the horn array. In Milano-Bicocca 200 mm focal length systems were investigated to combine 100 GHz beams. These focal lengths represent the middle ground between the 100 mm and 400 mm focal length systems listed in Table 2.1. Investigating these focal lengths

[1]University of Milano-Bicocca - Piazza dell'Ateneo Nuovo, 1 - 20126, Milano. For more information visit `http://www.unimib.it/`.

provides an assessment of whether it would be possible to implement an off-axis dual reflector system for QUBIC in the near future.

The 14° FWHM of the QUBIC re-emitting horns is equivalent to the field-of-view of a telescope. Therefore it is immediately recognizable that designing any dual reflector system for QUBIC will be extremely difficult. At 150 GHz QUBIC has an f-number of 2.14 while at 100 GHz the f-number drops to unity. Considering that the field of view of QUBIC is 14° these f-numbers are extremely small compared to standard telescopes. The simplest way to minimize the wavefront aberrations that will affect the fringe patterns from equivalent baselines is to implement a system with a large focal length, a small entrance diameter and a narrow field of view. These options are not available to us in QUBIC so it is reasonable to assume that aberrations will be present within the combining wavefronts. This chapter details our efforts to design and model a dual reflector that minimizes these aberrations.

We will now present the dual reflectors we have designed for QUBIC. As previously explained the various types of reflectors that can be employed are extremely restricted by QUBIC's low focal ratio. In Chapter 3 we concluded that ideally a CATR similar to CLOVER should be implemented within a bolometric interferometric CMB mission. Such a dual reflector ensures low traditional wavefront aberrations as well as minimal Gaussian beam amplitude distortion. However due to geometric restrictions the minimum focal length required by such a system to cater for a 12×12 array of 150 GHz horns is ~ 800 mm. This is unsuitable for QUBIC.

If we were to design a long-focal length combiner, with no restrictions on size, then Section 3.3.1 attests that a CATR design, followed by a front-end-fed Cassegrain and an inverted crossed Cassegrain should be considered. However, the very low $F/\#$ of the QUBIC combiner essentially rules out crossed designs (due to geometrical shadowing by relatively large components). Unfortunately even the front-fed Cassegrain cannot accommodate the large focal plane required. With a focal length of 300 mm there are two particular off-axis dual reflectors that are suitable for QUBIC. These are:

- **a general crossed Cassegrain (GCC)** .
- **a compensated Gregorian (CG)** .

In this chapter we will discuss why we consider these systems to be the most suitable for QUBIC. We will discuss the advantages and disadvantages associated with each reflector. For the purposes of bolometric interferometry the GCC performs better than the CG. However any GCC will have practically no tolerances to any adjustments to the original QUBIC design discussed in Chapter 2[2].

4.1.2 General crossed Cassegrain (GCC)

The unique aspect of a CATR reflector is that the focal and object planes are perpendicular. This is obviously a huge benefit for cryostat construction. For QUBIC we must relax the requirement that these two planes are exactly perpendicular. This has enabled us to design the dual reflector system shown in Figure 4.1. This is a general crossed Cassegrain system (GCC) with no restriction on the feed or bending angles. The fringe patterns produced by this combiner are shown in Figures 4.2 - 4.3. These fringes have been generated by the 40 mm baselines shown Figure 3.5 [3]. A lenght 40 mm was chosen as it is approximately in the middle of the range of baselines to be used. When the performance of specific designs was later modelled (see Section 6.4) all the baselines to be used, with the correct weighting, were included.

Recall that in order to ensure a CATR the sum of angles $\alpha + \beta$ shown in Figure 3.3 must equal 90° [107]. To design a GCC we set $\alpha + \beta = \zeta$ where ζ is a variable angle. For the system shown Figure 4.1 $\zeta = 103°$ and the tilt $\beta = 72°$. From trial and error we concluded that these values led to the most suitable GCC for implementation in QUBIC. Choosing these angles allowed us to design a dual reflector with a primary

[2]Such adjustments include increasing the size of the QUBIC back-to-back horn array or placing a polarizing grid before the detector array

[3]As previously explained the patch of sky at which the BB power spectrum is most likely to be observed is between $l_{min} = 30$ and $l_{max} = 200$. Assuming a flat sky approximation $l = 2\pi \times u$ and $u = \frac{\mathbf{d}}{\lambda}$ [71]. Here $|\mathbf{d}|$ is the physical separation of the antennas of a given baseline and u is the spatial frequency of the fringe patterns. The multipoles at which we must observe the sky are related to the baseline lengths by $l = \frac{2\pi}{\lambda} \times \mathbf{d}$. Therefore at 150 GHz the maximum and minimum baselines for QUBIC are $\mathbf{d_{min}} = 10$ mm and $\mathbf{d_{max}} = 64$ mm. All systems in this chapter were modeled using 40 mm baselines as they approximate the average range of all QUBIC baselines. The fringes modeled using these baselines are indicative of the results that would be obtained for all values of $\mathbf{d}$.

mirror large enough to accommodate a 12 × 12 array of back-to-back horns. This primary mirror will be unblocked by the secondary while $\beta = 72°$ will ensure a crossed reflector whose geometry leads to minimum beam distortion. Once the above parameters were established we set the equivalent focal length to 300 mm and solved equations (3.2.1), (3.2.2) and (3.3.1) to find the primary focal length, secondary eccentricity and angle of throw [108]. The fact that this system obeys the Dragone condition leads to minimal astigmatism and cross polarization. Also the beams from the secondary horns remain moderately collimated as they propagate through the combiner. This ensures low amplitude distortion.

As well as obeying the Dragone condition, the shape of the mirrors of these systems have been optimized using Zemax in order to produce the smallest possible third order Seidel aberrations. Using Zemax's default merit function (spot radius) the primary and secondary mirrors of the CCG were deformed from their traditional parabolic and hyperbolic shapes respectively[4]. The mirrors' surfaces were reshaped into the higher order polynomials

$$z(\rho) = f(\rho) + \alpha_1\rho^4 + \alpha_2\rho^6 + \alpha_3\rho^8 \tag{4.1.1}$$

where $f(\rho)$ indicates the original quadratic polynomial describing the classic conic section and $\rho^2 = x^2 + y^2$. The coefficients $\alpha_{1/2/3}$ have been calculated by Zemax optimizations using the default merit function.

As shown in Figure 4.1 the GCC has a DLFOV of greater than 14° at 150 GHz. This essentially implies that wavefront aberrations are so slight, that the performance of the system is restricted solely by the diffraction properties of light. Thus the performance of the GCC from a telescope's perspective is as good as can be produced. Also as shown in Figures 4.2 - 4.3 this system induces little or no amplitude distortion on the propagating beams. Therefore the GCC fulfills the two criteria we introduced in Chapter 3 for the QUBIC combiner. It produces low wavefront aberrations and induces low levels of amplitude distortion in the combining beams.

The GCC has been designed for a 12 × 12 array of 14° FWHM back-to-back horns. At 150 GHz the waist radius of a 14° Gaussian beam is 3.074 mm. Optimum coupling

[4]The operation of Zemax's default merit function has been previously explained.

between a Gaussian beam and a corrugated conical horn occurs when $\frac{w}{a} = 0.64$ where a is the aperture radius and so the diameter of a single horn that produces such a beam is $\approx$ 10 mm plus 2 mm for the rim thickness [110]. Therefore the above GCC must accommodate a back-to-back horn array of 140×140 mm^2. Due to the geometry of the GCC these parameters push the limit that the GCC will allow and as we shall see leakage of power from the horn array onto the detector plane is inevitable. Here we have taken standard conical corrugated horns (scalar horns) as an example[5]. This distance between horn centres could possibly be reduced, though not significantly, if CLOVER-type horns are used.

There are other possible draw backs to implementing this system. Using GRASP9 we have calculated that only 96% of the power from the edge horns in the array will reach the bolometer detectors[6]. This is due to spillover at the primary mirror. This mirror's size is restricted in order to prevent it shadowing the detector plane. Therefore seemingly minor adjustments such as increasing the horn array to 150×150 mm^2 will generate a large amount of spillover at the primary. These restrictions will be somewhat relaxed if 10° or 12° FWHM beams could be used. A significant concern of the system is the proximity of the back-to-back horn array to the detector plane. Leakage from the horn array to the detector plane may be high enough to significantly reduce the sensitivity of the bolometer detectors to the produced fringes.

Another concern is the insertion of any optical window separating the focal plane from the combiner's chamber. There is only a 20 mm region into which the window can be inserted between the primary mirror and the focal plane. Also in order to minimize spillover the back-to-back horns must be as close to the primary mirror as possible. This means that if required we will not be able to place a half-wave plate between back-to-back array and the primary mirror. If dramatic changes are forced on the QUBIC apparatus the GCC will not posses the versatility we require to enable the adjustment of the experiment's components.

[5]QUBIC will most likely use profiled corrugated horns but at this stage standard conical corrugated horns were used for the fringe pattern simulations. Later work showed that the exact choice of beam pattern did not have a noticeable effect on the level of aberrations found.

[6]This figure is regardless of the size of the detector plane. The power loss is due the restricted size of the mirrors in order to prevent them overlapping one another.

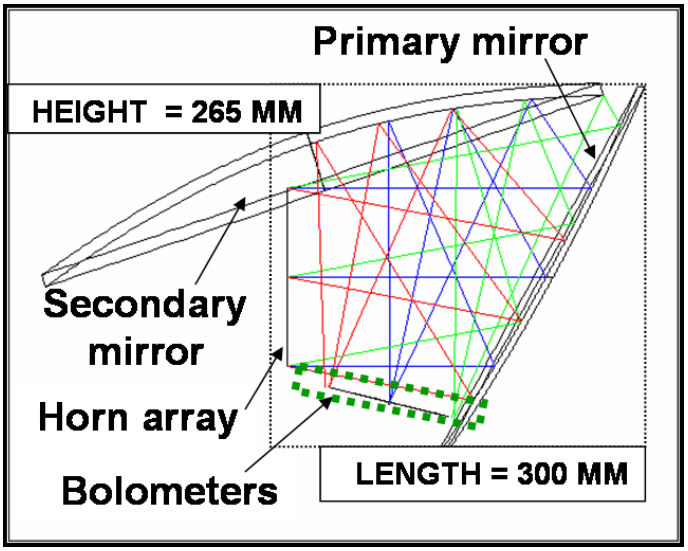

(a) General crossed Cassegrain reflector. The tilt between the reflector axes is 72°. The eccentricity of the secondary ellipsoid is -2.23. The dark green dashed box indicates the area into which any window separating the 4 K pulse tube cryostat from the lower temperature detector unit must fit. This area is at most 20 mm wide.

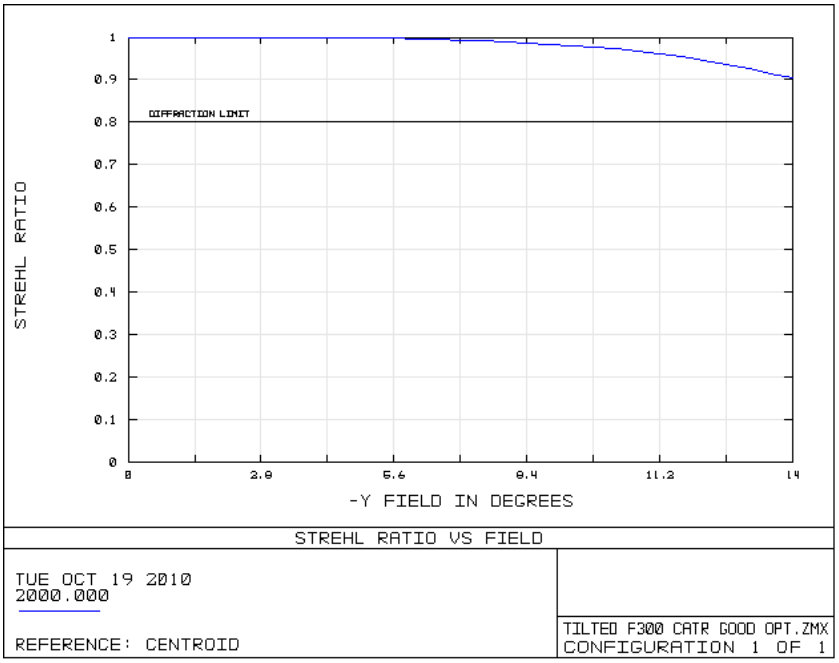

(b) The DLFOV of the general crossed Cassegrain is greater than 14° for a 140 mm entrance aperture.

Figure 4.1: General crossed Cassegrain for QUBIC. The focal length of this system is 300 mm.

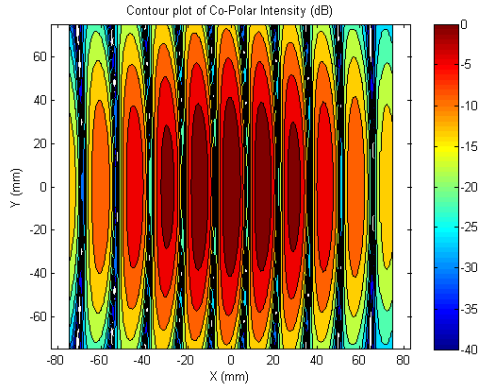

(a) CEN baseline.

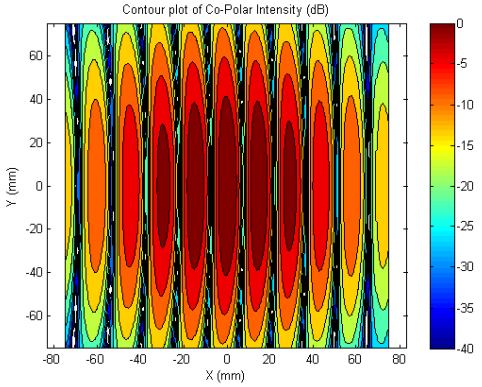

(b) UPL baseline.

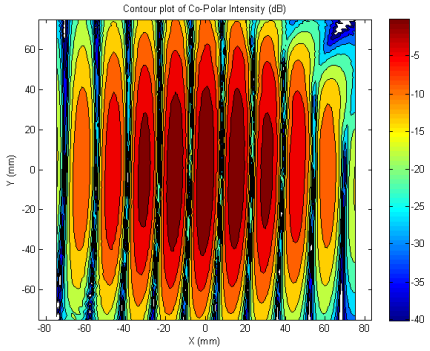

(c) UPR baseline.

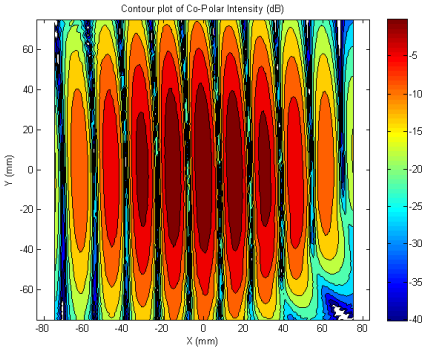

(d) LOWL baseline.

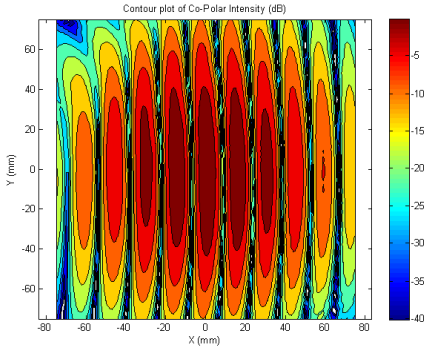

(e) LOWR baseline.

Figure 4.2: Fringe patterns from 5 equivalent horizontal baselines produced by the general crossed Cassegrain for QUBIC. Fringes have been formed using 14° FWHM Gaussian beams and the five 40 mm baselines shown in Figure 3.5.

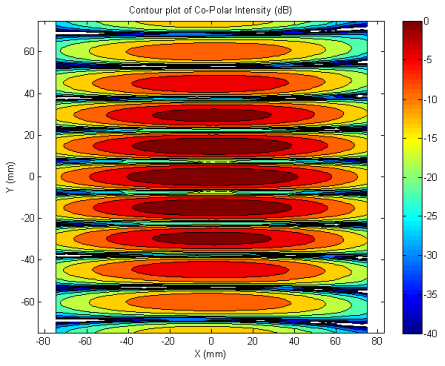

(a) CEN baseline.

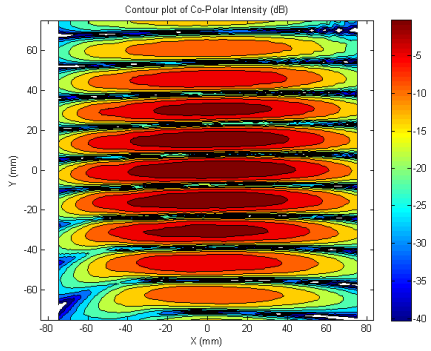

(b) UPL baseline.

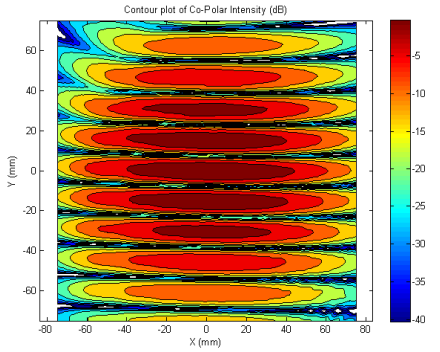

(c) UPR baseline.

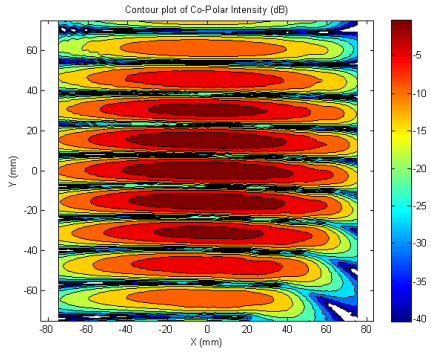

(d) LOWL baseline.

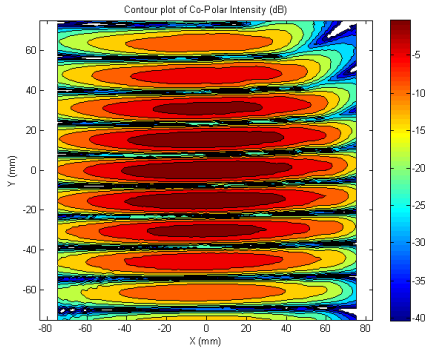

(e) LOWR baseline.

Figure 4.3: Fringe patterns from 5 equivalent vertical baselines. Fringes have been formed using 14° FWHM Gaussian beams and the five 40 mm baselines shown in Figure 3.5.

4.1.3 Compensated Gregorian (CG)

A Compensated Gregorian (CG) suitable for QUBIC is shown in Figure 4.4. The fringe patterns produced by this combiner are shown in Figures 4.5 - 4.6. These fringes have been generated by the 40 mm baselines shown Figure 3.5. The values of the tilt between the reflectors (β) and the angle of throw at primary mirror (θ_u) were set along with the equivalent focal length. Equations (3.2.1), (3.2.2) and (3.3.1) were then solved to find the eccentricity (e) and the feed angle (α) as discussed in [106]. Finally a value for the distance between the secondary foci was chosen to give the smallest secondary reflector that still captured all rays reflected from the primary mirror. The DLFOV of this Gregorian is slightly less than the 14° required by QUBIC yet it is still remarkably high. However the performance of this system is not as good as the GCC. Not only is the DFLOV slightly less than the GCC but the geometry of the CG ensures that amplitude distortion will be present in the final fringe patterns. Once again the curved fringe patterns suggest that the Gaussian beams reflected by this combiner have suffered amplitude and phase distortions.

However there are reasons why this CG may be considered suitable for QUBIC. These concern the versatility of the combiner to design adjustments. Firstly the size of the back-to-back horn array is less restricted than that of the GCC. If the horn array needs to be widened the primary mirror can easily be enlarged to ensure a near zero edge taper of all beams. Secondly the leakage of power from the back-to-back array onto the detector plane that occurs in the GCC will not occur in the CG. Also although the CG is larger than the GCC its size is still within the confines of cryostat limitations[7].

[7]It is expected that the optical combiner will have to fit inside a $900 \times 900 \times 600$ mm^3 "box".

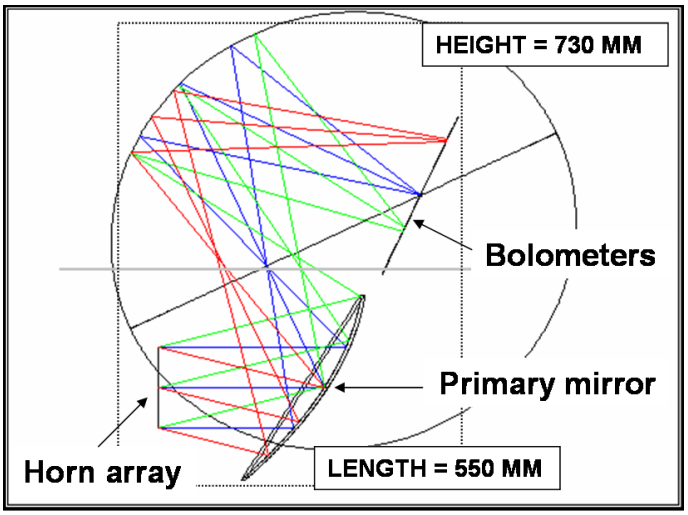

(a) Compensated Gregorian reflector.The tilt between the reflector axes is 25°. The eccentricity of the secondary ellipsoid is 0.359

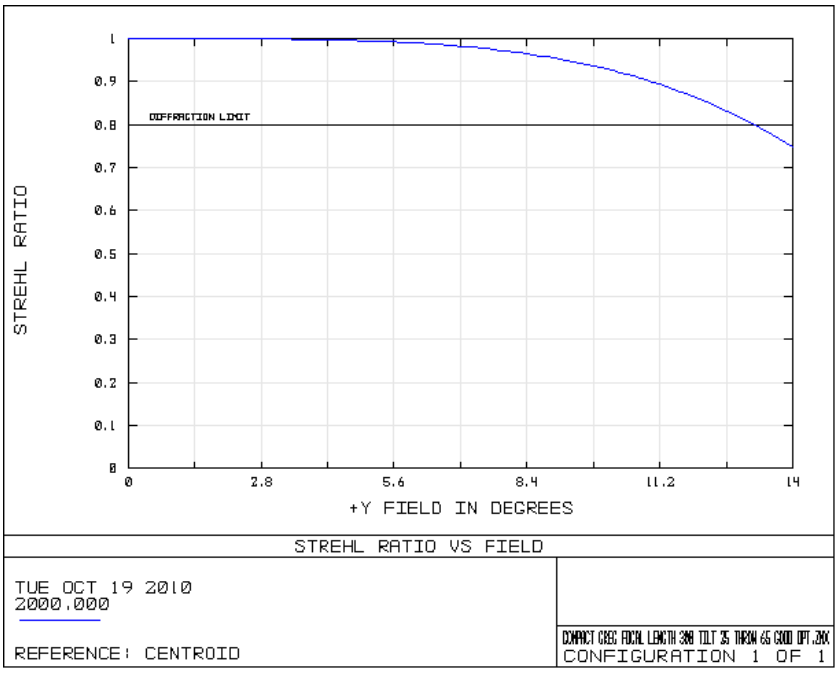

(b) The DLFOV of the compensated Gregorian is short of 14° for a 140 mm entrance aperture.

Figure 4.4: Compensated Gregorian reflector for QUBIC. The focal length of this system is 300 mm.

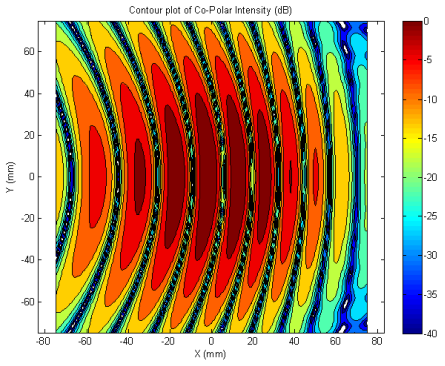

(a) CEN baseline.

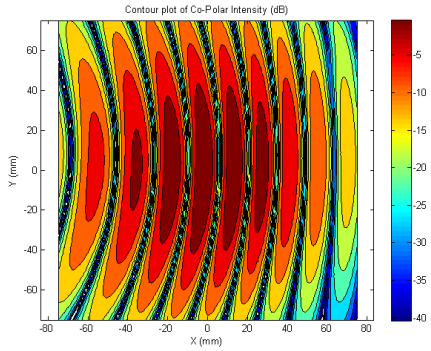

(b) UPL baseline.

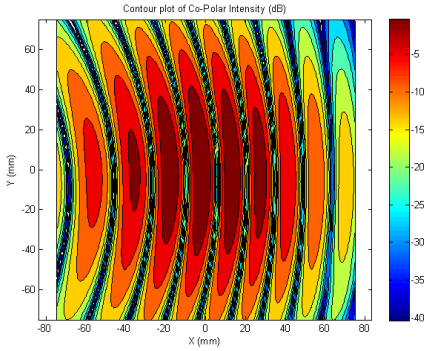

(c) UPR baseline.

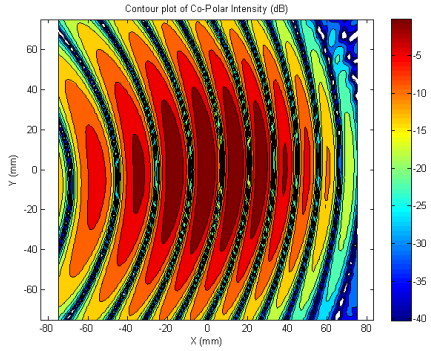

(d) LOWL baseline.

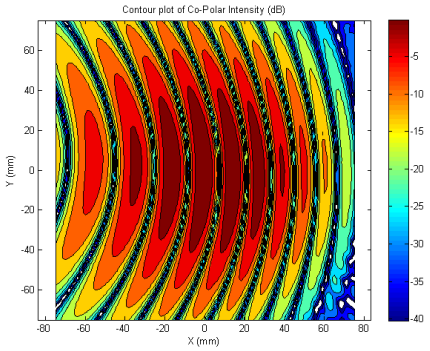

(e) LOWR baseline.

Figure 4.5: Fringe patterns from 5 horizontal equivalent baselines produced by the compensated Gregorian for QUBIC. Fringes have been formed using 14° FWHM Gaussian beams and the five 40 mm baselines shown in Figure 3.5.

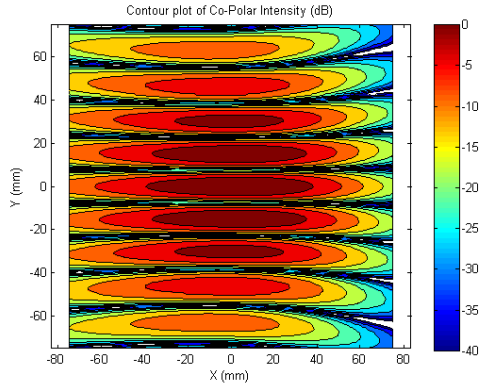

(a) CEN baseline.

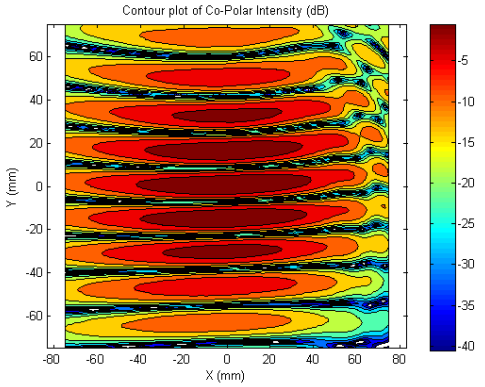

(b) UPL baseline.

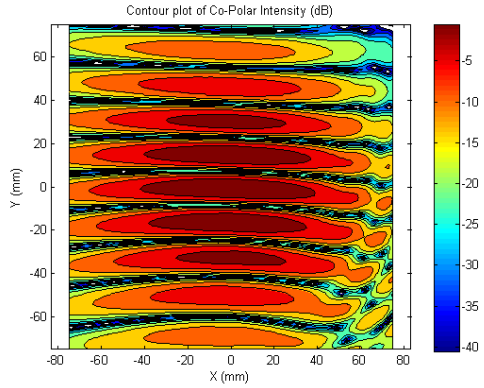

(c) UPR baseline.

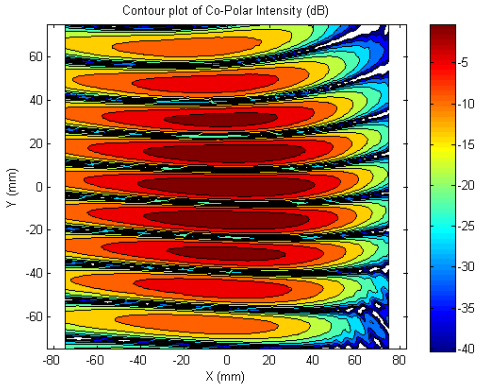

(d) LOWL baseline.

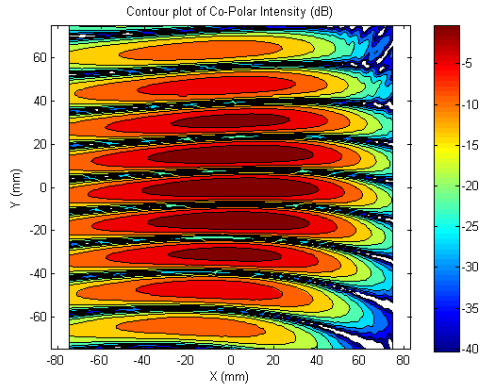

(e) LOWR baseline.

Figure 4.6: Fringe patterns from 5 vertical equivalent baselines produced by the compensated Gregorian for QUBIC. Fringes have been formed using 14° FWHM Gaussian beams and the five 40 mm baselines shown in Figure 3.5.

The decision of which reflector system to implement becomes a compromise between the quality of fringe patterns required versus the practicality of system construction. As demonstrated in Figures 4.2 - 4.3 the GCC design minimizes amplitude distortion within the fringe patterns. Fringes from equivalent baselines are therefore similar on the focal plane. If the quality of the required fringes is an absolute requirement the GCC must be implemented (providing leakage from the horns array does not overwhelm system sensitivity). However if some distortion of the fringe patterns is acceptable the CG is the likely candidate for implementation[8]. Unlike the GCC the CG also accommodates the placing of a half wave plate between the horn array and the primary mirror. It is apparent from Figures 4.5 - 4.6 that the beam distortion induced by the CG is significant. Presently work is on going investigating whether this distortion will adversely affect the recovery of the Stokes visibilities. We shall return to this topic in Chapter 6. The details of the GCC and CG dual reflectors are listed in Table 4.3.

4.1.4 Constraints on the mirror dimension in the GCC and CG

As shown in Figure 4.1(a) the primary and secondary reflectors in the CGG are in close proximity to one another. Unfortunately this means that the sizes of these mirrors must be restricted in order to prevent overlapping of the reflectors. Therefore even if levels of spillover at the primary or secondary mirrors are large the reflector sizes cannot be increased due to geometrical restrictions.

The size of the mirrors we can use in the CG reflector are dependent on restrictions in cryostat dimensions. We have momentarily ignored this constraint when considering the Gregorian reflectors. In this case the mirrors in the CG are separated by a distance large enough that allows them to be set to a size that permits practically zero edge taper on all beams. In contrast, even without the cryostat constraints, the mirror sizes of the GCC system must be restricted in order to prevent overlapping of the reflectors. Therefore the sizes of the mirrors in the GCC cannot be increased to produce an extremely low edge taper due to geometrical rather than cryostat restrictions.

[8]Such matters are currently under investigation at both the APC Paris and NUIM.

Spillover values for individual Gaussian beams propagating through the GCC and the CG are shown in Table 4.1 and Table 4.2. The horns from which these beams propagate form the baselines which are shown in Figure 3.5. Beam spillover is much larger in the GCC than for the CG. The preliminary cryostat limitations placed on QUBIC are 600 mm × 900 mm × 900 mm. Both the GCC and the CG fit within these dimensions. The values shown in Table 4.2 suggest that the size of this cryostat is generous enough to allow large enough mirrors to effectively remove spillover at the mirrors in the CG reflector.

Table 4.1: Spillover (calculated as $-10\log(P_{reflected}/P_{in})$ at each mirror) at the primary and secondary reflector in the GCC. X displacement refers to the horizontal baselines shown in Figure 3.5. Y displacement refers to the vertical baselines shown in Figure 3.5. Beam 1 and Beam 2 refer to the individual horns that make up the 40 mm baselines.

	X Displacement.				Y Displacement.			
	Beam 1.		Beam 2.		Beam 1.		Beam 2.	
	Primary Mirror.	Secondary Mirror.	Primary Mirror.	Secondary Mirror.	Primary Mirror.	Secondary Mirror.	Primary Mirror.	Secondary Mirror.
CEN.	0.0001 dB	0.0002 dB	0 dB	0.0029 dB	0 dB	0.0011 dB	0 dB	0.0011 dB
UPL	0.1123 dB	0.1224 dB	0.008 dB	0.0126 dB	0.1123 dB	0.1124 dB	0.0207 dB	0.0339 dB
UPR	0.1123 dB	0.1124 dB	0.008 dB	0.0126 dB	0.1123 dB	0.1224 dB	0.0207 dB	0.0339 dB
LOWL	0.0096 dB	0.1205 dB	0.0006 dB	0.0273 dB	0.0096 dB	0.1205 dB	0 dB	0.0538 dB
LOWR	0.0096 dB	0.1205 dB	0.0006 dB	0.0273 dB	0.0096 dB	0.1205 dB	0 dB	0.0538 dB

4.2 Effect of changes in QUBIC requirements

Further investigation of the QUBIC at the APC Paris led to the stipulation that in order to achieve the minimum sensitivity required to reach a tensor-to-scalar ratio of 0.01 the size of the back-to-back horn array must be increased to at least 20 × 20 horns elements[9]. This means at 150 GHz the size of the back-to-back array must be

[9] As explained the noise (N_{ij}) received by each bolometer, $N_{ij} = \delta_{ij}\frac{4(NET^2)\Omega^2 N_h}{N_t}\frac{1}{N_{eq}^2}$, is inversely proportional to the number of equivalent baselines implemented N_{eq}. Here N_h is the number of horns while N_t is the number of time samples Ω is the beam size of the sky horns and NET is the noise equivalent temperature of the individual bolometers. The relationship between noise reduction and the number of equivalent baselines has been fully explained in both Chapter 2 and

Table 4.2: Spillover (calculated as $-10\log(P_{reflected}/P_{in})$ at each mirror) at the primary and secondary reflector in the CG. X displacement refers to the horizontal baselines shown in Figure 3.5. Y displacement refers to the vertical baselines shown in Figure 3.5. Beam 1 and Beam 2 refer to the individual horns that make up the 40 mm baselines.

	X Displacement.				Y Displacement.			
	Beam 1.		Beam 2.		Beam 1.		Beam 2.	
	Primary Mirror.	Secondary Mirror.	Primary Mirror.	Secondary Mirror.	Primary Mirror.	Secondary Mirror.	Primary Mirror.	Secondary Mirror.
CEN.	0 dB	0.0016 dB	0 dB	0.0001 dB	0 dB	0.0001 dB	0 dB	0.0001 dB
UPL	0.004 dB	0.0053 dB	0.0006 dB	0.0015 dB	0.004 dB	0.0053 dB	0.001 dB	0.0287 dB
UPR	0.004 dB	0.0053 dB	0.0006 dB	0.0015 dB	0.004 dB	0.0053 dB	0.001 dB	0.0287 dB
LOWL	0.0035 dB	0.0037 dB	0.0003 dB	0.0003 dB	0.0035 dB	0.0037 dB	0.0002 dB	0.0002 dB
LOWR	0.0035 dB	0.0037 dB	0.0003 dB	0.0003 dB	0.0035 dB	0.0037 dB	0.0037 dB	0.0002 dB

increased to 240×240 mm^2. We therefore must re-examine the 300 mm dual reflectors discussed above and asses their ability to handle such a large horn array.

4.2.1 Adjustment to combiners

Increasing the size of the sky horn array means implementation of the GCC system is not possible. Due to the geometry of the system it is not possible to increase the diameter of the primary and secondary mirrors to capture the beams from the outer most horns. Any significant increase to the diameters listed in Table 4.3 will cause the mirrors to overlap and the primary mirror to shadow the detector plane. Therefore the only off-axis dual reflector **physically** applicable to QUBIC is the CG. At this point all other dual reflector combiners must be ruled out.

We have performed a PO analysis of the CG in which the location of the corner horns in Figure 3.5 has been changed to $\pm$ 120 mm. For this analysis we once again tested 40 mm baselines. The fringe patterns generated by these baselines are shown below in Figures 4.7 and 4.8. As we can see the effects of amplitude distortion induced by

in [69]. A reassessment of the implications of this relationship has led to the conclusion that when 14° FWHM back-to-back horns are implemented at least 400 of these horns will be required to ensure that the sensitivity of QUBIC is comparable with that of a bolometric imager.

the CG system become extremely detrimental when we examine baselines from the extremities of the enlarged horn array. Also we must expect that classical wavefront aberrations will severely affect the quality of the fringe patterns due to the fact that the system is no longer diffraction limited for 14° FWHM beams propagating from an array 240×240 mm^2 in size.

In Figures 4.9 and 4.10 we compare the spot diagrams for the CG reflector when the entrance diameter is 120×120 mm^2 and 240×240 mm^2 in size respectively. In both these figures a $\pm 14°$ FOV is incident over the entrance apertures[10]. The black circle in each figure represents the Airy disk for a 150 GHz optical system. That fact that the rays in Figure 4.10 are incident on the image plane outside this disk means that wavefront aberrations dominate the imaging qualities of this system. This can be compared with the equivalent spot diagram for the 120×120 mm^2 array shown in Figure 4.9. Here we can see that when the smaller entrance aperture is used the system is very close to being diffraction limited. Similar Zemax optimizations to those discussed above failed to produce a diffraction limited CG. When the size of the back-to-back horn array is increased to 240 mm the focal ratio of the combiner becomes 1.25. From the author's knowledge it is simply not possible to design a dual reflector of such a low focal ratio that will produce diffraction limited beams over a $\pm 14°$ FOV.

[10] In the context of QUBIC a $\pm 7°$ FOV is equivalent to the 14° FWHM of the propagating Gaussian beams. In order to design a system that captures the full power of these Gaussian beams we analyze the systems using a $\pm 14°$ FOV.

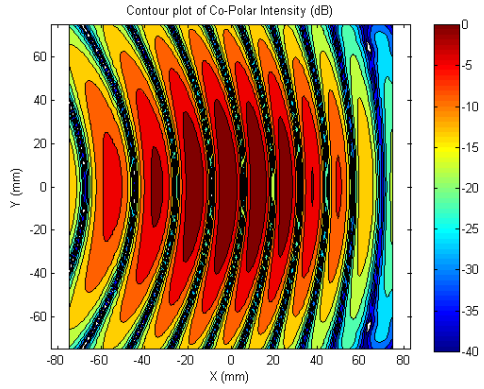

(a) CEN baseline.

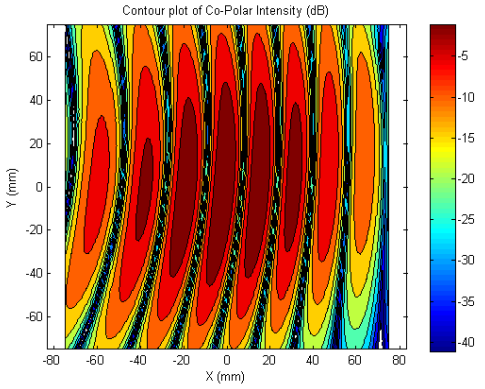

(b) UPL baseline.

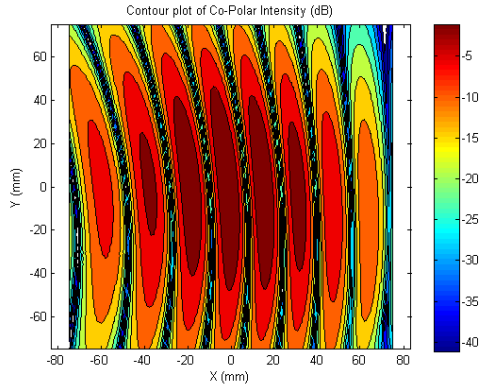

(c) UPR baseline.

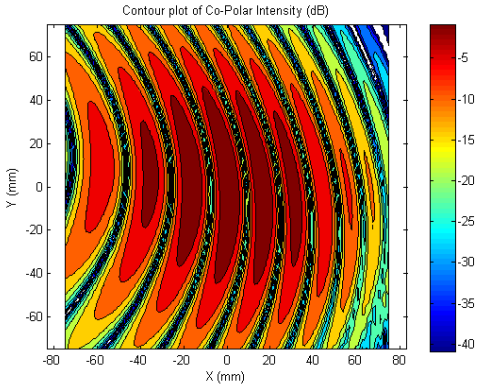

(d) LOWL baseline.

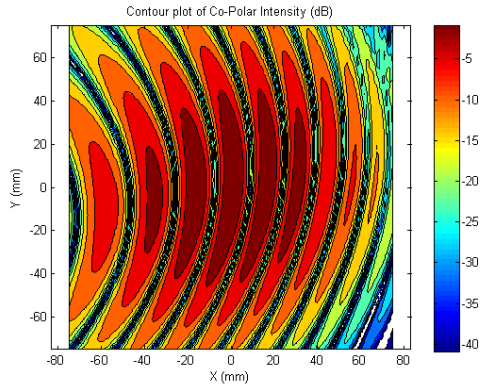

(e) LOWR baseline.

Figure 4.7: Fringe patterns from 5 horizontal equivalent baselines produced by the compensated Gregorian for QUBIC. Fringes have been formed using 14° FWHM Gaussian beams and the five 40 mm baselines shown in Figure 3.5. The position of the horns in the off-axis baselines have been adjusted to model the outer most beams from a 20×20 horn array.

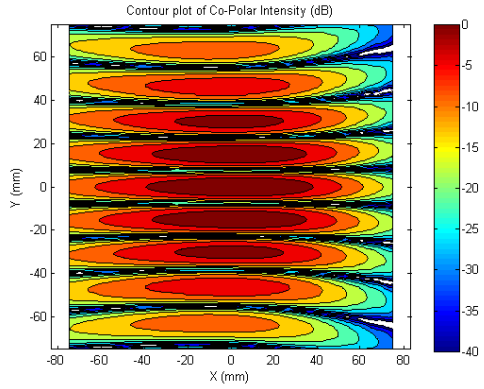

(a) CEN baseline.

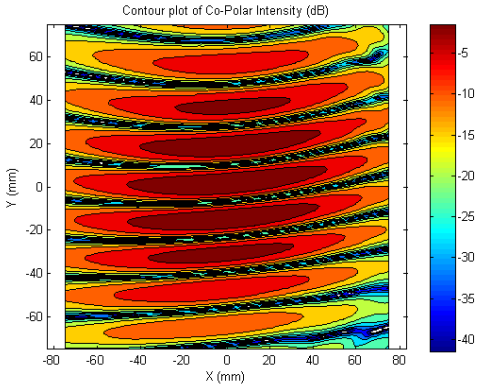

(b) UPL baseline.

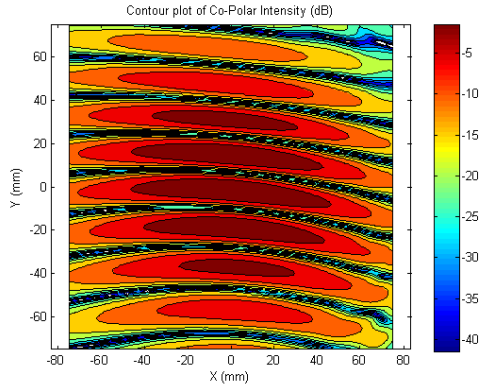

(c) UPR baseline.

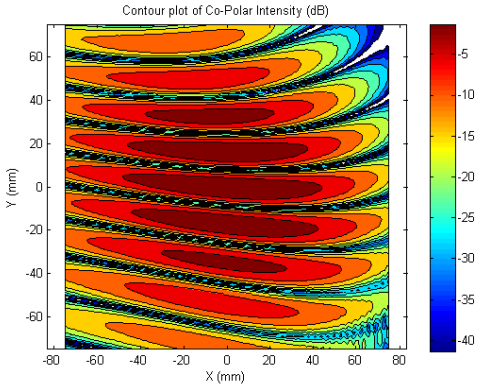

(d) LOWL baseline.

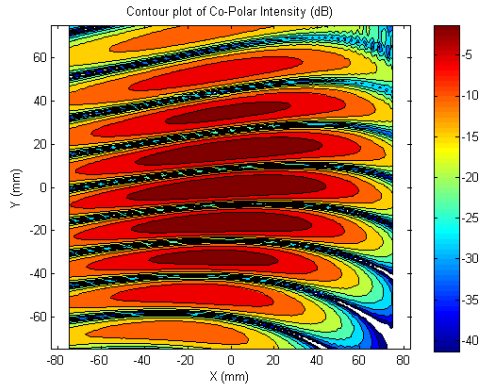

(e) LOWR baseline.

Figure 4.8: Fringe patterns from 5 vertical equivalent baselines produced by the compensated Gregorian for QUBIC. Fringes have been formed using 14° FWHM Gaussian beams and the five 40 mm baselines shown in Figure 3.5. The position of the horns in the off-axis baselines have been adjusted to model the outer most beams from a 20×20 horn array.

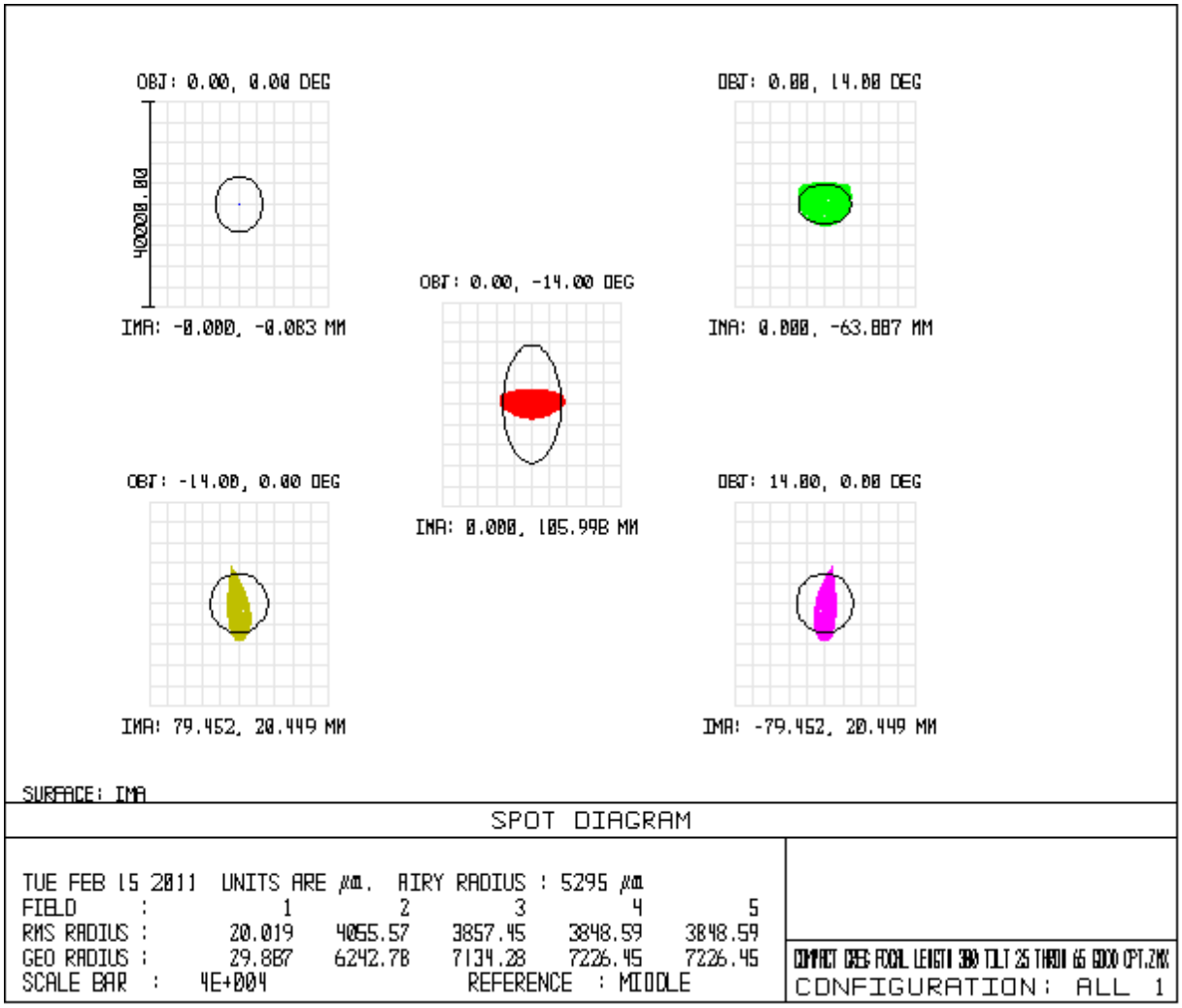

Figure 4.9: Spot diagram for a ±14° FOV incident over an entrance diameter equivalent to a 12 × 12 horn array. The black line shows the Airy' disk for each spot diagram. Also shown is the Airy ellipse (the Airy disk radius is 1.22 times the primary wavelength times the $F/\#$ of the system. In general this depends upon the field position and pupil orientation. In some cases there is also significant asymmetry giving an elliptical rather than a circular shape).

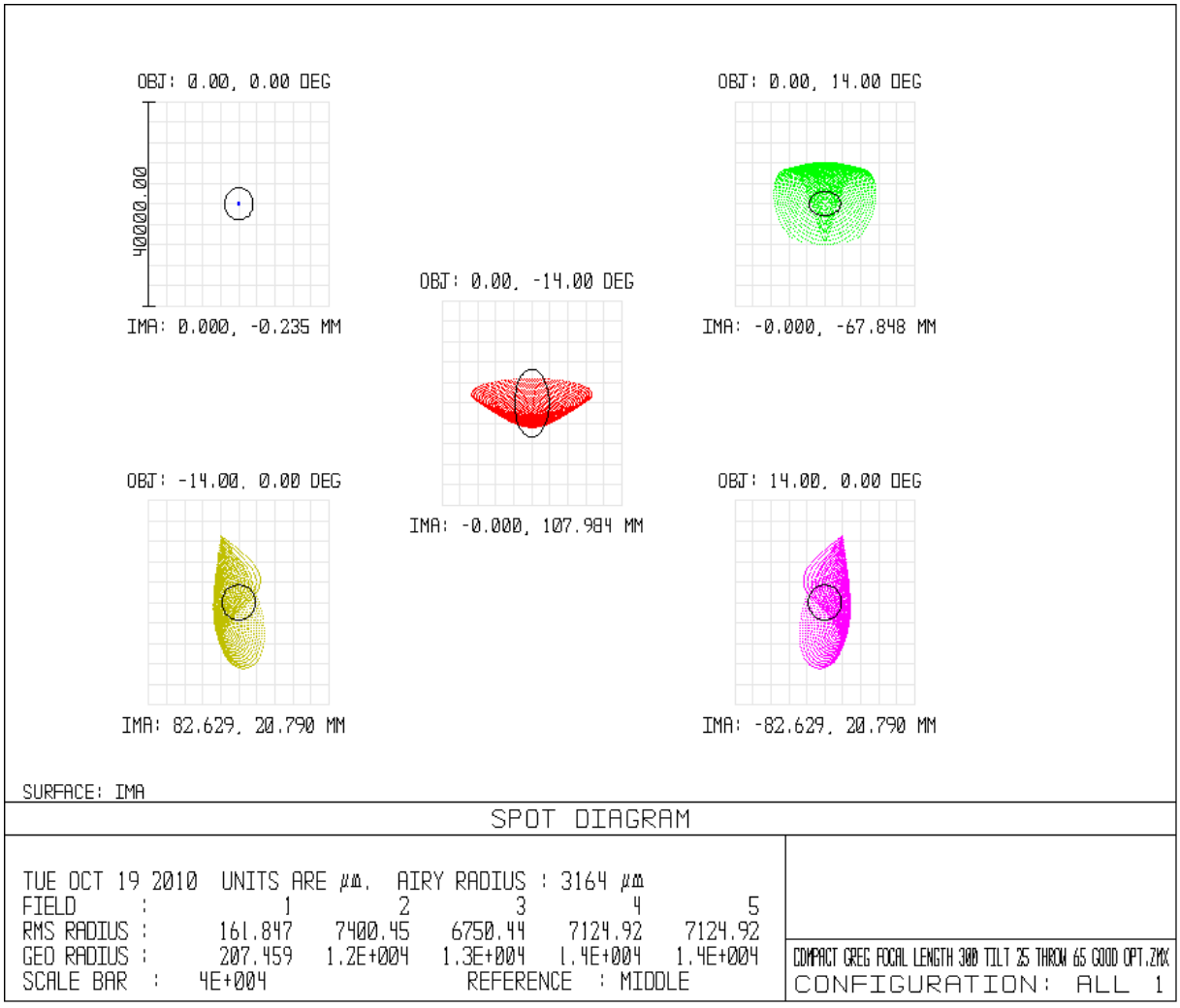

Figure 4.10: Spot diagram for a ±14° FOV incident over an entrance diameter equivalent to a 20 × 20 horn array. The black line shows the Airy' disk for each spot diagram. Also shown is the Airy ellipse (the Airy disk radius is 1.22 times the primary wavelength times the $F/\#$ of the system. In general this depends upon the field position and pupil orientation. In some cases there is also significant asymmetry giving an elliptical rather than a circular shape).

Although the CG is physically capable of combining the large 14° FWHM beams from the enlarged horn array and producing fringe patterns on the focal plane such a system is not an ideal candidate for QUBIC. The presence of a large number of back-to-back horns and the large FWHM Gaussian beams means that any short focal length systems will induce wavefront aberrations of large magnitude. Also the implementation of a CG reflector will result in the fringe patterns becoming deformed by amplitude distortion as well as wavefront aberrations. We have therefore attempted to attempt to design a novel class of dual reflector more suitable to the QUBIC requirements than the CG.

4.2.2 Zemax optimization to generate Telecentric combiners

As we have shown beam distortion is effectively minimized with a crossed Cassegrain design. Such a design is applicable to bolometric interferometry due to the fact that it approximates a telecentric optical system. This is demonstrated in Figure 4.11 where we have shown the system from the point of view of three separate 14° FWHM beams propagating through the combiner. A telecentric optical system is one in which either the entrance or exit pupil is placed at infinity [111].

If the hard aperture of an optical systems is placed in front of the focusing device it becomes the entrance pupil of the system. In QUBIC the hard aperture is the back-to-back horn array. We therefore require an object-space telecentric system. In Figure 4.12 a 300 mm focal length ideal lens has been used to transfer three pencils of rays representing beams propagating from horn apertures into the far field. The horns are located at the front focal point of the ideal lens. Recalling that the exit pupil is simply the image of the entrance pupil it is apparent when we trace the virtual rays that the exit pupil of this system will be located at infinity. This system is therefore also image-space telecentric (doubly telecentric) [112]. From Figure 4.11 we can clearly see that the 300 mm crossed Cassegrain approaches such behavior.

Implementation of a crossed Cassegrain will provide an off-axis system that is also very close to becoming doubly telecentric. This behavior is desirable for the optical combiner and illustrates why a crossed Cassegrain is most suitable for QUBIC. The well collimated beams in the image space of Figures 4.11 and 4.12 mean that almost planar wavefronts are combining to form fringes. The fact that the wavefronts are

planar indicate that the beams are within the far field away from their waist radii. As discussed in the previous chapter this minimizes possible amplitude distortion due to the fact the Gaussian beams' phase slippage is practically constant throughout the image space. In comparison Figure 4.13 illustrates that rather than being collimated at the detector plane the interfering beams in the compensated Gregorian are rapidly diverging. It is this divergence that is responsible for the large amount of amplitude distortion induced by the CG. This is primary reason why these systems are unsuitable for QUBIC.

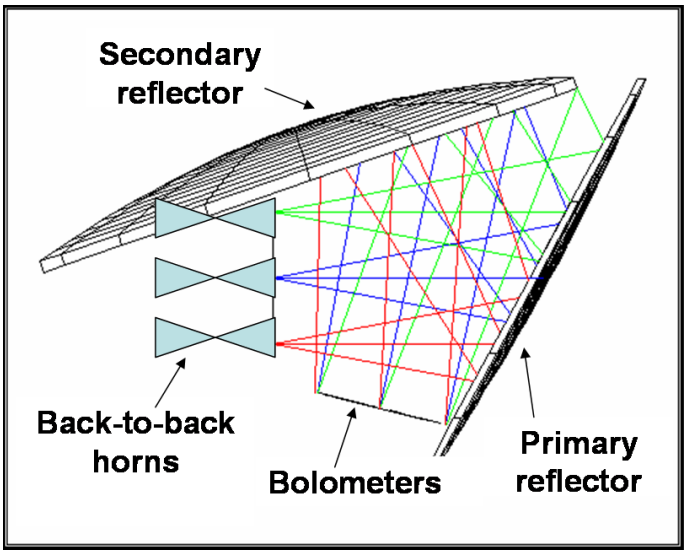

Figure 4.11: General Crossed Casegrain implemented as a object space telecentric combiner.

We have implemented several Zemax optimizations in order to create a doubly telecentric optical system that will accommodate a 20 × 20 back-to-back horn array. For each optimization we entered a different basic structure for a combiner into Zemax. The focal length of these designs was 300 mm and the surface shapes consisted of standard conic sections. The first two optimized systems began as a pair of parabolas whose combined focal lengths were 300 mm. They were originally tilted by angles chosen to allow a crossed and back-fed design. The third system began as a compensated Gregorian whose secondary mirror was chosen to induce minimum distortion. As discussed in the previous chapter these three particular conditions, crossed, back-fed and minimal distortion set specific constraints on the tilts of the reflector axes

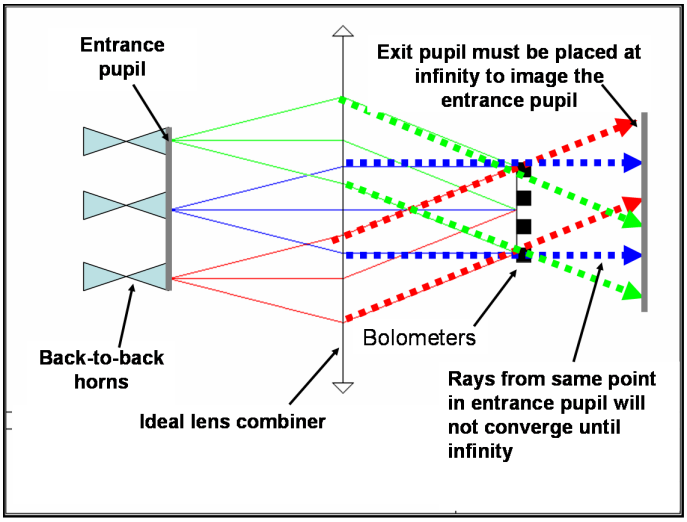

Figure 4.12: An ideal image space telecentric system.

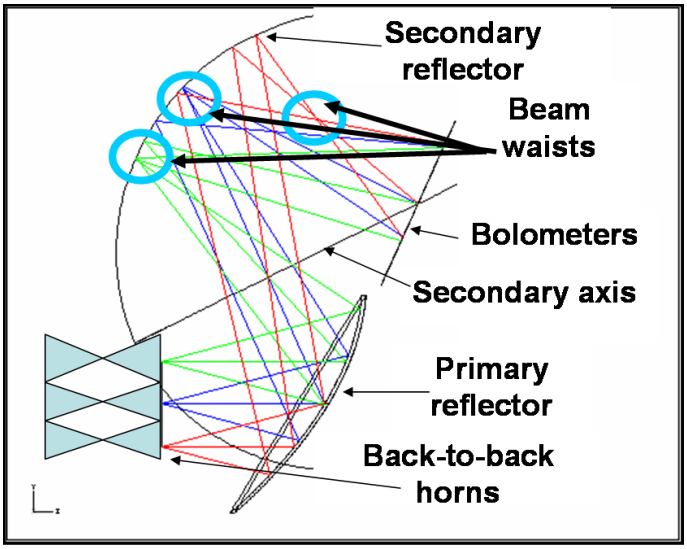

Figure 4.13: The primary focus of a compensated Gregorian prevents it from acting as a telecentric system

and the tilt of the focal plane[11]. This restricts the number of variables we have allowed Zemax to adjust thus preventing the optimizations returning nonsensical systems.

The tilt angles of all systems were kept constant while Zemax was instructed to deform the mirror surfaces in order to force rays that are parallel in object space to intersect

[11] As previously discussed these initial angles can be readily calculated using the aforementioned Rusch and Dragone conditions.

at the focal plane. In all case the angles of tilt were pre-chosen in order to ensure the primary and secondary mirrors as well as the detector plane were all unblocked. Also all rays from a signal point on the object plane were forced to travel parallel at the focal plane (thus forcing image-space telecentricity). The desired heights and angles of the points of intersection of the rays were calculated by hand assuming the geometry of a 300 mm focal length system. For example $\tan^{-1}(\frac{120}{300}) = 21.8^\circ$ gives the angle at which any marginal ray must intersect the focal plane. A Zemax merit function was written that calculated orientations of 16 $\pm 14^\circ$ FOV rays propagating from a 240×240 mm^2 entrance diameter. Upon optimization the surface shapes of the reflectors were adjusted until these orientations converged on the predetermined values. The combiners returned from these optimizations are shown in Figure 4.14. Here the predetermined constant tilts between the reflectors are also listed.

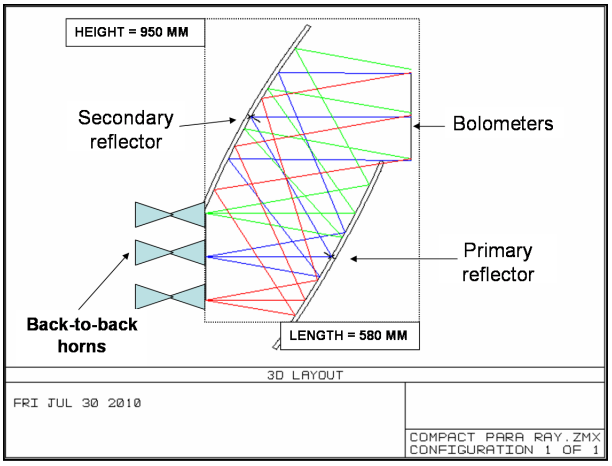

(a) Optimized back-fed optical combiner. The tilt between the reflectors is 30°.

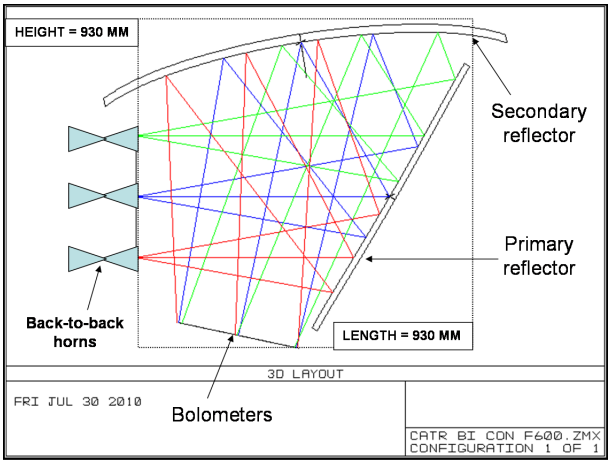

(b) Optimized crossed optical combiner. The tilt between the reflectors is 72°.

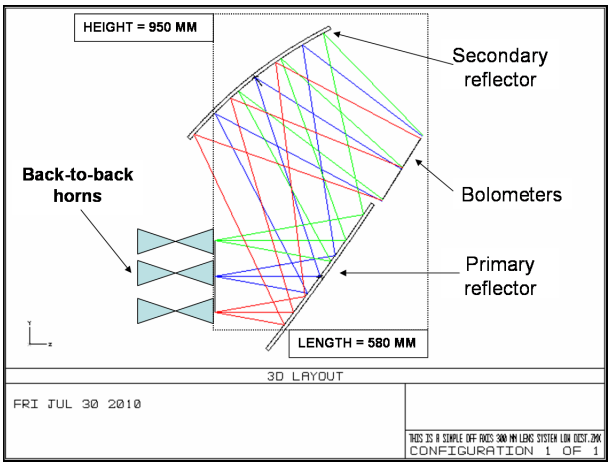

(c) Optimized compensated Gregorian. The tilt between the reflectors is 56°.

Figure 4.14: Optimized optical combiners. Theses systems were constructed by forcing Zemax to alter the surface shapes until the systems become telecentric.

All optimized systems consisted of biconic mirrors deformed into higher order polynomial surfaces. The general formula for such surfaces is

$$z = \frac{c_x^2 + c_y^2}{1 + \sqrt{1 - (1 + k_x)c_x^2 x^2 - (1 + k_y)c_y^2 y^2}} + \sum_{i=1}^{16} \alpha_i x^i + \sum_{i=1}^{16} \beta_i y^i \qquad (4.2.1)$$

for which Zemax was instructed to optimize the curvatures (c_x and c_y) as well as the deformation coefficients (α_i and β_i)[12]. A biconic surface is one which $k_x \neq k_y$. In all three optimizations the minimum size of the focal plane that Zemax could combine the rays in the required manner corresponded to a focal length of 600 mm. The optimized surface geometries were entered into GRASP9 in the form of a regular grid. GRASP9 then used a cubic interpolation technique to calculate a surface shape over which a PO analysis was performed. The fringe patterns of two central 40 mm baselines generated by each optimized combiner is shown in Figure 4.15. Although these fringes are not completely straight we can see that enforcing telecentric in the reflectors does remove the curved profile caused by amplitude distortion (compared with Figure 4.5)[13] .

It is extremely unlikely the general optimizations performed in the above manner will return a suitable system. The role of optimizations in reflector design is to merely "hammer out" the last trinket of performance of a system designed using well set parameters and methods. In general optimizations and surface deformations are the last step in a long design process. However the results of this section are important to the QUBIC combiner. It is desirable that the optical combiner be a telecentric system and our colleagues in APC Paris have indicated that for QUBIC to possess a sensitivity comparable to that of an imager we must observe the sky using a 20 $\times$ 20 horn array. Unfortunately the above Zemax optimizations suggest that it is not possible to implement a 300 mm telecentric system to cater for such a large entrance

[12]This formula is taken from the Zemax manual. For more information on the various surface types available in Zemax visit `http://www.zemax.com/`.

[13]This was only an exploratory study to investigate whether Zemax could directly optimize a low-focal-length-telecentric combiner. As discussed, we discovered that the minimum focal length required by Zemax to force telecentricity on the initial combiners was 600 mm (twice the focal length permitted by the QUBIC design specifications). Therefore the author did not see the necessity to model the two sets of five equivalent baselines used in previous examples.

diameter and 14° FWHM Gaussian beams. Critically these optimizations agree with systems designed by proven methods within the literature.

It was found that a minimum 600 mm effective focal was required in order to design a GCC that could accommodate a 20 × 20 back-to-back horn array. The details of this system are shown in Figure 4.16 while the fringe patterns from equivalent baselines are shown in Figure 4.17. In order to design the system shown Figure 4.16 we set $\zeta = 102°$ and the tilt $\beta = 35°$ and proceeded as before following the methods discussed in [107] and [108].

The fringe patterns generated by the 600 mm effective focal GCC are shown in Figure 4.17. The 600 mm GCC produces better quality fringe patterns then all the above telecentric optimized systems shown in Figure 4.14. This is a testament to the unique geometry of the crossed Cassegrain. This standard regular conic reflector arrangement is a higher performing optical combiner then the systems optimized from more complex surface shapes. At this point we discontinued investigating whether or not brute force Zemax optimization would return a suitable combiner for QUBIC. Although the optimizations successfully eliminated significant beam distortion by enforcing telecentricity it is clear the fringe patterns generated by an equivalent focal length CCG are of a higher quality. However it is apparent that spillover and leakage concerns will also emerge for the 600 mm focal length GCC. Therefore even with an increased focal length a GCC system will struggle to accommodate a 20 × 20 element aperture.

4.2.3 Off-axis parabolas

The main reason for inclusion of a secondary reflector in dual reflector systems is to magnify the focal length of the primary mirror and thus increase the effective focal length of the entire system. A type of reflector we have overlooked up to this point is a simple off-axis parabola. The fact that QUBIC has such a short focal length begs the question as to whether or not a secondary reflector is genuinely required. The geometry of an off-axis paraboloid is less complicated than equivalent off axis systems. The required cryostat size would be significantly smaller.

A draw back of a single reflector is that the lack of the secondary mirror essentially halves the system's capacity to reduce wavefront aberrations. To counteract this we

performed a Zemax optimization on a conventional paraboloid slice to attempt to design a single element off-axis telecentric reflector. These optimization followed the same protocol as before when we attempted to optimize telecentric dual combiners. The single surface was described in Zemax using equation (4.2.1). As it is the minimum angle that would produce an unblocked system the angle of throw of the paraboloid was set to 50° and Zemax was instructed to force the system to become telecentric by adjusting the surface curvatures, conic constants and higher order polynomial coefficients shown in equation (4.2.1).

This optimization returned an elliptical biconic surface (i.e. with different curvatures along both axes). As shown in Figure 4.18 the final system approaches a telecentric design. We entered the geometry of this single surface into GRASP9 in the form of a regular gird. GRASP9 then used a cubic interpolation technique to calculate a surface shape over which a PO analysis was performed. We calculated the fringe patterns generated by this single biconic surface for both the initial baseline structure of Figure 3.5 and the enlarged 20 × 20 array. The results are shown below in Figures 4.19 and 4.22. However as we can clearly see fringe patterns produced by equivalent baselines are very different.

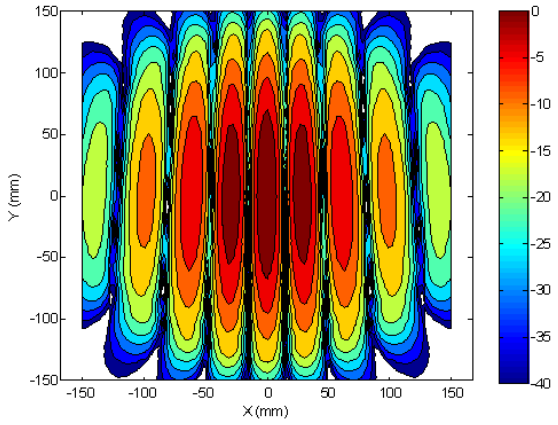

(a) Optimized crossed combiner. Baseline along x-axis of horn array.

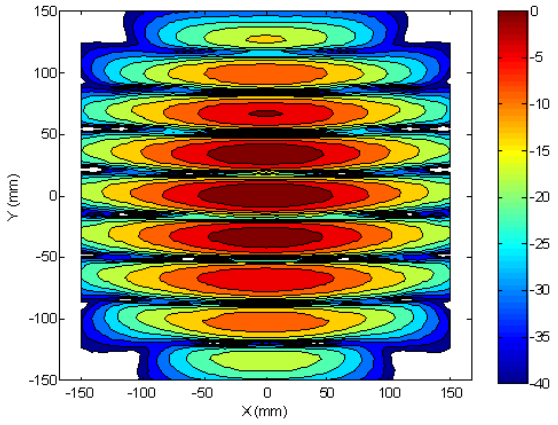

(b) Optimized crossed combiner. Baseline along y-axis of horn array.

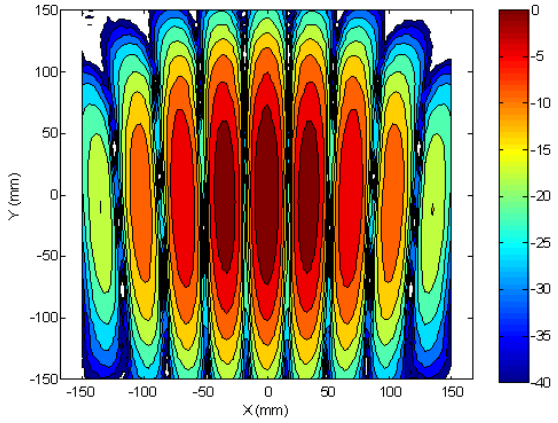

(c) Optimized back-fed combiner. Baseline along x-axis of horn array.

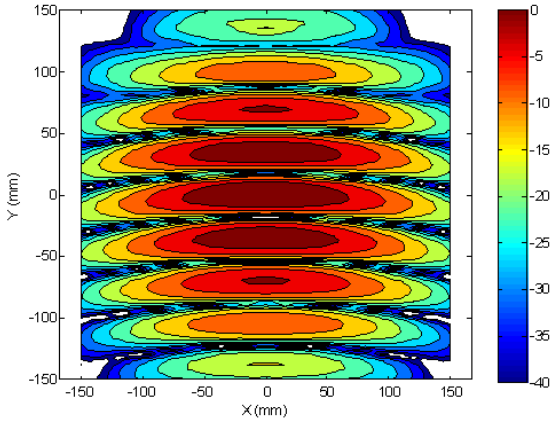

(d) Optimized back-fed combiner. Baseline along y-axis of horn array.

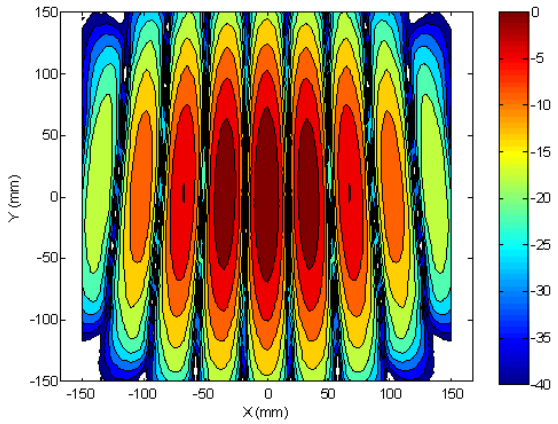

(e) Optimized CG combiner. Baseline along x-axis of horn array.

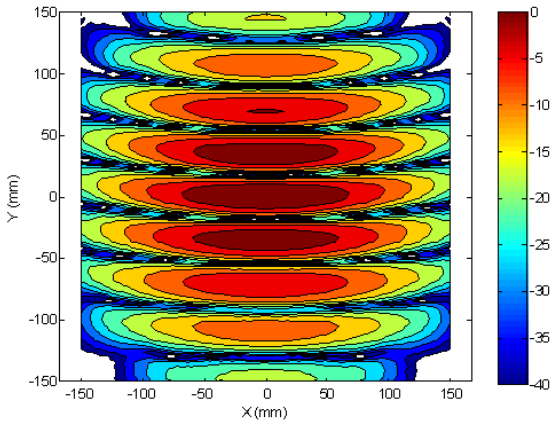

(f) Optimized CG combiner. Baseline along y-axis of horn array.

Figure 4.15: Fringe patterns generated by optimized telecentric systems. These patterns are produced by beams propagating from the 40 mm CEN baseline shown in Figure 3.5. All scales are in decibels.

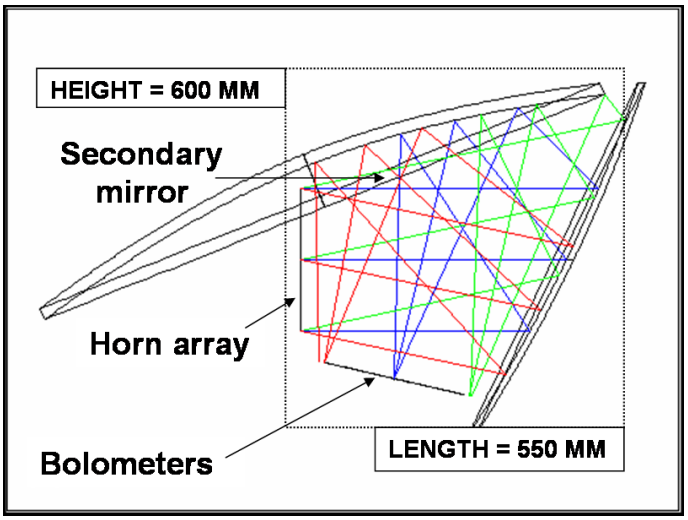

(a) General crossed Cassegrain reflector. The tilt between the reflector axes is 68°. The eccentricity of the secondary ellipsoid is -2.76

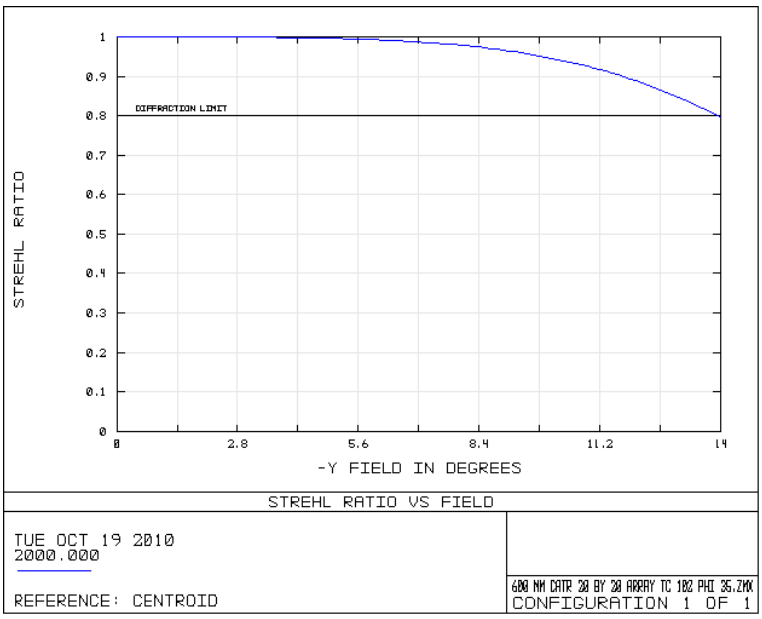

(b) The DLFOV of the 600 mm focal length general crossed Cassegrain is greater than 14° for a 240 mm entrance aperture. This will accommodate a 20 × 20 back-to-back array of horns.

Figure 4.16: A 600 mm focal length General Crossed Cassegrain.

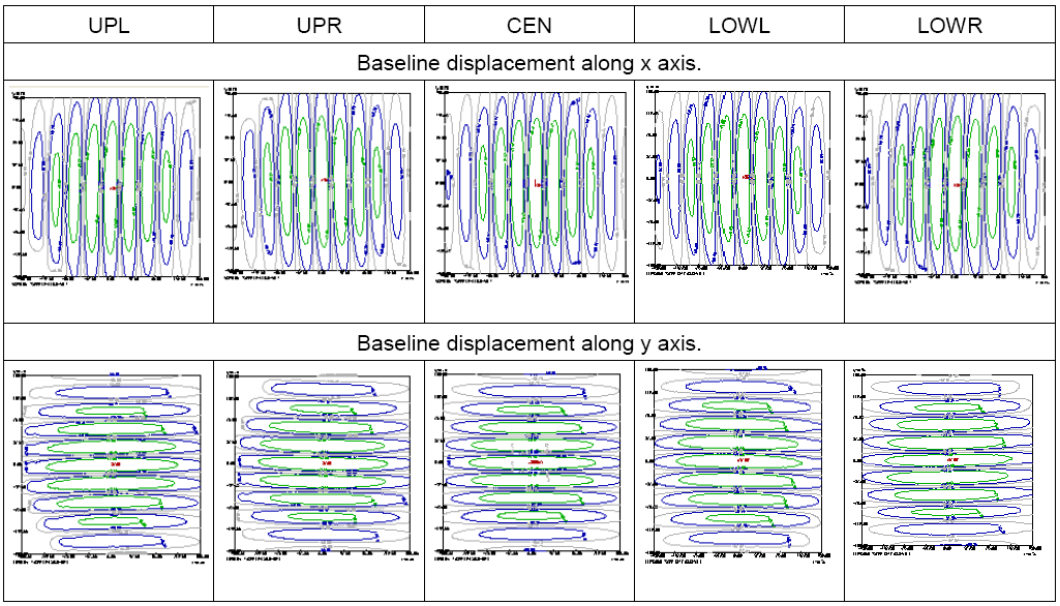

Figure 4.17: Fringes produced by GC designed to accommodate a 20 × 20 horn array.

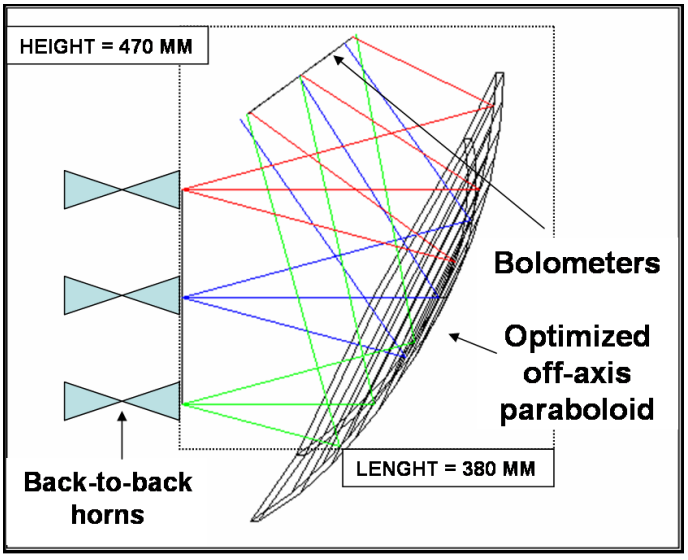

Figure 4.18: Single surface combiner optimized to approach a telecentric system.

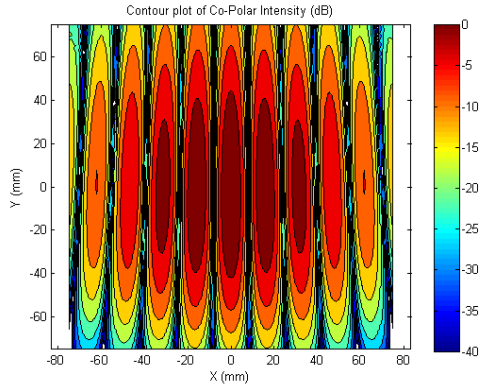

(a) CEN baseline.

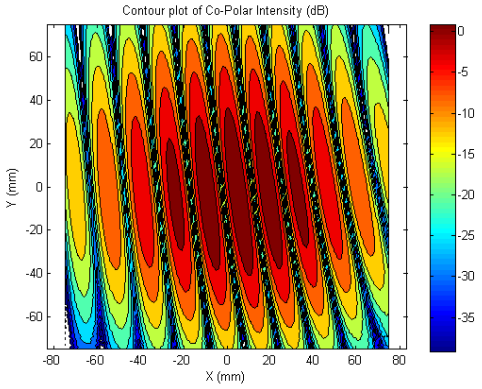

(b) UPL baseline.

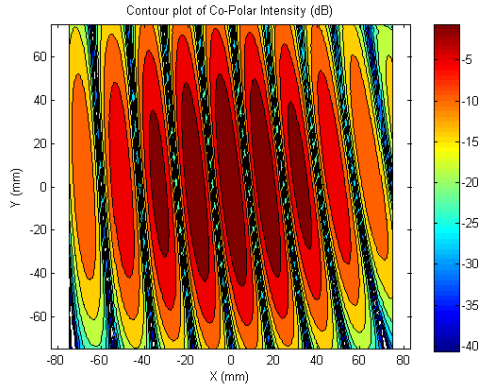

(c) UPR baseline.

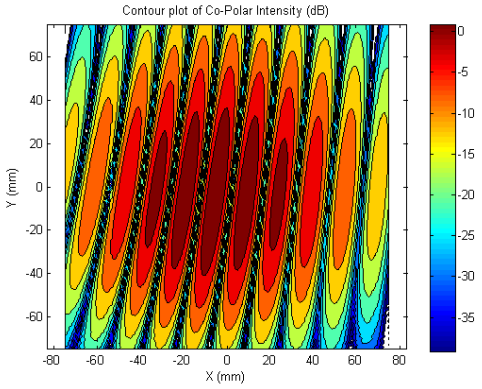

(d) LOWL baseline.

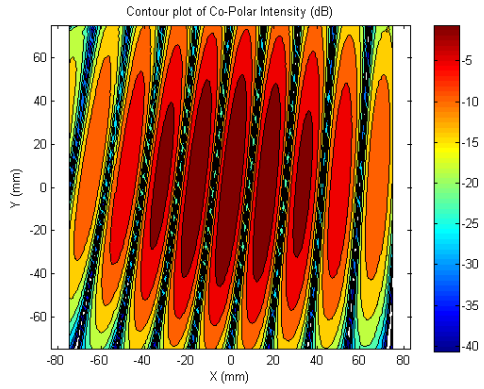

(e) LOWR baseline.

Figure 4.19: Fringe patterns from 5 horizontal equivalent baselines produced by the optimized off-axis paraboloid for QUBIC. Fringes have been formed using 14° FWHM Gaussian beams and the five 40 mm baselines shown in Figure 3.5. The outer horns correspond to those in the 12×12 horn array. All scales are in decibels.

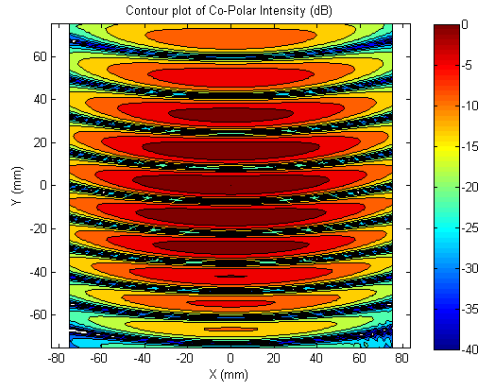

(a) CEN baseline.

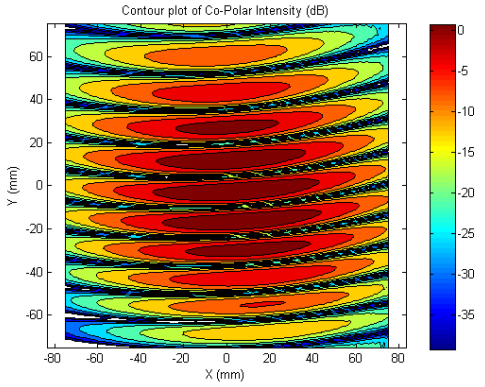

(b) UPL baseline.

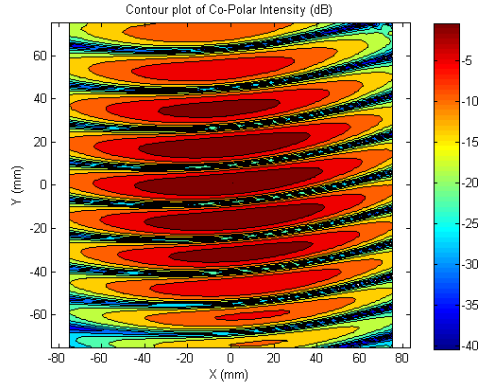

(c) UPR baseline.

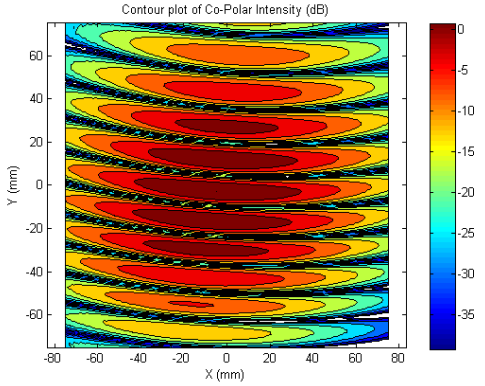

(d) LOWL baseline.

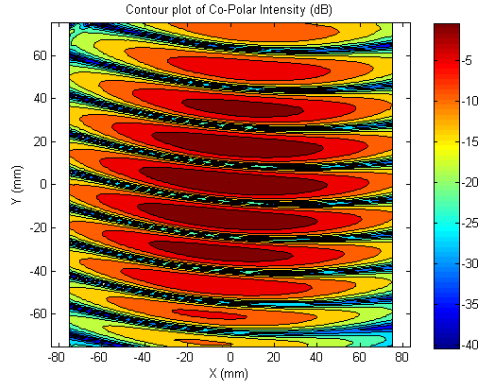

(e) LOWR baseline.

Figure 4.20: Fringe patterns from 5 vertical equivalent baselines produced by the optimized off-axis paraboloid for QUBIC. Fringes have been formed using 14° FWHM Gaussian beams and the five 40 mm baselines shown in Figure 3.5. The outer horns correspond to those in the 12 × 12 horn array. All scales are in decibels.

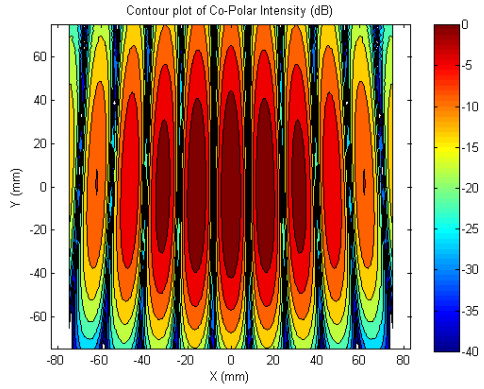

(a) CEN baseline.

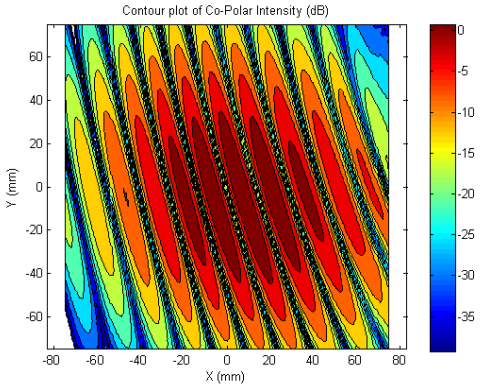

(b) UPL baseline.

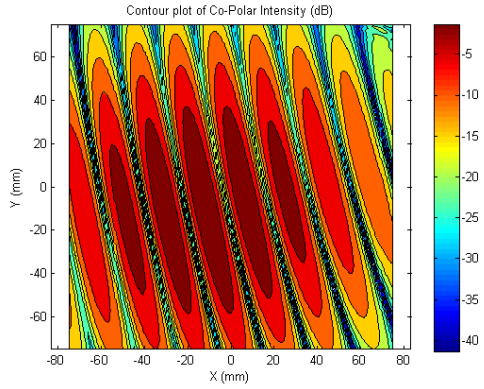

(c) UPR baseline.

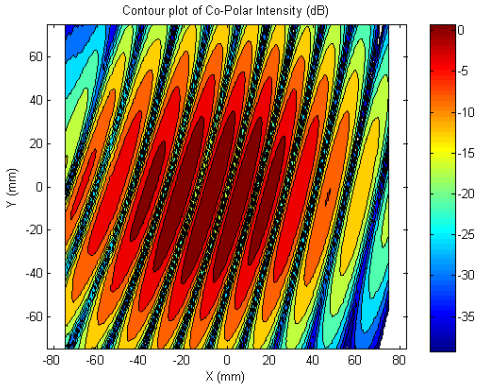

(d) LOWL baseline.

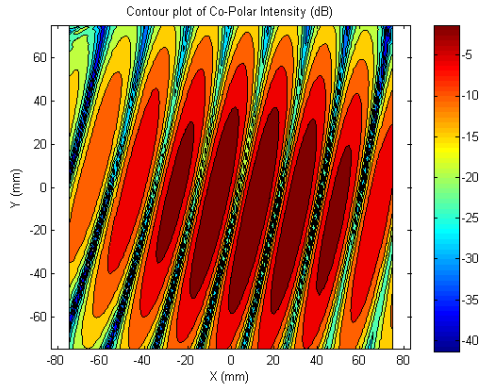

(e) LOWR baseline.

Figure 4.21: Fringe patterns from 5 horizontal equivalent baselines produced by the optimized off-axis paraboloid for QUBIC. Fringes have been formed using 14° FWHM Gaussian beams and the five 40 mm baselines shown in Figure 3.5. The position of the horns in the off-axis baselines have been adjusted to model the outer most beams from a 20×20 horn array. All scales are in decibels.

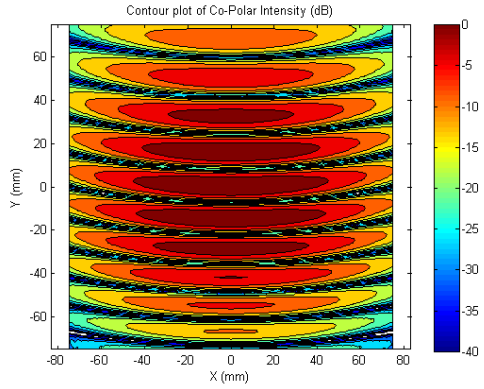

(a) CEN baseline.

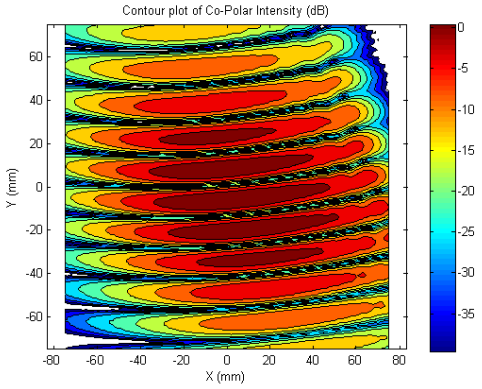

(b) UPL baseline.

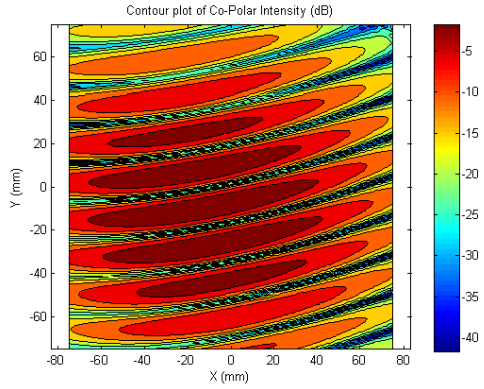

(c) UPR baseline.

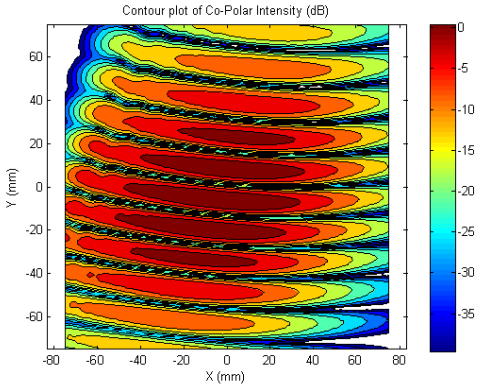

(d) LOWL baseline.

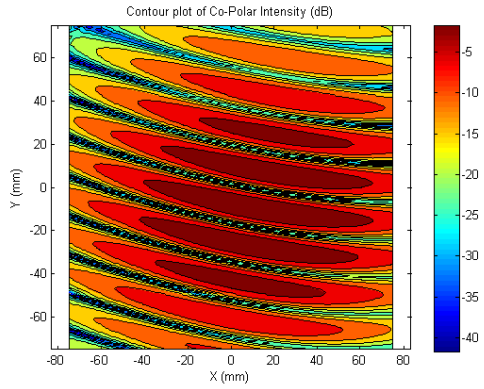

(e) LOWR baseline.

Figure 4.22: Fringe patterns from 5 vertical equivalent baselines produced by the optimized off-axis paraboloid for QUBIC. Fringes have been formed using 14° FWHM Gaussian beams and the five 40 mm baselines shown in Figure 3.5. The position of the horns in the off-axis baselines have been adjusted to model the outer most beams from a 20×20 horn array. All scales are in decibels.

4.2.4 Details of the geometry of the dual reflectors

The details of the geometry of the 300 mm focal length GCC and CG systems are listed in Table 4.3. Also shown is the details of the CG when its size is increased to accommodate a 20×20 array of back-to-back horns. It is apparent that the cost of implementing a 20×20 array of back-to-back horns is that in order to achieve a low edge taper on all beams the size of the mirrors in the CG must be significantly enlarged.

Table 4.3: Geometry details of the 300 mm focal length CG and GCC systems. Also GCC_{20} is the geometry for the 600 mm focal length GCC system. The term **PF** is the primary focal length, k is the secondary conic constant, **ROCS** is the radius of curvature of the secondary mirror, β_T is the tilt between the reflectors, $\mathbf{PD_{12}}$ is the diameter of the primary mirror and $\mathbf{SD_{12}}$ is the diameter of the secondary mirror for a 12×12 array of back-to-back horns. $\mathbf{PD_{20}}$ is the diameter of the primary mirror and $\mathbf{SD_{20}}$ is the diameter of the secondary mirror for a 20×20 array of back-to-back horns. The coefficients α_1, α_2 and α_3 from equation (4.1.1) for the primary mirror of the CG ($\mathbf{PM_{CG}}$), the secondary mirror of the CG ($\mathbf{SM_{CG}}$), the primary mirror of the GCC ($\mathbf{PM_{GCC}}$) and the secondary mirror of the CGG ($\mathbf{SM_{GCC}}$) have also been included.

	PF (mm)	k	**ROCS** (mm)	β_T (Degrees)	$\mathbf{PD_{12}}$ (mm)	$\mathbf{SD_{12}}$ (mm)	$\mathbf{PD_{20}}$ (mm)	$\mathbf{SD_{20}}$ (mm)
CG	164.48	-0.13	348.23	25	440	440		
GCC	553.97	-4.99	692.54	72	300	310		
$\mathbf{GCC_{20}}$	969.89	- 7.59	1459.49	68	260	380	600	60
	α_1	α_2	α_3					
$\mathbf{PM_{GCC}}$	-3.31e-013	2.48e-019	0					
$\mathbf{SM_{GCC}}$	8.06e-014	1.29e-017	0					
$\mathbf{PM_{CG}}$	-1.94e-011	3.17e-016	-1.82e-021					
$\mathbf{SM_{CG}}$	0	0	0					

4.3 Power coupled to the bolometers

Up until this point we have merely been visually analyzing the fringe patterns from various combiners. We will now describe a more quantitative means to asses the applicability of the GCC and the GC to QUBIC. In order to completely quantify which reflector performs better as an optical combiner we have calculated the power coupled over each individual 3 mm bolometer in a 50×50 element array for each baseline shown in Figure 3.5. The coupled power is calculated using the overlap integral of the fringe pattern and the bolometer field pattern [113], [114]. We then compute the standard deviation between the power coupled to a single bolometer for 5 equivalent baselines. This analysis was carried out for fringe patterns generated by baselines distributed over both a 12×12 and 20×20 back-to-back horn array.

The power coupled to each bolometer was calculated as follows. The fringe patterns from an individual baseline was calculated using GRASP9 over a square grid equal to the size of the bolometer detector array. The intensity of the fringes was calculated at the points $(x_{f,i}, y_{f,j})$, given by

$$x_{f,i} = x_{f0} + \Delta x_f (i - 1) \tag{4.3.1}$$

and

$$y_{f,j} = y_{f0} + \Delta y_f (j - 1), \tag{4.3.2}$$

along a square grid. Here i and j run through the values

$$i = 1, 2..., N_x \tag{4.3.3}$$

and

$$j = 1, 2..., N_y \tag{4.3.4}$$

where N_x and N_x are the number of samples taken along the x and y axes. The spacing between each sample point is given by

$$\Delta x_f = (x_{fn} - x_{f0})/(N_x - 1) \tag{4.3.5}$$

and

$$\Delta y_f = (y_{fn} - y_{f0})/(N_y - 1) \tag{4.3.6}$$

where x_{f0} and y_{f0} are the start values of the grid coordinates while x_{fn} and y_{fn} are the end values. These start and end values represent points on the very edge of the detector plane.

In GRASP9 the values x_{f0} and y_{f0} were set to - 75 mm while x_{fn} and y_{fn} equaled 75 mm. The number of points to be sampled was set to $N_x = N_y = 151$. Therefore the fields are calculated at every integer point from -75 mm, -74 mm, -73 mm .... 75 mm along the x and y axes.

In the absence of any detailed information we have approximated the bolometers as single moded square waveguides. More accurate models of the detectors will become available as work on their development progresses. The aim of this work is compare different combiner optics designs when including some level of averaging over typical bolometer sizes. The optimal coupling of a Gaussian beam to a square waveguide occurs when the waist of the Gaussian beam is 0.43 times the length of the square [115]. Therefore we have coupled the fringe patterns to an array of 1.29 mm Gaussian beams with a flat phase front.

The power coupled to each bolometer in a 50×50 grid by a given fringe pattern was calculated by

$$c_{l,m} = \left(\sum_{i}^{4} \sum_{j}^{4} E^*_{f,(1+3(l-1))\,(1+3(m-1))} E_{g,ij} \Delta x \Delta y \right)^2 \tag{4.3.7}$$

where the $c_{l,m}$ is the power coupling coefficient at the bolometer located at position (l,m) on the 50×50 element detector grid. The term E_g represents the Gaussian field

of the bolometer. Essentially E_g is a fundamental Gaussian beam with a 1.29 mm waist radius and a flat phase front. As can be seen from the summation in equation (4.3.7) this Gaussian beam is sampled at 4 points, over 3 1 mm intervals, in both the horizontal and vertical directions. Therefore the power contained in a 3×3 mm^2 patch of a given fringe pattern is coupled to the fundamental Gaussian beam E_g. This allows us the calculate the power coupled to an individual bolometer.

The term E_f is the electric field of the fringe patterns. This value has been calculated from the electric field grid files calculated by GRASP9 and is equal to

$$E_{f,lm} = \sqrt{\mathbf{Re}(E_{f,lm})^2 + \mathbf{Im}(E_{f,lm})^2} \tag{4.3.8}$$

where $\mathbf{Re}(E_{f,lm})$ and $\mathbf{Im}(E_{f,lm})$ the real and imaginary components of the co-polar fringe patterns calculated by GRASP9 respectively. We are momentarily not concerned about the cross polar fringe intensities as at this point we are simply attempting to find a basic analytical method that will rank possible combiners according to QUBIC requirements.

As the final bolometer sizes have not yet been fixed, and may be up to 5×5 mm^2, we also coupled the fringe patterns to an array of 25 mm^2 bolometers. The parameters in the above method were reset accordingly to accommodate a 30×30 array of 25 mm^2 bolometer detectors. The power coupled to the bolometer is calculated using equations (4.3.7) and (4.3.8).

The power coupled to the bolometers by the fringe patterns generated by the GCC combiner for the CEN baseline of Figure 3.5 are shown in Figure 4.23. Similar patterns to these have been generated for all 40 mm baselines shown in Figure 3.5. Each square in the below plots represents a 9 mm^2 or 25 mm^2 squared bolometer. For each square there is a single data value corresponding to the power coupled between the fringe patterns generated by a single baseline and the bolometer. Figure 4.24 also shows the coupled fringe patterns generated by the CG reflector. Unfortunately it is apparent that integrating over the surface of the bolometer detectors does not "average out" the amplitude distortion induced in the fringe patterns by the CG.

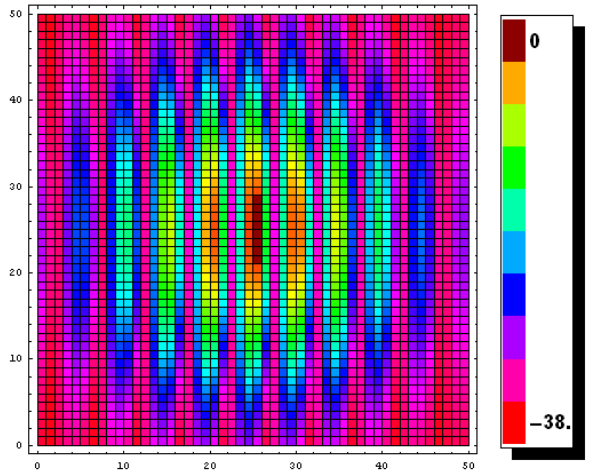

(a) Fringes generated by a horizontal baseline coupled to 9 mm^2 bolometers.

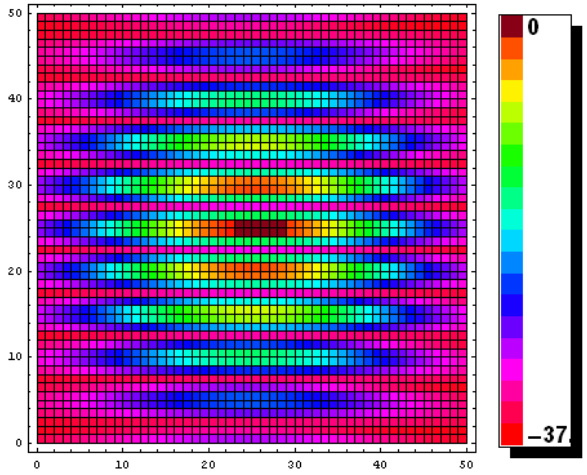

(b) Fringes generated by a vertical baseline coupled to 9 mm^2 bolometers.

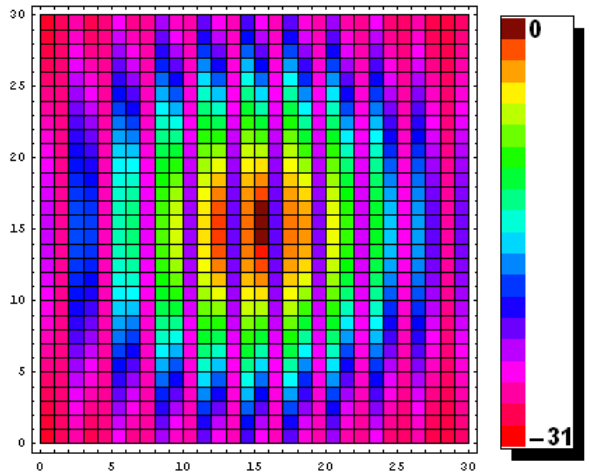

(c) Fringes generated by a horizontal baseline coupled to 25 mm^2 bolometers.

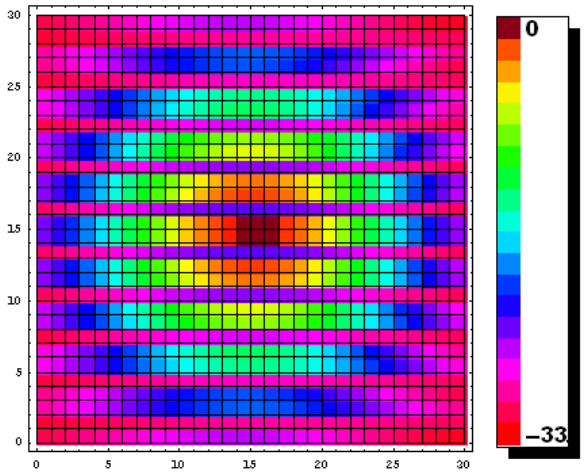

(d) Fringes generated by a vertical baseline coupled to 25 mm^2 bolometers.

Figure 4.23: Power coupled to bolometer detectors by fringe patterns generated using the 300 mm focal length GCC. The patterns shown are generated by the the 40 mm CEN baseline of Figure 3.5. All units are in decibels and normalized to the max power coupled to the pixels.

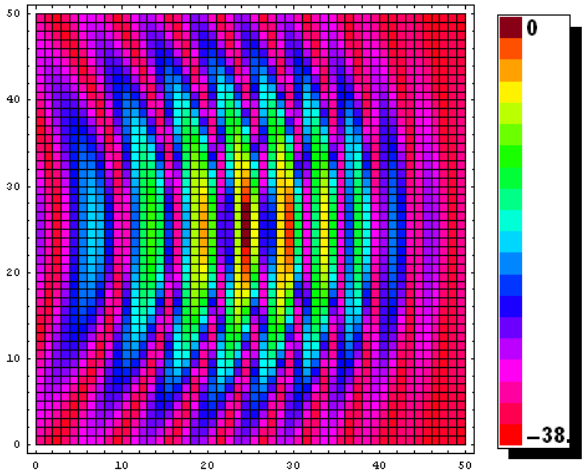

(a) Fringes generated by a horizontal baseline coupled to 9 mm^2 bolometers.

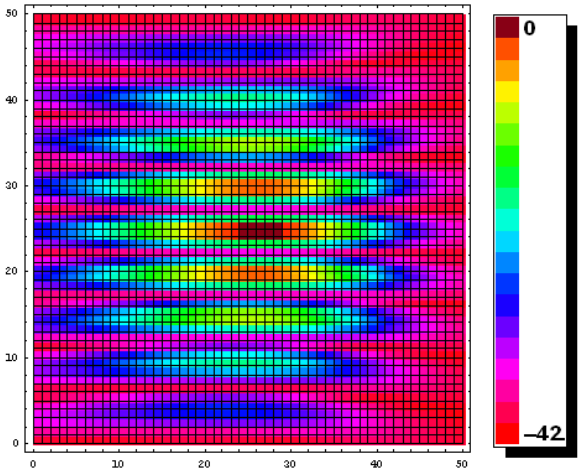

(b) Fringes generated by a vertical baseline coupled to 9 mm^2 bolometers.

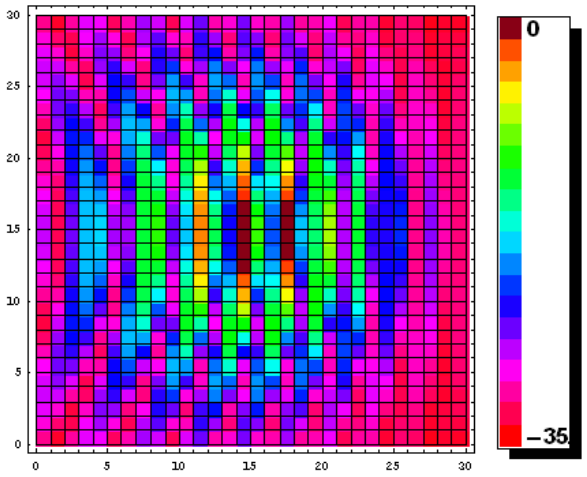

(c) Fringes generated by a horizontal baseline coupled to 25 mm^2 bolometers.

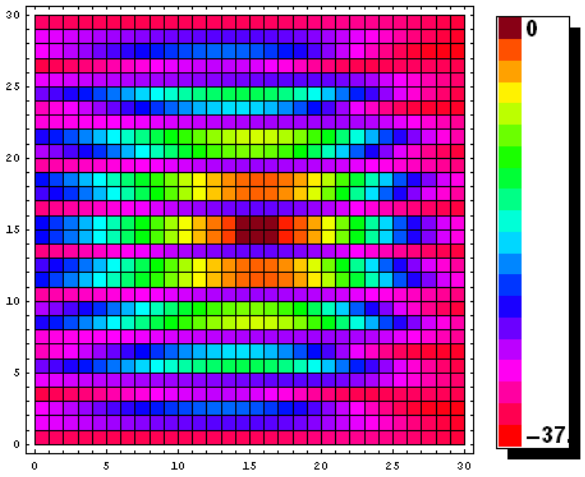

(d) Fringes generated by a vertical baseline coupled to 25 mm^2 bolometers.

Figure 4.24: Power coupled to bolometer detectors by fringe patterns generated using the 300 mm focal length CG. The patterns are displayed over the surface area of a grid of square bolometers. The patterns shown are generated by the the 40 mm CEN baseline of Figure 3.5. All units are in decibels and normalized to the max power coupled to the pixels.

Using equation (4.3.7) we calculated the power coupling coefficients, $c_{l,m}$, for each bolometer (l, m) to the fringe patterns produced by 2 sets of equivalent baselines. We then calculated the standard deviation of the coupling coefficients by

$$c_{\sigma;l,m} = \sigma \left(\frac{c_{bl;l,m}}{\bar{c_{bl;l,m}}} \right). \tag{4.3.9}$$

Here $c_{bl;l,m}$ is an array containing the power coupled to the bolometer (l, m) by all baselines in the set bl of equivalent baselines. Meanwhile the symbol σ indicates that the standard deviation of this array is calculated in the usual manner. As shown the array $c_{bl;l,m}$ is normalized using the mean power coupled to each bolometer from the entire set of equivalent baselines. The values of $c_{bl;l,m}$, generated by the various 300 mm focal length combiners we have designed, are shown in Figures 4.25 -4.29. The deviation of fringe patterns generated by both a 12×12 and a 20×20 array of back-to-back horns is considered. These figures indicate that the variance between fringe patterns generated by equivalent baselines is highest where the signal is low. High standard deviations mean that the fringe patterns generated by equivalent baselines differ significantly (due to aberrations). For QUBIC, as discussed in Chapter 6, this is equivalent to a loss in sensitivity for the instrument.

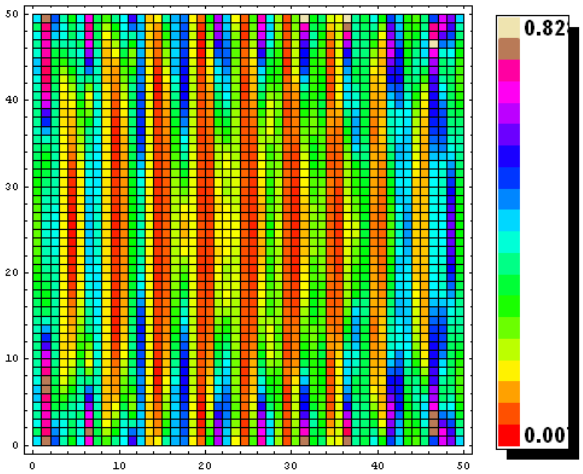

(a) Standard deviation of fringes generated horizontal baselines. The surface area of each bolometer is 3 mm^2.

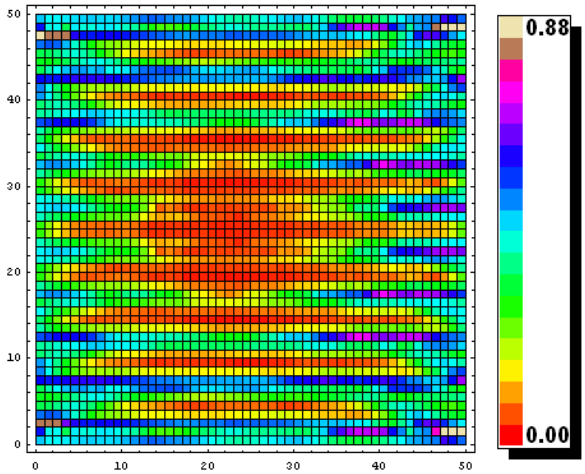

(b) Standard deviation of fringes generated vertical baselines. The surface area of each bolometer is 3 mm^2.

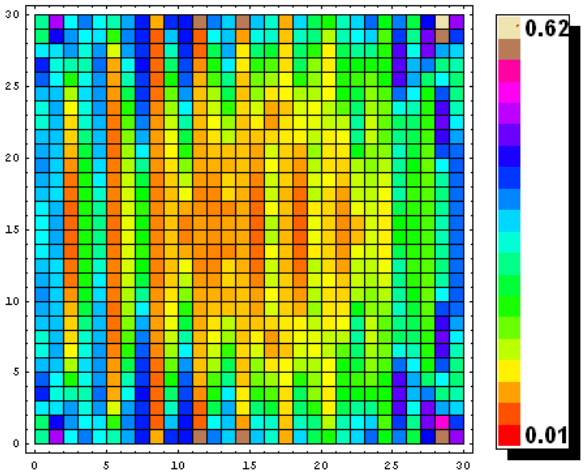

(c) Standard deviation of fringes generated horizontal baselines. The surface area of each bolometer is 5 mm^2.

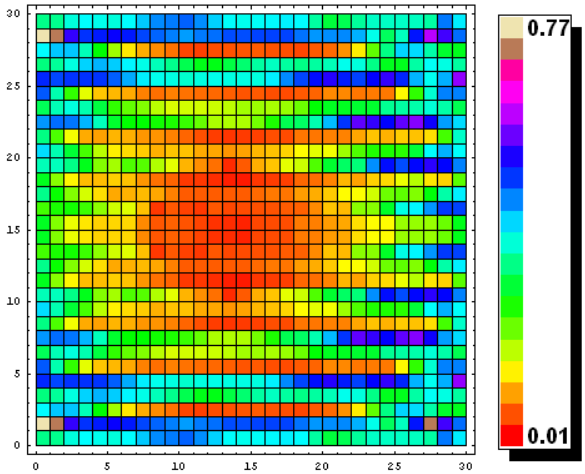

(d) Standard deviation of fringes generated vertical baselines. The surface area of each bolometer is 5 mm^2.

Figure 4.25: Standard deviation of the power coupled to bolometer detectors by the fringe patterns generated by a 300 mm focal length GCC. These values have been calculated from five 40 mm equivalent baselines in both the horizontal and vertical directions along the back-to-back horn array. The baselines are shown in Figure 3.5. The standard deviation is expressed as a ratio of the average power coupled to each bolometer.

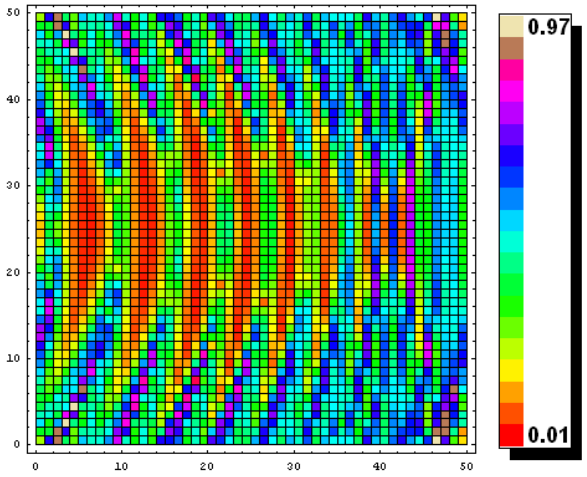

(a) Standard deviation of fringes generated horizontal baselines. The surface area of each bolometer is 3 mm^2.

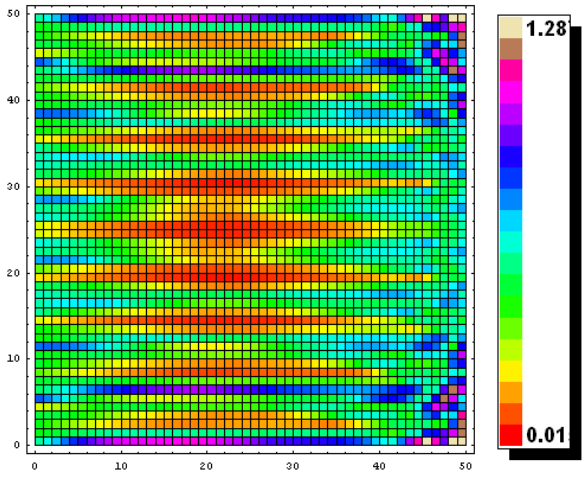

(b) Standard deviation of fringes generated vertical baselines. The surface area of each bolometer is 3 mm^2.

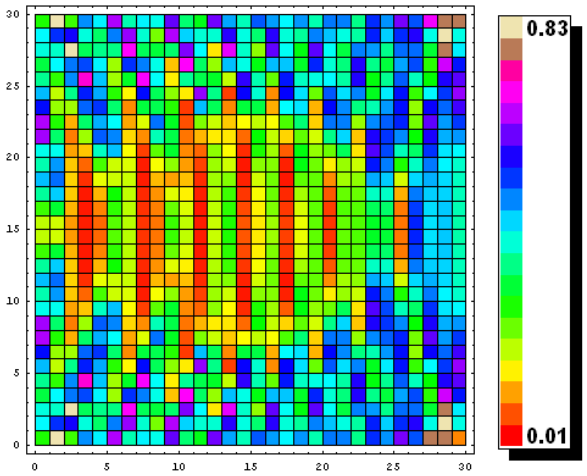

(c) Standard deviation of fringes generated horizontal baselines. The surface area of each bolometer is 5 mm^2.

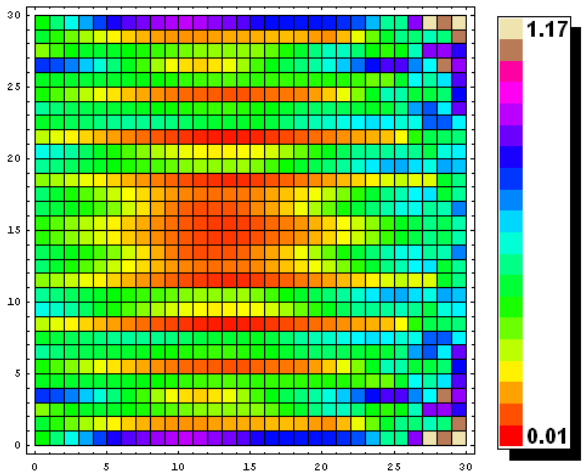

(d) Standard deviation of fringes generated vertical baselines. The surface area of each bolometer is 5 mm^2.

Figure 4.26: Standard deviation of the power coupled to bolometer detectors by the fringe patterns generated by a 300 mm focal length CG. These values have been calculated from five 40 mm equivalent baselines in both the horizontal and vertical directions along the back-to-back horn array. The baselines are shown in Figure 3.5. The standard deviation is expressed as a ratio of the average power coupled to each bolometer.

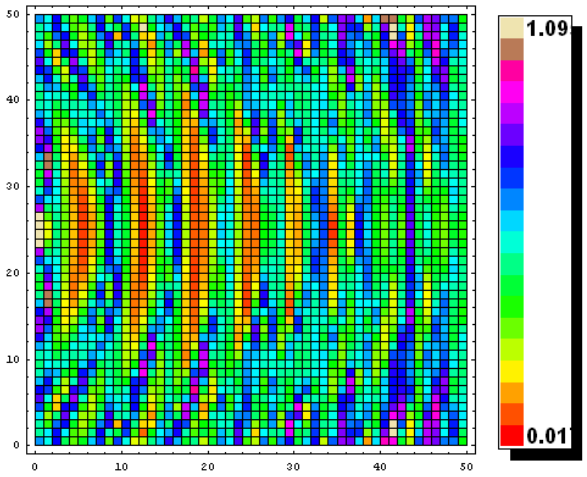

(a) Standard deviation of fringes generated horizontal baselines. The surface area of each bolometer is 3 mm^2.

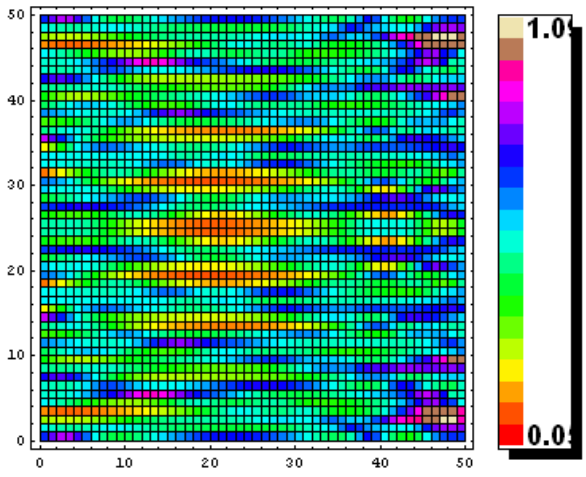

(b) Standard deviation of fringes generated vertical baselines. The surface area of each bolometer is 3 mm^2.

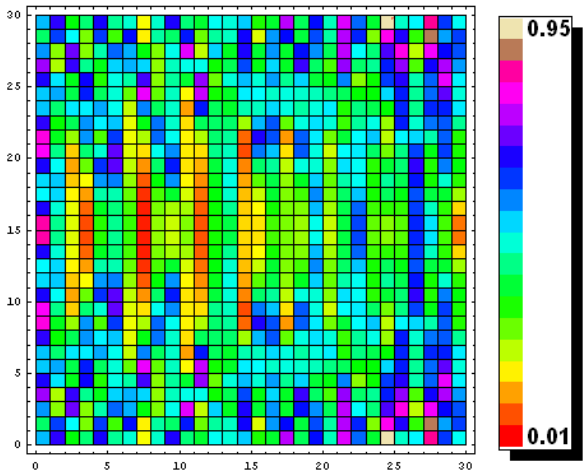

(c) Standard deviation of fringes generated horizontal baselines. The surface area of each bolometer is is 5 mm^2.

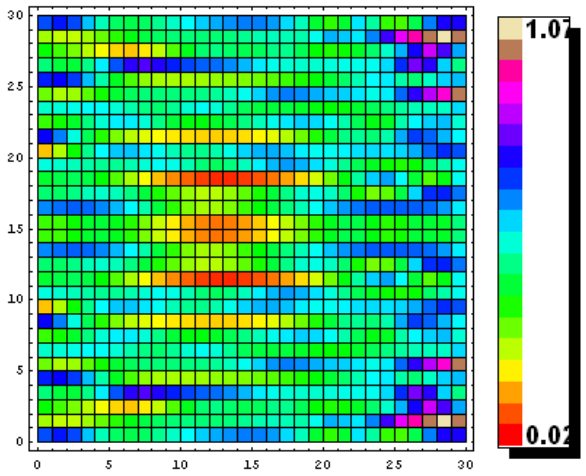

(d) Standard deviation of fringes generated vertical baselines. The surface area of each bolometer is 5 mm^2.

Figure 4.27: Standard deviation of the power coupled to bolometer detectors by the fringe patterns generated by a 300 mm focal length CG. These values have been calculated from five 40 mm equivalent baselines in both the horizontal and vertical directions along the back-to-back horn array. Here the position of the baselines have been extended to replicate beams from a 20 × 20 back-to-back horn array. The baselines are shown in Figure 3.5. The standard deviation is expressed as a ratio of the average power coupled to each bolometer.

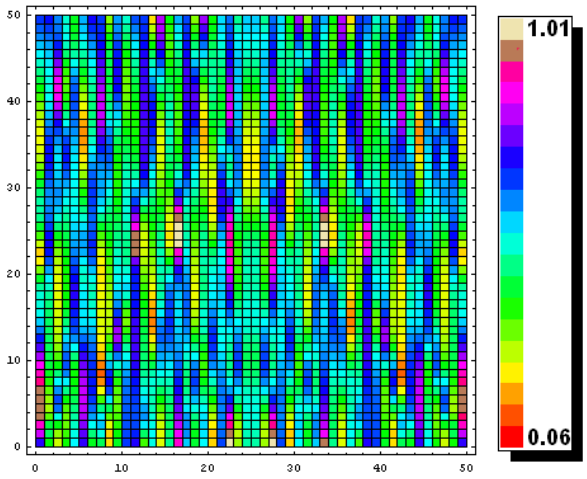

(a) Standard deviation of fringes generated horizontal baselines. The surface area of each bolometer is 3 mm^2.

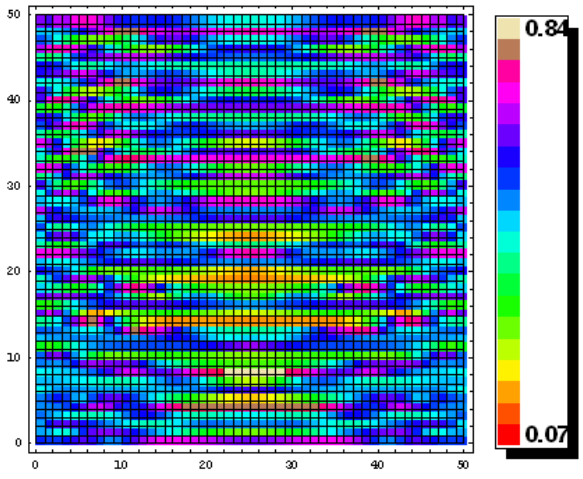

(b) Standard deviation of fringes generated vertical baselines. The surface area of each bolometer is 3 mm^2.

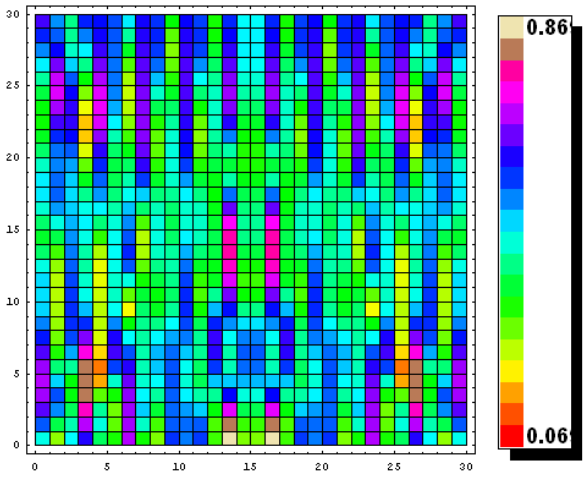

(c) Standard deviation of fringes generated horizontal baselines. The surface area of each bolometer is is 5 mm^2.

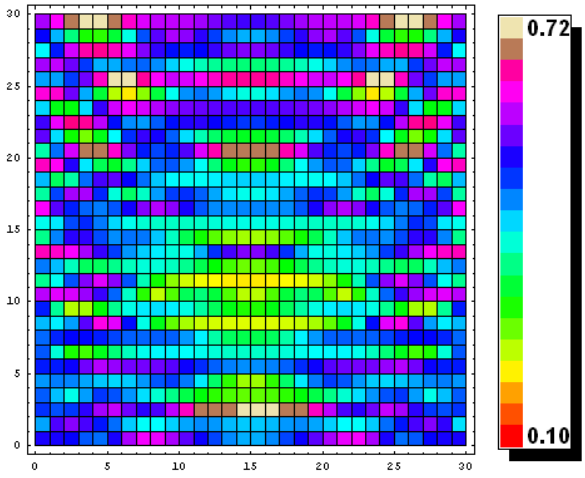

(d) Standard deviation of fringes generated vertical baselines. The surface area of each bolometer is 5 mm^2.

Figure 4.28: Standard deviation of the power coupled to bolometer detectors by the fringe patterns generated by a 300 mm focal length optimized off-axis paraboloid. These values have been calculated from five 40 mm equivalent baselines in both the horizontal and vertical directions along the back-to-back horn array. The baselines are shown in Figure 3.5. The standard deviation is expressed as a ratio of the average power coupled to each bolometer.

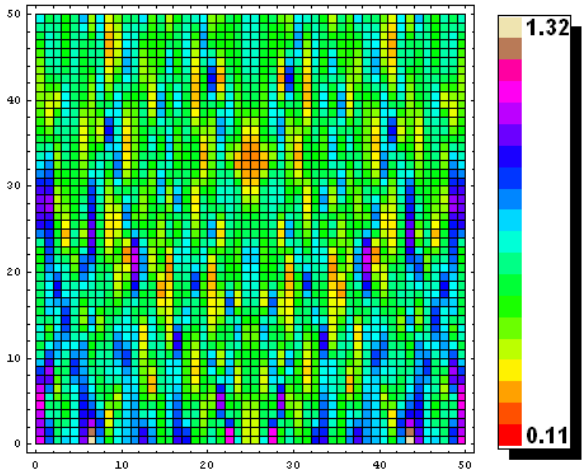

(a) Standard deviation of fringes generated horizontal baselines. The surface area of each bolometer is 3 mm^2.

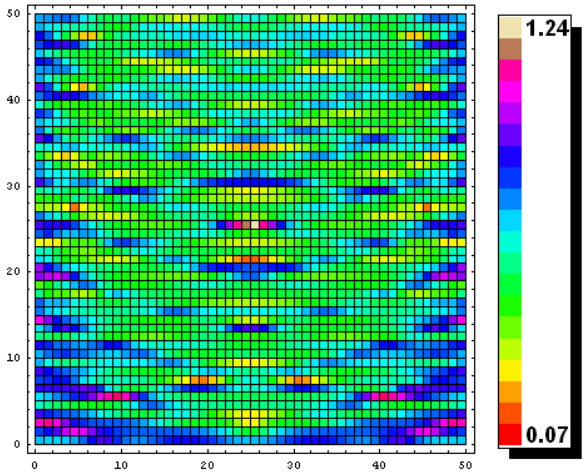

(b) Standard deviation of fringes generated vertical baselines. The surface area of each bolometer is 3 mm^2.

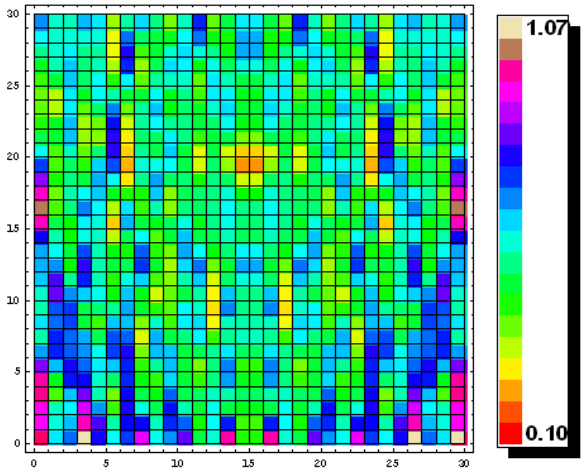

(c) Standard deviation of fringes generated horizontal baselines. The surface area of each bolometer is 5 mm^2.

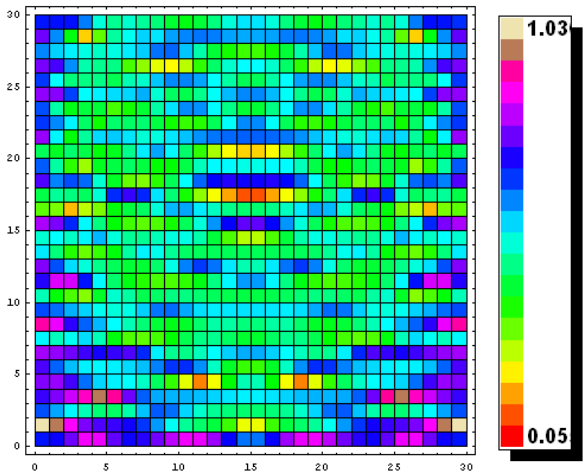

(d) Standard deviation of fringes generated vertical baselines. The surface area of each bolometer is 5 mm^2.

Figure 4.29: Standard deviation of the power coupled to bolometer detectors by the fringe patterns generated by a 300 mm focal length optimized off-axis paraboloid. These values have been calculated from five 40 mm equivalent baselines in both the horizontal and vertical directions along the back-to-back horn array. Here the position of the baselines have been extended to replicate beams from a 20×20 back-to-back horn array. The baselines are shown in Figure 3.5. The standard deviation is expressed as a ratio of the average power coupled to each bolometer.

The initial performance specification placed on the optical combiner is that it must produce fringe patterns from equivalent baselines whose amplitude and phase profiles differ by less than 1%. This means we require the average value of the array $c_{\sigma;l,m}$ to be less than 0.01[14]. We calculated the average standard deviation of the power coupled to all bolometers using equation (4.3.10). Here N_b is the number of bolometers.

$$\overline{\Delta_c} = \frac{1}{N_b} \sum_{l,m}^{N_b} c_{\sigma;l,m}. \tag{4.3.10}$$

Once again for QUBIC we require $\overline{\Delta_c}$ to be less than 0.01. The values of $\overline{\Delta_c}$ for the various optical combiners we have designed are presented in Tables 4.4 and 4.5[15].

Table 4.4: Mean standard deviation of power coupled to 9 mm^2 bolometers for a 12×12 back-to-back horn array.

Reflector system	Horizontal baselines $\overline{\Delta_c}$	Vertical baselines $\overline{\Delta_c}$
GCC	0.25	0.28
CG	0.37	0.42
OP	0.48	0.47

Table 4.5: Mean standard deviation of power coupled to 25 mm^2 bolometers for a 12×12 back-to-back horn array.

Reflector system	Horizontal baselines	Vertical baselines
GCC	0.20	0.24
CG	0.32	0.37
OP	0.43	0.42

As we can see none of the above combiners perform as well as required for QUBIC. The above results led to a rethinking of the operation and the requirements of QUBIC. For instance it has been suggested that the requirement that the fringe patterns from

[14]Here we have converted a percentage to a ratio

[15]The term OP in indicates we have performed these calculations on the optimized off-axis paraboloid discussed in the preceding section.

Table 4.6: Mean standard deviation of power coupled to 9 mm^2 bolometers for a 20×20 back-to-back horn array.

Reflector system	Horizontal baselines	Vertical baselines
CG	0.45	0.49
OP	0.52	0.54

Table 4.7: Mean standard deviation of power coupled to 25 mm^2 bolometers for a 20×20 back-to-back horn array.

Reflector system	Horizontal baselines	Vertical baselines
CG	0.41	0.45
OP	0.48	0.50

equivalent baselines differ by less than 1% is simply too stringent a condition to force upon the optical combiner. Such a condition may not be necessary to achieve the science goals of QUBIC. This will be discussed in Chapter 6. It should also be noted that the values in Tables 4.4 - 4.7 are skewed because the bolometers which experience the highest variance of power from the various fringes, are also the bolometers that observe the lowest amount of coupled power.

As explained the GCC has been used in many state-of-the-art telescopes due to the quality of images it produces. Also the fact that such a system is near telecentric means that it will produce the most undistorted fringe patterns of all standard dual reflectors. The fact that such a system cannot perform at the standard initially thought to be required by QUBIC has led to a re-examination of the QUBIC parameters and requirements[16,17].

[16]This is of course assuming we require a small equivalent focal length. Increasing the focal length will significantly reduce the standard deviations listed in Tables 4.4 - 4.7

[17]As we shall discuss in the next chapter it was not only the difficulties experienced by the optical combiner work group that led to a re-examination of the QUBIC parameters.

4.4 Leakage concerns in a general crossed Cassegrain (GCC).

Finally we must briefly mention that we considered the possibility of leakage of power from the horn array directly onto the bolometer detectors in the GCC. This is a consequence of the compactness of the system which requires the horn array to be practically adjacent to the detector plane. We have used GRASP9 to calculate the effects of such leakage on the fringe patterns from the familiar baselines shown in Figure 3.5. The results of accounting for power leakage are shown in Figure 4.30. Here we have expressed the results as a one dimensional cut through the centre of the detector plane. These plots also account for spillover from the primary mirror onto the detector plane.

These plots were calculated as by GRASP9 as follows. The electric field from a fundamental Gaussian beam propagating from a point on the back-to-back horn array directly to the detector plane was calculated. We call this field E_s. GRASP9 then calculated the electric field incident on the detector array that was produced by the primary surface currents induced by the propagating beams. We call this field E_p. The resultant electric field at the focal plane is calculated by $E_l = E_f + E_p + E_s$ where E_f is the "ideal" field calculate by propagating a fundamental Gaussian beam through the system using physical optics as discussed in Chapter 2. The two extra fields take account of the fields that propagate from the horn array to the focal plane directly and the fields that reach the bolometer array after striking the primary mirror only.

In our GCC the LOWL and LOWR baselines are closer to the detector plane then the UPL and UPR baselines of Figure 3.5. It is clear that the fringes generated by 40 mm baselines whose horns are furthest from the focal plane are relatively unaffected. However the fringes generated by the baselines closest to the detector plane have become slightly obscured. These figures combined with the power loss due to spillover at the primary and secondary mirror (Table 4.1) fully demonstrate the drawbacks of implementing the crossed Cassegrain. However as we can see the effects of power leakage from the horn array and the primary mirror on the final fringes patterns are not entirely detrimental.

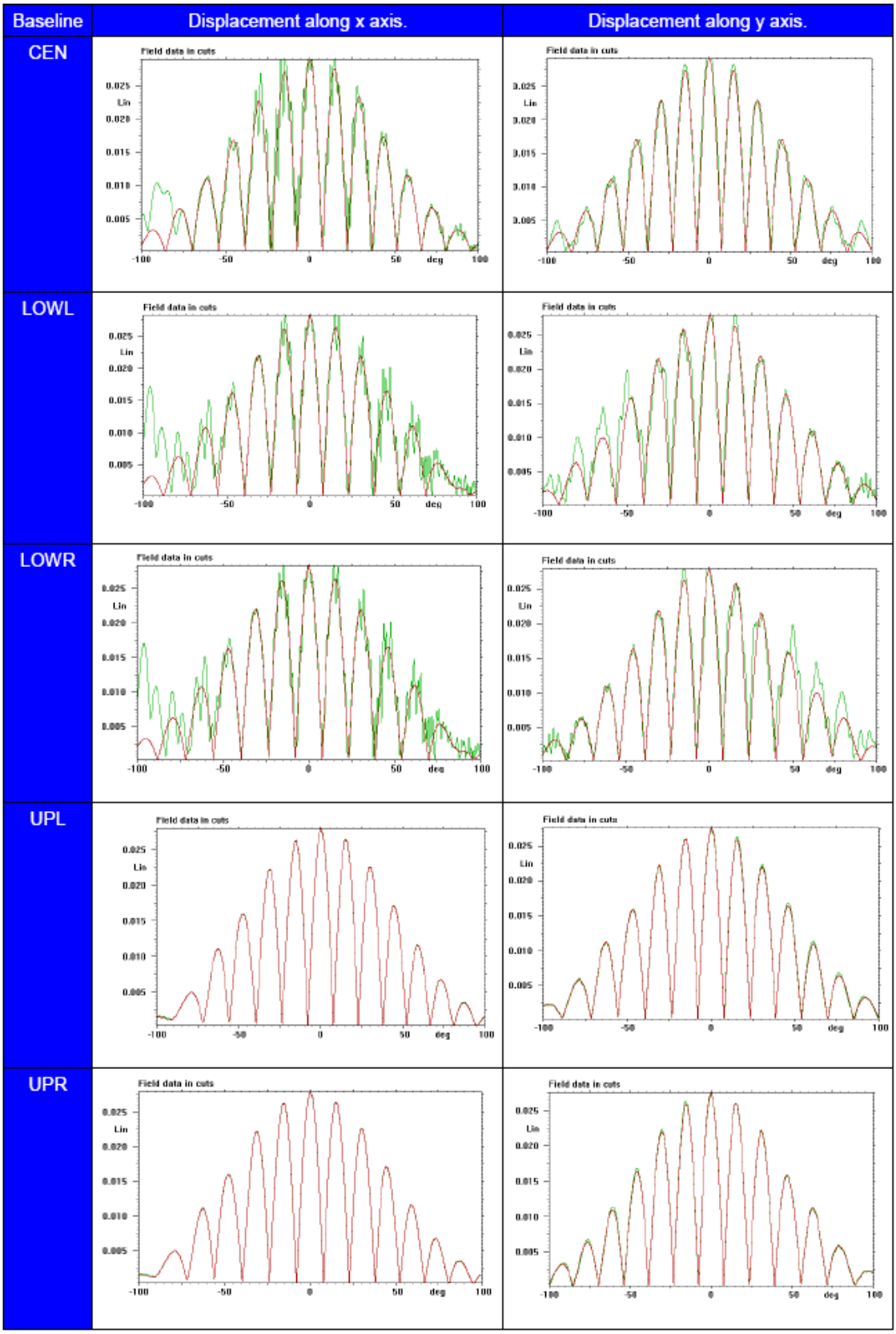

Figure 4.30: Effect of spillover on fringe patterns generated by the crossed Cassegrain. The green lines represent the fringe patterns generated when radiation arriving directly from the horns or primary mirror is included. In comparison the brown line shows an "ideal" fringe pattern.

4.5 Conclusions

As we have seen in this chapter the benefits of the unique geometry of the GCC is that it results in a diffraction limited yet highly compact combiner. However these benefits emerge at the expense of a slight loss of power from the most extreme horns (due to the size limitations of the reflectors) and also at the expense of a slight deterioration of the quality of the fringe patterns due to a leakage of power from the back-to-back array onto the detector plane. This geometry cannot be extended to the small focal lengths of QUBIC.

We have shown that a 300 mm focal length CG can be designed with mirrors large enough to capture and combine the power of all beams propagating from a 20 $\times$ 20 back-to-back horn array. However this system is not powerful enough to combine beams from a 20 $\times$ 20 horn array while inducing only minute wavefront aberrations QUBIC was said to require. We have also shown that while Zemax optimizations can find suitable telecentric reflector combinations, the minimum focal length of these systems was 600 mm which, due to the limited number of detectors we can employ, is too large for QUBIC.

We have shown that the GCC reflector is the only system whose performance is on par with an ideal telecentric combiner desirable for bolometric interferometry. Unfortunately such a device is unsuitable for QUBIC due to the large array of back-to-back horns required for optimal sensitivity. Due to geometrical restrictions on the size of the mirrors the GCC can not be implemented at the low focal lengths required to maintain a small number of bolometers while capturing the beams from all horns in a 20 $\times$ 20 element array.

The results of the analysis of the various optical combiners presented in this chapter as well as the results from other working groups led to reconsideration of the QUBIC mission. As we shall discuss in Chapter 6 many of the original performance criteria have been abandoned and a better understanding of the operation of the instrument has led to performance specifications that can in fact just be achieved by the 300 mm focal length CG. In Chapter 6 we will present the details of the "QUBIC2.0" mission and the optical combiners that have been suggested for implementation.

5 Lens Design

In Chapters 3-4 we concluded that if it were possible the optimal dual reflector to implement in QUBIC is the CATR. There were two reasons for this conclusion. The first is that as well as producing low wavefront aberrations such a reflector approximates a telecentric optical system and therefore minimizes beam distortion in the final fringe patterns. The second is that due to the compact size of the reflector system and its crossed nature cryostat construction is relatively uncomplicated. However, as we have seen, the small focal lengths at which QUBIC must operate, combined which a moderate to large number of back-to-back horns, limits the applicability of such a design. In Chapter 4 we demonstrated that a variation of the CATR we called a GCC could be used to combine beams from a 12×12 array of back-to-back horns. However as we explained such a system cannot accommodate a larger 20×20 array. In this chapter we present the results of an investigation into whether the use of lenses will allow the beam combiner to meet QUBIC's design and performance specifications.

5.1 Gaussian beam telescope and CATR combination

We have investigated the possibility of using a device called a Gaussian beam telescope (GBT) to decrease the size of the beams propagating from the back-to-back array. This means that a large focal length reflector system can be employed while a small detector plane is maintained. A Gaussian beam telescope is a refracting device consisting of two lenses separated by the sum of their focal lengths [116]. If the beam waist of an input Gaussian w_{in} is placed at the front focal point the size of the output beam at the back focal length w_{out} can be calculated by

$$w_{out} = \frac{f_2}{f_1} w_{in} \tag{5.1.1}$$

where f_1 is the focal length of the front lens and f_2 is the focal length of the back lens. If $f_2 > f_1$ the waist radius of the output beam will be increased. Recalling that $\theta_{FWHM} = \frac{\lambda}{1.18\pi w_0}$ where θ_{FWHM} is the FWHM size of the beam and w_0 is the waist radius we see that increasing the waist of the output beam will reduce the beams FWHM divergence angle [116].

For QUBIC we can place the back-to-back horn array at the front focal point of the GBT. The back-to-back array then becomes an object whose image appears at the back focal point of the GBT. If $f_2 > f_1$ then $w_{out} > w_{in}$ and the beams in the image plane appear larger than the beams at the object plane. For QUBIC this means that placing a Gaussian beam telescope in QUBIC after the back-to-back array will essentially magnify the size of the array but crucially will reduce the FWHM of the beams.

The reduction of the FWHM of the beams propagating into the combiner allows us to implement a larger focal length then previously allowed while maintaining a small size detector array. A unique aspect of the GBT is that equation (5.1.1) is wavelength independent. Thus the bandwidth requirements of QUBIC2.0 can be accommodated.

The increased focal length allows us to implement a CATR reflector such as those shown in Figure 5.1. The size of the detector plane in both these systems is 150×150 mm^2. This is equivalent to the size of the focal plane required for the 300 mm focal length GCC discussed in Chapter 4. In these systems we will first consider a 12×12 horn array whose size is 120×120 mm^2.

In each of the systems shown in Figure 5.1 we have set the focal length of the first lens to 300 mm. In comparison to the size of the horn array this means the focal ratio of the first lens is ~ 1.5. At lower focal ratio's it becomes extremely difficult to design any lens system that can effectively focus 14° beams [117]. Therefore 300 mm is the minimum value that f_1 can possess in any GBT implemented in QUBIC.

The focal length of the second lens f_2 is decided by the factor by which we increase the equivalent focal length of the dual reflector from the original 300 mm value set

for QUBIC. For example in Figure 5.1(a) the equivalent focal length of the CATR has been increased by a factor of three to 900 mm. The size of the Gaussian beam waist radii produced by the GBT must therefore also be increased by the same factor in order to keep the size of the detector plane constant. We see from equation (5.1.1) that the focal length of the second lens must equal 900 mm.

The same reasoning applies to Figure 5.1(b). Here we have increased the equivalent focal length of the dual reflector by a factor of 4 to 1200 mm. Therefore in order to keep the size of the focal plane fixed to that of a 300 mm focal length system we must decrease the beam FWHM sizes by a factor of 4. In order to decrease the FWHM sizes of the beams propagating into the combiner we must increase their waist radii. Therefore $w_{out} = 4 \times w_{in}$ where w_{in} is of course the size of the original beam. From equation 5.1.1 we have that $f_2 = 4f_1$ where we have previously set $f_1 = 300$ mm. Therefore the focal length of the second lens must equal 1200 mm.

Such an approach allows implementation of a telecentric CATR reflector and should reduce leakage from the horn array onto the detector plane. However we have found a GBT is unsuitable for implementation with a 20×20 horn array. Despite the reduction of the field-of-view the magnification of such a large object plane by the GBT generates a secondary image too large to refocus onto the small detector plane. In the authors judgment the largest array that could be implemented with a GBT is a 12×12 array.

We must also address the fact that the above examples have consisted of paraxial lenses. These are ideal lenses with no thickness in which every parallel ray in object space is brought to a signal point in the image space. A combiner with thick lenses is shown in Figure 5.2. This system has been optimized from an original system consisting of equi-convex 300 mm and 900 mm focal length lenses combined with a 900 mm focal length CATR[1].

[1]This system was optimized using the Zemax default merit function. We have previously explained how such an optimization functions. In all examples in this section the lenses are constructed from HDPE whose refractive index is 1.52.

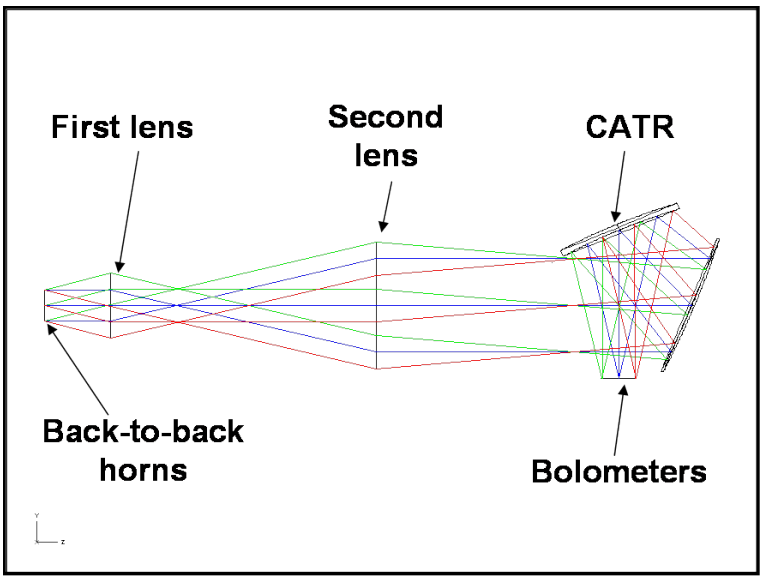

(a) The focal length of the dual reflector is 900 mm. The front lens focal length is 300 mm while the back lens focal length is 900 mm. The overall length of this combiner is over 2170 mm.

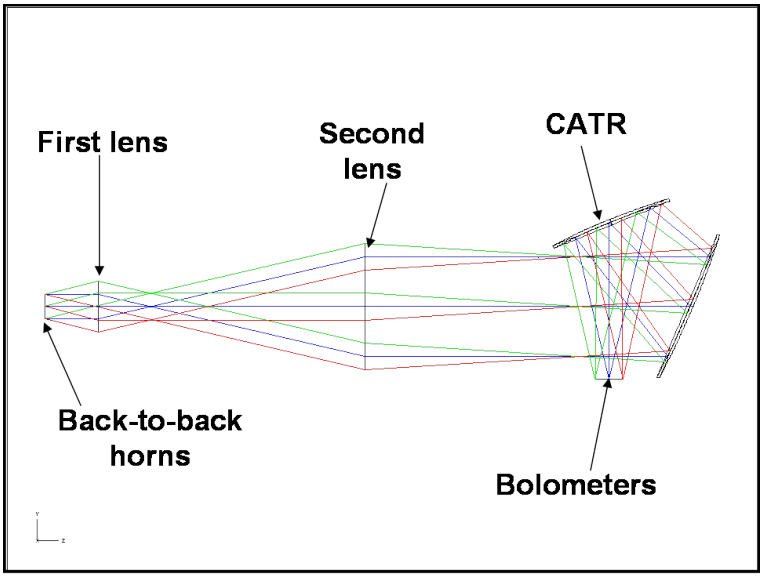

(b) The focal length of the dual reflector is 1200 mm. The front lens focal length is 300 mm while the back lens focal length is 1200 mm. The overall length of this combiner is over 2360 mm.

Figure 5.1: Gaussian beam telescopes in combination with a CATR reflector.

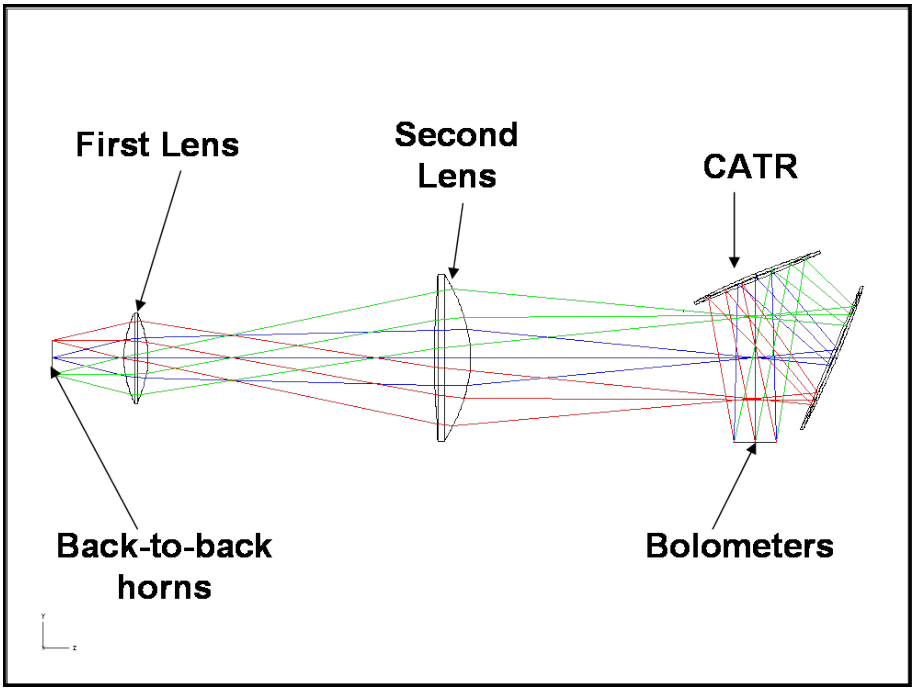

Figure 5.2: Optimized Gaussian beam telescopes in combination with a CATR reflector. The focal length of the dual reflector is 900 mm. The front lens focal length is $\sim$ 388 mm while the back lens focal length is $\sim$ 963 mm. The overall length of this combiner is over 2920 mm.

5.1.1 Using Zemax to model the fringe patterns generated by a Gaussian beam telescope and CATR combiner

Zemax provides some basic analysis techniques to model the propagation of a Gaussian field through lenses. These methods are based on Fourier scalar optics in which Fourier transforms are used to propagate the electric field from one surface to another. Essentially Zemax treats all surface as phase transforming devices and rather than compute the refracted electric field scattering through the lens the curvature of each surface is used to manipulate the shape of the field's wavefront.

We have used Zemax to preform a Fourier optical analysis of the combiner shown Figure 5.2. As we have explained in Chapter 2 Zemax uses paraxial scalar optics to model the propagation of electric fields through dielectric material. The fringe patterns produced by the above optimized system are shown in Figure 5.3. These fringes have been generated by 40 mm baselines orientated along the system's x and y-axes

(assuming that the z-axis is reserved to represent the direction of beam propagation). Unfortunately the inclusion of thick lenses increases the size of the the detector plane from 150 mm to 180 mm. This increases the number of 5 mm bolometer detectors from 900 to 1296. Zemax optimizations were unable to reduce the size of the detector plane. Also of concern is that the optimizations were unable to significantly reduce the length of the entire system.

The fact that the refractors within a GBT must be separated by the sum of their focal lengths leads to exceedingly long systems. The magnitude of this separation is problematic whether we implement a folded reflecting or refracting GBT. The length of the combiner in Figure 5.2 is over 3.2 m and although no restrictions have been placed on the length of the cryostat such large systems are simply not cost effective for cooling. We also note that in order to provide a sufficient number of variables to enable the Zemax to generate effective images the conic constants of the lenses were allowed to vary. Each optimized refractor contains hyperbolic surfaces of various eccentricities. Such lenses are more difficult to machine then spherical or parabolic surfaces. As we will show below this can be avoided by such methods as splitting a single lens into multiple elements.

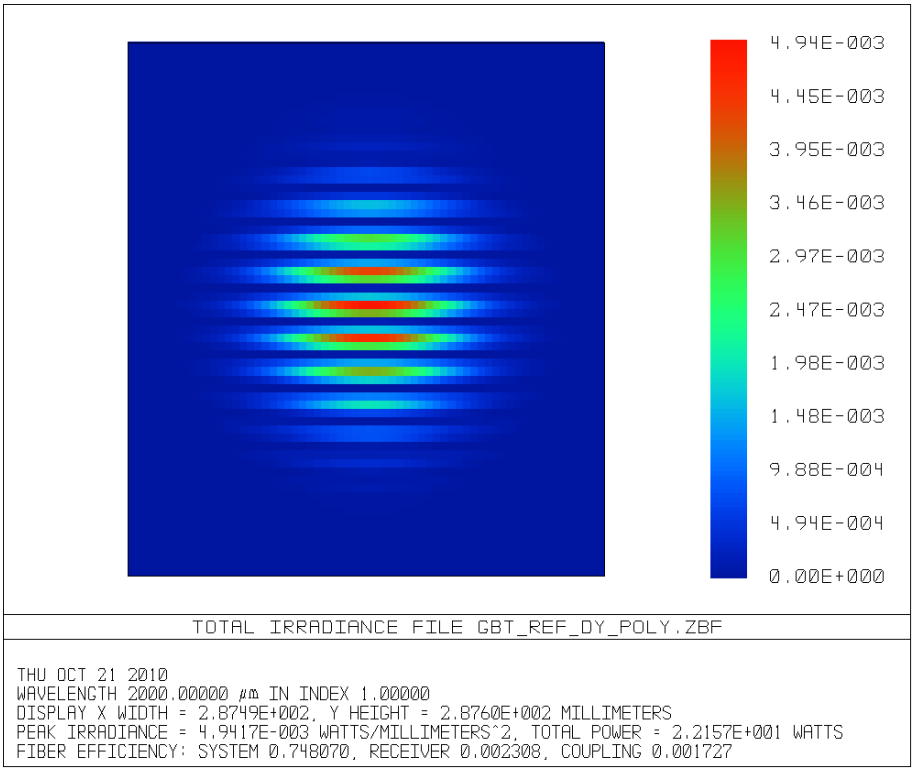

(a) Fringes generated by a 40 mm central baseline orientated along the systems x axis.

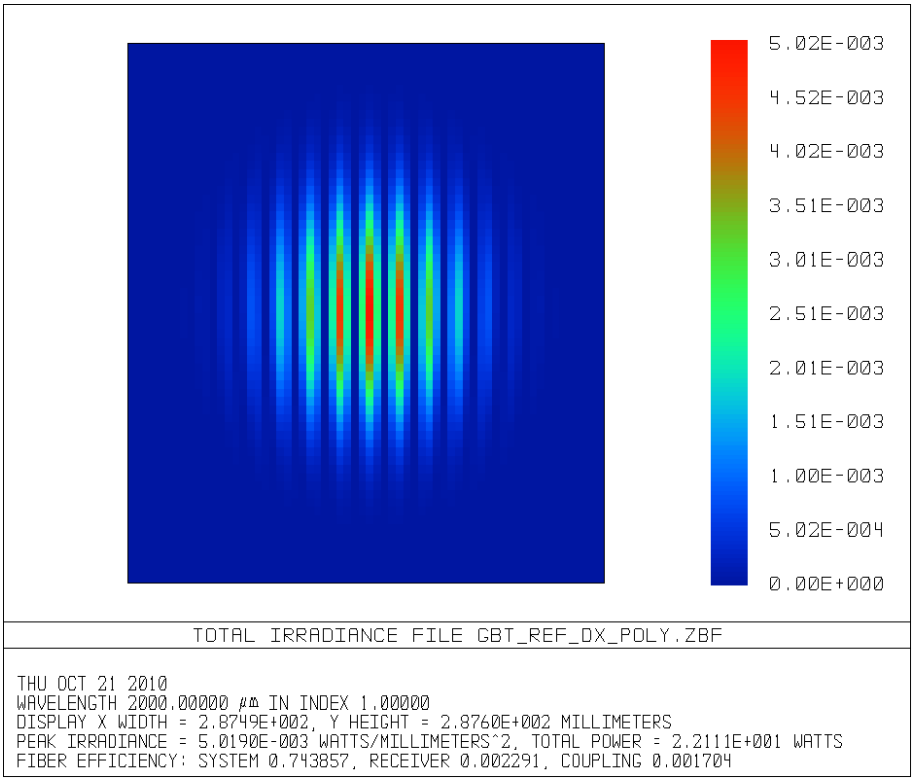

(b) Fringes generated by a 40 mm central baseline orientated along the systems y axis.

Figure 5.3: Fringe patterns generated by the optimized combiner.

5.2 Fully refractive combiner for QUBIC

5.2.1 Telecentric lens combiners.

In Chapter 4 we suggested the GCC and CG may be candidates from implementation in QUBIC. An analysis of the power coupled to the bolometers indicated that these combiners did not possess the performance levels required by QUBIC1.0. In the Autumn of 2010 work was on-going in the APC in order to ascertain the quality of the synthesized beams the QUBIC2.0 dirty imager would be required to produce. [2]. While a technique with which to examine and categorize the synthesized beams and the window functions generated by the GCC and CG was being derived we thought it prudent to investigate the implementation of lenses within QUBIC2.0.

If the neither the GCC or the CG produce sufficient quality synthesized beams then it is likely that we have exhausted all the leading contenders for reflector optical combiners within QUBIC2.0. Another option is to design lens based combiners. Fortunately the lack of options we have encountered when considering reflector combiners is contrasted by a large number of possible lens designs. In this section we will present the results of a general approach to designing symmetric doublet lenses. Later we will present the results of designing more complicated triplet refractors.

We have approached the design of these lens systems in the following manner. We began by describing a rudimentary blue print of a system that consisted of thin lenses. We then instructed Zemax to optimize these first principle designs to produce realistic thick lens that produce low wavefront aberration in the combining beams. In order to do so Zemax was allowed to alter the radii of curvature of all lens surfaces as well as the thickness of the lenses. The separation between the lenses was also adjusted as well as if necessary the conic constants of the surfaces. As before the Zemax default merit function was used to minimize the wavefront aberrations[3]. Also if necessary we informed Zemax to minimize particular aberrations such as coma or

[2]We now know the synthesized beams must be of sufficient quality so that any drop to the sensitivity of QUBIC2.0 caused by wavefront errors generated by the optical combiner is no greater than 10%.

[3]The operation of the default merit function has been explained in Chapter 2.

astigmatism[4]. Finally a Zemax optimization was performed on these systems to force them to approximate telecentric combiners. We instructed Zemax to force the angles and heights at which particular rays intersect the focal plane to equal those of an ideal 300 mm focal length telecentric system. The angles and heights to which these rays were forced to converge were calculated by hand using the geometry of a 300 mm focal length telecentric system. In all examples in this section the lenses are constructed from HDPE whose refractive index is 1.52[5].

Figure 5.4 is the simplest symmetric lens combiner we have designed for QUBIC2.0. This system began as two thin lenses with a 300 mm combined focal length. This ideal setup was optimized using Zemax in order to design realistic thick lenses separated by a reasonable distance. Zemax was instructed to minimize the magnitude of spherical aberration and coma by adjusting the radius of curvature of the lens surfaces. Meanwhile the levels of astigmatism and therefore field curvature were controlled by adjusting the distance between the lenses. Similar to all lens systems presented below this system is symmetric about an imaginary plane half way between the two centre lenses. Enforcing such symmetry leads to low values for both coma and distortion Seidel aberrations [78]. The LHS of Figure 5.4 shows the layout of this system while the RHS shows the spot diagrams generated by a $\pm 14^\circ$ FOV[6]. These spot diagrams indicate that this system is not diffraction limited over the entire extent of a 20×20 horn array. In this and following plots an extra surface has been included $after$ the image surface in all layout diagrams. This is merely an aid to display the degree of telecentricity of these systems. The detector plane is located where all three beams intersect. The black circle in the following spot diagrams indicates the size of the Airy disk. Within these diagrams the number of rays traced has been varied in order to allow the adequate display of the circumference of the Airy disk.

[4]Zemax has in-built classes that will directly calculate the contribution of individual wavefront aberrations to the merit function. Upon optimization Zemax will attempt to find an optical system that minimizes such contributions.

[5]Materials with higher refractive indices's may also be possible, I have taken the most difficult case here.

[6]We recall that a $\pm 14^\circ$ FOV allows us to examine the path of an entire 14° FWHM Gaussian beam through the combiner. As previously explained QUBIC will observe the sky using back-to-back horns that produce 14° FWHM Gaussian beams.

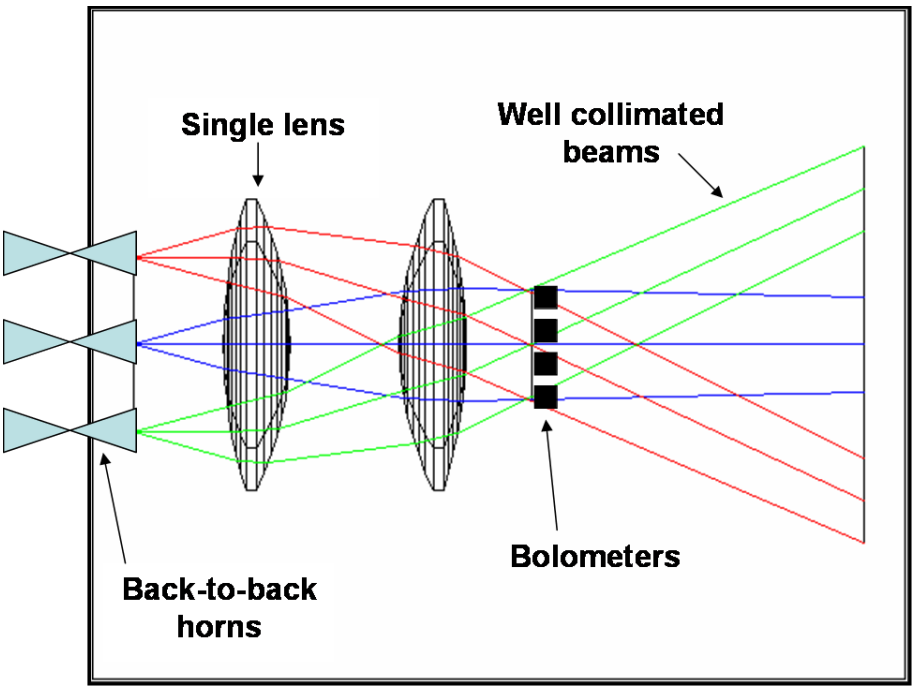

(a) Single symmetric 300 mm focal length lens optical combiner. The centre thickness of a single element is 100 mm.The distance from the horn array to the detectors is 600 mm. A height of at least 400 mm is required for a low edge taper.

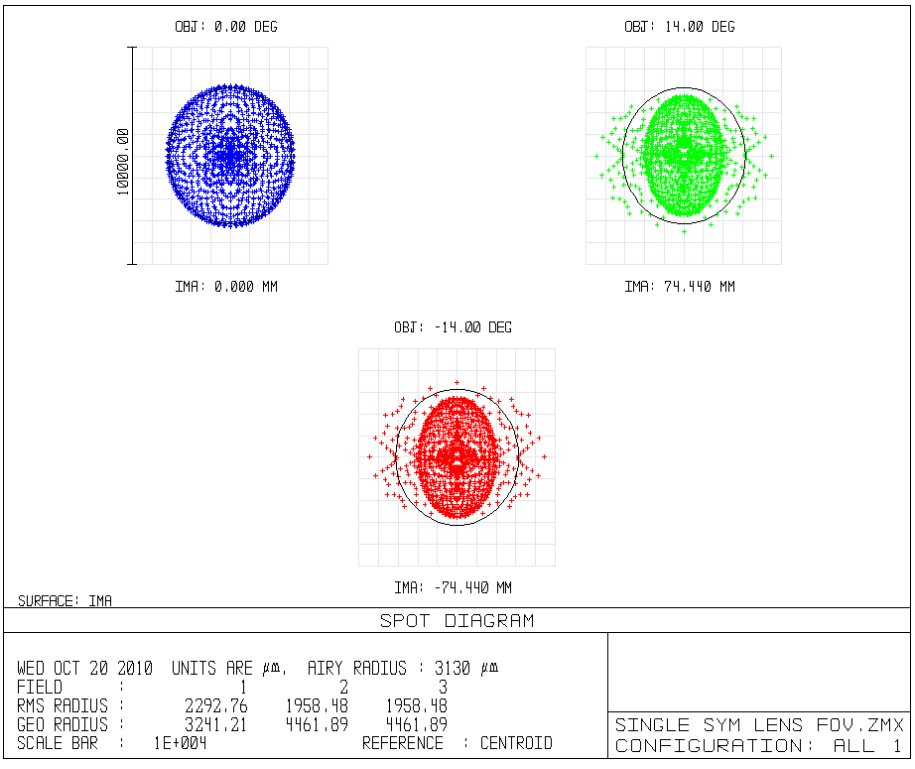

(b) Spot diagram for 0 and ± 14° fields of view. The circumference of the Airy disk is shown in black. Because rays intersect the detector plane outside the Airy ring this system is not diffraction limited.

Figure 5.4: Single symmetric lens system.

In order to produce a diffraction limited lens combiner over the entire horn array we must reduce wavefront aberrations induced by the lenses. The simplest way to achieve this is to split the individual lens into multiple elements. This generates more surfaces that can be reshaped to reduce wavefront aberrations. We instructed Zemax to optimize a symmetric 300 mm focal length telecentric doublet lens from the above symmetric single lens system. We ensured telecentricity by enforcing predetermined orientations on rays incident on the detector plane. As before these orientations were calculated by hand using the geometry of an ideal 300 mm focal length telecentric system. Zemax was then allowed to reshape the surface of the individual lenses until the combining rays possessed orientations as close as possible to those produced by an ideal telecentric system. The results of these optimizations are shown in Figure 5.5 for 3 ray angles. The spot diagram indicates that this system is very close to diffraction limited over a 20 $\times$ 20 back-to-back horn array for the field of view required (the 0° plots shows a spot diagram typical of most angles).

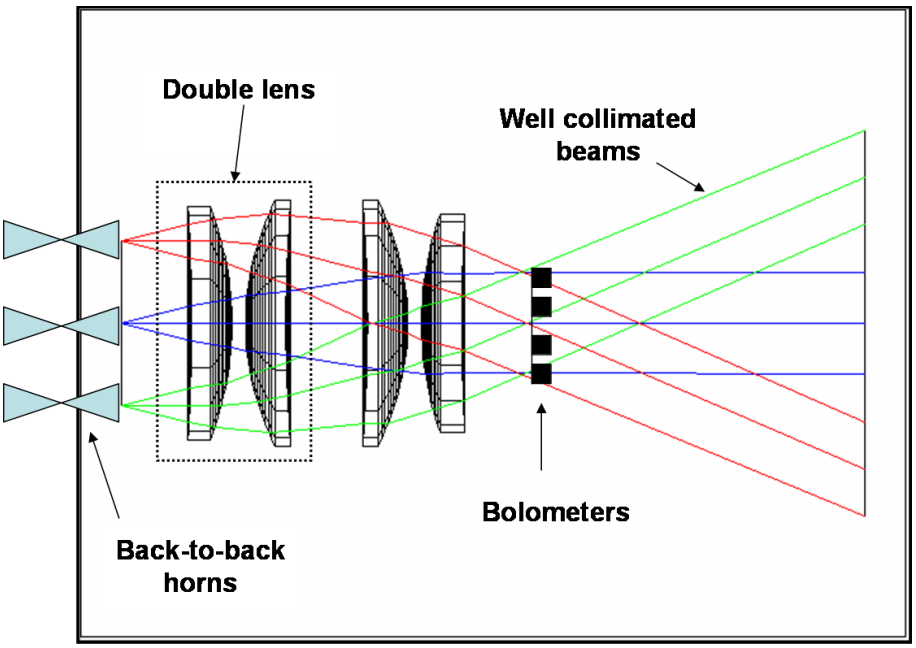

(a) Double symmetric 300 mm focal length lens optical combiner. The centre thickness of the double lens is 140 mm including air gaps. The distance from the horn array to the detectors is 600 mm. A height of at least 400 mm is required for a low edge taper.

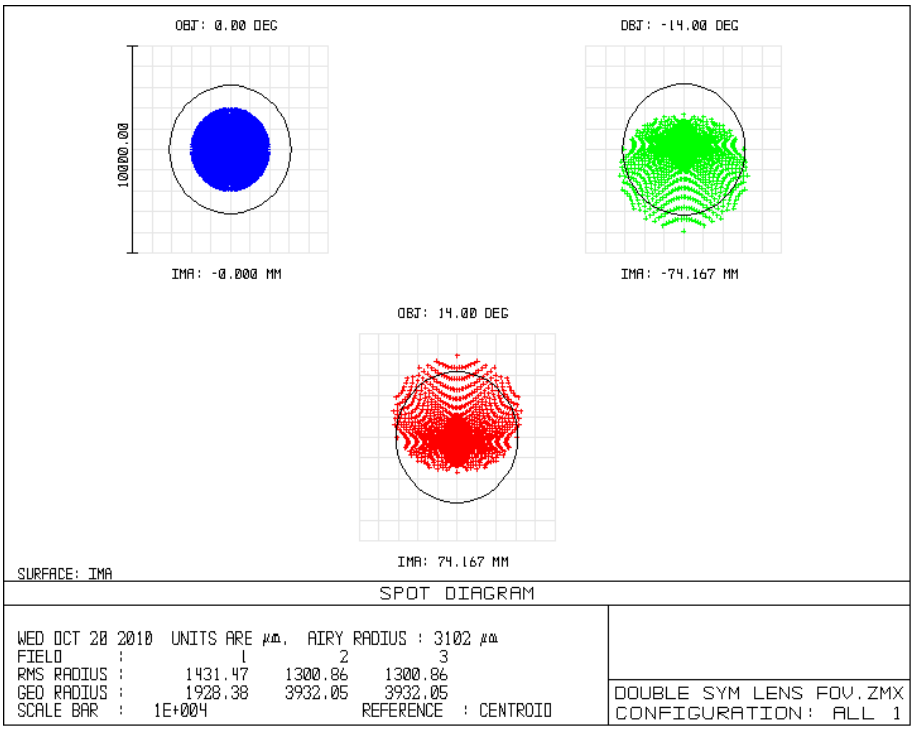

(b) Spot diagram for 0 and ± 14° fields of view. The circumference of the Airy disk is shown in black. The 14° FOV represents the maximum angle to which this system is diffraction limited.

Figure 5.5: Double symmetric lens system.

Also available for implementation is the corrected symmetric doublet. This is a system consisting of a symmetric combination of double lenses fully corrected for spherical aberration and coma. Figure 5.6 below displays such an optimized flint leading doublet. A flint leading doublet is simply one in which the thinest lens precedes the thickest lens. The mathematical solution for such a system was first introduced by Fraunhofer. This system was generated by instructing Zemax to directly reduce classical aberrations such as spherical aberration, coma and field curvature. Once these aberrations were reduced as much as possible we then instructed Zemax to optimize the system once again. Here Zemax was instructed to "hammer out" an approximate telecentric system using the pre-calculated values for the angles and heights that rays in a telecentric system would intersect the focal plane of a 300 mm focal length combiner. As shown in the spot diagrams in Figure 5.6 the corrected symmetric doublet is completely diffraction limited over the 20×20 horn array. However the reduction in aberrations leading to this result was due to the fact that the conic constant of the lens surfaces in addition to the radii of curvature of the surfaces were allowed to vary. Although such measures reduce aberrations the complexity of machining the lenses and applying any required coatings may be significantly increased.

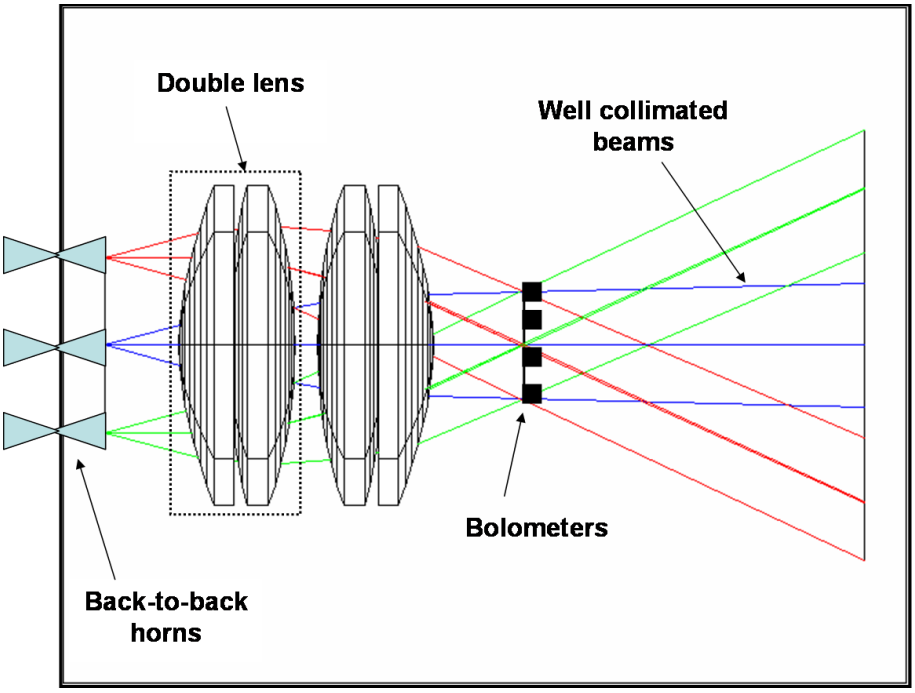

(a) Flint leading 300 mm corrected symmetric doublet lens combiner. The centre thickness of the double lens is 170 mm including air gaps. The distance from the horn array to the detectors is 620 mm. A height of at least 440 mm is required for a low edge taper.

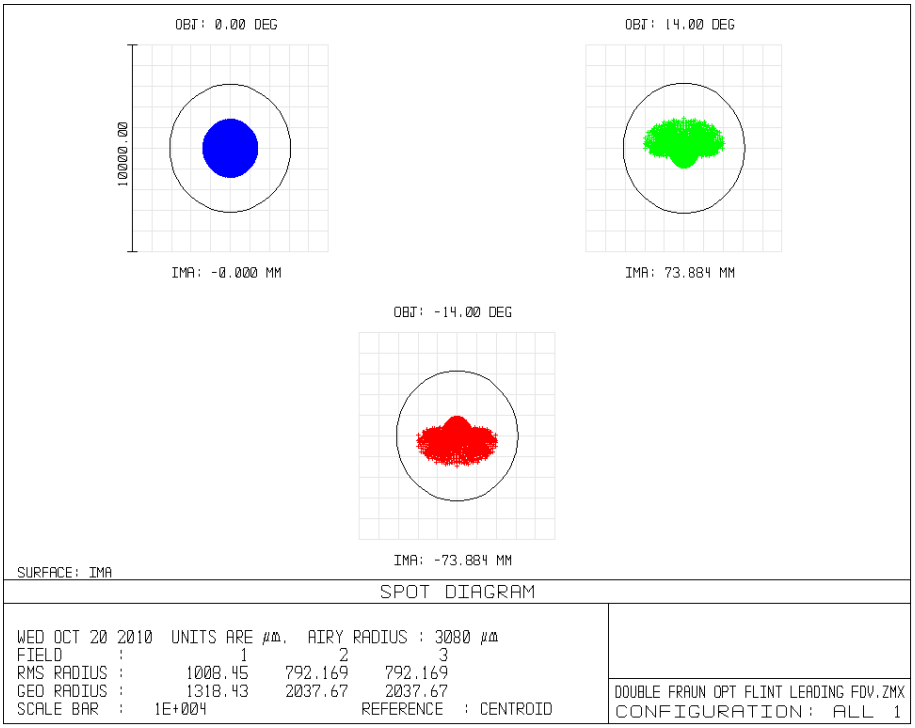

(b) Spot diagram for 0 and ± 14° fields of view. This system is diffraction limited.

Figure 5.6: Symmetric Fraunhofer flint leading corrected doublet lens system.

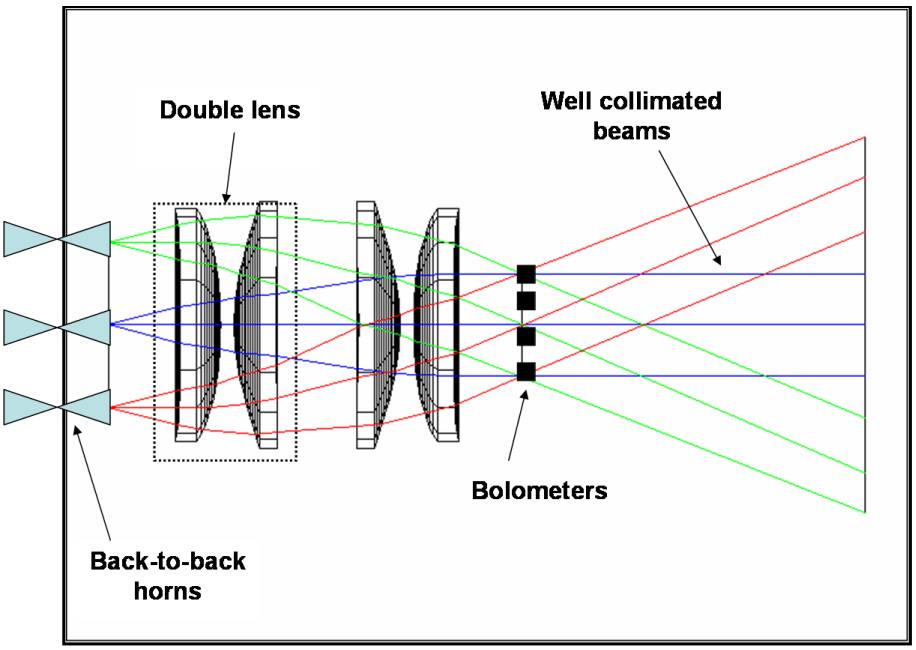

(a) Higher order 300 mm symmetric double lens combiner. The centre thickness of the double lens is 140 mm including air gaps. The distance from the horn array to the detectors is 600 mm. A height of at least 400 mm is required for a low edge taper.

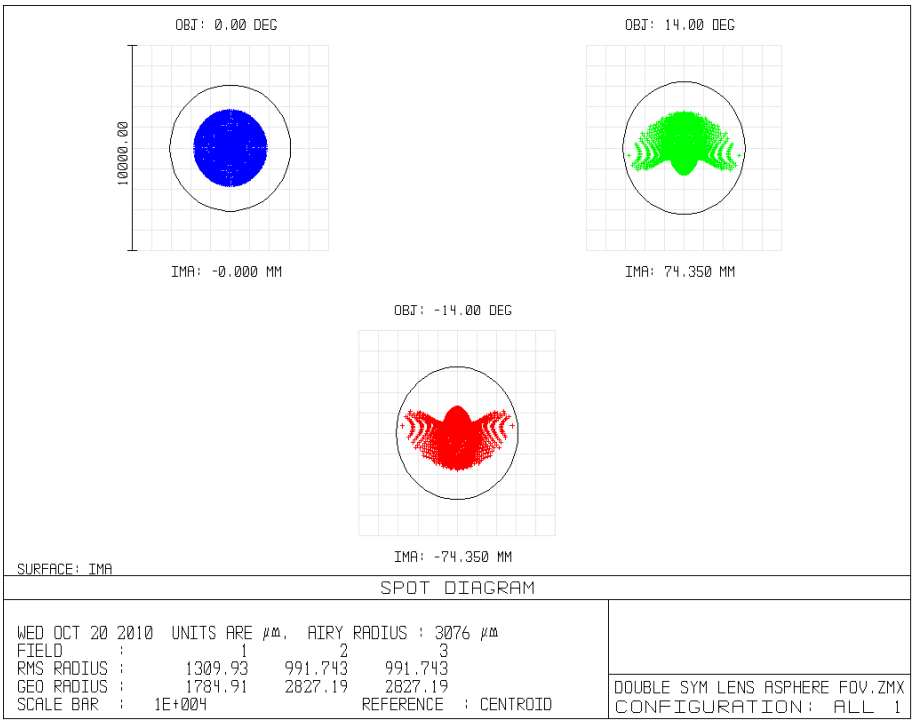

(b) Spot diagram for 0 and ± 14° fields of view. This system is diffraction limited.

Figure 5.7: Higher order symmetric telecentric doublet lens system.

Figure 5.7 shows the results of further optimizing the system shown in Figure 5.5. Here Zemax was allowed to adjust the higher order polynomial terms defining the lens surfaces. Once again Zemax was instructed to vary the higher order polynomial terms to produce low aberrations and then "hammer out" a telecentric system while maintaining low wavefront aberrations. As shown this system is also completely diffraction limited over the entire horn array.

5.2.2 Gaussian and Cooke Triplet designs

In previous sections we have shown that symmetric doublets can produce diffraction limited systems over the 20×20 horn array if exotic surface shapes are implemented. Such surfaces introduce complications during the manufacturing and coating processes. It is possible to generate the required diffraction limited systems consisting of standard parabolic surfaces if we consider a class of lenses referred to as triplets. The basic concept of the symmetric triplets is to split the single lenses of Figure 5.4 into 3 separate elements. In general this will create 6 variable surfaces whose shape can be modified to reduce wavefront aberrations.

We present a capped telecentric symmetric Gaussian and a symmetric Cooke triplet lens. These systems have be designed by following classical lens designs techniques to produce high performing imagers by shaping the surfaces in a manner that minimizes Seidel aberrations. This involved instructing Zemax to directly minimize wavefront aberrations such as coma and astigmatism. When an appropriate imager was produced a final optimization was carried out to set predetermined orientations for the refracted ways and thus creating a telecentric system.

A major target for these designs was the minimization of field curvature to accommodate a flat bolometer detector array. It is well known in optical design that the field curvature of a lens is independent of the lens shape but rather depends on the overall lens power. The wavefront curvature (ρ) induced by a lens pair can be expressed by

$$\frac{\phi_a}{n_a} + \frac{\phi_b}{n_b} = \rho. \tag{5.2.1}$$

In all designs below the power ($\phi_{a/b}$) and the refractive indices ($n_{a/b}$) of the back half pairs of the triplet lenses have been preselected to nullify the field curvature. This provided a blue print from which the final designs were optimized. In all optimizations the Zemax was instructed to maintain this initial low value of the field curvature. The lenses are constructed from HDPE with refractive index 1.52 and quartz whose refractive index is 2.2.

Figure 5.8 displays a capped telecentric symmetric Gaussian lens. Such a system is referred to as Gaussian because of the presence of a strong meniscus lens. In this system the central negative lenses are introduced to eliminate the field curvature of the adjacent double convex lenses. The system is then capped with a meniscus lenses to further minimize aberrations. As we can see this system is diffraction limited over the 20 $\times$ 20 horn array. Figure 5.9 displays a symmetric Cooke Triplet lens that is also diffraction limited to QUBIC specifications. This system is designed by placing negative lenses between two positive power elements[7]. Once again Zemax has been used to adjust the surface shapes of the lenses in order to reduce Seidel aberrations. Finally in both systems a final optimization was implemented to enforce telecentricity on the diffraction limited systems. As before the parameters used to enforced telecentricity were calculated by considering an ideal 300 mm telecentric combiner.

[7]The idea of placing a thin negative lens in between to positive lenses was introduced by Cooke in 1893. The lens design company founded by Cooke survives to this day, for information visit `http://www.cookeoptics.com/`.

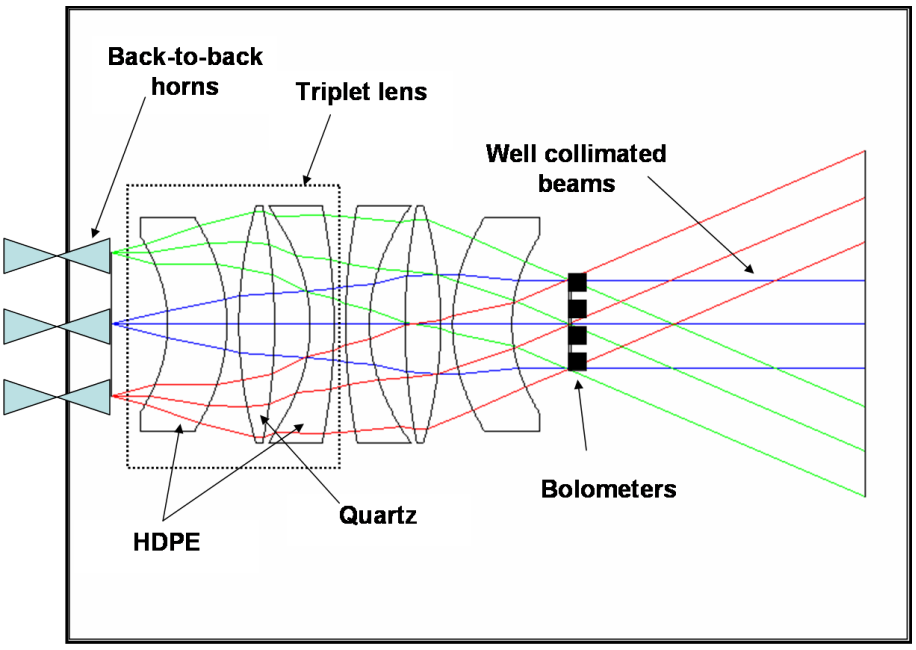

(a) Capped 300 mm symmetric Gaussian lens combiner. The distance from the horn array to the detectors is 800 mm. The centre thickness of the double lens is 280 mm including air gaps. A height of at least 400 mm is required for a low edge taper.

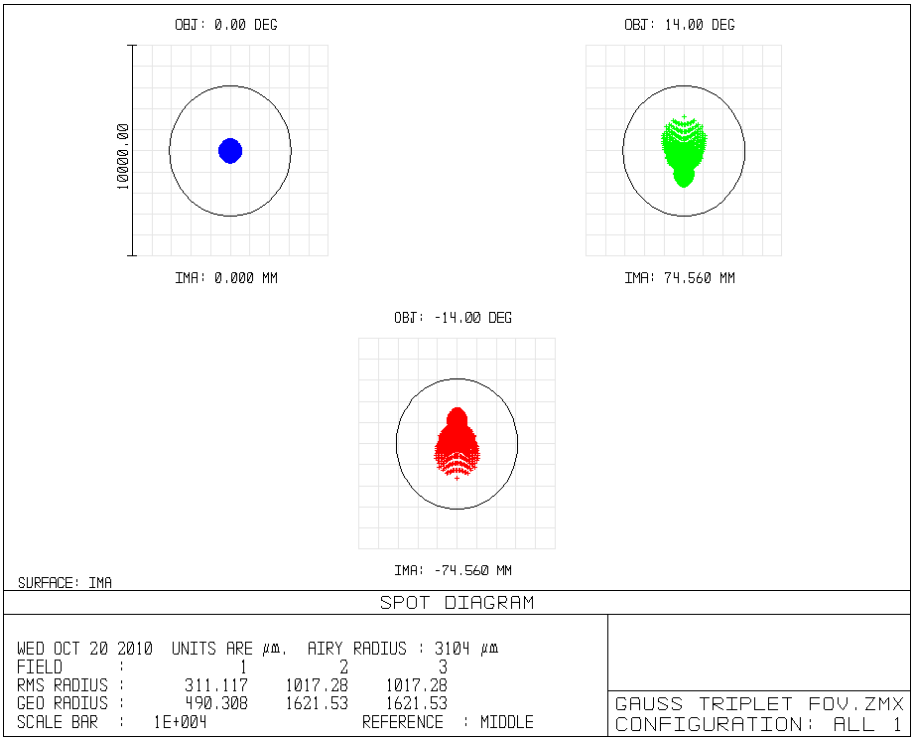

(b) Spot diagram for 0 and ± 14° fields of view. This system is diffraction limited while consisting of standard parabolic surfaces.

Figure 5.8: Capped symmetric telecentric Gaussian lens system.

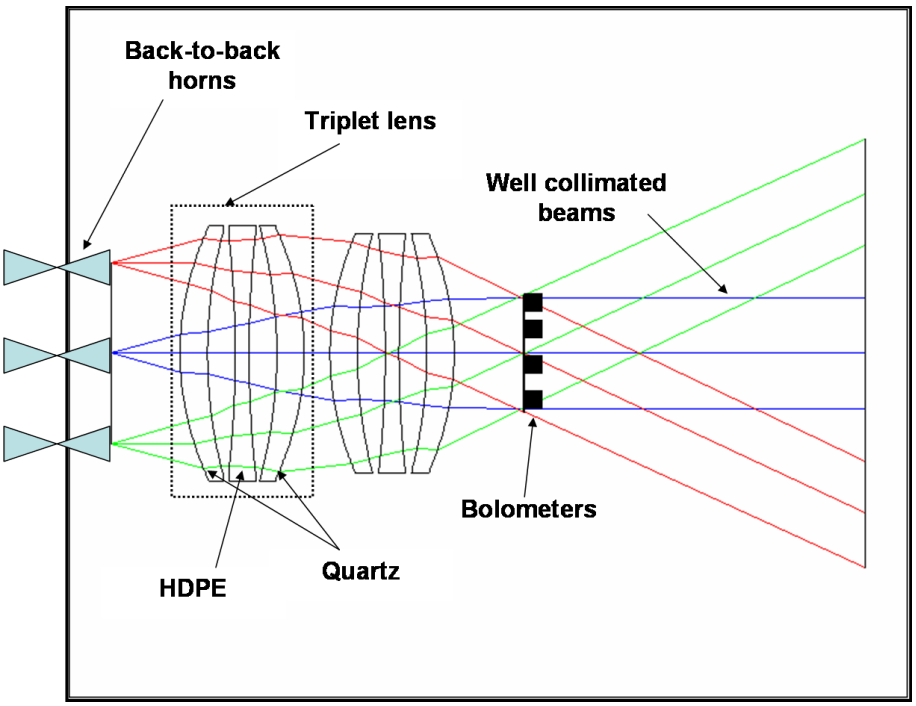

(a) Symmetric 300 mm Cooke Triplet lens combiner. The centre thickness of the double lens is 181 mm including air gaps. The distance from the horn array to the detectors is 600 mm. A height of at least 400 mm is required for a low edge taper.

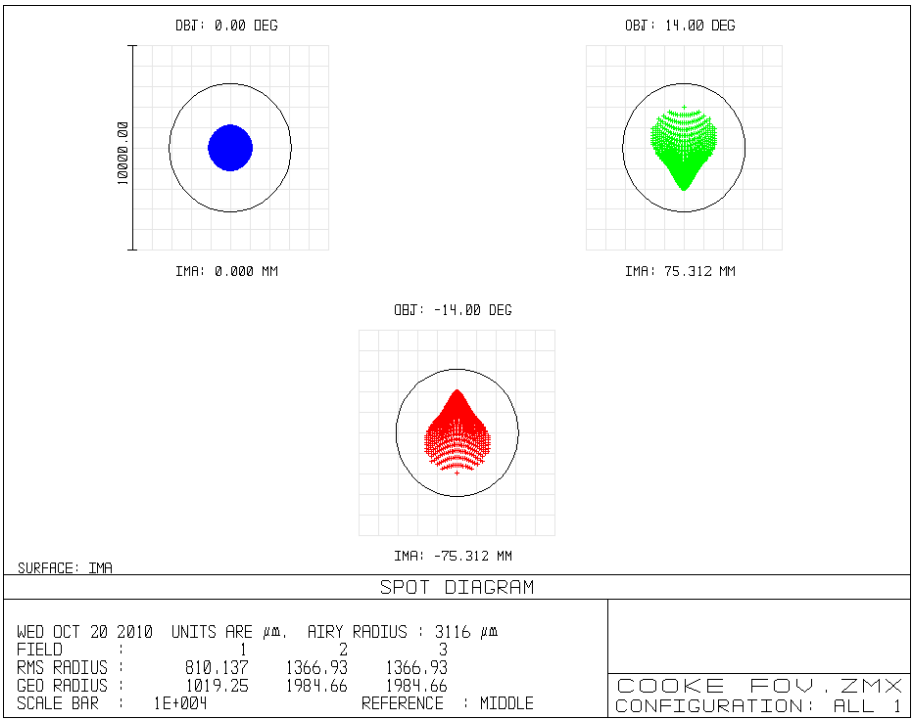

(b) Spot diagram for 0 and ± 14° fields of view. This system is diffraction limited while consisting of standard parabolic surfaces.

Figure 5.9: A Cooke triplet lens system.

The presence of enclosed negative lenses in the above triplets coincides with the solution of equation (5.2.1) that requires a negative element to eliminate field curvature. Enforcing symmetry during Zemax optimizations has lead to low values of coma and distortion. For these reasons and because of the use of several optimization steps these systems are diffraction-limited despite consisting of only simple lens shapes.

5.2.3 Symmetric double lenses that ignore field curvature.

The elimination of field curvature requires at least one lens of negative power. When this is combined with a positive lens we must reduce the focal length of the positive lens in order to maintain a given effective focal length. For short focal-length systems this leads to multiple lens splittings as we must find elements of appropriate focal lengths that are of a reasonable thickness. This is the primary reason that when we designed the symmetric Cooke triplet and capped Gaussian the system consisted of six separate lenses. The more elements in a given system the more costly it will be to construct. Also the possibility of error is increased with every element we add due to manufacturing flaws. The final system we present is a symmetric double convex lens. This system has been designed by instructing Zemax to minimize spherical aberration and coma whilst ignoring field curvature. For this reason no negative lenses are produced. Therefore multiple lens splittings are not required to permit elements of reasonable thickness but are implemented solely to reduce aberrations.

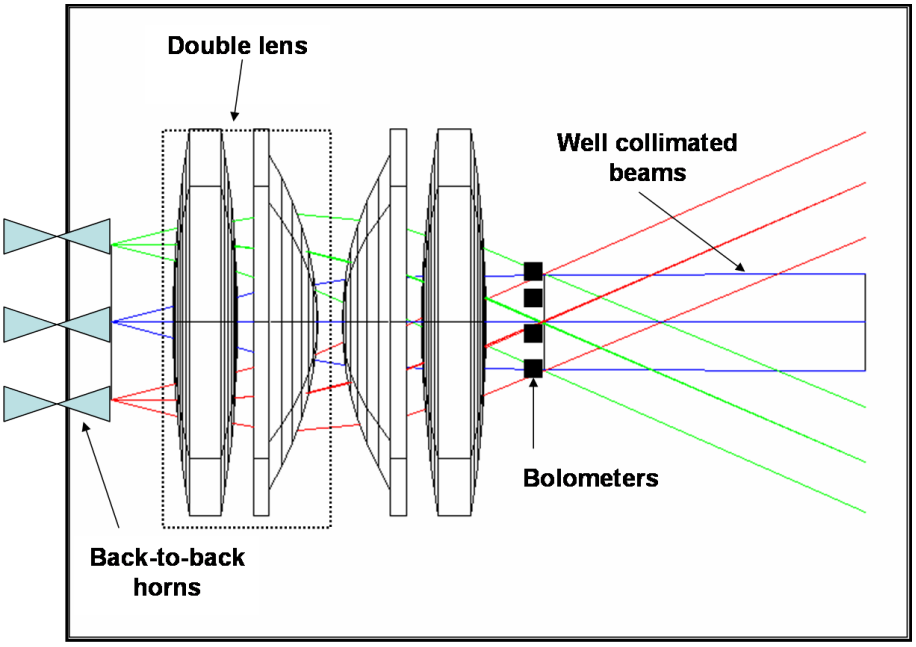

(a) Symmetric 300 mm double convex lens combiner. The distance from the horn array to the detectors is 700 mm. The centre thickness of the double lens is 225 mm including air gaps. A height of at least 400 mm is required for a low edge taper.

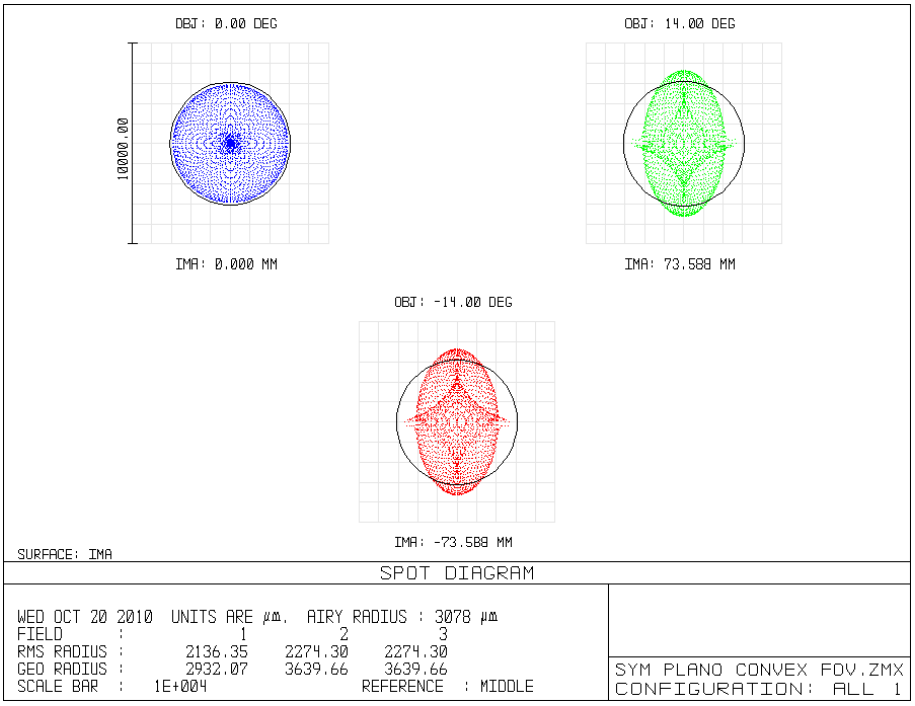

(b) Spot diagram for 0 and ± 14° fields of view.

Figure 5.10: Symmetric double convex lens system.

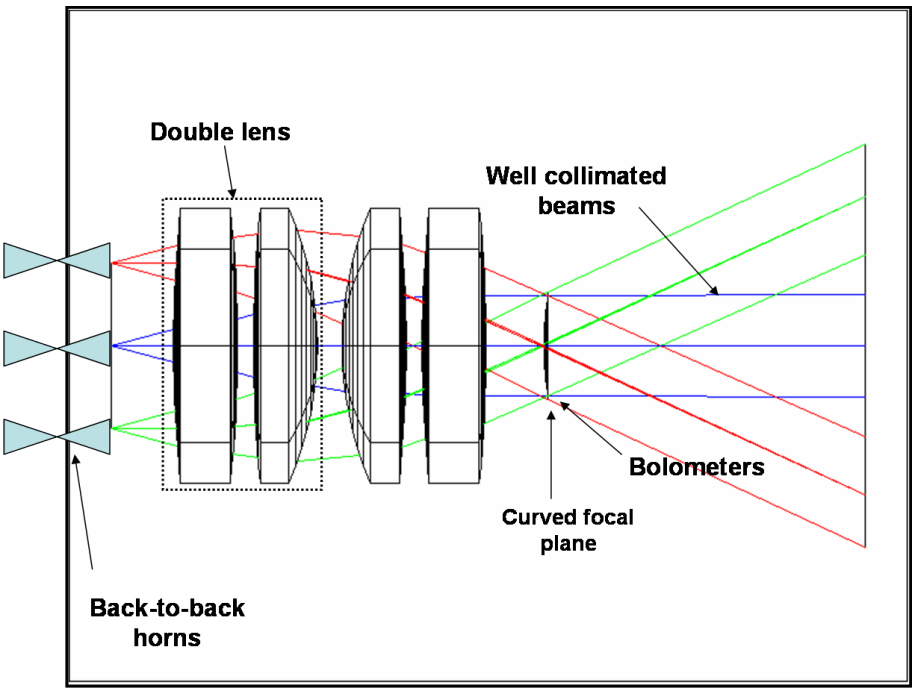

(a) Flat field symmetric 300 mm double convex lens combiner. The centre thickness of the double lens is 200 mm including air gaps. The distance from the horn array to the detectors is 700 mm. A height of at least 400 mm is required for a low edge taper.

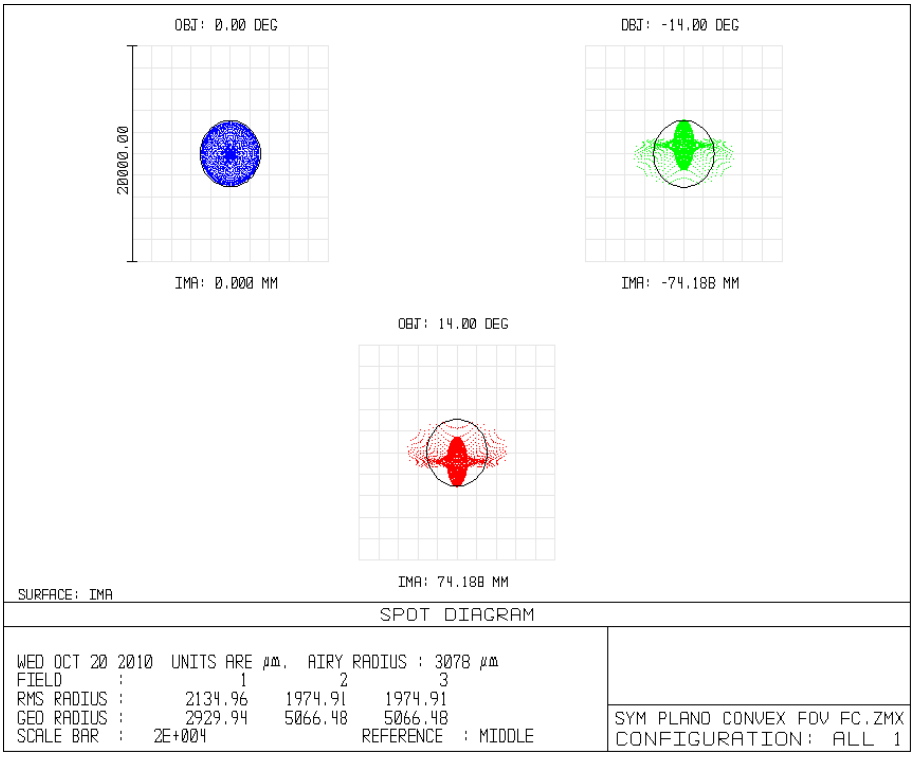

(b) Spot diagram for 0 and ± 14° fields of view.

Figure 5.11: Symmetric double convex lens adjusted for field curvature.

From Figure 5.10 we can see that a double lens design is adequate to produce a system that is nearly diffraction limited. The main aberration in the system is field curvature. This is apparent when we examine Figure 5.11. Here we have adjusted the curvature of the detector plane in order to compensate for the field curvature. Figure 5.11 demonstrates the best performance of the symmetric double convex when the field curvature is removed. For QUBIC2.0 the bending of the filled bolometer detector plane is not possible. A standard way of compensating for field curvature is to introduce a field flattener before the detector plane. This will generate a system that is barely diffraction limited while consisting of 5 lens components. In the above section we have clearly demonstrated how the addition of one more component will allow us to design symmetric triplets that perform extremely well. We conclude that implementing on-axis lenses will indeed generate a higher degree of choice and performance when compared to off-axis reflectors. However even with lenses the complexities introduced by QUBIC's short focal length and large entrance diameter cannot be avoided. In order to generate high performing systems multiple elements must be implemented.

The above systems are merely a demonstration of the applicability of lens combiners to QUBIC. Our conclusions are limited as we have, as of yet, no minimum space requirement in which to place a RHWP, an optical window or a polarizing grid. However it is apparent that lens combiners do provide the versatility and compactness we require from the optical combiner. Also since these systems are symmetric about the propagation axis higher order bilateral Seidel aberrations that deform the fringe patterns in off-axis combiners will not be present [118]. We are confident that once a definite template is decided upon for QUBIC2.0, for example the position, diameter and thickness of the RHWP and any polarization grids, a high performing lens combiner can be designed following the procedures outlined in [78] and [117].

5.3 Analysis of refracting combiners

5.3.1 Using Zemax to model the fringe patterns generated by a lens combiner

As previously discussed Zemax provides some basic analysis techniques to model the propagation of a Gaussian field through lenses. We present the results of examining the fringe patterns produced by the symmetric Cooke triplet in Figure 5.9. We have chosen to model the fringe patterns produced by the symmetric Cooke triplet because, as shown in Figure 5.9(b), geometric optics indicates that this lens is the best performing system we have designed. We have used Zemax to perform a Fourier optical analysis of the Cooke triplet in order to investigate whether this system also produces high quality fringe patterns. Figure 5.12 displays the results of a single 40 mm baseline while Figure 5.13 displays the results of considering a 60 mm baseline. These baselines have been centred around the optical axis of the lens. Both Figures 5.12 and 5.13 show very low levels of aberrations.

We note that for this initial investigation fringe quality was compared qualitatively only as the technology for manufacturing lenses of the required performance level was not considered sufficiently mature for the first QUBIC module. In the next few years this technology, as well as the ability of software packages such as GRASP to model lenses, is expected to improve significantly. Meanwhile Zemax remains and industry standard for the design of non-standard lenses.

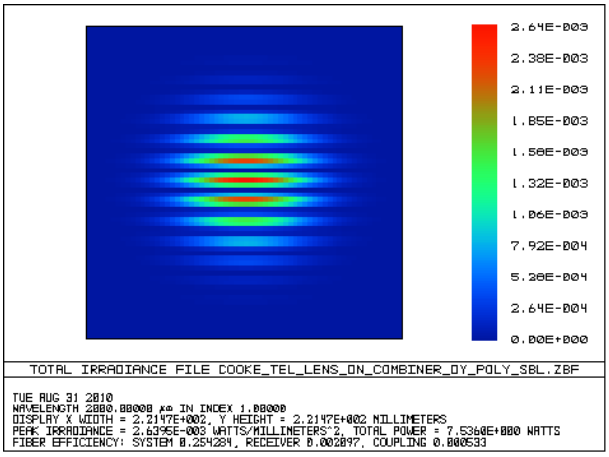

(a) Intensity of fringe pattern.

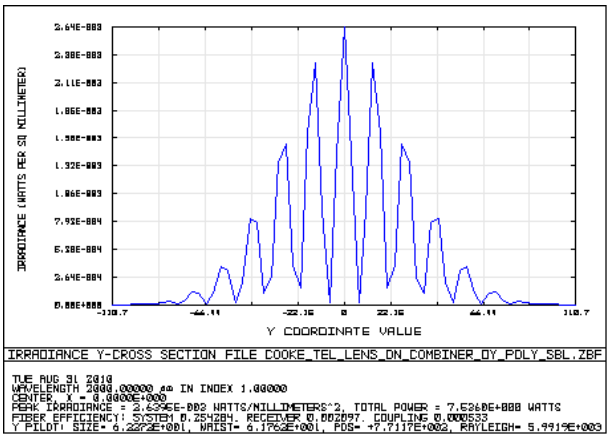

(b) One dimensional intensity cut through fringe pattern shown in part (a).

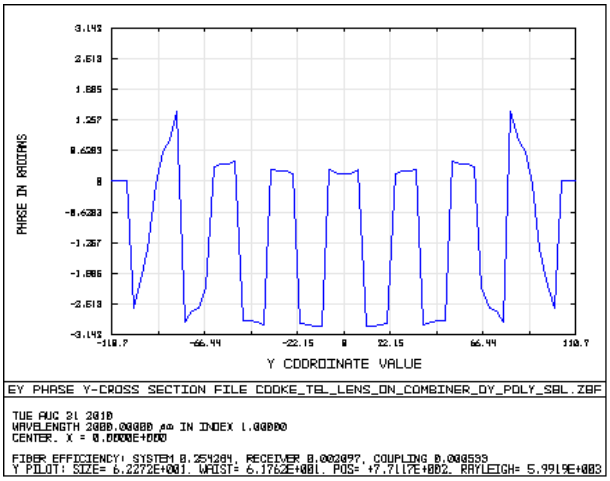

(c) One dimensional cut through the phase-front of obtained fringe pattern shown in part (a).

Figure 5.12: Fringe and phase patterns generated by 14° FWHM beams incident on the Cooke Triplet from a 40 mm central baseline.

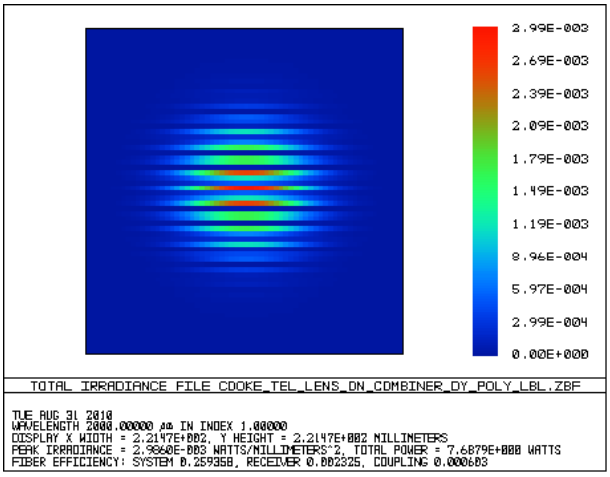

(a) Intensity of fringe pattern.

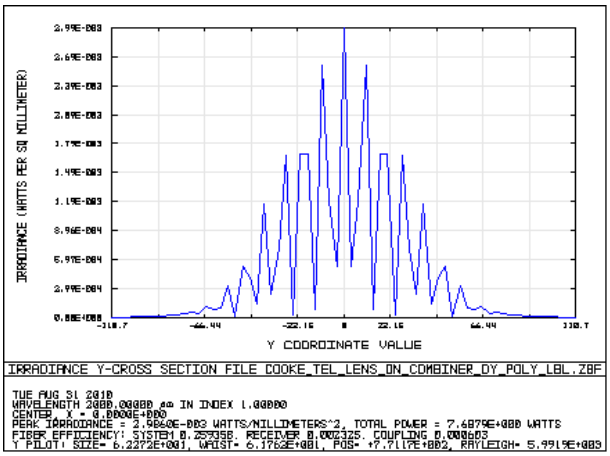

(b) One dimensional intensity cut through fringe pattern shown in part (a).

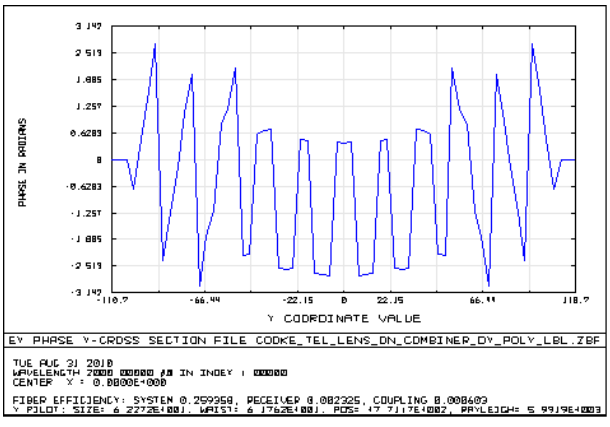

(c) One dimensional cut through the phase-front of obtained fringe pattern shown in part (a).

Figure 5.13: Fringe and phase patterns generated by 14° FWHM beams incident on the Cooke Triplet from a 60 mm central baseline.

5.4 Conclusions

We have presented several telecentric lens systems that produce low wavefront aberrations. These systems all fit into the QUBIC cryostat and will focus beams from a 20×20 array onto a small focal plane. However the primary concern regarding the implementation of refracting systems is our inability to accurately model the lenses. In the authors opinion one the most pressing advantages of implementing a lens system in QUBIC is the versatility offered by these designs. For example the only initial restriction placed on the above lens combiners when we started to design them was that the effective focal length of the entire system must equal 300 mm. We allowed the distance between the lenses and the distance of the lenses from the horn array and the bolometer detectors to vary during the optimizations. However if restrictions are placed on these distances to allow the optical system to accommodate a half wave plate or a polarizing grid we are confident the number of remaining free variables we can optimize in systems such as the Cooke triplet will still be large enough enable us to design a high performing combiner.

However it should also be noted that large lenses, like those required to make a Cooke Triplet, present manufacturing difficulties (and also operating difficulties at cryogenic temperatures). This is especially true when anti-reflection coatings are considered. In this chapter we have presented various designs for possible lens combiners for completeness from an optical point-of-view. However we still expect the main optical elements in QUBIC to be reflectors.

6 QUBIC2.0

6.1 Introduction

The QUBIC experiment described in Chapter 2 turned out to be too ambitious for the current state of the art technology. Severe impasses were encountered by all groups involved in the collaboration. These ranged from issues regarding the window size to the performance requirements placed on the optical combiner. The largest stalemate involved finding methods to individually phase modulate over 100 input channels. For these reasons the operation of QUBIC was revised in the spring of 2010. In this chapter we discuss the operation of the updated QUBIC2.0 CMB experiment.

6.2 QUBIC2.0

6.2.1 Problems with the QUBIC design

In Chapter 4 we discussed two reflector combiners applicable to QUBIC. All of these systems had limitations. For example beam distortion in the compensated Gregorian (CG) combiner deformed the resulting fringe patterns. Also it was shown that leakage of power from the secondary horns onto the detector plane will occur in the general crossed Cassegrain (GCC). This power leakage could adversely affect the instrument's sensitivity. Other layouts that looked promising were ruled out by the very low F-number of the QUBIC combiner.

A second design has been proposed for QUBIC that results in less serve restrictions on the optical combiner. In this section I will discuss the reasons for choosing this new design called QUBIC2.0. We will also present a review the suitability of several lens combiners as well as the GCC and the CG to QUBIC2.0.

An advantage of bolometric interferometry over heterodyne mixing is that bolometers are naturally broadband. The bolometer detectors used on QUBIC are likely to have a bandwidth of 20%. This is in contrast to heterodyne experiments such as DASI and CBI where due to technological limitations a bandwidth greater than 10% is not possible. However, the presence of multiple frequencies in QUBIC leads to smearing of the fringe patterns. A comprehensive study of the effects of fringe smearing on the sensitivity of QUBIC has being carried out at the APC Paris [70]. All formulas in this section have been reproduced from [70]. This investigation has shown that any gain in sensitivity due to the available bandwidth is offset by the degradation of the final fringe patterns. Assuming we are observing over a range of multipoles (Δl) centered around l this trade off is summarized by

$$\Delta C_l^{BI} = \sqrt{\frac{2}{2l\Delta l}} \times \left(\sqrt{\kappa_1} C_l + \frac{2 N_h N E T_{BI,20\%}^2 \Omega}{N_{eq}^2 t} \times \frac{0.20}{\Delta v / v_0} K_{sp}(l) \right), \tag{6.2.1}$$

where the noise in the angular power spectrum measured by a broadband bolometer, ΔC_l^{BI}, is expressed in terms of the noise equivalent temperature (NET) of the bolometer detectors, the beam size on the sky (Ω) and the number of equivalent baselines (N_{eq}). The term κ_1 in equation (6.2.1) is referred to as the smearing factor caused by QUBIC's bandwidth:

$$\kappa_1 = \sqrt{1 + 2\pi\Omega \left(\frac{\sigma_v}{v_0} \right)^2 \mathbf{u}_0^2} \tag{6.2.2}$$

where the noise in a visibility measured during a time t in Kelvin is $\sigma_v = \frac{\sqrt{N_h}}{N_{eq}} \frac{NET\Omega}{\sqrt{t}}$ when v_0 is the central frequency. The term $\mathbf{u}_0$ indicates a baseline expressed in spatial coordinates. We can see that the smearing factor equals unity when we consider a monochromatic instrument.

The term K_{sp} in equation (6.2.1) is defined as the smearing penalty factor and can be written as

$$K_{sp}(l) = \kappa_1^{3/2} = \left(1 + \frac{\Omega(\sigma_v/v_0)^2 l^2}{2\pi}\right)^{3/4}. \tag{6.2.3}$$

Equation (6.2.1) indicates that the extra sensitivity gained by the natural bandwidth of the bolometers competes with the deterioration of the fringe patterns due to smearing caused by the presence of multiple frequencies. A plot of the smearing penalty on QUBIC's sensitivity outlined in equation (6.2.3) as a function of the sky multipoles is displayed in Figure 6.1. Also shown is a plot of the smearing penalty factor on sensitivity versus the percentage bandwidth for $l = 100$. In both plots 15° FWHM Gaussian beams are assumed. The conclusion of the investigation pertaining to QUBIC is that the total loss on sensitivity approaches a factor of 2 for $l = 150$ for a 20% bandwidth.

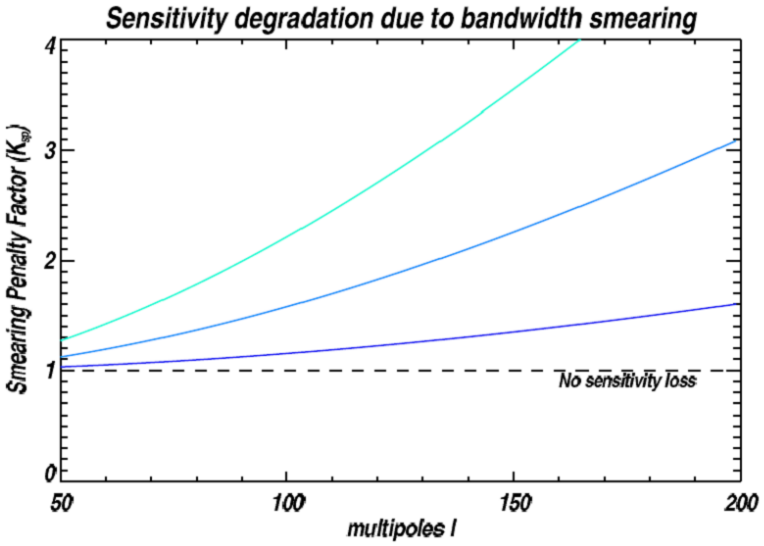

(a) The sensitivity degradation due to smearing for multipoles between 50 and 200. The smearing penalty factor is plotted for $\Delta v/v_0 = 10\%$ (dark blue), 20% (blue) and 30% (light blue) bandwidths. At $l \approx 150$ the penalty on the sensitivity for the bandwidth of TES bolometers, $\sim 20\%$, is a factor of 2.

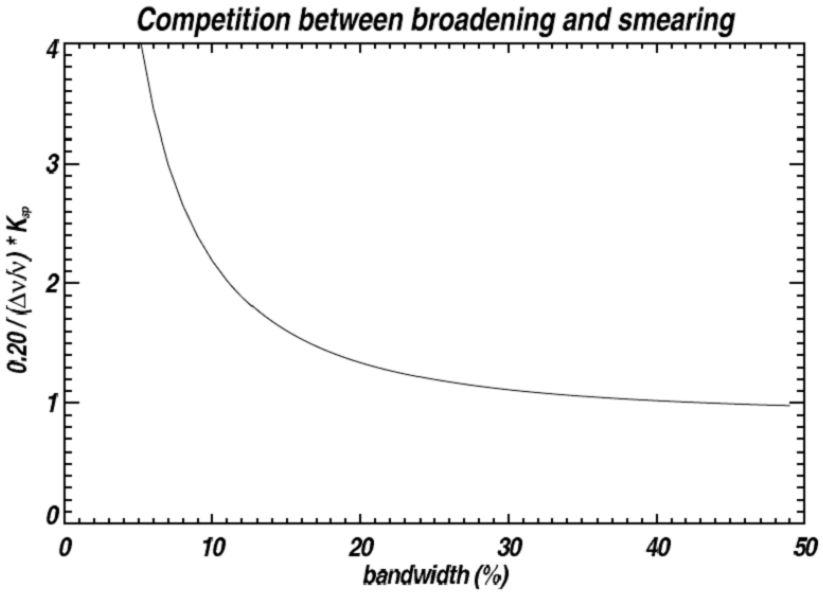

(b) The penalty factor on the sensitivity of QUBIC versus bandwidth for $l = 100$. We see that at $\Delta v/v_0 = 20\%$ the penalty factor is less than 2.

Figure 6.1: The effect of bandwidth in QUBIC. These figures are taken from [70]. Here a thorough discussion of the effect of bandwidth on a CMB bolometer interferometer is presented in detail.

Figure 6.1 indicates that QUBIC's bandwidth offers no direct sensitivity advantages over CMB imagers such as QUaD or heterodyne observers such as DASI and CBI. We note that the above loss of a factor of 2 is not fatal. Monte Carlo simulations carried out at the APC Paris have shown that a maximum penalty factor of 2 is quite acceptable while attempting B-mode recovery. The construction of QUBIC2.0 remains as justified as the construction of any CMB imager or a heterodyne mixer. Especially as the advantage of QUBIC2.0 is not only its sensitivity but its capability to control and nullify systematic errors.

However a more troublesome aspect of the frequency bandwidth was discovered when considering the operation of the phase shifters. From the collaboration's best knowledge only two options exist for QUBIC when considering phase shifting sequences for equivalent baselines. The first is that the phase shift values are independent of the frequency. The second is that the phase shifts vary linearly with respect to the frequency.

Similar to a monochromatic instrument, in a broadband interferometer the signal on each bolometer S_k is the sum of the auto- and cross- correlation between the beams from each separate polarization channel ($S_k = S_K^{auto} + S_k^{cross}$). As we have previously demonstrated information regarding the sky polarization is contained in the cross correlation terms. As discussed in Chapter 3 in order to recover the monochromatic Stokes visibilities of the CMB the received signal undergoes a time domain modulation performed by controlled phase shifters. These phase shifters are located behind each separate polarization channel of the sky horns. As explained in equation (2.4.4) the Stokes visibilities on each bolometer can then be recovered by solving a linear problem $S = A \cdot X$ where X is the visibilities vector, S is a vector containing the received signal on each bolometer and A is the coefficient matrix containing the known phase shifting sequences.

For the monochromatic case some excellent methods to calculate phase shifting sequences have been provided by our colleagues in the APC Paris and University of Richmond[1]. However calculating these sequences becomes more complex when we consider a broadband interferometer. The first approach is the simple scenario where

[1]University of Richmond, 28 Westhampton Way University of Richmond, VA 23173, U.S.A. For more information visit `http://www.richmond.edu/`

the phase shifting values do not depend on the frequency. Under such conditions $\Delta\Phi^2_{b,p}(v) = \Delta\Phi^2_{b,p}(v_0)$ where $\Delta\Phi_{b,p} = \Phi_{b,i} - \Phi_{b,j}$. Here Φ indicates the phase of an input signal while $\Delta\Phi$ represents the phase shift values and includes the geometrical phase shift induced by the optical combiner, also i and j indicate the horns that make the baseline p and b is the bolometer under consideration. As in the monochromatic case the entire system is reduced to a linear problem that can be inverted to recover the Stokes visibilities. The linear system produced is

$$S_k^{cross} = \sum_{\beta=0}^{N_{\neq}-1} \Gamma_{k,\beta} \cdot \mathbf{V}_{\beta}^{\Delta_v} \tag{6.2.4}$$

where $\Gamma_{k,\beta}$ contains the phase shifting values. Unfortunately as indicated by $\mathbf{V}_{\beta}^{\Delta_v}$ the recovered visibilities are broadband visibilities. Therefore such a method will not enable QUBIC to map the sky at a particular frequency.

The second method is the more complicated scenario in which the modulation of the phase shifters varies linearly with the frequency. For example if $\Delta\Phi^2_{b,p}(v) = \Delta\Phi^2_{b,p}(v_0) \times \frac{v}{v_0}$ then the phase imposed by the shifters will vary linearly with respect to frequency. However it has been shown that such an approach would be disastrous for QUBIC. Under such conditions the relationship between the power received by the bolometer detectors and the Stoke visibilities is no longer a linear problem. This means that the value of every visibility will slightly change according to a change in the phase shifting value. Monte Carlo simulations presented in [70] have suggested that such an occurrence will lead to a leakage from intensity visibilities into polarization visibilities.

In order to avoid leakage from the Stokes intensity visibility into the polarization parameters phase shifting sequences constant with respect to frequency must be implemented. However such an approach places huge constraints on the phase shifters. It was originally planned that each channel would be phase-modulated with mechanical waveguide phase-modulators developed by the Manchester team. These phase modulators are based on a rotating waveguide operated by cryogenic motors producing continuous phase-modulation from 0 to 360 degrees[2]. It is estimated that the

[2] A summary of waveguides currently under development at Manchester can be found at `http://www.mrao.cam.ac.uk/projects/cmb/workshop_jul09/talks/rtg_development.pdf`. The presenta-

phase shifting sequence must be calculated so that they vary by less than 1 % across the entire bandwidth. These conclusions heralded the end of implementation of phase shifters in QUBIC to modulate the sky signal. Following discussions during the July 2009 collaboration meeting it was concluded that the design and construction of fast and lossless phase shifters that could function as required would be highly unlikely (or would at least require several years of research and development). It was decided that the use of phase shifters and therefore the QUBIC1.0 mission should be abandoned.

As of spring 2010 the current design of QUBIC involves using a rotating half wave plate (RHWP) to modulate the polarization of the sky signal. The elimination of the controlled phase shifters also removes the necessity for the OMTs and thus the two separate polarization channels for each sky horn. Therefore accompanying the RHWP is a simple array of singular back-to-back horn antennas. Polarization sensitive switches will be inserted into these horns in order to assist calibration. This new design is the basis of the QUBIC2.0 experiment and is outlined in Figure 6.2. Although the position of the RHWP is still undecided, QUBIC2.0 has been greeted with optimism by the entire collaboration. Many design criteria such as the size of the horn array and the optical window are less restrictive and the entire instrument is more scalable with the only restriction the size of the cryostat itself.

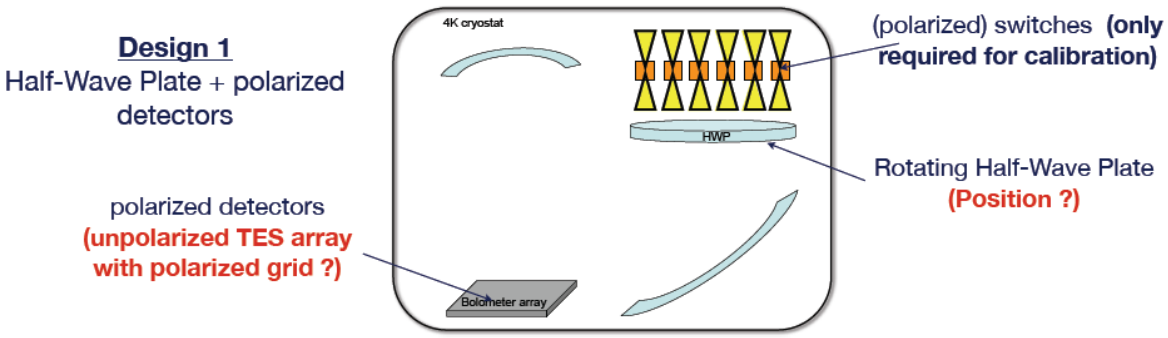

Figure 6.2: Preliminary design of QUBIC2.0

tion shown here was presented at the RadioNet Engineering Forum Workshop, Bonn, November 2009.

6.2.2 Modulating the sky polarization using a rotating half wave plate

The power measured by a single bolometer at location ($\mathbf{d}_p$) from two identical horns separated by a displacement ($\mathbf{x}_i$) and affected by the standard $\frac{1}{\lambda D_f}$ phase shift where D_f is the focal length of the combiner is

$$R_\eta(\mathbf{d}_p) = \left| \int\int\int E'_\eta(\mathbf{n}) B_\eta(\mathbf{n}) exp\left[i2\pi \frac{\mathbf{x}_i \cdot (\mathbf{d}-\mathbf{n})}{\lambda D_f} \right] J(v) H(\mathbf{d}-\mathbf{d_p}) d\mathbf{n} dv d\mathbf{d} \right|^2. \quad (6.2.5)$$

where the vector $\mathbf{n}$ indicates the pointing direction of the instrument while $\mathbf{d}$ indicates a position on the focal plane. Here we are considering a broadband spectrum (dv) and we are integrating over the surface of a bolometer whose reception pattern is given by the square function $H(d-d_p)$. The term $J(v)$ is the Gaussian band pass function of the instrument. We note that all formulas and conclusions in this section have been taken from the internal note. "*QUBIC 2.0: a new design for bolometric interferometry*". This was composed by our colleagues in the APC Paris and distributed in February 2010.

The change in coordinate systems of the polarization of the incident signal, E'_η, is a result of the rotating half wave plate. Here $E'_\eta = E'_{x/y}$ indicates the separate polarization channels of the final beams that will combine at two separate focal planes. These channels will be split using a polarization grid placed after the optical combiner. We assume that the half wave plate rotates at an angular velocity ω. Therefore the two orthogonal polarization states of the sky signal, $E'_\eta = E'_{x/y}$, are modulated by

$$\begin{pmatrix} |E'_x|^2 \\ |E'_y|^2 \end{pmatrix} = \frac{1}{2} \begin{pmatrix} 1 & \cos(4\omega t) & \sin(4\omega t) \\ 1 & -\cos(4\omega t) & -\sin(4\omega t) \end{pmatrix} \begin{pmatrix} S_I \\ S_Q \\ S_U \end{pmatrix} \quad (6.2.6)$$

where we can once again use the Stoke parameters to describe the signal polarization. The power incident on a single bolometer in the detector array that has been polarized along the system's x-axis is

$$R_x(\mathbf{d}_p) = S_I(\mathbf{d}_p) + \cos(8\pi\omega t)S_Q(\mathbf{d}_p) + \sin(8\pi\omega t)S_U(\mathbf{d}_p) \tag{6.2.7}$$

while the power incident on a bolometer in the detector array that has been polarized along the system's y-axis is

$$R_y(\mathbf{d}_p) = S_I(\mathbf{d}_p) - \cos(8\pi\omega t)S_Q(\mathbf{d}_p) - \sin(8\pi\omega t)S_U(\mathbf{d}_p) \tag{6.2.8}$$

where $R_{x/y}$ pertains to the power in a particular direction. Equations (6.2.7) and (6.2.8) show that the use of a rotating halfwave plate allows us to separately reconstruct synthetic images of the I, Q and U Stokes parameters (as they are each modulated in a different way). The TT, TE, EE and BB power spectra can then be reconstructed from the Stokes parameters' using standard techniques. In addition, since for QUBIC the half-wave plate is located right after the sky horns any cross-polarization induced by the combiner optics or the polarizing grid will not be modulated in the same way as the sky signal and will therefore not affect this signal. In accordance with classical radio astronomy we refer to the term S_X where $X = \{I, Q, U\}$ as a "dirty image". We can obtain the broadband Stokes visibilities by performing an inverse Fourier transform of this dirty image. The pure sky signal $X(\mathbf{n})$ is degraded by the synthesized beam.

$$S_X(\mathbf{d}_p) = \int X(\mathbf{n})B(\mathbf{n})^2|A_s(\mathbf{d}_p - \mathbf{n})|^2 d\mathbf{n} \tag{6.2.9}$$

where the term $A_s(d_p - n)$ is the synthesized beam and can be expanded into

$$A_s(\mathbf{d}_p - \mathbf{n}) = \int\int exp\left[i2\pi\frac{\mathbf{x}_i \cdot (\mathbf{d} - \mathbf{n})}{\lambda D_f}\right] J(v)H(\mathbf{d} - \mathbf{d_p})dvd\mathbf{d}. \tag{6.2.10}$$

From equation (6.2.9) we see that if the synthesized beam equals unity the sensitivity of QUBIC is only restricted by the antenna sensitivity $B(\mathbf{n})$. The simplest way of allowing this is by implementing zero length baselines across QUBIC. This essentially means removing the horn antennas and allowing a completely transparent entrance aperture. Therefore QUBIC will be fully optimized by converting the system into an imager. This can also be viewed as creating an infinite number of baselines and thus the QUBIC aperture becomes analogous to Huygens principle in which infinitesimally

small points become a source of propagating spherical wavelets. However as we will discuss the advantages of filling the entrance aperture of QUBIC with a back-to-back horn array is that the presence of equivalent baselines allows us to apply unique and comprehensive calibration techniques to the instrument. But of course the larger the number of back-to-back horn antennas the higher the sensitivity of QUBIC2.0

The current state of the art for a RHWP is being investigated by our colleagues in both the University of Manchester and Brown University [119][3,4]. As with every optical device involved with CMB astronomy the requirements placed on the RHWP in order to allow QUBIC to achieve the necessary sensitivity are demanding. The RHWP must have a large diameter yet also remain light and robust. It must be a practically lossless dielectric while all polarization characteristics must be well understood. The manufacturing and modelling of these waveplates are detailed in references [120] and [121], we do not include them in the optical models of this thesis. The two possibilities currently under consideration for the RHWP are listed below.

- *Sapphire or Quartz HWP*

These plates function on the basis of birefringence. A number of individual plates are stacked together while their crystal axes undergo a slight rotation relative to one another. A basic schematic is shown in Figure 6.3. The diameter of these plates are limited (Quartz ≈ 110 mm and Sapphire ≈ 280 mm). These plates are expensive to manufacture and heavy yet they are extremely robust. With cooling a low absorption level of $2-4\%$ is possible. If such a HWP is chosen Sapphire is most likely due to the 240 mm diameter of QUBIC2.0 20×20 horn array.

- *Mesh HWP*

These HWPs consist of two separate wire meshes combined to form a single HWP. The polarization of the incident beam becomes modified due the the conductive and capacitive qualities of the separate meshes. The mesh can either be air filled (max diameter ≈ 100 mm) or filled with a dielectric (max diameter ≈ 300 mm). A simple diagram of such a HWP is shown in Figure 6.4. These HWPs are fragile yet they

[3]The University of Manchester, Oxford Road, Manchester, M13 9PL, UK. For more information visit `http://www.mdc.manchester.ac.uk/`.

[4]Brown University, Providence, Rhode Island 02912, USA. For more information visit `http://www.brown.edu/`.

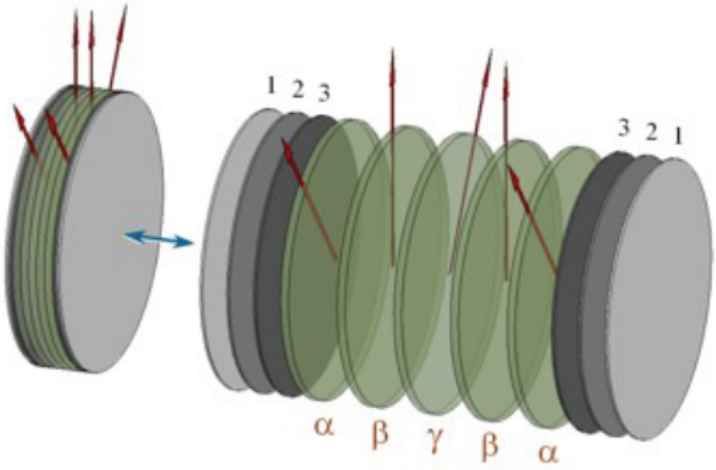

(a) The wave plate is constructed of multiple layers of birefringent materials. The symbols α, β and γ indicate that a symmetry of the crystal axes of the separate layers is required.

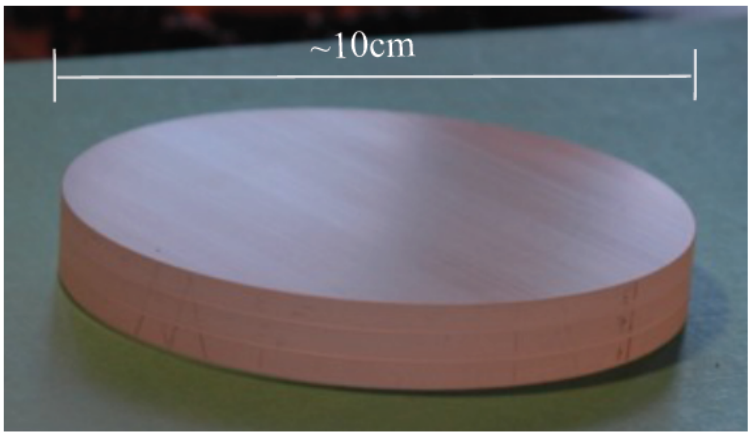

(b) Completed wave birefringent wave plate.

Figure 6.3: Birefringent HWP for QUBIC2.0. Figures taken from [120].

have the advantage that they do not require anti-reflective coatings. Absorption is approximately 1.5% at room temperature.

Inclusion of a HWP into QUBIC2.0 allows us to instantaneously measure all visibilities. A very recent concern of the collaboration is that sky apodization by the finite size of the primary beam (i.e. the sky horns have a beam FWHM of 14 degrees and are therefore not sensitive to all angles on the sky) will reduce the resolution of the "dirty image" produced by QUBIC2.0.. Further analysis in the APC Paris has shown that if the effects of sky apodisation cannot be nullified by scanning QUBIC2.0 will have a

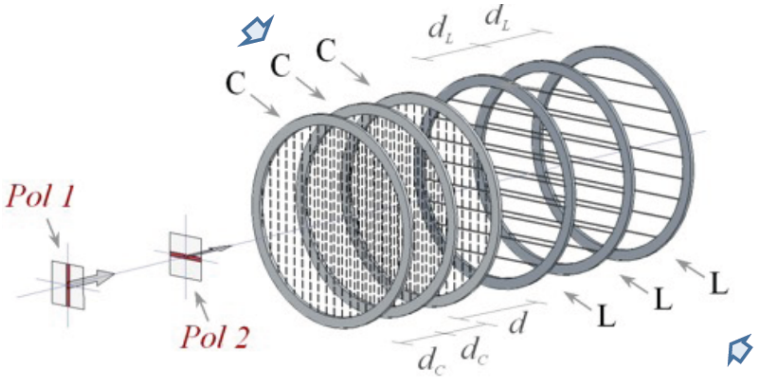

(a) The wave plate is constructed of multiple layers of metal wires and grids. Here **C** points to the capacitive stacks while **L** is the inductive stack. The terms $d_{C/L}$ indicate there separations.

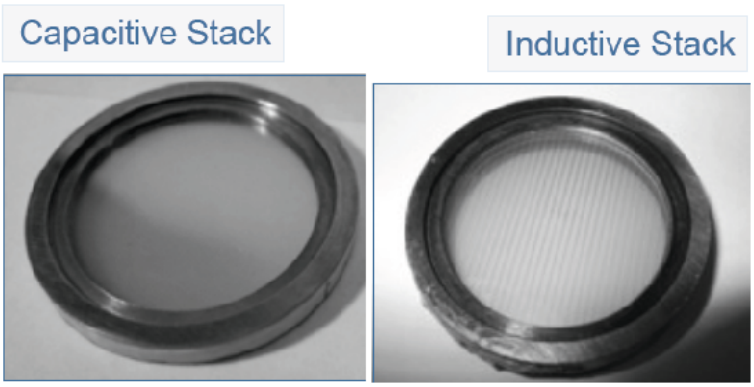

(b) Completed conductive and capacitive stacks. Combining multiple numbers of these stacks will produce the final wave plate.

Figure 6.4: Birefringent HWP for QUBIC2.0. Images taken from [121].

sensitivity factor of 3 below an imager. However if the dirty image can be successfully cleaned this may drop to a factor of 1.6 below an imager. The current scanning strategy for QUBIC2.0 is to scan $\sim 10°$ in the azimuth with a slowly varying elevation from $45° - 60°$. The fraction of the sky covered is $\sim 2\%$. A comparison of the sensitivity of QUBIC2.0 to that of a CMB imager is shown in Figure 6.5. Here the effects of sky apodization have been fully calculated. The red lines in Figure 6.5 show the most realistic scenario of an imager with a sky apodization of $\eta_{Im} = 1.4$ similar to QUaD and QUBIC2.0 possessing an apodization of $\eta_{BL} = 1.6$. As shown QUBIC2.0 will be slightly less sensitive than the imager but the difference is only marginal. Therefore construction of the QUBIC2.0 CMB polarimeter that implements the novel observing

technique of bolometric interferometry remains justified. Figure 6.5 is formed assuming an array of 400 back-to-back horns and an ideal optical combiner. A full discussion of the calculation of QUBIC2.0's sensitivity and the effects of sky apodization is found in [122]. Here a discussion of QUBIC2.0's scanning strategy is also presented.

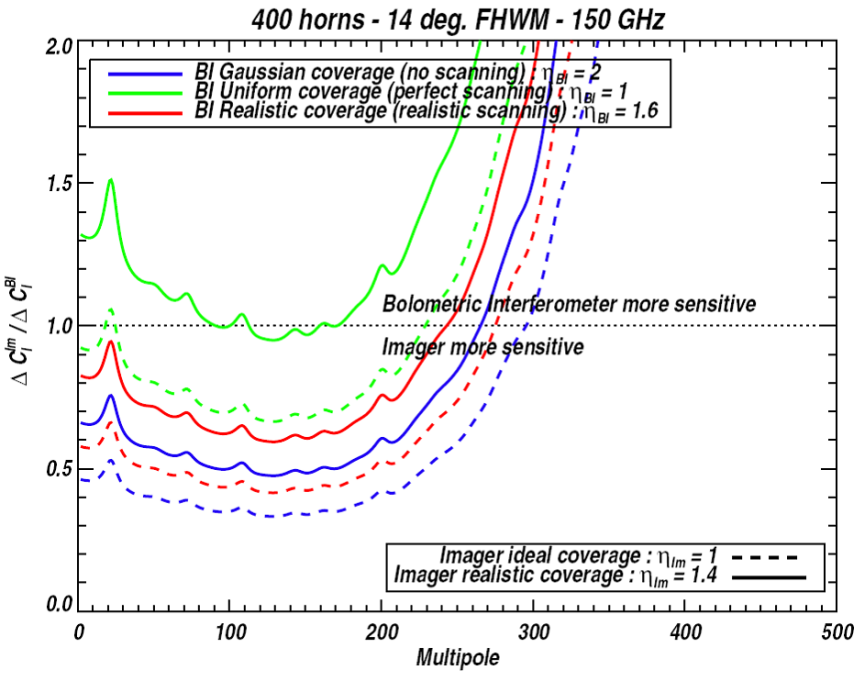

Figure 6.5: Sensitivity of QUBIC2.0 to the CMB power spectrum versus that of an imagers. Here the solid lines pertain to QUBIC while the dashed lines indicate an imager. The different colours indicate the achievable sensitivity due to various values of sky apodization due to various scanning techniques. These include a simple Gaussian beam sky coverage with no scanning $\eta_{Im/BL} = 2$.

6.2.3 QUBIC2.0 as a dirty imager

QUBIC2.0 will implement a RHWP in order to separate the polarization of the sky signal into it's Stokes parameters. The power measured by each bolometer is a linear combination of a dirty image of the I, Q and U sky signals. If one follows the premise of classical interferometry the visibilities can be reconstructed through a fast Fourier

transform of the dirty images. The power spectrum of the CMB polarization can then be extracted by calculating the covariance of the visibilities.

A novel technique is proposed for QUBIC2.0 that will allow us to obtain the CMB polarization power spectrum directly from the synthesized image without having to reconstruct the Stokes visibilities. In fact we can generate the CMB power spectrum from the dirty image following the methods used to calculate the density power spectrum from the signal received by a radiometer. For QUBIC2.0 the dirty image S generated from the unpolarized sky signal X is

$$S(\mathbf{d}_p) = \int X(\mathbf{n}) B(\mathbf{n})^2 |A_s(\mathbf{d}_p - \mathbf{n})|^2 d\mathbf{n} \tag{6.2.11}$$

here again $\mathbf{n}$ indicates direction of the incident signal while $\mathbf{d}_p$ is the location of the bolometer of the focal plane. The term $A_s(\mathbf{d}_p - \mathbf{n})$ is the synthesized beam as explained in equation (6.2.10). If the sky signal is expanded in terms of spherical harmonics and the instrument points in the direction $\mathbf{n}_0$ we can fully describe the dirty image generated by all baselines as

$$S_I(\mathbf{d}_p) = \int \sum_{lm} a_{lm} Y_{lm}(\mathbf{n}) \beta(\mathbf{d}, \mathbf{n}, \mathbf{n}_0) d\mathbf{n} \tag{6.2.12}$$

where

$$\beta(\mathbf{d}, \mathbf{n}, \mathbf{n}_0) = B^2(\mathbf{n} - \mathbf{n}_0) |A_s(\mathbf{d} - (\mathbf{n} - \mathbf{n}_0))|^2 \tag{6.2.13}$$

is an amalgamation of the synthesized beam and the antenna response. Finally we set $\int Y_{lm}(\mathbf{n}) \beta(\mathbf{d}, \mathbf{n}, \mathbf{n}_0) d\mathbf{n} = \beta_{lm}(\mathbf{d}, \mathbf{n}_0)$ in equation (6.2.12). The dirty image can now be written in the compact form

$$S_I(\mathbf{d}_p) = \sum_{lm} a_{lm} \beta_{lm}(\mathbf{d}, \mathbf{n}_0). \tag{6.2.14}$$

The covariance of this synthesized image

$$\left\langle S_I(\mathbf{d}, \mathbf{n}_k, \theta_i) \cdot S_I^{\star}(\mathbf{d}, \mathbf{n}_k, \theta_j) \right\rangle = \sum_l C_l W_l(\mathbf{d}, \mathbf{d}', \mathbf{n}_k, \mathbf{n}_l', \theta_i, \theta_j) \tag{6.2.15}$$

is directly related to the power spectrum of the sky signal and the so-called window function derived from the synthesized beam. This window function

$$\sum_l C_l W_l(\mathbf{d}, \mathbf{d}', \mathbf{n}_k, \mathbf{n}_l', \theta_i, \theta_j) = \sum_m \beta_{lm}(\mathbf{d}, \mathbf{n}_k, \theta_i) \beta_{lm}(\mathbf{d}', \mathbf{n}_l, \theta_j) \tag{6.2.16}$$

can be calculated directly from the synthetic beam. Therefore we have a direct relationship between the data covariance matrix of the signal received by QUBIC and power of the sky signal. By considering the angular modulation of the RHWP the Stokes polarization parameters of the sky signal can then be recovered. In essence the synthesized beam/image is the point spread function of the QUBIC2.0 optical system. Any sky signal entering QUBIC2.0's aperture will be convolved by this function and imaged on the focal plane as the final dirty image. As can plainly be seen the nature of the window function is decided solely by the geometry of the optical combiner and the baselines.

From Fourier optics we expect a square grid of horns to produce regular square pattern of diminishing bright spots from a central maximum. Such synthesized beams are precisely what has been modeled by our colleagues in the APC Paris. In Figures 6.6 and 6.7 we present the modeled ideal synthesized beams generated when 3 mm bolometers and a 25% bandwidth are considered. All patterns were generated assuming an array of 144 identical horns. The plots on the left of these figures are shown on a linear scale, on the right hand side the same beam is shown on a log plot.

These figures illustrate the effect of both finite bolometer size and finite bandwidth (finite bandwidth was not considered in my earlier analysis of fringe patterns). These synthesised beams are used to sample model CMB skies before subjecting the resulting data to the QUBIC analysis procedure in order to produce a quantitative measure of the beam combiner performance (e.g. Figure 6.17).

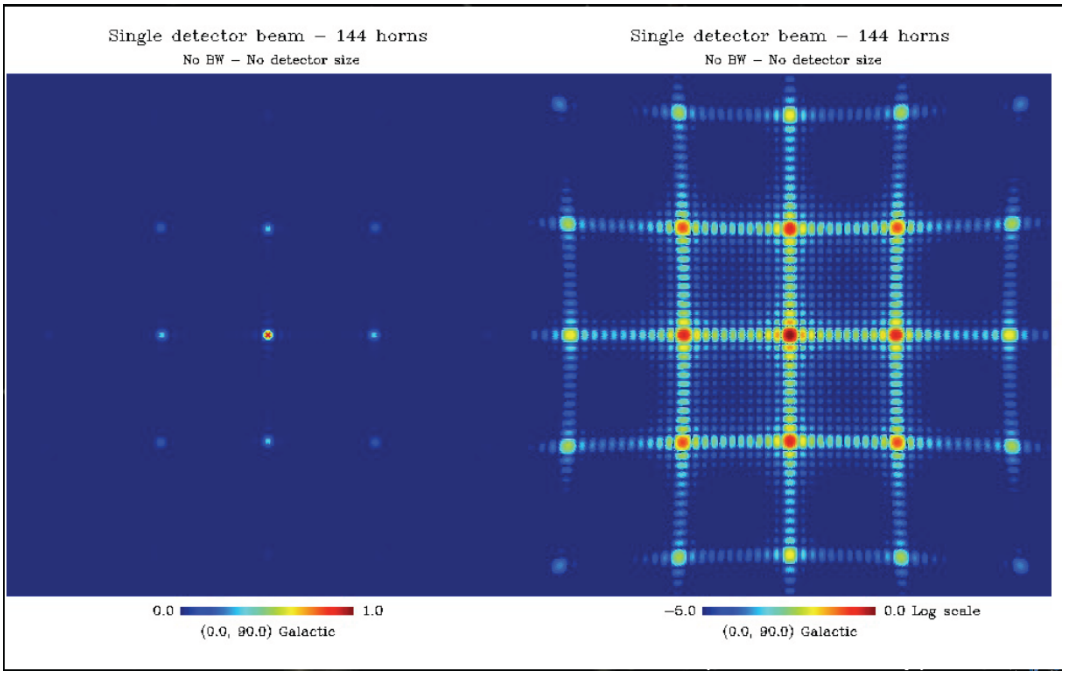

(a) The monochromatic synthesized beam obtained from 144 horns arranged in a square grid. Here a normalized power scale is shown. The single detector beam indicates that this is the synthesized beam "seen" by a single central pixel only.

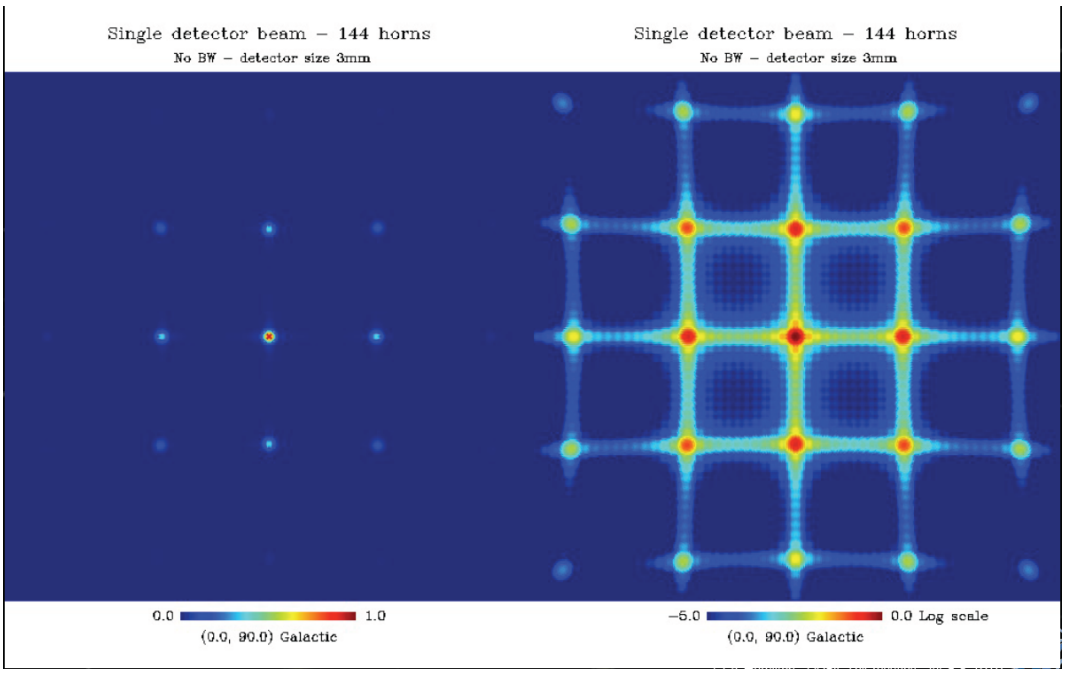

(b) The monochromatic synthesized beam integrated over 3 mm bolometers. Here the a logarithmic scale is shown. The single detector beam indicates that this is the synthesized beam "seen" by a single central pixel only.

Figure 6.6: Monochromatic synthesized beams. These are essentially the point spread function of a prefect monochromatic optical combiner. These figures have been provided by J. Ch. Hamilton from the APC Paris.

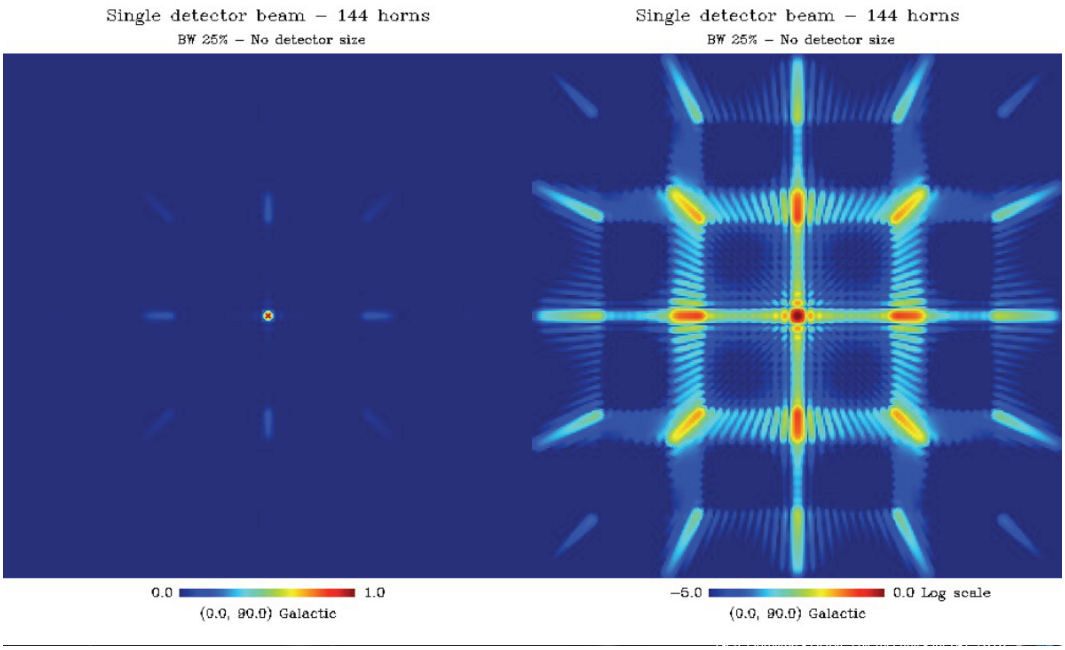

(a) The synthesized beam obtained from 144 horns arranged in a square grid when a 25 % bandwidth is considered. The smearing effects of the bandwidth are clearly visible. Here we show a normalized power scale. The single detector beam indicates that this is the synthesized beam "seen" by a single central pixel only.

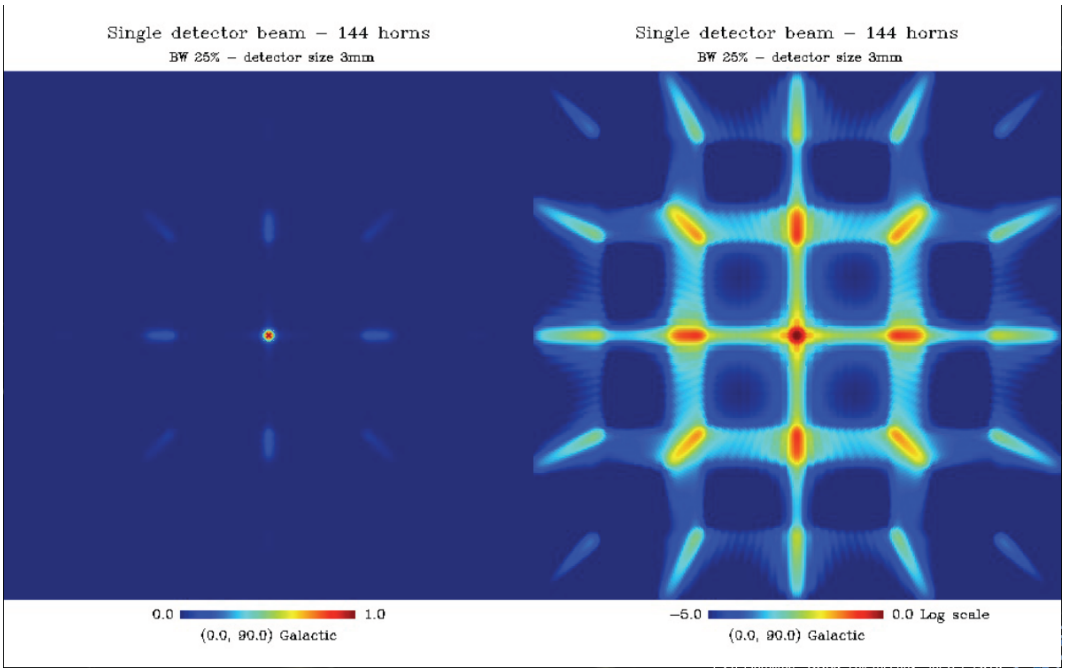

(b) The board band synthesized beam integrated over 3 mm bolometers. Here we shown a logarithmic scale. The single detector beam indicates that this is the synthesized beam "seen" by a single central pixel only.

Figure 6.7: Broadband synthesized beams. These are essentially the point spread function of an unaberrated optical combiner taking a 25 % bandwidth into account. These figures have been provided by J. Ch. Hamilton from the APC Paris.

There are several advantages of this revamped approach to QUBIC. The most glaring is that the concept of Stokes visibilities can be completely abandoned. QUBIC2.0 is simply a synthetic imager producing dirty sky maps. Such an approach makes the data analysis involved in QUBIC2.0 vastly simpler than QUBIC. It is of course apparent that the initial goal to somehow manufacture an additive CMB interferometer with a greater sensitivity than a bolometric imager is not possible in QUBIC2.0. The filled horn entrance aperture essentially prohibits such sensitivity. Although QUBIC2.0 is effectively an imager the essence of interferometry still dominates the reasoning behind such an experiment. Again as we will show in the next section it is believed that calibration techniques and error control afforded to us by combining several antennas will allow QUBIC2.0 to sample the CMB at "resolutions" not yet achievable with conventional imagers and heterodyne mixers. In Figure 6.8 below we have shown the sky image recreated from a modeled CMB spectrum and imaged through the above window functions. Here a bandwidth of 25% is assumed. The rotating half-wave plate allows reconstruction of synthetic images of the I, Q and U Stokes parameters.

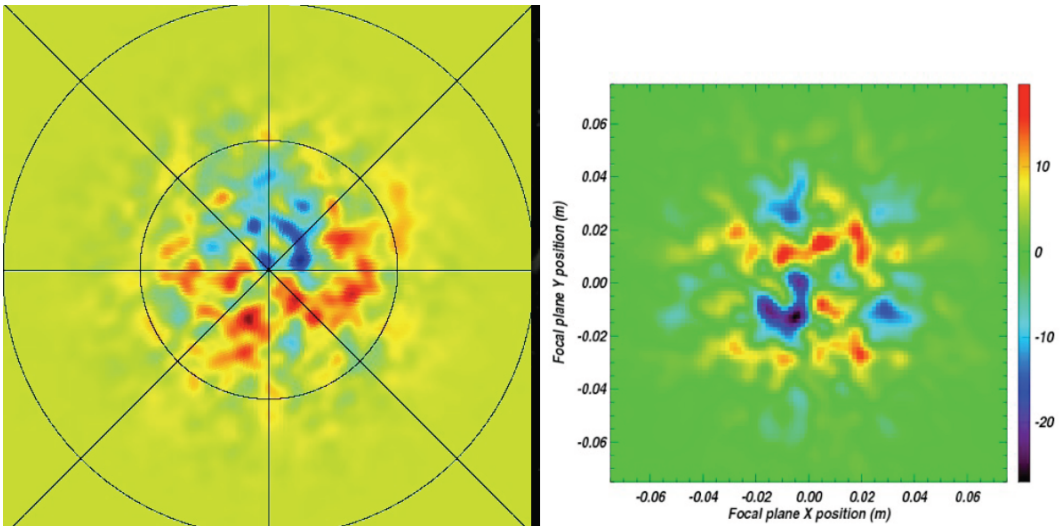

Figure 6.8: Synthetic CMB images created by considering the above window functions as QUBIC2.0's point spread function. These figures have been provided by J. Ch. Hamilton from the APC Paris.

6.2.4 Calibration techniques

An extremely powerful calibration technique based on the redundancy of equivalent baselines can be implemented in QUBIC2.0. The basic calibration technique is as follows. In an instrument consisting of prefect and identical back-to-back horns and a flawless combiner all redundant baselines will generate equivalent ideal fringes.

$$\begin{aligned} V_{12} &= g_1 g_2 V \\ V_{34} &= g_3 g_4 V \end{aligned} \quad , \tag{6.2.17}$$

Firstly the value V, represents the ideal visibility and is related to the measured visibilities, V_{12} and V_{34}, by the gain matrices, $g_{\{1,2,3,4\}}$, associated with each horn and the optical combiner. A complete diagnostic of the gain matrices will allow us completely calibrate every single input channel of QUBIC2.0. The general self calibration procedure for a polarization sensitive instrument is

$$\tilde{V}_{ij}^{X} = M_{ij} \cdot V_{\beta}^{X} + \eta_{ij} \tag{6.2.18}$$

where the term $\tilde{V}_{ij}^{X}$ contains $N(N-1)/2$ measured visibilities from N back-to-back horns. The matrix V_{β}^{X} contains the ideal visibilities. The term M_{ij} is a 4×4 matrix that describes the tilt, gain and beam mismatch due to the QUBIC2.0 instrument.

Secondly the characteristics of the back-to-back horns can be calibrated by considering the relationship $E_i' = J_i E_i$ where E_i' is an output horn signal and E_i is an input signal. The term J_i ,

$$J_i = \begin{pmatrix} 1 + g_{x,i} & \epsilon_{x,i} \\ \epsilon_{y,i} & 1 + g_{y,i} \end{pmatrix} \quad , \tag{6.2.19}$$

is a Jones polarization matrix. The values within the Jones matrix represent the gain ($g_{\{x,y\},i}$) and error ($\epsilon_{\{x,y\},i}$) induced on the emerging beams by imperfections in the horn antenna.

Therefore quantifying both the M_{ij} and J_i matrices will allow us to diagnose all the errors in QUBIC and completely calibrate the instrument. In order to quantify these

matrices we will use the fact that in the absence of aberrations in equivalent baselines should generate equivalent fringe patterns. Using switches located in the back-to-back horns every single baseline pair can be modulated on/off in order to access the visibilities measured by this baseline alone. Using all baseline pairs a system of equations whose unknowns are the systematic errors contained in the M_{ij} and J_i matrices can be formed. If an array of 400 back-to-back horns is implemented this system of equations is over constrained and we can solve to completely quantify the M_{ij} and J_i matrices. Similar to the approach of data recovery explained in Chapter 2 for QUBIC the notion of equivalent baselines can be used to reduce the complexity of solving the generated system of equations. A full discussion regarding the calibration of an interferometer in which redundant baselines are present can be found in [123]. Also a host of possible errors that may occur in QUBIC2.0 from beam mismatch to tilt have been fully discussed by [124].

A tentative procedure for the calibration of QUBIC2.0 is to measure the N primary beams by scanning a source. This is effectively equal to calibrating N imagers. This should provide the N Jones matrices required to profile the horn antennas. When these matrices have been calculated we will then calibrate QUBIC by generating the ideal visibilities and measuring the $N(N-1)/2$ corrupted visibilities. We then solve the non-linear system of (6.2.18) with a standard least squares method such as a Levenberg - Marquardt based algorithm. The time required to fully calibrate QUBIC is uncertain although initial estimates suggest approximately 9 hours to measure the $N(N-1)/2$ corrupted visibilities while 30 minutes may be required to characterize the Jones matrices for a 20×20 array[5].

The above calibration techniques require the implementation of switches that essentially allow us to turn on and off the horns. Various methods of implementing such switches are being investigated by our colleagues in Manchester University. There are currently 2 different switching methods being considered. We very briefly mention these below. These switches must be able to allow us to examine every single back-to-back pair whilst open and closed and also transmitting two orthogonal polarization

[5]With the QUBIC observing and using auto-calibration techniques the effect of an aberrated combiner is a reduction in efficiency. Since efficiency is a crucial consideration for such sensitive observations my earlier work on combiner designs is necessary for both the QUBIC 1.0 and 2.0 scenarios.

states.

- *Polarized needle switches.*

These switches are cylindrical waveguides filled with strips of conducting material. The operation of these switches is shown in Figure 6.9. These images have been provided by G. Pisano of the Radioastronomy Technology Group, Jodrell Bank Centre for Astrophysics, University of Manchester, UK[6]. Depending on the orientation of the needle strips parts of the polarized beam will be reflected or transmitted. If the two switches shown in Figure 6.9 are cascaded it is obvious the entire signal will be blocked. These needles are placed within rotating blocks inserted in between the flange of the back-to-back horns. Although readily available technologies an immediate drawback to these switches is that they are very expensive to purchase.

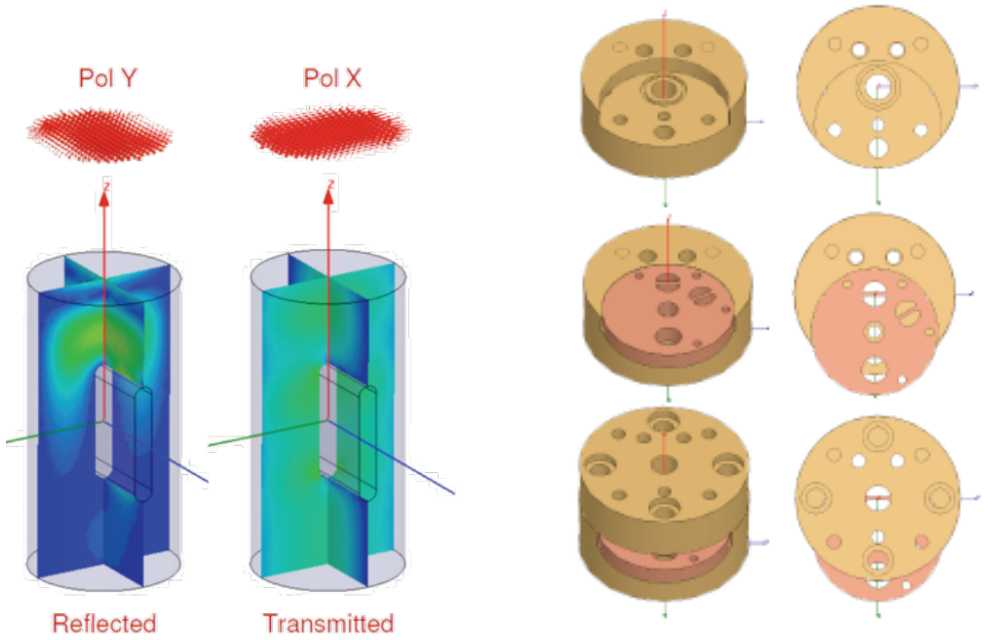

(a) The needle or blade polarization switches suggested for the QUBIC2.0 horn array.

(b) Rotating blade switches inserted between the flange of two back-to-back horns.

Figure 6.9: Possible polarization needle switches that can be implemented for the calibration of QUBIC2.0.

- *Arrays of rotating polarized switches.*

[6]For more information visit `http://www.jodrellbank.manchester.ac.uk/`

Another more cost-effective approach is to use a rotating array of polarization switches shared between several waveguides. These switches are placed between the flanges of the sky and re-emitting horns. Variations of such a system are shown in Figure 6.10. Consideration of the type of polarization switches to implement is currently in the preliminary stages.

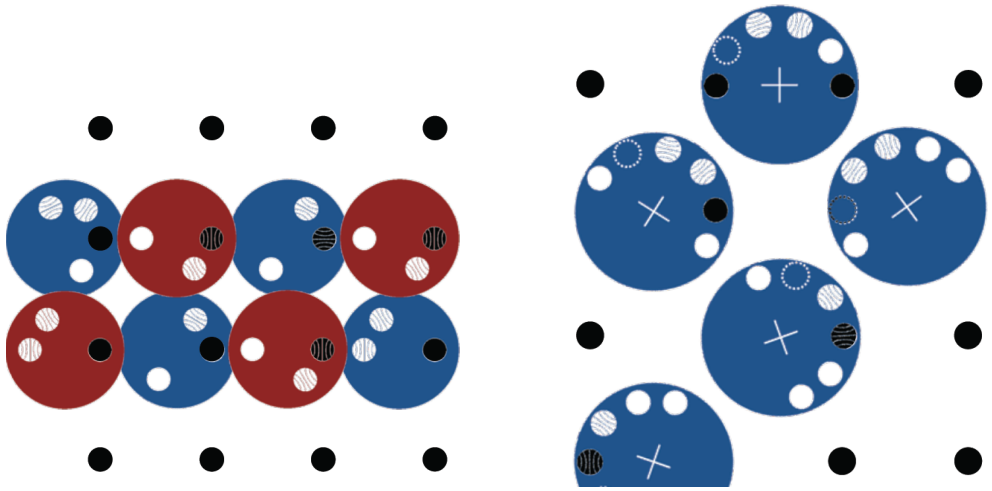

(a) Polarizing switches placed on a rotating plate that can cover multiple channels.

(b) An alternative configuration of polarizing switches placed on a rotating plate that can cover multiple channels.

Figure 6.10: Possible configurations of rotating polarization switches that can be implemented for the calibration of QUBIC2.0. Once again these images have been provided by G. Pisano of the Radioastronomy Technology Group, Jodrell Bank Centre for Astrophysics, University of Manchester, UK.

6.2.5 Cyrostat upgrades

The cryostat design for QUBIC2.0 is largely unchanged from QUBIC. However further testing of various systems in Università di Roma has allowed the maximum dimensions of the QUBIC2.0 cryostat to be clearly defined. The cryostat will be have a cylindrical shape whose maximum diameter can be 900 mm. The three proposed reflector combiners for QUBIC are consistent with these limitations. The length of the cryostat is variable yet is preferred to be under 1 meter. The cryostat design for QUBIC and the likely design for QUBIC2.0 is shown in Figure 6.11. These images have been

provided by Silva Masi of Università di Roma − La Sapienza[7]. As we can see the usual restrictions on the window size and therefore the back-to-back horn array are still applicable. Materials currently available from which to construct the window are mylar or polypropylene. Both of these materials will require anti-reflective coatings. The window may also be constructed of propozote foam however the thickness of such a window would be large.

[7]Università degli Studi di Roma La Sapienza − Piazzale Aldo Moro 5, 00185 Roma. For more information visit `http://www.uniroma1.it/`

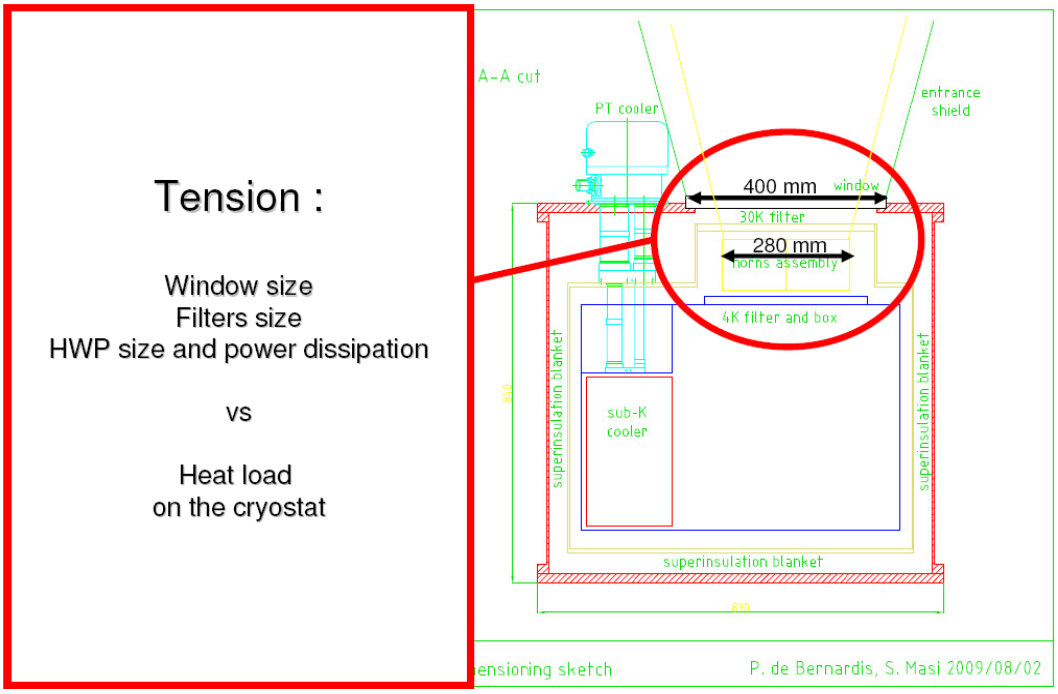

(a) Side view of QUBIC2.0 cryostat. The restrictions of the size of the optical window are clearly visible. The topics listed under **Tension** simply refer to the main issues that must be compromised for during the cryostat design.

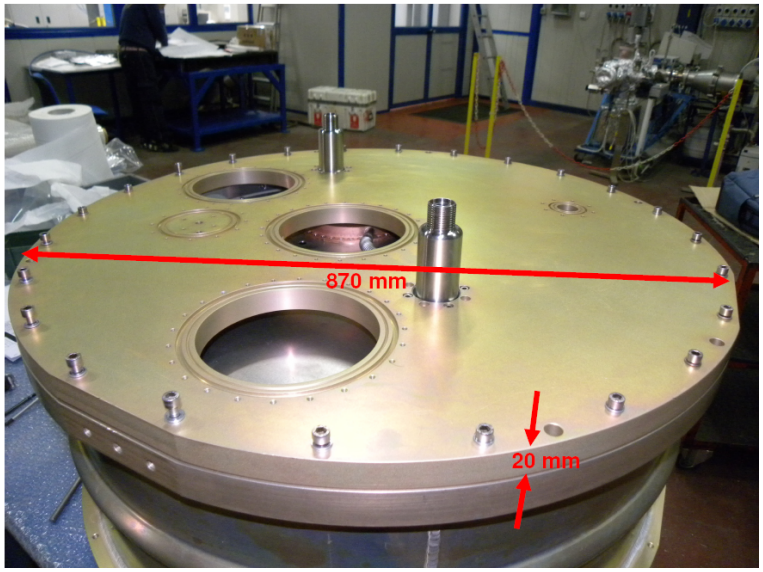

(b) An example of a cyrostat unit under testing.

Figure 6.11: Cryostat design for the QUBIC and QUBIC2.0 experiments.

6.2.6 Remaining issues

Finally we will address the remaining characteristics of QUBIC2.0. In this section we will briefly discuss the implementation of the incoherent detector arrays and the back-to-back horn antennas. These topics have not deviated from the original QUBIC design. As such the reader is referred to Chapter 2 for a full discussion of these issues. Here we will merely provide information of any updates due to on-going research.

- *Incoherent detector array.*

The detector array will be composed of either incoherent bolometer detectors or the new kinetic inductance detectors (KIDS) devices. The fundamental principle of all bolometer devices is that their resistance changes upon contact with incident radiation. By monitoring the change of resistance we can fully quantify the flux of the received signal. There are two choices of bolometer detectors for QUBIC2.0. These are are either hot electron bolometers (HEB) or transition edge sensors (TES). These topics are discussed in [65]. Apart from the bolometers we can also chose to implement KID detector devices. These may be more attractive due to simpler multiplexing methods. They are also robust with no fragile components and only one single layer of material is required in their manufacture. In comparison, the TES detectors are manufactured from 5 layers of various materials. Unfortunately broken membranes are common during the manufacturing stage of the TES bolometers due to the silicone nitride edging process. A full discussion of the development of TES detectors for sub-mm telescopes is presented in [125]. The development of KIDs for mm-wave astronomy is discussed in [126].

- *Back-to-back horn array.*

The most important development as regards the back-to-back horn array is the construction of a corrugated horn using a method called stereolithography. This process is carried out by a company called Tera-X [8]. The technique involves building a layered polymer model of a horn antenna by using a laser to carve the individual corrugations. The completed plastic model is then coated with a conductive metal layer. Using this method construction of 8 CLOVER type horns cost $400. These horns also have a low

[8]Tera-X, 8551 Research Way, Suite 175 Middleton, WI 53562, USA. For more information visit `http://www.tera-x.com/index.html`.

mass density of 1.2 g/cm^3 compared to 8.2 g/cm^3 for horns consisting of pure copper. Another consideration for the horn array is to use a platelet construction technique. In this technique the profiles of a single corrugation of 4 horn antennas are machined or chemically edged into a thin metallic sheet. Multiple sheets each representing an individual corrugation are then stacked on top of one another to form the final 4×4 horn array. The initial costs for chemical etching the platelets are \$100 per horn. Work is currently on-going in the APC Paris to expand this technique in order to create an array of 20×20 horns. One of the earliest discussions regarding the use of platelet technology to fabricate horn arrays is presented in [127]. A number of traditional machining technique used to manufacture corrugated horns are discussed in [128]. Here the benefits and difficulties of the techniques are also discussed.

6.3 QUBIC2.0 optical combiner

A revision of QUBIC has led to the fundamental conclusion that the greater the number of horn antennas the greater the sensitivity of the instrument due to the increased intensity of the point spread function. However as discussed the maximum number of horns implemented will be restricted by window size as well as the number of QUBIC modules we wish to construct. The possible configurations for QUBIC2.0 that will allow us to detect a tensor-to-scalar ratio of 0.01 within $1 \sim 2$ years of operation are shown in Figure 6.12. These parameters have been calculated for 90 and 150 GHz. The most likely choice for QUBIC2.0 is to implement of gird of 20×20 back-to-back horns. This is the reason fringe patterns generated from baselines extending a 20×20 array were presented in Chapter 3. From Figure 6.12(b) we can see that implementing 3 QUBIC modules of 20×20 back-to-back horns observing at a centre frequency of 150 GHz will allow us to detect a tensor-to-scalar ratio of 0.01. The beams from the back-to-back horns will have a FWHM of 14°. These are the instrument parameters agreed upon by the QUBIC collaboration as of July 2010.

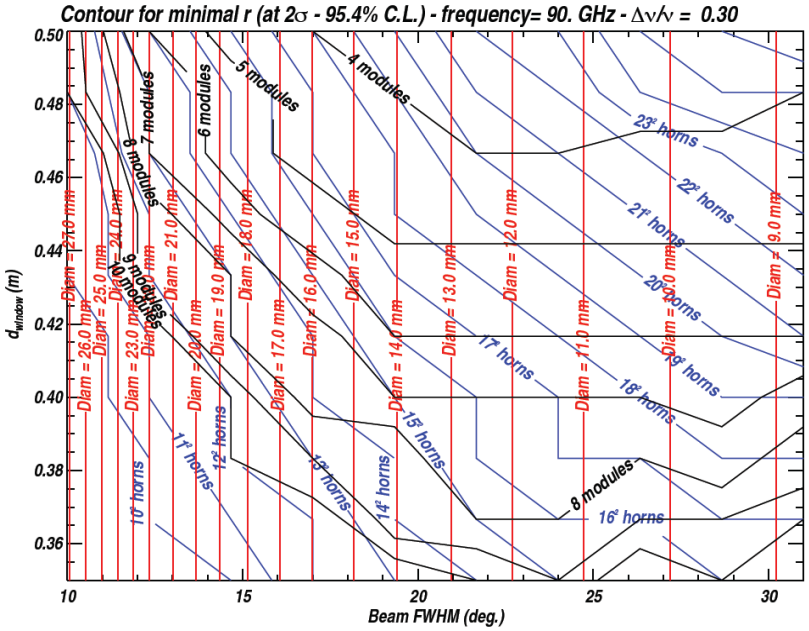

(a) Minimal tensor-to-scalar attainable at 90 GHz.

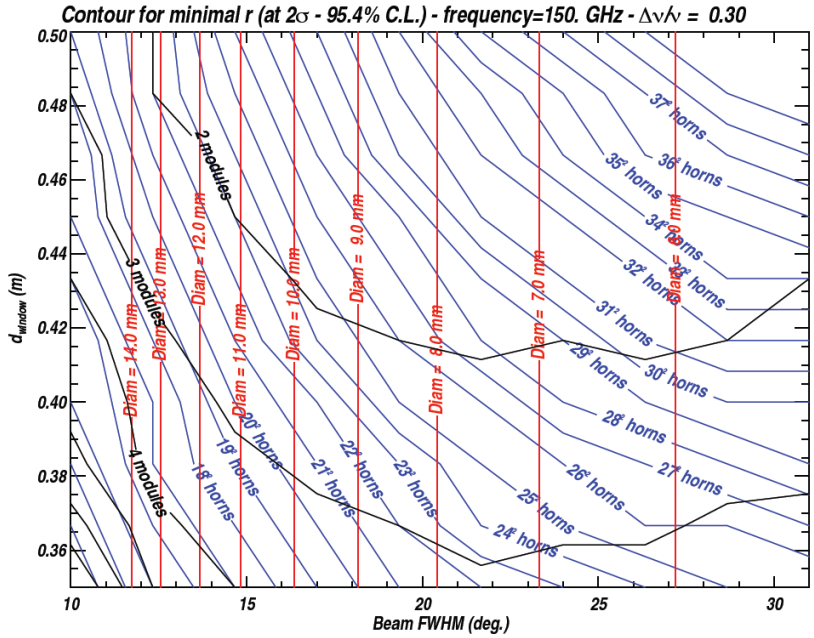

(b) Minimal tensor-to-scalar attainable at 150 GHz.

Figure 6.12: Minimal tensor-to-scalar attainable given a variable number of back-to-back horns, variable beam sizes, the size of the optical window and a variable number of modules. The choice of these parameters will dictate the minimum tensor-to-scalar ratio detectable by QUBIC2.0. These figures have been provided by J. Ch. Hamilton from the APC Paris.

6.3.1 Analysis of optical combiners

We have previously presented a review of various 300 mm reflector combiners for QUBIC. This review consisted of plots of fringe patterns produced by multiple equivalent baselines accompanied by a variance analysis of the power coupled to each bolometer. Considering QUBIC2.0 as a dirty imager provides us with another way to compare the performance of various optical systems. To do this we will generate the point spread function (PSF) of QUBIC2.0. The PSF of the combiner is the interference pattern formed by ideal Gaussian beams propagating from the horn array. We remind ourselves that the PSF is similar to the synthesized beams from which the window function can be recovered.

6.3.2 PSF of reflector combiners

In Figures 6.13 and 6.14 we have displayed the synthesized beams/PSFs of the $reflector$ *optical combiners* discussed in previous chapters. We have used GRASP9 to model these PSFs. Using GRASP9 batch files we propagated a 14° FWHM Gaussian beam from the location of every back-to-back horn, through the optical combiner and onto the detector plane. GRASP9 then summed all the resultant fields to calculate the PSF of the combiner[9]. This analysis was performed for both a 12×12 and 20×20 array of back-to-back sky horns. The results are in accordance with what we expect from the fringes generated by the various baselines displayed in previous chapters. We can see that the PSF of the GCC is almost identical to the PSF shown in Figure 6.6 in which an ideal optical combiner was assumed. The presence of beam distortion is once again evident in the PSF formed by the compensated CG reflector. We note an additional problem with beam distortion is that the focal plane had to be enlarged to in order the capture all the power of the asymmetric fringe patterns formed by the CG. Also shown is the window function generated by the optimized off-axis paraboloid (OP). Figures 6.15 to 6.14 highlight the differences between our current abilities to model the behavior of lens and reflector systems. The fringe patterns in Figure 6.13 and 6.14 are

[9]In our analysis we refer to the final image of the beams from every sky horn combined at the detector plane as the systems PSF.

shown in remarkable detail. Understanding the behavior of the optical components with such accuracy is critical when we wish to search for CMB B-modes.

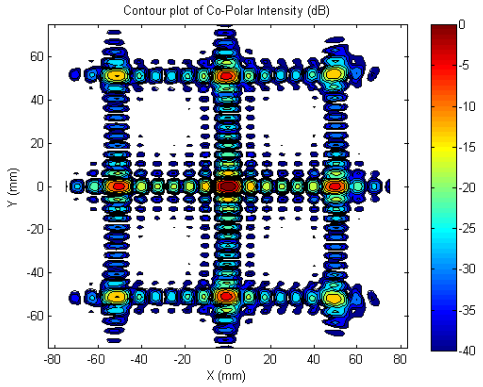

(a) Co-polar intensity of the synthesized beam generated by the GCC.

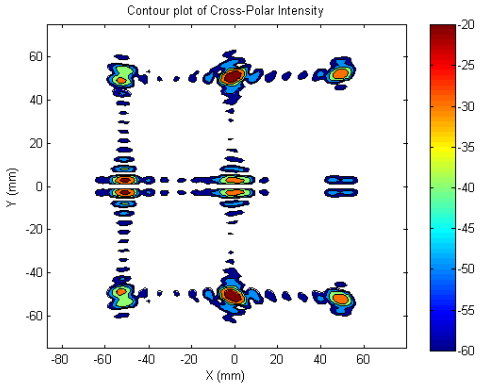

(b) Cross-polar intensity of the synthesized beam generated by the GCC.

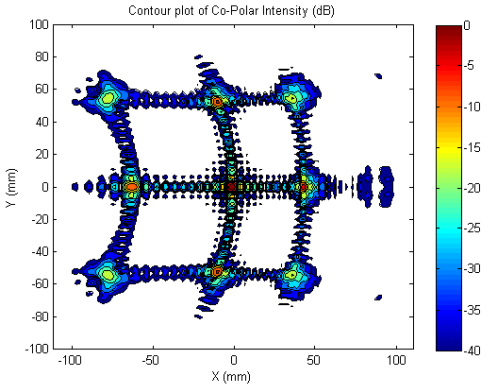

(c) Co-polar intensity of the synthesized beam generated by the CG.

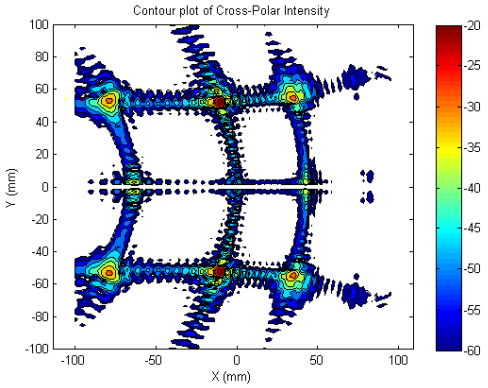

(d) Cross-polar intensity of the synthesized beam generated by the CG.

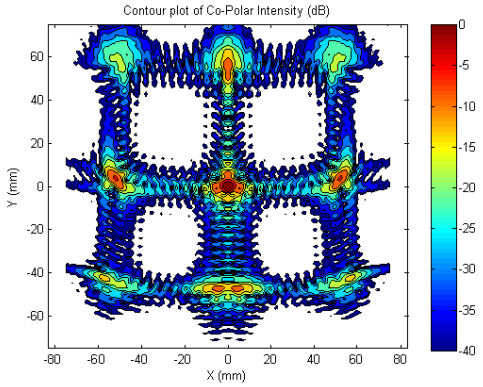

(e) Co-polar intensity of the synthesized beam generated by the OP.

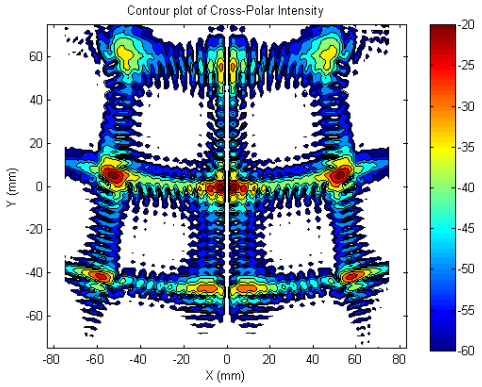

(f) Cross-polar intensity of the synthesized beam generated by the OP.

Figure 6.13: The synthesized beam/PSF generated by 144 14° Gaussian beams propagating through reflector combiners.

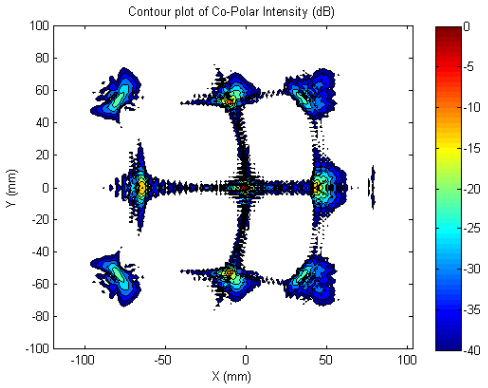

(a) Co-polar intensity of the synthesized beam generated by the CG.

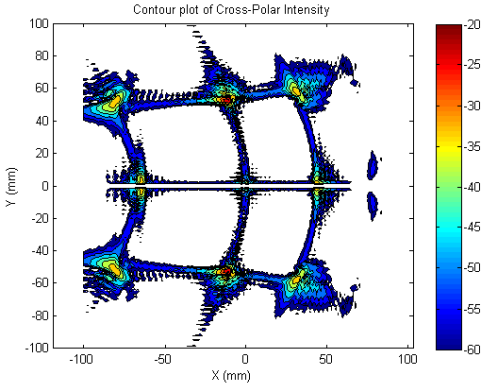

(b) Cross-polar intensity of the synthesized beam generated by the CG.

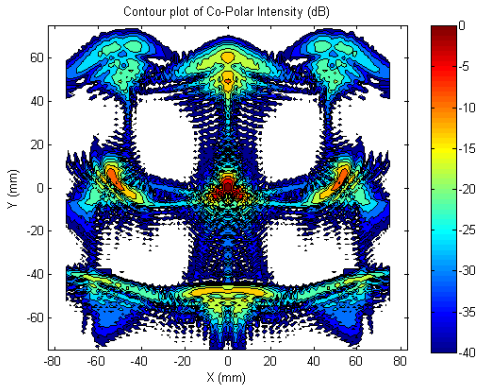

(c) Co-polar intensity of the synthesized beam generated by the OP.

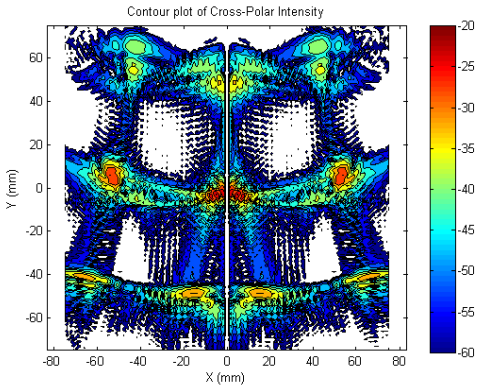

(d) Cross-polar intensity of the synthesized beam generated by the OP.

Figure 6.14: The synthesized beam/PSF generated by 400 14° Gaussian beams propagating through reflector combiners.

6.3.3 PSF of lens combiners

We have used Zemax to compute the PSF of the symmetric Cooke Triplet lens and the symmetric dual convex lens. The PSFs below have been calculated from 14° FWHM Gaussian beams propagating from 9 field locations. The reason we choose only to calculate the PSF from 9 field locations is for convenience because we are unable to dynamically change field position of the propagating Gaussians using the Zemax programming language. The field position had to be altered manually. We felt that beams from a 3 × 3 horn array were sufficient to demonstrate the PSFs of the lens combiners. The PSFs of the symmetric Cooke triplet lens and the symmetric dual convex lens are shown in Figures 6.15 and 6.16. The locations from which the Gaussian beams were propagated in order to form these PSFs are listed in 6.1.

Table 6.1: Coordinates (x_i, y_i) of back-to-back horns used to form Figures 6.15 and 6.16.

(-20,20)	(0,20)	(20,20)
(-20,0)	(-20,0)	(20,0)
(-20,-20)	(0,-20)	(20,-20)

Unfortunately Zemax will not allow us to carry out a conclusive analysis of the lens combiners we have presented. This is because analysis techniques implemented by Zemax become completely inaccurate when the incident wavefronts propagate from off-axis locations. The Zemax manual states that prorogation algorithms implemented in Zemax will not accurately predict the diffraction of the wavefronts for a fast optical system. This is because these algorithms assume that the medium through which a wavefront is propagating is constant. As such the Zemax algorithms break down and become completely inaccurate once the wavefront being sampled encounters any edge effects.

When we examine layouts of the above lens combiners it is apparent that in order to achieve any accurate modeling of the beams propagated from the most extreme back-to-back horns the surface of the lens must be sampled over an area whose size will undoubtedly include edge effects. Therefore any precise analysis of these systems will be confined to a small area around the optical axis. For QUBIC this is especially

problematic as conventional geometrical optics tells us that the beams propagating from the most extreme horns on the back-to-back array will be the most aberrated. We expect all the above systems will produce high quality synthesized beams when we only consider beams propagating from short off-axis locations.

In order to select the best lens combiner for QUBIC2.0 we are interested in the complete synthesized beams formed by all horns in the back-to-back array. Unfortunately Zemax will not allows us to fully distinguish which lens combiner is most suitable for QUBIC2.0. Trial and error has led us to conclude that a Zemax Fourier optical analysis of the lens combiners will only produce trustworthy results within a radius of 30 mm around the optical axis. Hence the displacement values used to obtain the above fringe patterns and point spread functions. Although due to its wider DLFOV the symmetric Cooke triplet is a higher performing system then the symmetric double convex system, as we can see from Figures 6.15 and 6.16, it is difficult to distinguish from our limited Zemax analysis whether the Cooke triplet will produce higher quality synthesized beams than the dual convex system.

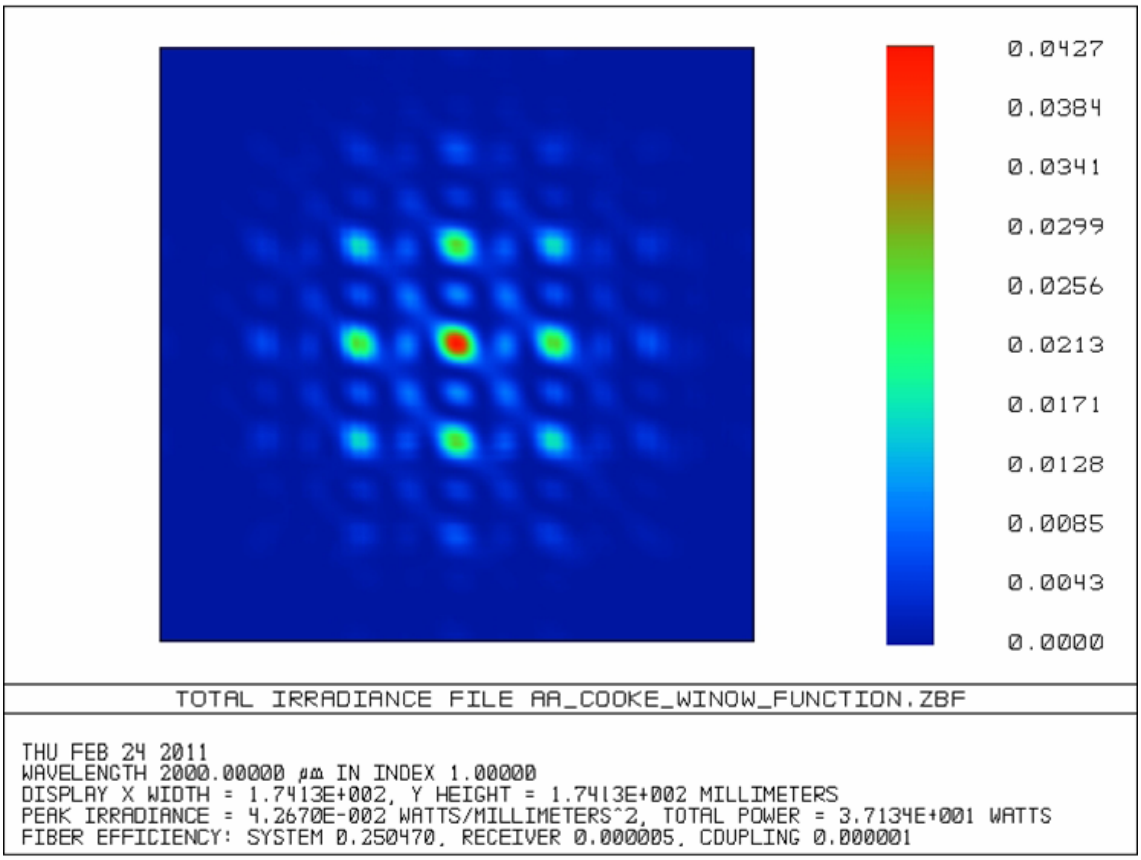

Figure 6.15: The PSF generated by 9 Gaussian beams propagating through the Cooke triplet lens combiner shown in Figure 5.9.

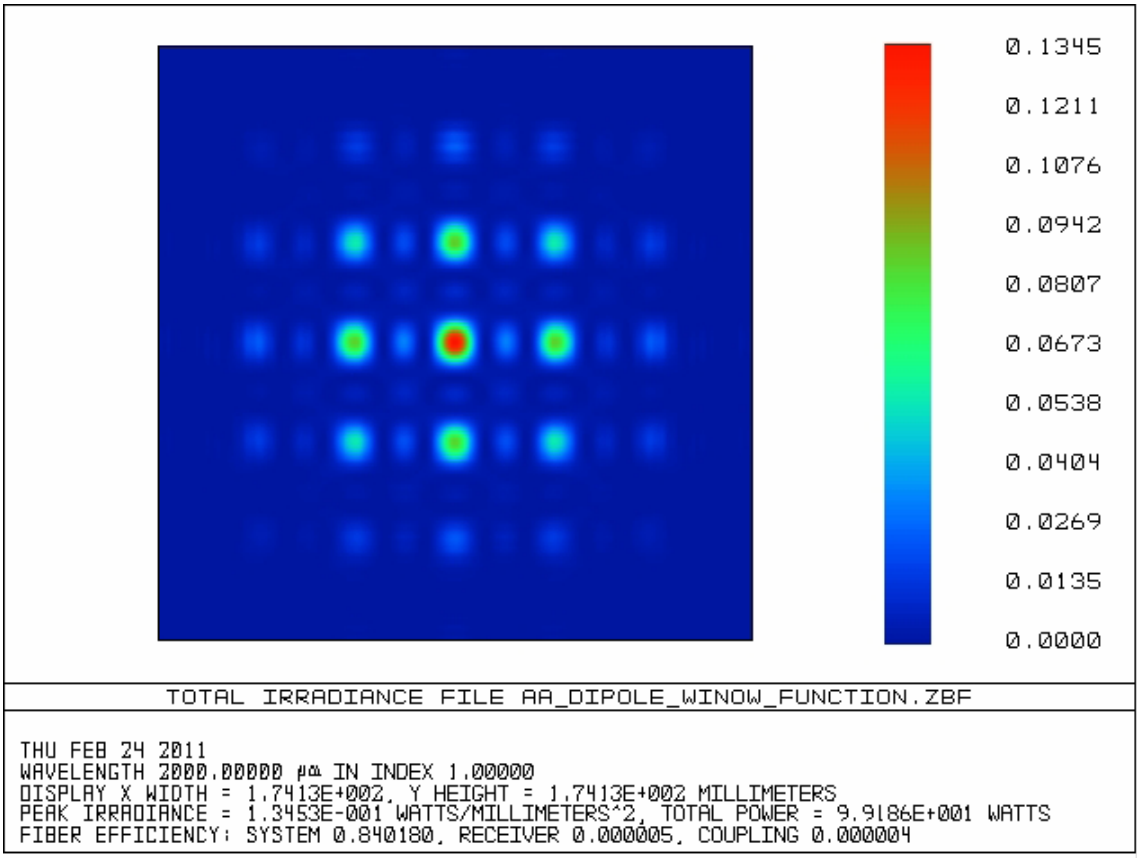

Figure 6.16: The PSF generated by 9 Gaussian beams propagating through the symmetric double convex lens combiner shown in Figure 5.10.

GRASP9 has no faculty for modeling lens combiners. Currently work is on-going in NUIM to attempt to model the fringe patterns produced by the above lens combiners using an in-house optical software package called MODAL. This package will attempt to calculate the window function produced by the lenses using a variation of physical optics. The operation of MODAL has been briefly explained in Chapter 2 [10].

6.4 Loss of sensitivity caused by optical combiners

We will now revisit the 300 mm focal length compensated Gregorian (CG) shown in Figure 4.4. The geometric details of this reflector are listed in Table 4.3. We have previously demonstrated that this system can image all beams from a 20×20 back-to-back horn array onto the bolometer detectors. Also we have shown that the behavior of a reflector combiner can be more accurately modeled using physical optics than that of a lens combiner. Finally the manufacturing of a reflector combiner that will be placed in an extremely low temperature cryostat is somewhat less difficult than a refractive combiner such as a Cooke Triplet that uses large lenses[11]. For these reasons we conclude that the CG discussed in Chapter 4 is the most suitable optical combiner for QUBIC2.0.

In Figure 6.5 it was shown that QUBIC2.0 could achieve a level of sensitivity comparable with a CMB imager. Here we assumed an ideal window function generated by an ideal optical combiner. We must now take account of the loss of sensitivity in QUBIC2.0 due to the implementation of a realistic combiner that will generate wavefront aberrations in the combining beams. This is in fact the best way to judge the proposed design for the combiner (rather than the variance in power coupled to the bolometers by sets of equivalent baselines as discussed in Chapter 4).

Donnacha Gayer of NUIM along with our colleagues in the APC Paris have examined the loss in sensitivity due to aberrations in the 300 mm focal length CG combiner presented in Chapter 4. A fundamental 14° Gaussian beam was propagated from

[10] For more information on MODAL visit `http://physicsresearch.nuim.ie/modal/modal.html`. Also an article detailing the use of MODAL for the optical analysis of CMB telescopes can be found in the SPIE newsroom at `http://spie.org/x14026.xml?ArticleID=x14026`

[11] The Cooke Triplet to which we refer is shown in Figure 5.9.

every horn in a 20×20 array. A 13.7 mm diameter, consistent with the expected values for the QUBIC2.0, was assumed for each horn. We have assumed that all beams are propagating from "ultra-Gaussian" horns in which 99.9% of the beam power is coupled into a fundamental Gaussian beam. Such horns were designed for the CLOVER mission [129]. Also we assume that the phase radius at the mouth of these horns is flat. We have therefore propagated a fundamental Gaussian beam through the combiner whose waist radius is located at the mouth of the re-emitting back-to-back horn.

The positions from which each Gaussian beam was propagated in the object plane were calculated using a simple sweep algorithm[12]. Using GRASP9 the amplitude and phase of each Gaussian beam was calculated at the focal plane.

These files were then sent to our colleagues in the APC Paris. From these files our colleagues calculated the window function in terms of multipoles on the sky. The window function was then compared with that of a perfect combiners. The results are shown in Figure 6.17. Here both bandwidth **BW** and the size of the bolometer detector have been taken into account. The peaks are readily explained by the interferometric nature of QUBIC2.0. Essentially the Airy pattern generated by the QUBIC2.0 combiner consisting of an unblocked entrance aperture is convolved with the fringe pattern generated by the presence of the back-to-back array. The peaks clearly shown that the CG will allow us access to a discrete number of multipoles over the sky. Each of these multipoles will be sampled with a resolution $\sim \frac{1}{\sigma_{primary}}$ where $\sigma_{primary}$ is the FWHM of back-to-back horns with which we view the sky. Figure 6.17 shows that the loss of sensitivity caused by the CG combiners is $\sim 10\%$. This is shown by the difference between the solid and dashed red lines. Within the overall error budget of the project (bearing in mind that QUBIC must compete with imaging experiments in terms of efficiency) such a loss has been deemed quite satisfactory. Therefore we have conclusively shown that the CG introduced on Chapter 4 will allow QUBIC2.0 to sample the CMB with sensitivity comparable with that of an imager.

[12]We have previously discussed this algorithm. For example see equations (4.3.1) - (4.3.6) where the appropriate terms have been altered to accommodate a 14° FWHM beam that must be swept 12×12 times at 12 mm intervals.

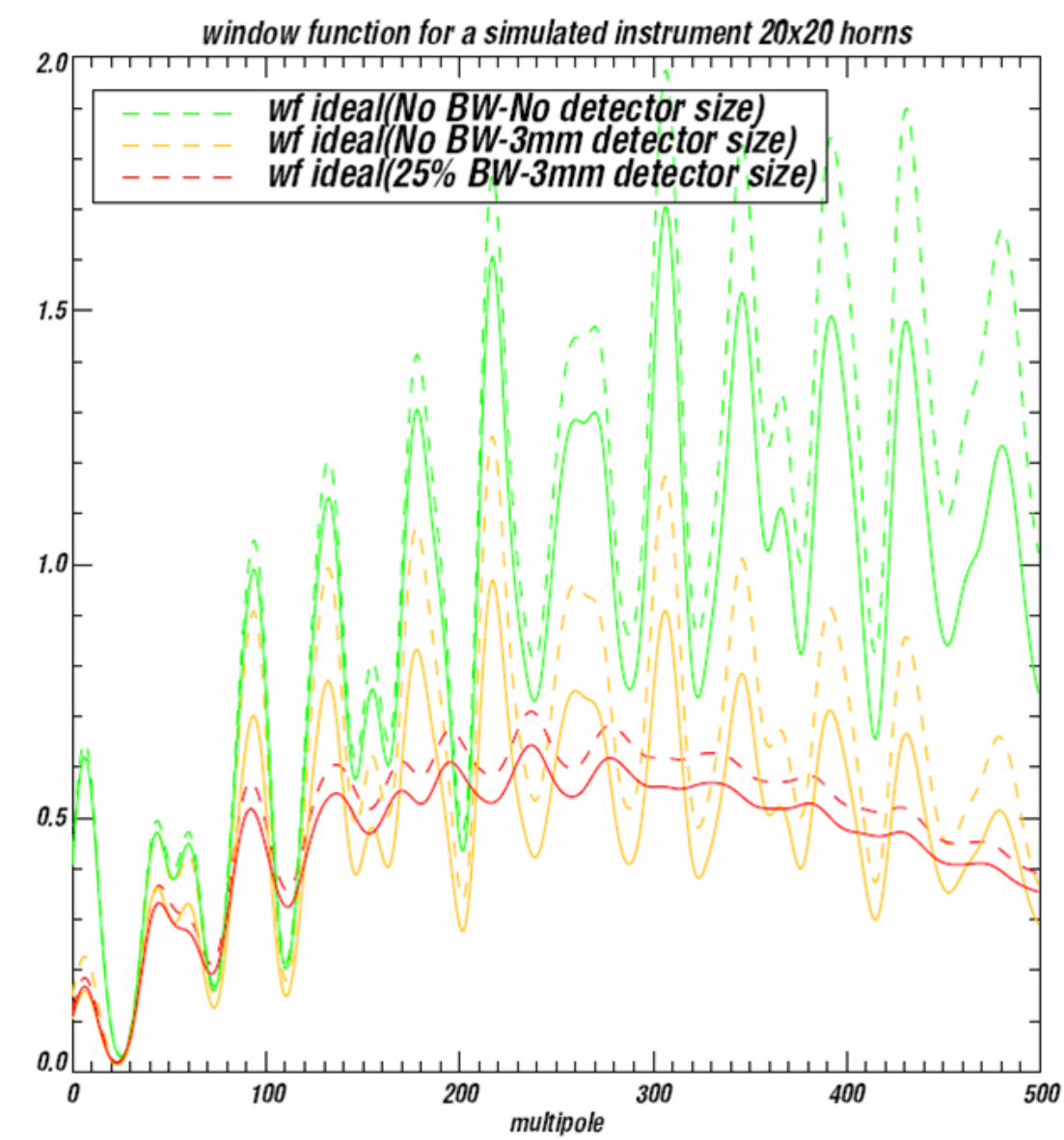

Figure 6.17: The window function of the 300 mm focal length CG designed for QUBIC2.0. The dashed lines show the window function of the CG. The full lines indicate the window function obtained from an aberration free ideal combiner. We note that the units on the y-axis are arbitrary. Both bandwidth **BW** and the 3 mm^2 size of the detectors have been taken into account. This image has been provided by Marie-Anne Bigot-Sazy of the APC Paris.

6.5 Conclusions

In this chapter we have presented the revamped QUBIC experiment entitled QUBIC2.0. The QUBIC2.0 will attempt to recover the CMB polarization from a "dirty image" formed on an array of bolometer detectors. This "dirty image" is a convolution of the synthesized beam generated by the QUBIC2.0 optical system and the incident sky signal. Essentially the synthesized beam is the point spread function formed by the back-to-back horns array and the optical combiner. As such it has been our task to design an optical combiner that produces a high quality synthesized beam over the smallest possible detector array. As we established in Chapter 4 the criterion that an optical combiner for QUBIC must obey is that it must be a good imager forming wavefronts with low aberrations at the focal plane. We have concluded that the best candidate design for the QUBIC2.0 is the CG we presented in Chapter 4. In this chapter we have shown the PSF of this system calculated using a physical optics analysis of the beams propagating from each horn in a 20×20 array.

In the authors opinion the most important conclusion of this chapter concerns Figure 6.17. This plot indicates that the drop in sensitivity of QUBIC2.0 due to wavefront aberrations and beam distortion in the synthesized beams generated by the CG is on average $\sim 8 - 10\%$. Such a loss has been deemed within tolerable levels for QUBIC2.0.

We have previously shown that this combiner induces a greater amount of amplitude distortion in the synthesized beam than the GCC. However the fact that the CG allows a larger amount of back-to-back horns to be implemented means the overall drop of sensitivity caused by the CG is less than the GCC. Therefore the CG we introduced in Chapter 4 fulfills all requirements for the QUBIC combiner. The wavefront aberrations generated by this combiner do not adversely affect the instruments sensitivity, the system can accommodate a large array of 20×20 back-to-back horns and finally the system will fit inside a cryostat of realistic dimensions. Provided we are able to include both the RHWP and the polarizing grid along with the CG inside the cryostat it is quite probable we have found a fixed design for the QUBIC2.0 combiner. Such technical issues are currently been investigated by Donnacha Gayer at NUIM.

7 Birefringence in CMB Polarimeters

7.1 Introduction

It was mentioned in Chapter 5 that, despite there being several promising optical designs, lenses were not a favored option for the QUBIC telescope. In addition to mechanical and modeling issues, the possibility of birefringence in lenses is a potential difficulty for QUBIC. In this chapter I review some data from a CMB imager called QUaD and investigate whether birefringence in one or more lenses could be the cause of some possible problems encountered.

The QUaD experiment concluded after a third winter of observation in the South Pole. We can now review the experiment with the benefit of hindsight and analyze the optical system implemented in the telescope. Such a review will lead to the improvement of the next generation of CMB polarimeters.

7.2 A brief summary of QUaD

7.2.1 The QUaD polarimeter

QUaD was a ground based high-resolution CMB polarimeter. The optical design of QUaD consisted of bolometric receivers, two re-imaging lenses and a 2.6 m Cassegrain telescope. The large diameter of the primary mirror allowed QUaD to observe the CMB at multipoles up to $l \approx 2500$. QUaD's focal plane consisted of 31 polarization

sensitive bolometers (PSB). Of these PSB 12 operated at 100 GHz while the remaining 19 operated at 150 GHz. The telescope was located in the MAPO observatory approximately 1 km from the South Pole. First light was achieved in February 2005. Observations of the CMB were carried out over 3 seasons beginning in May 2005. The experiment was completed in 2008 and the results were published in November 2009. These are shown in Figure 7.1. Here the results are compared to those from the WMAP, ACBAR, BICEP, Boomerang, CBI, CAPMAP, MAXIPOL, and DASI CMB experiments. The results and their impact on modern cosmology has been fully discussed in [130]. A full account of the operation of the QUaD polarimeter can be found in [131] while a detailed description and analysis of the full optical system is provided by [132]. An excellent summary of the various technical aspects of QUaD is also presented in [133]. The layout of QUaD is shown in Figure 7.2. The position of the 31 fields and the orientation of the PSBs at these locations are shown in Figures 7.3 and Table 7.1.

During operation it was discovered that orthogonally polarized beams from the same pixel in the focal plane (even the on-axis one) had slightly different locations on the sky. The displacements of orthogonally polarized beams led to the suspicion that one of the HDPE elements in the focusing system was birefringent. This chapter is concerned with assessing whether or not the displacements between orthogonally polarized beams that occurred at QUaD's focal plane can be accounted for by birefringence in either the lenses or the optical window of the cryostat.

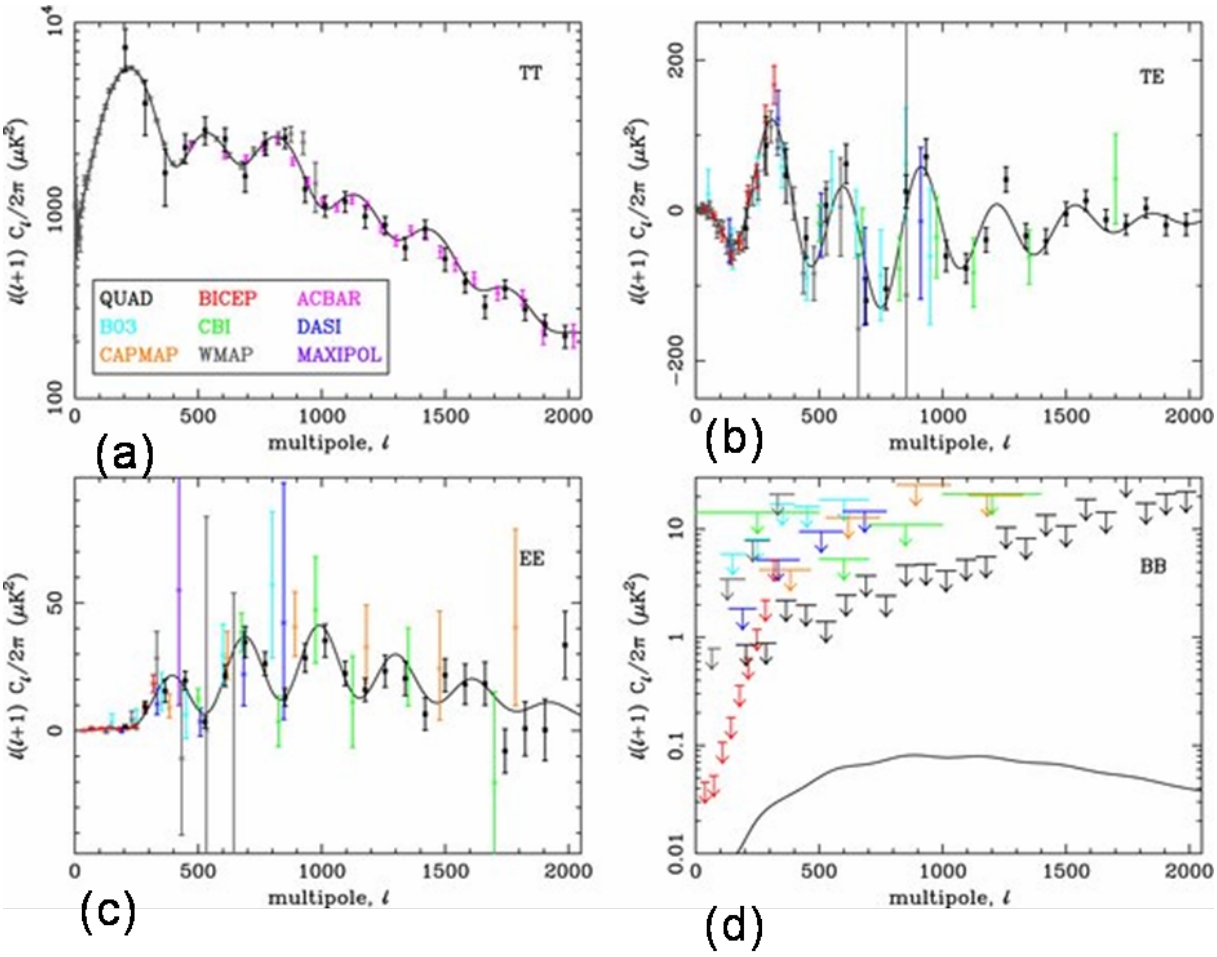

Figure 7.1: QUaD measurements of the (a) TT, (b) TE, (c) EE, and (d) BB CMB power spectra. The black lines are the power spectra expected from the best-fit ΛCDM model to the WMAP 5-year data. These figure have been taken from [130].

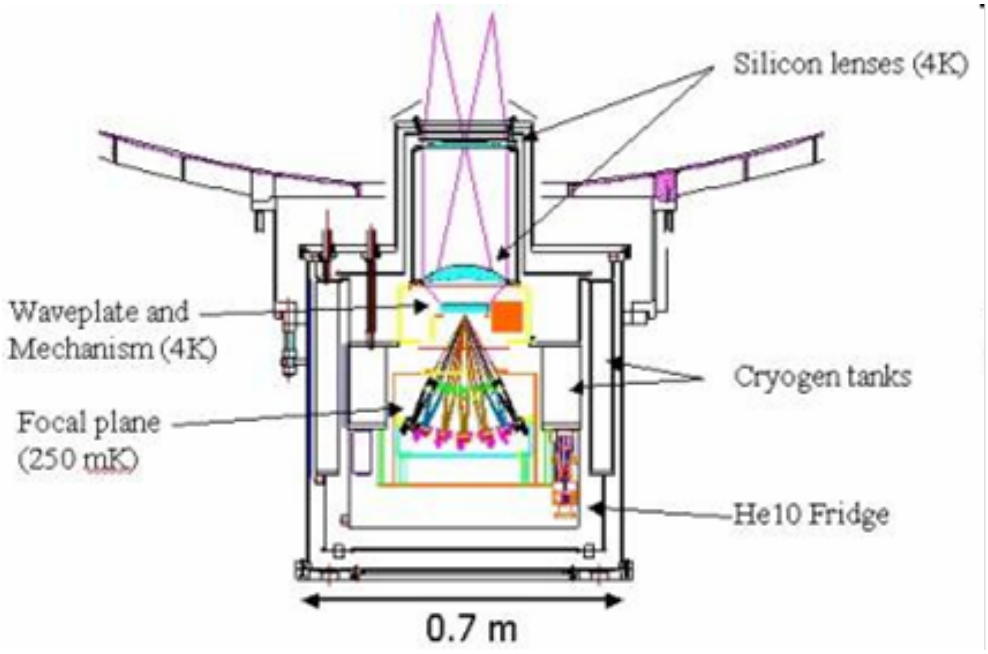

(a) The QUaD cryostat contained two cold lenses that coupled the radiation from the telescope onto the focal plane.

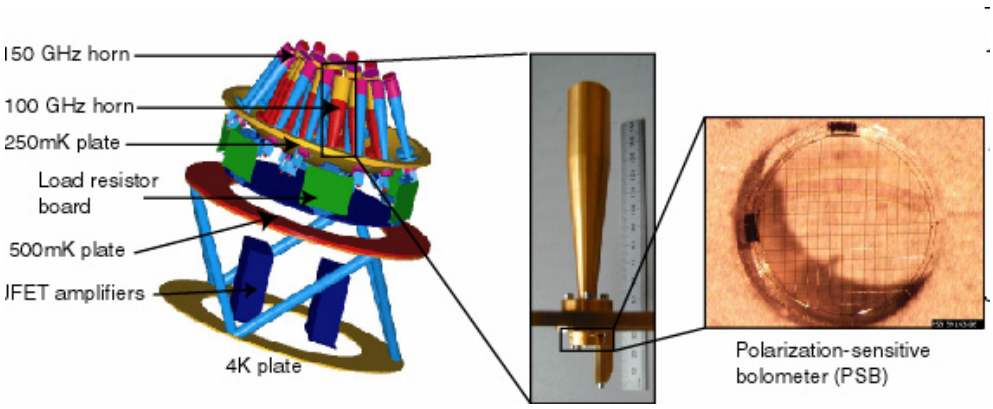

(b) QUaD's focal plane consisted of 31 corrugated feed horns each feeding a polarization-sensitive bolometer (PSB).

Figure 7.2: Schematic diagram of the components in the QUaD CMB telescope. These images have been taken from `http://www.stanford.edu/~schurch/quad_results.html`.

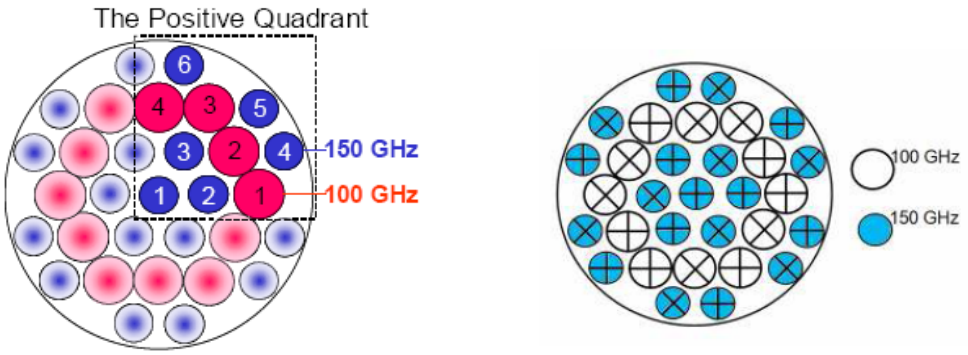

(a) The position of QUaD's 100 and 150 GHz detector horns on the instruments focal plane. The detector numbers correspond to those listed in Table 7.1.

(b) Polarization orientation of QUAD's 100 GHz and 150 GHz fields.

Figure 7.3: The position of the 31 detector horns over QUaD's focal plane.

7.2.2 QUaD model in Zemax

When analyzing QUaD using Zemax we fix the entrance aperture of the optical system at the Lyot stop 168 mm in front of the horn detectors. The horn detectors then represent the system's object plane from which we use Zemax to trace rays from each field position through the telescope. An ideal paraxial lens is placed in the Zemax model file after the full optical system. This lens focuses rays propagating from the horn detectors onto an image plane. This image plane is implemented to allow us to examine where the rays traced from the horn detectors end up on the sky. The focal length of the paraxial lens was set to 3437.74 mm and due to QUaD's geometry this forces one millimeter on the image plane to equal one arc minute on the sky. We will examine the behavior of a number of rays propagated from QUaD's 31 field positions at the object plane shown in Figure 7.4.

7.2.3 Introduction to birefringence.

Birefringence is the result of electrical anisotropies that may occur within dielectric optical components. These can be introduced in the manufacturing process (alignment

Table 7.1: The coordinate locations of QUaD's focal plane pixels for horns number 1-6 in Figure 7.3. All horns are placed on a circular curved plane whose radius is 168 mm. The coordinates below have been projected onto a flat surface behind this curved surface.

	150 GHz		100 GHz	
	X (mm)	Y (mm)	X (mm)	Y (mm)
1	0	0	65.56	0
2	33.39	0	50.04	28.89
3	16.7	28.92	32.78	56.77
4	81.12	27.55	0.00	57.78
5	64.42	56.47		
6	16.7	84.0		

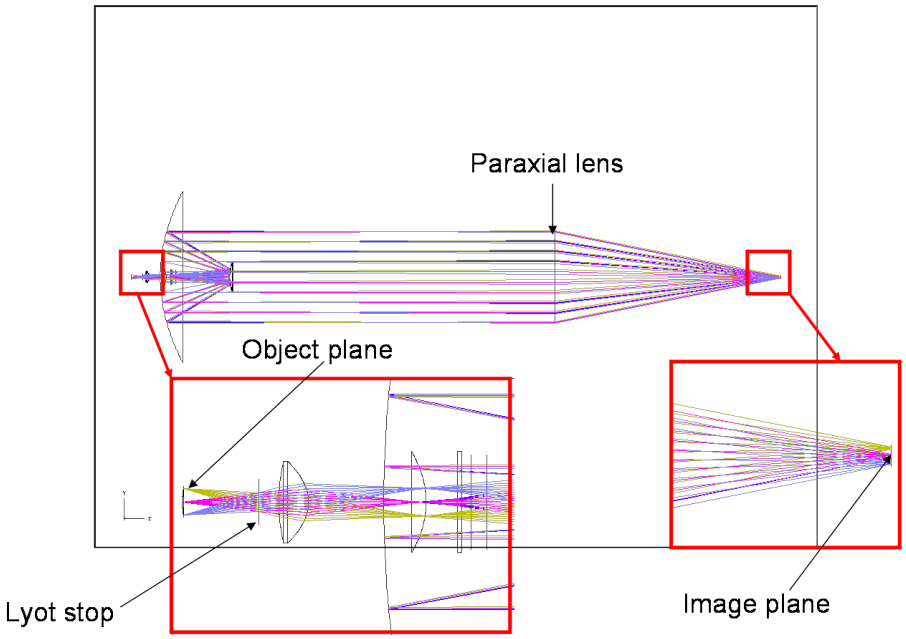

Figure 7.4: The QUaD telescope.

of long-chain polymers) or caused by stress (for example on a cryostat window, for example). As a result, when a wavefront propagates through a birefringent material the displacement electric field vector **D** is no longer aligned with the electric field vector **E**. Usually any electrical anisotropies encountered by an incident wave depend on its polarization. Therefore if partially polarized light is incident on a birefringent material

the light will become split into two separate fields $\mathbf{S}$ and $\mathbf{S_e}$. Here $\mathbf{S}$ is the Poynting vector of the ordinary refracted light whose direction is altered in accordance with Snell's law. The term $\mathbf{S_e}$ represents the so-called extraordinary refracted Poynting vector whose direction is dependent on the extraordinary refractive index and the crystal axis of the material. The crystal axis is the surface normal around which the polarized wave appears to have been bent by an angle dependent on the extraordinary refractive index. A simple diagram of such a scenario is shown in Figure 7.5. A succinct discussion of birefringence in optical crystals including a full explanation of the origins of both the extraordinary index and crystal axis is presented in [134]. Two excellent techniques for ray-tracing through dielectric slabs are presented in [135] and [136]. Meanwhile a comprehensive technique to ray-trace through paraxial birefringent lenses is presented in [137]. These techniques are applicable, provided that both the crystal axis and the extraordinary refractive index can be predetermined.

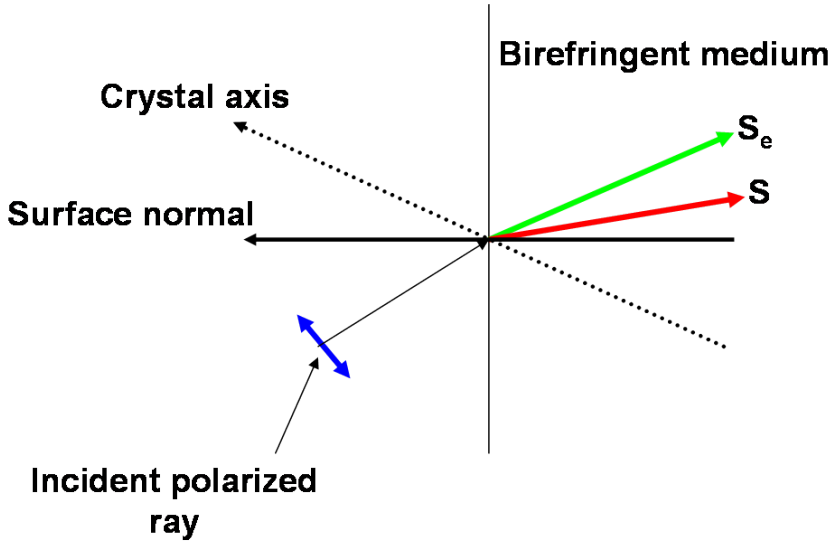

Figure 7.5: Polarized light incident on a piece of dielectric material. The Poynting vector $\mathbf{S}$ is bent towards the surface normal in accordance with Snell's law. The direction of the extraordinary refracted Poynting vector $\mathbf{S_e}$ is altered by the crystal axis and the extraordinary refractive index of the medium.

The displacements of orthogonally polarized beams propagating through QUaD have been measured and made available to the author for analysis. We will now attempt to confirm whether birefringence in QUaD's HDPE elements could produce such offsets. If we can show that birefringence is a possible cause of such beam displacements we

will attempt to uncover exactly which part of the QUaD system is responsible and estimate the optical axis and the extraordinary refractive index of that element. In order to accomplish these tasks we have traced rays from QUaD's detector horns through the telescope onto the sky. We have re-defined QUaD's dielectric lenses as birefringent elements whose properties are similar to uniaxial crystals. Using estimates of the extraordinary refractive index and/or the crystal axis obtained from the relevant literature we have modeled several birefringent QUaD designs in Zemax and analyzed the outputs.

The QUAD telescope provides a unique opportunity to investigate birefringence within CMB polarimeters. Such work is now of critical importance because several separate CMB experiments have all experienced optical problems that may be attributed to birefringent materials. The QUAD telescope contains an optical window and two refocusing lenses. Of these lenses one acts as a focusing device while the other serves as a collimating device. We can therefore investigate the effects birefringence occurring in three various dielectric components that one would find in a CMB experiment. The displacement of orthogonally polarized beams propagating through QUaD have been measured and are shown in Figures 7.6c and 7.6d. Here we see the displacement between the orthogonal beams increases roughly with the distance of the QUaD fields from the bore sight.

7.3 Investigation of possible birefringence in QUaD

7.3.1 Using Zemax to investigate birefringence in QUaD

A diagram of the optical arrangement of the QUaD telescope is shown in Figure 7.7. QUaD is a symmetric system therefore the optical axes/bore sight is parallel to the z-axis and runs along the centre of the telescope. This chapter is dedicated to investigating whether birefringence in the first lens (**L1**), the second lens (**L2**) or the window (**WD**) can account for displacements similar to those shown in Figure 7.6.

The most difficult aspect of modeling a suspected birefringent material is the number of possible free variables for which to account. There are two primary defining characteristics of any birefringent material. The first is the extraordinary refractive

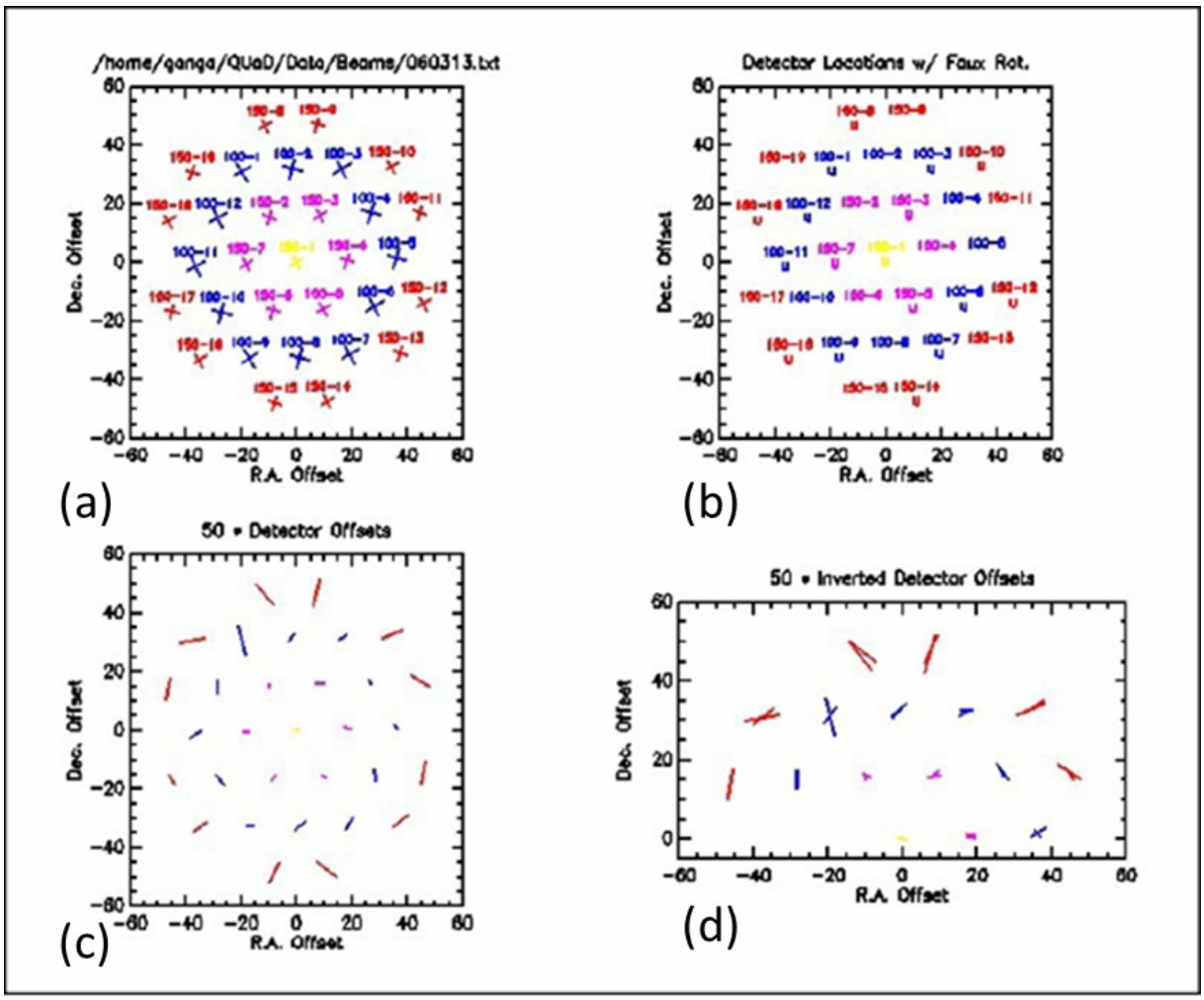

Figure 7.6: Measured displacements between polarized beams within QUaD. The end of each line shows the location of a beam centre. The yellow, purple and red locations indicate the 150 GHz detectors. The blue locations shown the 100 GHz detectors. (a) The orientation of the polarized 100 & 150 GHz detectors. (b) Detector locations in the focal plane. (c) Displacements between orthogonally polarized beams on the sky (i.e. the lines join the location on the sky whereof orthogonally polarised beams from the same horn. If there were no birefringence then the lines would all be of zero length). Here the units of both axes are arc minutes on the sky ($\times 50$). (d) Here the displacements shown in part (c) have been folded about the x-axis. Once again the units of both axes are arc minutes on the sky ($\times 50$).

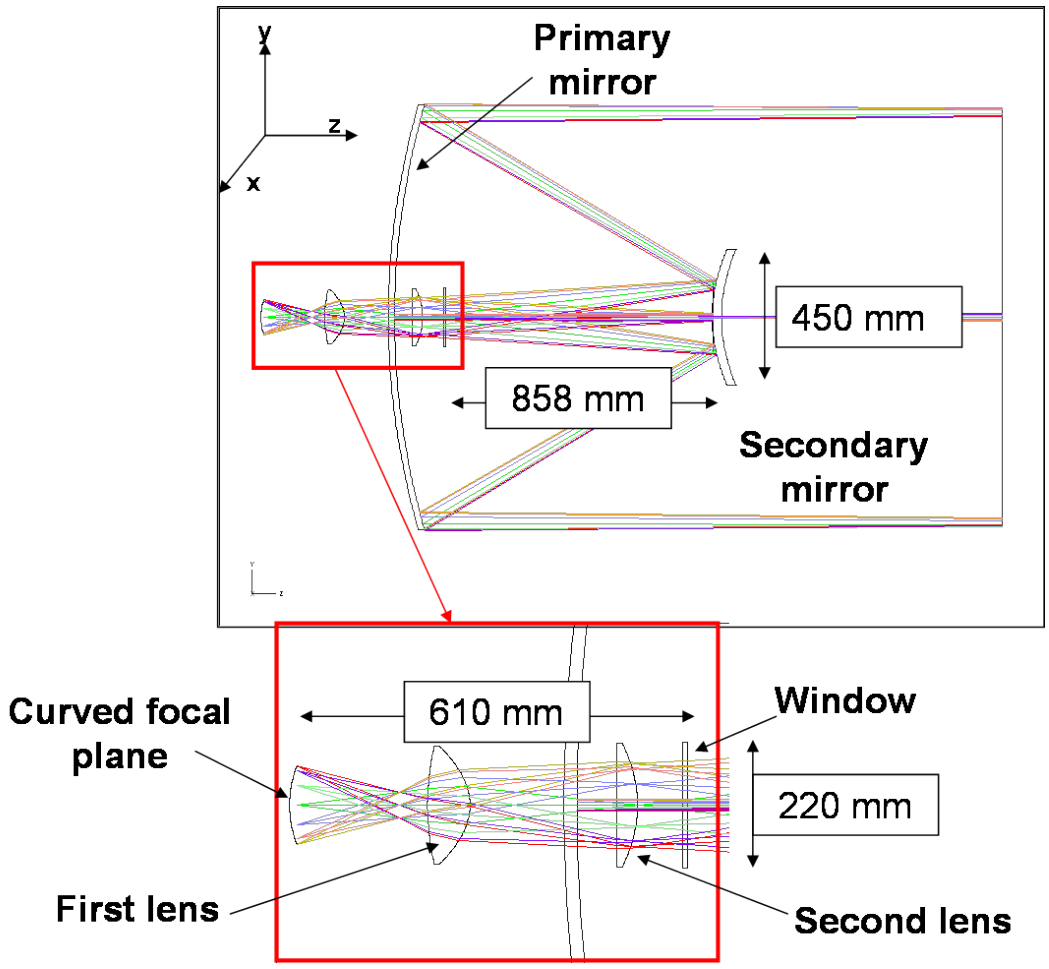

Figure 7.7: The optical layout of the QUaD telescope. The diameter of the primary mirror is 2600 mm. Here we have shown rays propagating from QUaD's 150 GHz detector horns.

index that defines how much a polarized ray is bent as it is incident on the material. The second is the crystal axis which defines the orientation of the surface normal around which the incident ray is bent[1]. There is an inherent difficulty trying to exactly diagnose birefringence in QUaD because *neither* of these quantities are known. Also Zemax will not allow a dynamical variation of the extraordinary refractive index. Therefore simply writing an optimization program to vary the birefringent proprieties of the dielectrics until displacements similar to those seen in QUaD is produced is not likely to be possible.

[1]The lenses are not made of crystal but of plastic, long-chain polymers may produce a varying birefringence effect depending on the details of the manufacturing process.

The purpose of this section is to examine whether or not birefringence in any of QUaD's dielectric elements can produce patterns of displacements of beams on the sky similar to those observed. As a starting point for this investigation we have assumed very simplex birefringent conditions in QUaD's dielectric elements. We have assumed that all beams are normally incident on the HDPE elements and that the crystal axis of the birefringent material is co-planar with the propagation axis of an incident Gaussian beam and QUaD's x-axis. A simple diagram of these two assumptions is shown in Figure 7.8.

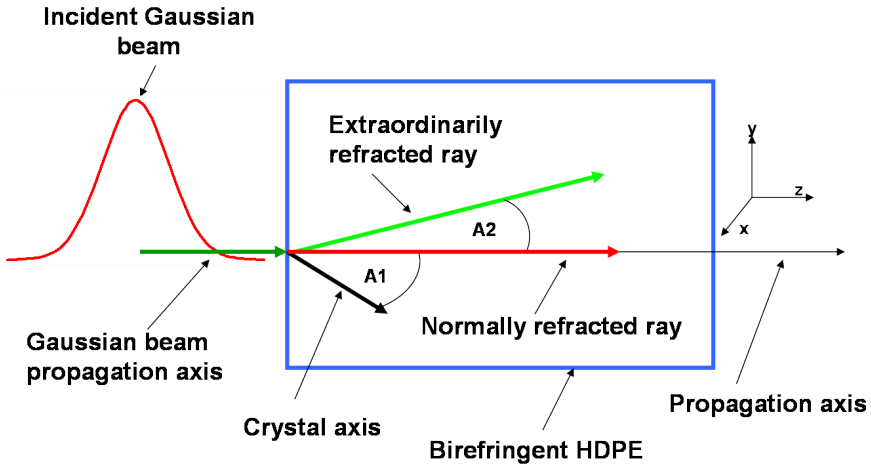

Figure 7.8: A Gaussian beam normally incident on a slab of birefringent HDPE. Here **A1** is the angle between the propagation axis and the crystal axis. Also **A2** is the angle between the two refracted rays. These angles are denoted as ϕ_{CA} and θ_e respectively in the accompanying text.

Finally we assume that the maximum possible angle θ_e occurs between the two refracted rays. When this occurs both the wave vector $\mathbf{k_e}$ and the Poynting vector $\mathbf{S_e}$ for the extraordinary ray align with one other. It has been shown under such circumstances that

$$\phi_{CA} = \frac{1}{2} \arccos \frac{{n_o}^2 - {n_e}^2}{{n_o}^2 + {n_e}^2} \quad , \tag{7.3.1}$$

where n_o is the normal refractive index and n_e is the extraordinary index. Also the components of the crystal axis are $(\sin\phi_{CA}, 0, \cos\phi_{CA})$ [137]. A peak birefringence, β_{max}, of 0.021 at 0.3 THz has been observed during the investigation of plastic photonic

crystal fibers fabricated from HDPE tubes. Here $\beta_{max} = n_x - n_y$ where $n_{x/y}$ are the different refractive indexes seen by orthogonally polarized waves [138]. The refractive index (n_o) of the HDPE lens in QUaD is 1.5833. Therefore using the value of β_{max} we can calculate a lower limit of the extraordinary index (n_e) of the HPDE lenses of 1.56 and an upper limit of 1.61. In order to account for the fact that QUaD functioned at lower frequency values than 0.3 THz we have decided to carry out our analysis over a range of extraordinary indexes from 1.53 to 1.62 for the lenses. Using these values for n_o and n_e we can calculate appropriate values for ϕ_{CA} using equation (7.3.1). The components of the crystal axis are then $(\sin\phi_{CA}, 0, \cos\phi_{CA})$ where we have assumed that the crystal axis has no component along QUaD's y-axis and the z-axis is parallel to QUaD's propagation axis. Similar arrangements have been made for the optical window. The values we have chosen for the extraordinary indexes and the corresponding crystal axes are shown in Tables 7.2 and 7.3[2].

Table 7.2: Birefringent characteristics for QUaD lenses.

Ordinary index	Extraordinary index	ϕ_{CA} (radians)	Crystal axis
1.5833	1.53	0.77	(0.69, 0, 0.72)
1.5833	1.56	0.78	(0.7, 0, 0.71)
1.5833	1.59	0.79	(0.71, 0, 0.70)
1.5833	1.62	0.8	(0.72, 0, 0.69)

Table 7.3: Birefringent characteristics for QUaD window.

Ordinary index	Extraordinary index	ϕ_{CA} (radians)	Crystal axis
1.52	1.50	0.77	(0.71, 0, 0.70)
1.52	1.51	0.78	(0.70, 0, 0.70)
1.52	1.53	0.79	(0.70, 0, 0.71)
1.52	1.55	0.8	(0.70, 0, 0.71)

We have used the characteristics of Tables 7.2 and 7.3 to examine birefringence in QUaD. Using Zemax we have ray-traced both ordinary and extraordinary refracted

[2]We note that birefringence in polarization maintaining terahertz optical fibers has been investigated in [139]. Here it is shown that HDPE is more birefringent then both polypropylene and polytetrafluoroethylene (teflon). Such issues should receive some attention if lens combiners are chosen for QUBIC.

rays through QUaD. Using the paraxial lens we then calculated the position at which these rays end up on the sky. If birefringence is responsible for the displacements encountered in QUaD we except our analysis to return results similar to Figure 7.6c.

We note that Zemax does not consider the polarization of the incident electric field when calculating the orientation of rays refracted about the crystal axis. The user simply tells Zemax which surface is birefringent, the crystal axis of that surface and the extraordinary refractive index. At this surface Zemax ray-traces using equations specifically derived for uniaxial crystals [136]. As such all incident fields were arbitrarily polarized along the x-axis.

The depth of our analysis is therefore restricted by the limitations of Zemax. Zemax was not designed to extrapolation any information about a possible birefringent material. The software requires the user to input the crystal axis of a birefringent material and its extraordinary index. Both these values of course depend on the orientation of the incident polarization and such characteristics are again excepted to be known by the user. Zemax then uses the ray-tracing equations (7.3.2) - (7.3.4) to calculate the path of the extraordinary ray. These equations are taken from [136] and like all ray-tracing equation are solely based on geometrical considerations and do not take account of the wave nature of the incident field or its polarization. Therefore using Zemax we are limited to investigating the displacements on the sky between ordinary and extraordinary rays propagating through QUaD. Although since birefringence is dependent on the polarization of the incident fields we can draw some tentative conclusions regarding birefringence in the QUaD polarimeter. However we have no direct way of modeling or extrapolating information regarding how the orientation of the PSBs alter the displacements observed on the sky.

The birefringent characteristics we consider in this initial analysis are extremely simple. We have assumed the conditions that would be encountered by an on-axis beam incident on a piece of material whose crystal axis is orientated co-planar to the surface normal. This has allowed us to calculate the initial estimates for the crystal axes and corresponding extraordinary indexes listed in Tables 7.2 and 7.3.

In general a much more complex scenario is envisioned within QUaD however the above assumptions are valid for two reasons. The first reason is due to an analysis of narrow on-axis beams propagating through QUAD. Here it was revealed that the magnitude

of the displacements of these beams occurred mostly along the x-axis of the focal plane [3]. This means that comparatively little or no deflection occurs along QUaD's y-axis. Therefore there is no great loss of generality if we momentarily consider the crystal axes to exhibit an orientation in just two planes so we momentarily assume that the component of the crystal axis along the y-axis is zero. The second reason is due to the paraxial nature of QUaD. The orientation of the extraordinarily refracted Poynting vector $\mathbf{S_e}$ can be comprehensively calculated by

$$\begin{aligned} S_{e,x} &= \cos\alpha\cos\theta_e + \frac{\sin\theta_e \sin\alpha(x_0\sin\theta_e - y_0\cos\theta_e)}{\sqrt{z_0^2+(x_0\sin\theta_e - y_0\cos\theta_e)^2}} \\ S_{e,y} &= \cos\alpha\sin\theta_e + \frac{\cos\theta_e \sin\alpha(x_0\sin\theta_e - y_0\cos\theta_e)}{\sqrt{z_0^2+(x_0\sin\theta_e - y_0\cos\theta_e)^2}} \\ S_{e,z} &= \frac{z_0\sin\alpha}{\sqrt{z_0^2+(x_0\sin\theta_e - y_0\cos\theta_e)^2}} \end{aligned} \tag{7.3.2}$$

where (x_0, y_0, z_0) is the crystal axis, n_0 is the ordinary refractive index and n_e is the extraordinary refractive index. The angle α is

$$\tan\alpha = \frac{(n_e^2 - n_0^2)\tan\theta}{n_e^2 - n_0^2\tan^2\theta} \tag{7.3.3}$$

while the angle θ_e can be found by solving

$$\left(n_0^2 + x_0^2(n_e^2 - n_0^2)\right)\cot^2\theta_e + 2x_0y_0(n_e^2 - n_0^2)\cot\theta_e - \frac{n_0^2n_e^2}{\sin^2\theta} \tag{7.3.4}$$

where θ is the angle of incidence [136]. In Table 7.4 we have listed the components of the $\mathbf{S_e}$ vector from a piece of quartz whose birefringent properties have been well categorized as $n_0 = 1.54$, $n_e = 1.55$ and the crystal axis is (0.75,0.5,0.433) [136]. We have calculated $\mathbf{S_e}$ using angles of incidence up to 30°.

[3]The results of this analysis were obtained through a personal communiqué between NUIM and Ken Ganga of the APC Paris. We note that if one closely examines the very centre displacement in Figure 7.6c we see confirmation of this analysis. We can see that the "yellow" displacement occurs along the x-axis of the focal plane.

Table 7.4: Values of $\mathbf{S_e}$ for a piece of Quartz for various angles of incidence.

θ°)	$S_{e,x}$	$S_{e,y}$	$S_{e,z}$
5	0.99	0.05	0.00
10	0.99	0.11	0.00
15	0.98	0.17	0.00
30	0.95	0.32	0.01

Strictly speaking the crystal axes we have calculated in Tables 7.2 and 7.3 for various extraordinary indexes will only produce an accurate value for the vector $\mathbf{S_e}$ if the incident rays are normal to the HDPE elements. However as we have shown in Table 7.4 the difference between the values for $\mathbf{S_e}$ once the angles of incidence are less than 30° are marginal. Due to the paraxial nature of the system, the chief rays propagating from the various field positions in QUaD have angles of incidence on each of the refractive elements of at most $\sim 26^\circ$. Therefore although the crystal axes in Tables 7.2 and 7.3 are unlikely to be the exact crystal axes for any birefringent element in QUaD the results they provide will allow us to make some informed conclusions regarding possible birefringence in the QUaD CMB telescope.

The Zemax programing language (ZPL) is a C based language that enables the user to write short programs called macros that instruct Zemax to perform specific calculations on an optical system. In order to investigate the effects of birefringence in QUaD we have written a Zemax macro that functions according to the following algorithm:

- **Begin macro.**
- Set birefringent element. Here either one of the two lenses or the cryostat window is selected for investigation.
- Set the extraordinary index and the crystal axis to a value shown in either Table 7.2 or Table 7.3.
- Trace a single chief ray from each field position through the centre of the Lyot stop. We have traced the chief rays as they represent the propagation axes of the Gaussian beams from each detector horn. Therefore these rays trace the route of each PSB beam through the telescope.

- Calculate the position, $(x_{i,o}, y_{i,o})$, on the sky of the ordinary refracted chief ray propagating from every field position.
- Calculate the position, $(x_{i,e}, y_{i,e})$, on the sky of the extraordinary refracted chief ray propagating from every field position.
- Export all values $(x_{i,o}, y_{i,o})$ and $(x_{i,e}, y_{i,e})$.
- **Repeat as necessary.** The macro continues until rays from all fields have been traced onto the sky when each dielectric element in QUaD has a birefringent surface.

For every set of values $(x_{i,o}, y_{i,o})$ and $(x_{i,e}, y_{i,e})$ we formed a parametric line $\big(x_i, y_i\big) = \big(x_{i,o} + (x_{i,e} - x_{i,o})t_i, y_{i,o} + (y_{i,e} - y_{i,o})t_i\big)$ between the points. Plots of these parametric lines represent the displacements on the sky between the ordinary and extraordinary refracted rays passing through QUaD. Such displacements have been calculated for each of the 100 and 150 GHz pixels in QUaD. The results are shown in Figures 7.10 - 7.12. The chief rays propagating from the 100 GHz detector horns are shown in Figure 7.9. Tracing these rays through QUaD should provide an example of how the peak intensities of orthogonally polarized Gaussian beams on the sky may become displaced by a birefringent element.

We note that for presentation purpose the values t_i in the above parametric plots have be set to different values. This has been done merely to allow us to display the displacements in an appropriate manner so that we can investigate their orientations. For every optical component the values of t_i are shown in Table 7.5.

Table 7.5: Values of t_i for Figures 7.10 - 7.12.

	t_i
First lens	0.5
Second lens	4
Window	30

When we compare the displacements due to the lenses to those of the window shown in Figures 7.10 - 7.12 it is apparent that the most important determinant that decides the orientation of the displacements are the dielectric surface shapes. The details of

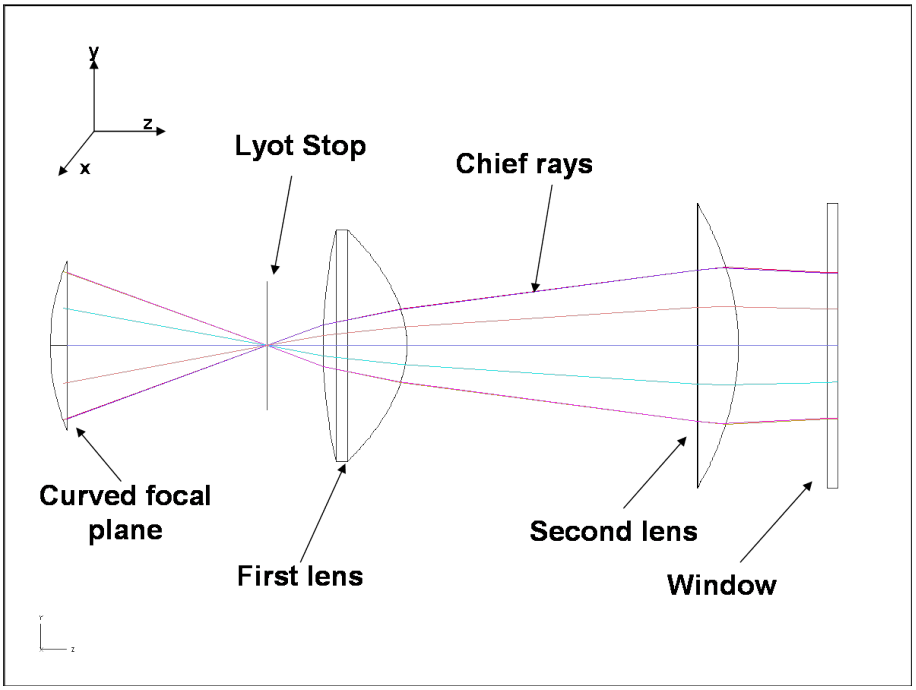

Figure 7.9: Chief rays from 100 GHz detector horns.

the dielectric elements in QUaD are listed in Table 7.6. The first lens within QUaD is fully convex whereas the second lens is plano-convex.

In Figures 7.10 - 7.12 we have clearly shown that a simple ray-trace analysis of QUaD indicates that when an electric field is incident over a curved lens surface the further off-axis the beam the greater the displacements of the differently refracted beams will be on the sky. These results concur with what is expected when we study equations (7.3.2). Here we see that the greater the incident angle θ the greater the magnitude of the off-axis $S_{e,x}$ and $S_{e,y}$ components of the Poynting vector. Using Zemax we have traced chief rays through the centre of QUaD's aperture stop onto the sky. As shown in Figure 7.9 the further off-axis QUaD's fields are placed the greater the incident angle of the chief ray from each of these fields at the first and second lens. Obviously the greater the curvature of the lens surfaces the greater the angle of incidence between the off-axis chief rays and the surface normal. Also if we examine Figure 7.8 we see that the thicker a piece of birefringent material the greater the separation of the ordinary and extraordinary refracted rays. Therefore due to the fact that it is the thickest element with the greatest curvature we expect the first lens to cause the greatest displacements. We then expect the slightly curved secondary lens to produce

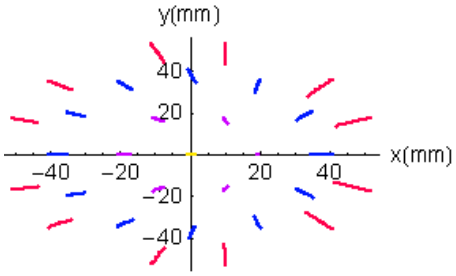

(a) 1.53 extraordinary index. The average value of the displacements is 3.73 mm (≡ 3.37 arcmin on the sky).

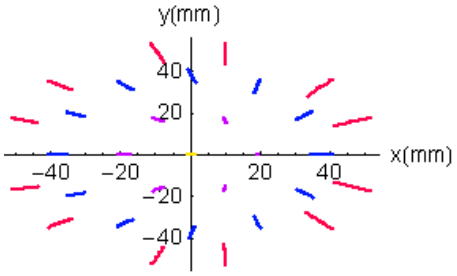

(b) 1.56 extraordinary index. The average value of the displacements is 3.77 mm (≡ 3.77 arcmin on the sky).

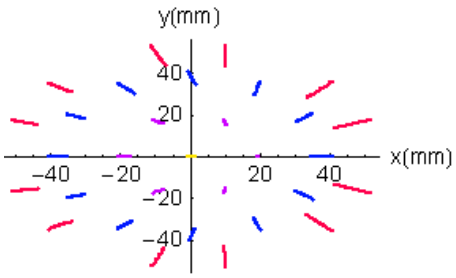

(c) 1.59 extraordinary index. The average value of the displacements is 3.73 mm (≡ 3.73 arcmin on the sky).

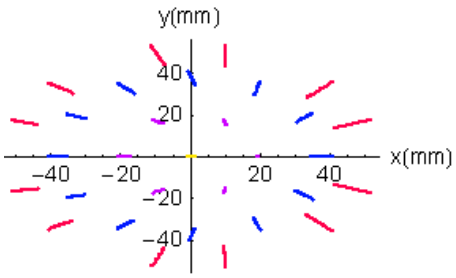

(d) 1.62 extraordinary index. The average value of the displacements is 3.82 mm (≡ 3.82 arcmin on the sky).

Figure 7.10: Birefringent first lens using x-polarized rays.

the second greatest displacements. Finally due to the fact that the beams intersect the window almost perpendicularly we expect this element should cause the smallest displacements. We also expect the displacement caused by the birefringent lens to increase as we consider the off-axis pixels.

These expectations exactly match the results shown Figures 7.10 - 7.12. Here we have listed the average displacements caused by each optical element. The average values off all displacements caused over the various extraordinary indexes have been listed along with the details of the optical components in Table 7.6. These results suggest that in order to avoid complications due to birefringence in further CMB polarimeters thin dielectric elements with small curvatures should be implemented. The large value of t_i required to display the displacements by the window and the small values required to display the displacements due to the first lens also concur with the above expectations. These results have some important consequences for QUBIC2.0 that we will discuss in

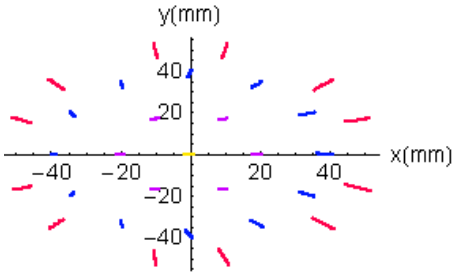

(a) 1.53 extraordinary index. The average value of the displacements is 1.197 mm (≡ 1.197 arcmin on the sky).

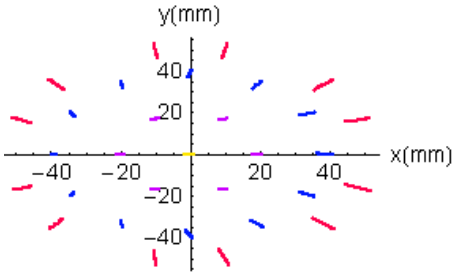

(b) 1.56 extraordinary index. The average value of the displacements is 1.195 mm (≡ 1.195 arcmin on the sky).

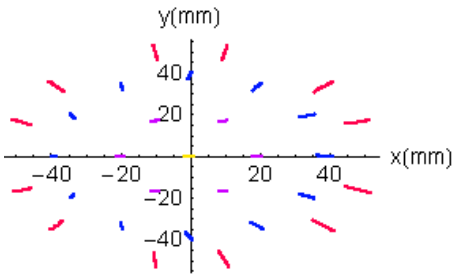

(c) 1.59 extraordinary index. The average value of the displacements is 1.2 mm (≡ 1.2 arcmin on the sky).

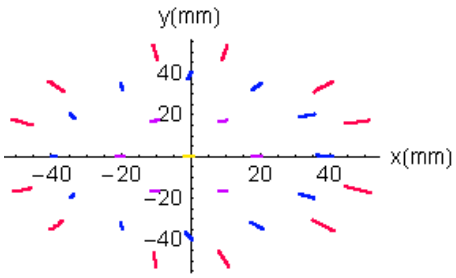

(d) 1.62 extraordinary index. The average value of the displacements is 1.2 mm (≡ 1.2 arcmin on the sky).

Figure 7.11: Birefringent second lens investigated using x-polarized rays.

the next section. Our results indicate that the magnitude of the displacements seen in QUaD could indeed be caused by levels of birefringence that have been measured elsewhere in the lens material.

In the author's opinion the most interesting result in this section is the uniformity of the displacements caused by the completely flat optical window. The displacements caused by the lenses show a radial pattern pointing towards the lenses' axes of symmetry. However the orientations of displacements caused by a birefringent window are parallel and aligned with the orientation of the crystal axis. Also the length of the displacement is almost constant over all pixels. In order to confirm this result we examined the orientations caused by various crystal axes in a birefringent window. These crystal axes and the displacements caused are shown in Figure 7.13. Once again we seen that due to the dual plane surfaces of the optical window the displacements are aligned with the crystal axes and not the propagation axis. The crystal axes were chosen so that

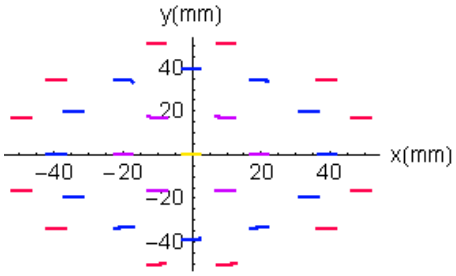

(a) 1.50 extraordinary index. The average value of the displacements is 1.009 mm (= 1.009 arcmin on the sky).

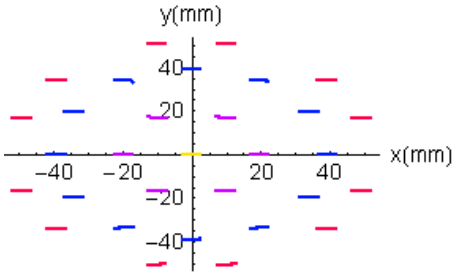

(b) 1.51 extraordinary index. The average value of the displacements is 1.008 mm (= 1.008 arcmin on the sky).

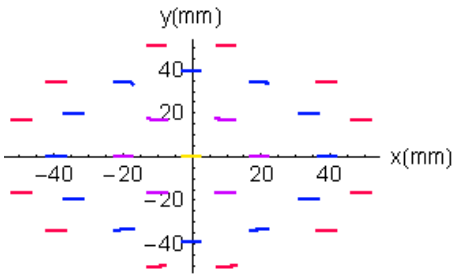

(c) 1.53 extraordinary index. The average value of the displacements is 1.01 mm (= 1.01 arcmin on the sky).

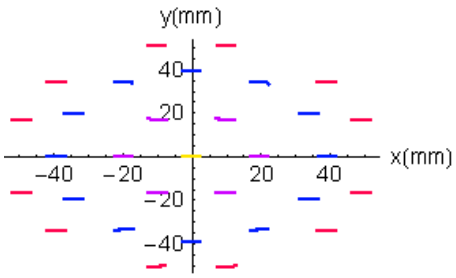

(d) 1.55 extraordinary index. The average value of the displacements is 0.99 mm (= 0.99 arcmin on the sky).

Figure 7.12: Birefringent window investigated using x-polarized rays.

each axis is a unit vector with equal length components in all directions. As clearly shown in Figure 7.13 the orientation of the displacements form lines whose slopes are 45°. Therefore if a flat optical component is implemented the displacements caused by birefringence will align with the crystal axis. Also the length of the displacements on the sky should be almost constant for each pixel. This behavior completely contrasting to birefringent lenses and also different to the behavior seen in QUaD. Therefore based on these results we must exclude a birefringent window with a uniform crystal axis causing the displacements in QUaD.

We have also calculated the displacements on the sky caused by the crystal axis (0.75,0.5,0.433) for quartz given in [136]. These displacements are shown in 7.14. We note that Figure 7.14(a) is beginning to show broadly the features seen in the real data (resemble displacements shown in Figure 7.6). Once again we see that the flat surface of the window combined with its narrowness results in the smallest

Table 7.6: The curvature (**curv**) and thickness of dielectric elements in QUaD.

	curv (mm) Front surface	**curv** (mm) Back surface	Thickness (mm)	Displacements (mm)
First lens	0.002	0.012	65	3.76
Second lens	0	0.005	32	1.2
Window	0	0	8	1.0

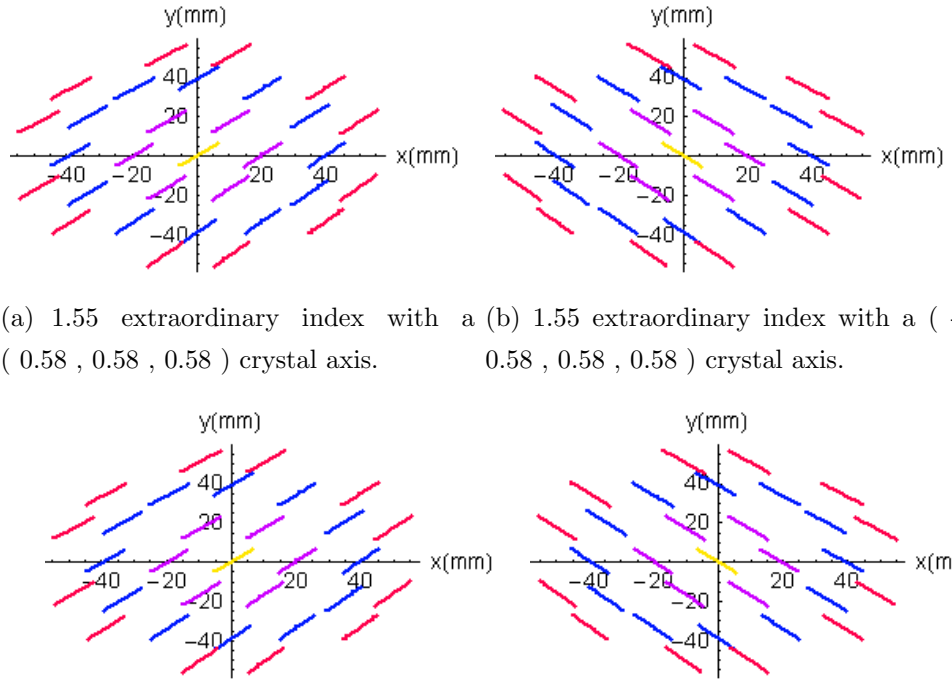

(a) 1.55 extraordinary index with a (0.58 , 0.58 , 0.58) crystal axis.

(b) 1.55 extraordinary index with a (-0.58 , 0.58 , 0.58) crystal axis.

(c) 1.55 extraordinary index with a (-0.58 , -0.58 , 0.58) crystal axis.

(d) 1.55 extraordinary index with a (–0.58 , -0.58 , 0.58) crystal axis.

Figure 7.13: Birefringent window investigated at 150 GHz using x-polarized rays.

displacements. Finally we have plotted the displacements of 30 rays, launched from each position, on a patch of sky seen by 12 of QUaD's 150 GHz pixels . The birefringent conditions are equal to those used to calculate the displacements shown in Figure 7.14. The displacements on the sky are shown in Figures 7.15 - 7.17. Here all normally refracted rays are shown in blue while the extraordinary refracted rays are shown in green. As we can see the effects of birefringence in the second lens and the optical window are only slightly noticeable. However the displacements of the beams of rays due to birefringence in the first lens is apparent. We conclude from this work

that levels of birefringence measured in the HDPE and Quartz at GHz frequencies could cause effects at the levels seen by QUaD. This simple analysis predicts that the first lens is the dominant cause in QUaD. The displacement of orthogonally polarized beams due to birefringence means that an instrument will effectively see orthogonal E and B-modes coming from two different areas of the sky. Such issues are of course extremely troublesome if one wishes to form maps of the CMB polarization. Here I have shown that differences in the ordinary and extraordinary refractive index HDPE, of a level typically reported in the literature, can cause the effects (displacement of orthogonally polarised beams on the sky) seen in QUaD. The exact pattern of the displacements depends on the "crystal" axis direction as well as on which component is the dominant cause. In the next section I see whether it is possible to recover a single axis direction or dominant refractive component (the QUaD lenses were not available to us for testing).

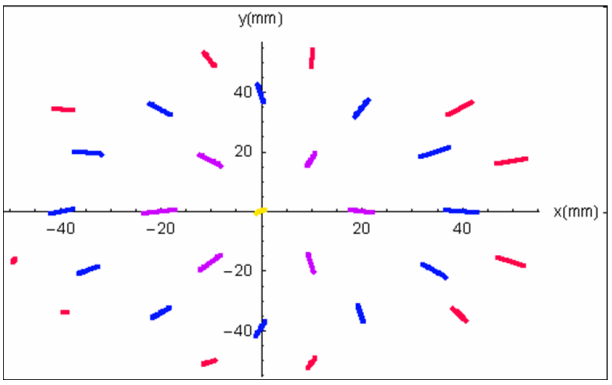

(a) Birefringent first lens with extraordinary index 1.56. The average value of the displacements is 0.48 mm.

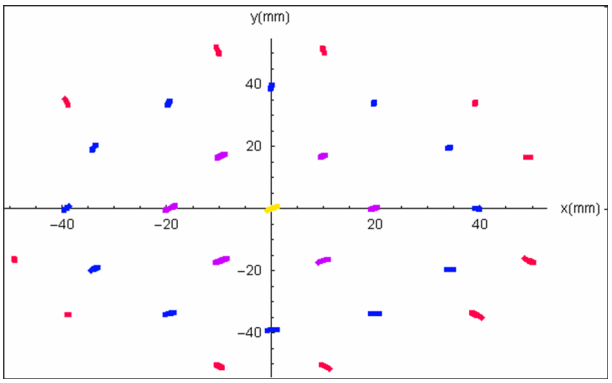

(b) Birefringent second lens with extraordinary index 1.56. The average value of the displacements is 0.20 mm.

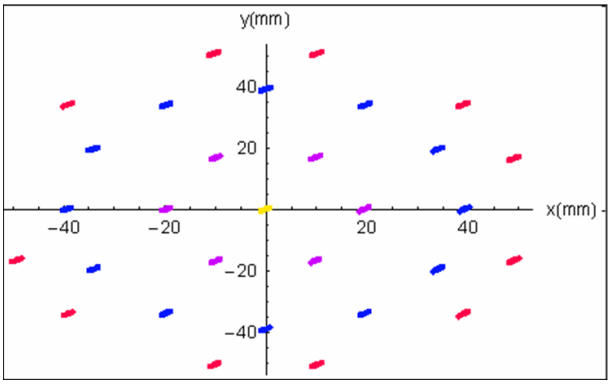

(c) Birefringent window with extraordinary index 1.53. The average value of the displacements is 0.03 mm

Figure 7.14: Birefringent elements investigated at 150 and 100 GHz using x-polarized rays.

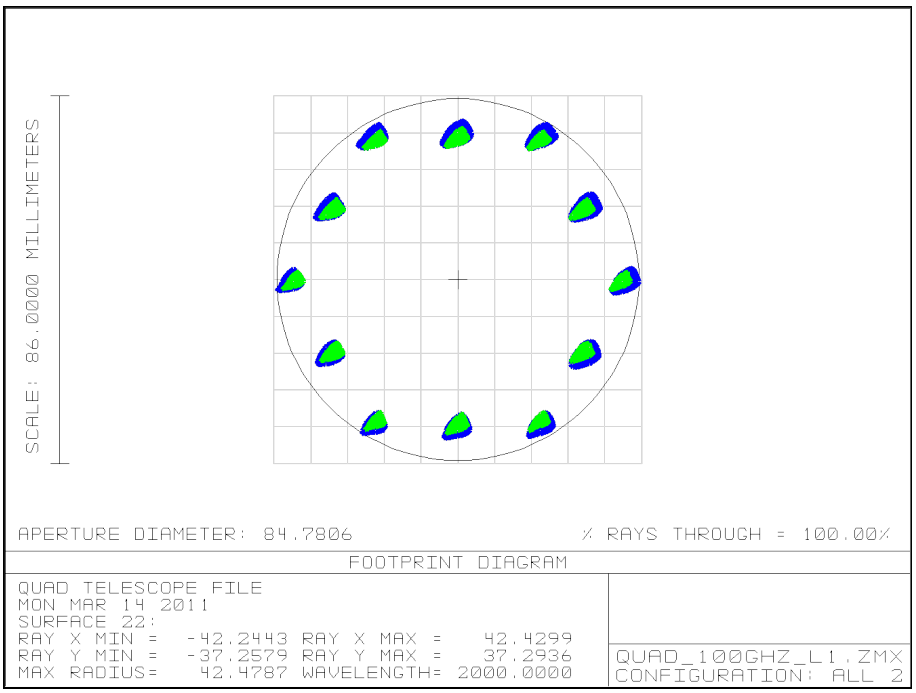

Figure 7.15: Displacement of 100 GHz beams on sky caused by birefringence in the first lens. Here all normally refracted rays are shown in blue while the extraordinary refracted rays are shown in green.

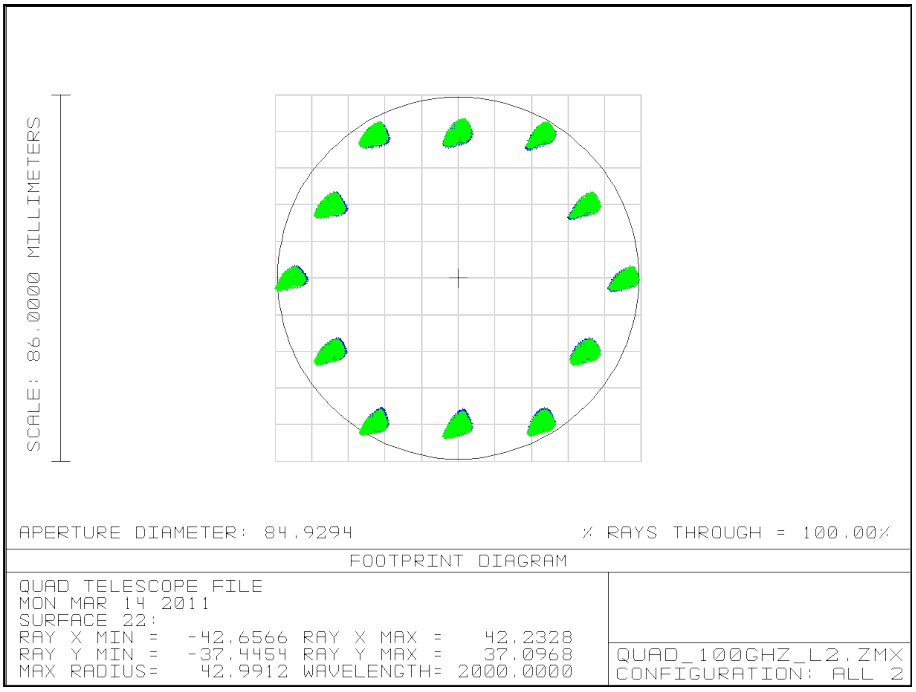

Figure 7.16: Displacement of 100 GHz beams on sky caused by birefringence in the second lens. Here all normally refracted rays are shown in blue while the extraordinary refracted rays are shown in green.

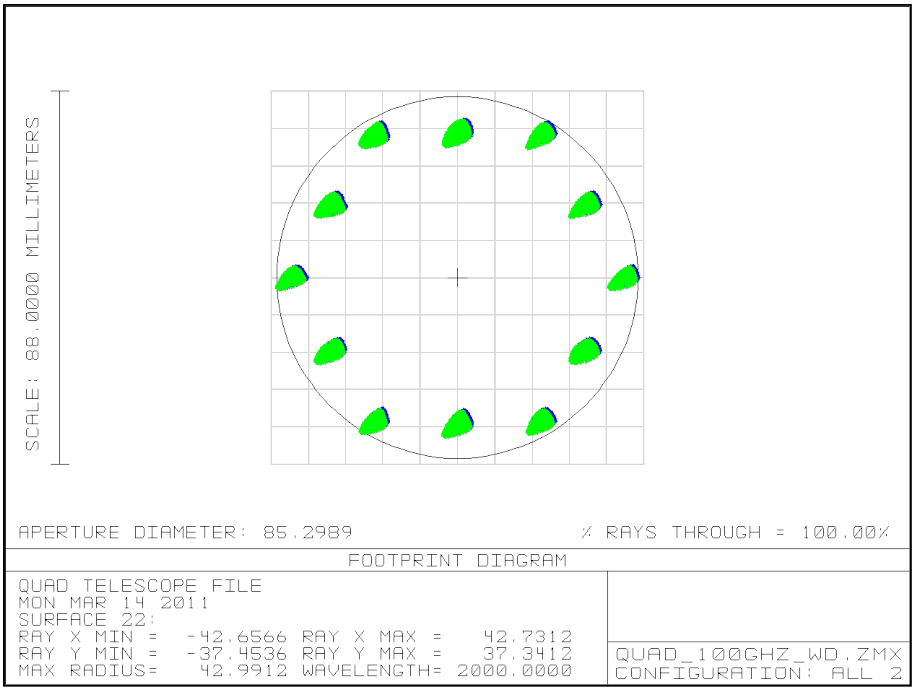

Figure 7.17: Displacement of 100 GHz beams on sky caused by birefringence in the cryostat window. Here all normally refracted rays are shown in blue while the extraordinary refracted rays are shown in green.

7.4 Optimizations to identify QUaD crystal axes

7.5 Zemax optimizations

We have established that birefringence in QUaD's HDPE elements can lead to displacements between orthogonally polarized beams on the sky. We will now attempt to recreate the exact displacements observed in QUaD. A previous analysis of QUaD showed that various orthogonally polarized on-axis beams propagating through QUaD experienced an average displacement of $\Delta_{arc} = 0.05345$ arc minutes on the sky.

We have used the above values to write a Zemax optimization with which we optimized a value for the crystal axis of a birefringent element. In order to carry out these optimizations we used QUaD's geometry shown in Figure 7.4. As before due to the focal length of the paraxial lens a displacement on the sky of $\Delta_{arc} = 0.05345$ arc minutes will equal $\Delta_{dist} = 0.05345$ mm in the image plane indicated in Figure 7.4.

We have also attempted to optimize a value for the crystal axis causing the displacements observed by the 150 GHz pixels located at coordinates (64.42,56.47) and (-64.42,-56.47) on the focal plane only. These pixels were chosen due to the fact the orientation of the PSBs at these points is similar to the centre pixel. We refer to them as pixel 1 and pixel 2 respectively. The displacements and slopes for these pixels were calculated from Figure 7.6. The length and slope of the displacement for pixel 1 are 0.015 mm and 0.14. Also the length and slope of the displacement for pixel 2 are 0.012 mm and 0.19. Due to the fact that the frequencies of these pixels are equal we expect the optimizations to return a similar crystal axis if the birefringence in QUaD is similar to that of uniaxial crystals.

7.5.1 Displacements due to optimized crystal axes.

We implemented a ZPL macro that attempted to find an accurate value for any crystal axis occurring in QUaD. This macro functioned as follows:

- **Begin macro.**

- Set the birefringent element.
- Set the value of the extraordinary index.
- Trace a cone 600 rays from the centre of the detector horn onto "the sky". This means we trace the cone of rays onto the image plane formed by the paraxial lens. The cone of rays represents an on-axis Gaussian beam propagating through QUaD.
- Calculate the position, $(x_{i,o}, y_{i,o})$, on the sky of the ordinary refracted rays.
- Calculate the position, $(x_{i,e}, y_{i,e})$, on the sky of the extraordinary refracted rays.
- Calculate the separation of each corresponding pair of points Δ_i.
- Calculate the slope of the line joining of each corresponding pair of points Δ_s.
- Calculate the average displacement $\overline{\Delta_i}$.
- Calculate the average slope $\overline{\Delta_s}$.
- Let $X_{opt} = \frac{\overline{\Delta_i}}{\Delta_{dist}}$.
- Let $Y_{opt} = \frac{\overline{\Delta_s}}{\Delta_{sl}}$.
- Return X_{opt} and Y_{opt}.
- **Optimize.**
- **Repeat as necessary.**

When this macro is implemented Zemax will use a damped least squares optimization to alter the (x, y, z) components of the crystal axes of a selected birefringent surface. This optimization will continue until the values X_{opt} and Y_{opt} converge as close as to possible to unity. These optimizations take place over a range of extraordinary indexes from 1.5 to 1.635 incrementing in values of 0.015.

This macro ran until the crystal axis that produced the lowest merit function at a given extraordinary refractive index was found. A plot of the final merit functions versus the extraordinary indexes are shown in Figure 7.19. The macro ran separately and calculated a crystal axis for each of the mentioned pixels and then finally for all

the pixels considered at once. In these plots the merit function is a measure of how far both the returned values of X_{opt} and Y_{opt} are from unity.

Table 7.7: The optimized crystal axes for QUaD's refractive elements.

First lens	
Centre pixel	(-0.004, 0.005, 0.98)
Pixel 1	(0.78, 0.72, 0.0)
Pixel 2	(0.0,0.0,1.0)
All pixels	(0.0,0.0,0.99)
Second lens	
Centre pixel	(0.001,0.0,0.98)
Pixel 1	(0.004,0.0,0.99)
Pixel 2	(0.001,0.0004,0.98)
All pixels	(0.0027,0.,0.987)
Window	
Centre pixel	(0.001,0.001,0.99)
Pixel 1	(0.0003, 0.0002,1.00)
Pixel 2	(0.0,0.01,0.92)
All pixels	(0.0,0.0,0.99)

We can see from Figure 7.19 that the Zemax optimizations could not distinguish which of the elements is most likely to be birefringent nor converge on an equal value for the extraordinary index[4]. The analysis of the central pixel produced the lowest merit functions for each optical element. Table 7.7 lists the optimized crystal axis that Zemax calculated as causing the observed displacements. Although not identical these results agree with our initial assumption that the majority of the crystal axes' magnitudes aligned with QUaD's prorogation axis. Slight variations of the axis x and y components across a birefringent material may account for the variation of the orientations of the displacements shown in Figure 7.6. It is also likely that the real crystal axis varies across the optical element, giving us too many degrees of freedom for the optimization.

The modeled displacements caused by these crystal axes optimized for all pixels are shown in Figures 7.19. When we compare Figure 7.19 to Figure 7.6 we see that the

[4]As stated Zemax was simply not designed to treat optical devices as a black boxes and extrapolate information about the device from user defined optimizations.

optimized crystal axes do not exactly reproduce displacements observed in QUaD. The extraordinary refractive index and the crystal axis for each component was set to the values that gave the lowest merit function for the purple lines in Figure 7.19

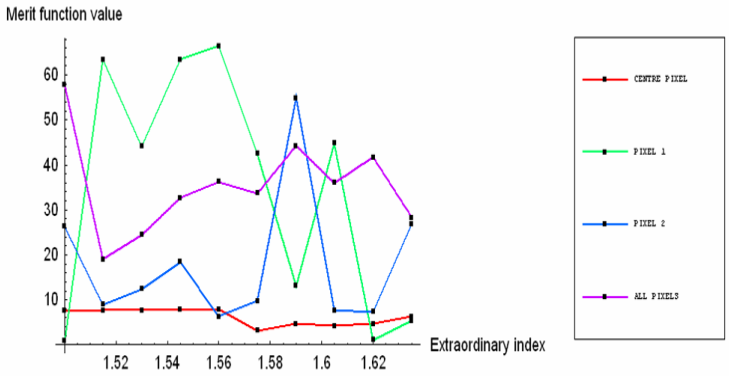

(a) First lens merit function.

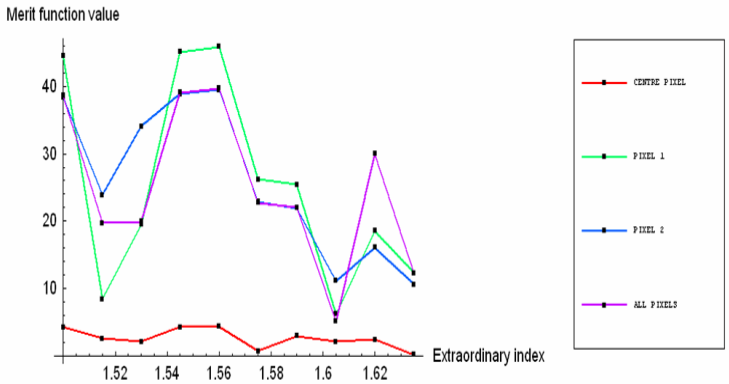

(b) Second lens merit function.

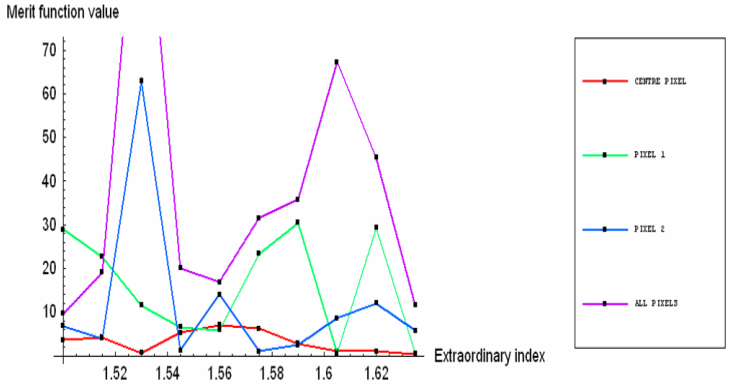

(c) Window merit function.

Figure 7.18: Zemax merit function for optimized crystal axes.

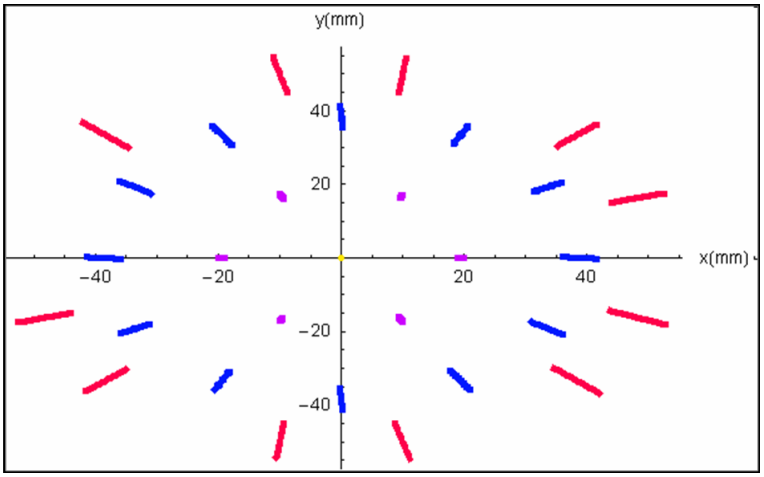

(a) First lens with 1.515 extraordinary refractive index.

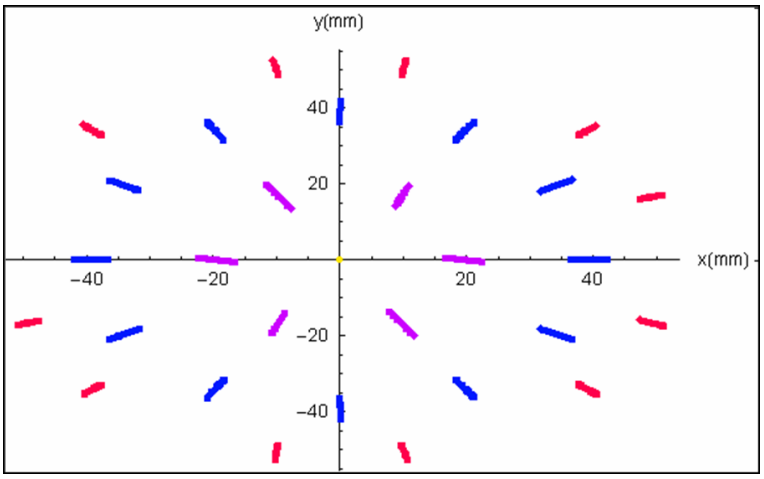

(b) Second lens with 1.605 extraordinary refractive index.

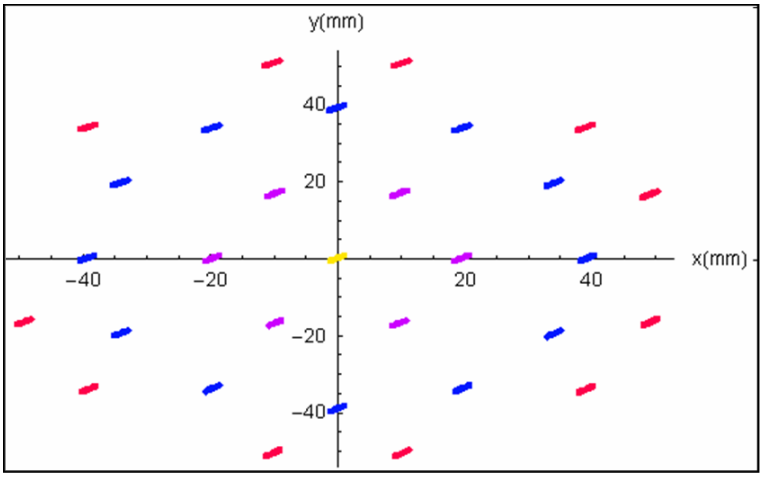

(c) Window with 1.635 extraordinary refractive index.

Figure 7.19: Orthogonal beam displacements for optimized crystal axes.

7.5.2 Results obtained by randomizing the crystal axis

The optimizations in the previous section showed that although mostly uniform the crystal axis in a dielectric component is likely to have varied across the material. The occurrence of non-uniformities in dielectric material that may cause various degrees of birefringence throughout the material is consistent with any stresses or strains the material may have undergone [134]. For a final analysis we have used Zemax to generate displacements due to random crystal axes the optical window and the first lens.

A final Zemax macro was written that ray-traced a chief ray from each pixel in QUaD's focal plane onto the sky. This macro generated a random crystal axis for every ray traced through the telescope. The results are shown in Figure 7.20. Here we see that despite the presence of a random crystal axis due to the fact that lens is a converging optical device the displacements still maintain a profile that also converges towards the propagation axis of QUaD. Meanwhile we can also see that due to the flatness of the device the length of the displacements caused by the optical window remain relatively constant over all pixels. Most importantly Figure 7.20 shows once again that if the crystal axis varies across the material the length of the displacements generated by a lens will increase as the incident rays move off-axis.

To summarize we have shown using Zemax optimizations that any crystal axis within QUaD will most likely vary across the dielectric material. Also Figure 7.20 shows that even if the crystal axis various throughout one of QUaD's lenses the length of the displacements of beams on the sky will increase as the beams move off-axis. Therefore a varying crystal axis throughout one of QUaD's lenses will lead to the displacements of polarized beams shown in Figure 7.6. A varying crystal axis will account for the various orientations of each of displacement while the curved surface of the lens will account for the increase in displacements as the pixels move off-axis. We therefore conclude that at least one of QUaD's lenses was birefringent during operation. Such results are somewhat unexpected as it was originally suspected by the QUaD collaboration that the optical window was the most likely candidate for the cause of birefringence. This was because in order to create polymer material robust enough to withstand the differences in temperature between the cryostat and the external environment the

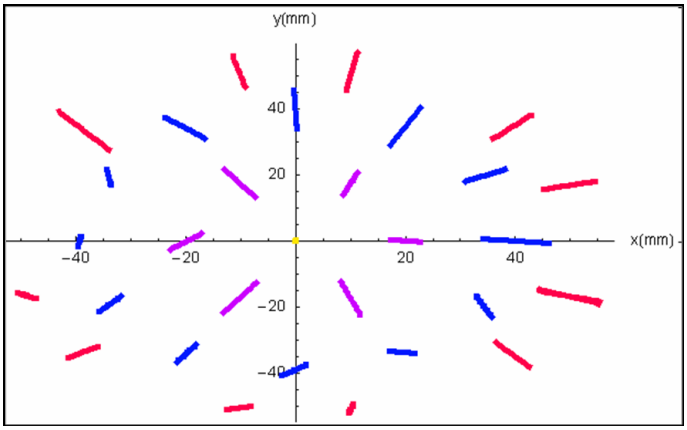

(a) Birefringence in QUaD's first lens. The extraordinary index is 1.56.

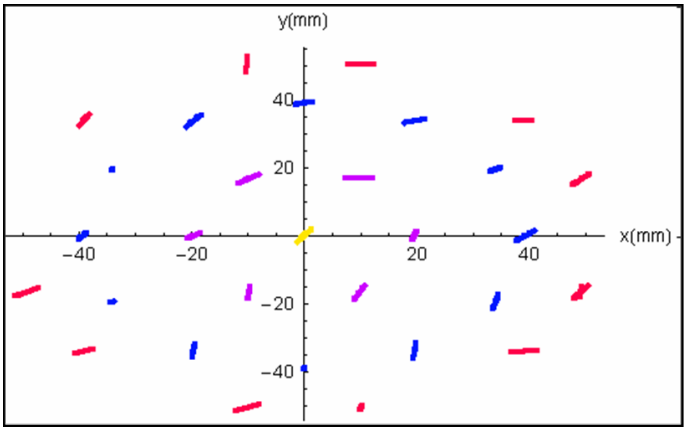

(b) Birefringence in QUaD's window. The extraordinary index is 1.53.

Figure 7.20: Displacements of rays due to birefringence in the optical window and first lens. The crystal axis for rays from each separate pixel have been randomized.

window underwent a number of compressions during construction, and would likely be under strain.

7.6 Birefringence in QUBIC lens combiners.

As discussed in Chapter 4 it we are now considering lens combiners for QUBIC2.0. An investigation of the QUaD system has suggested that birefringent lenses with greater

radii of curvatures will induce smaller displacements[5]. Also it has been shown that the narrower the birefringent surfaces the smaller displacements between ordinary and extraordinary rays. If we wish to reduce any errors due to birefringence we should attempt to avoid the implementation of thick lenses with small radii of curvature in QUBIC2.0. As such we will conclude this chapter by representing the results of a very basic tolerance analysis of birefringence occurring in one of the elements in three of the lens combiners discussed in Chapter 4. We will use these lenses to investigate two basic assumptions regarding possible birefringence in QUBIC.

We have investigated the displacement on the sky of 600 rays propagating from the centre of the bolometer detector array. Like QUaD we have implemented a 3437.75 mm focal length paraxial lens to simulate the location of these rays on the sky. Using Zemax we ray-traced a cone of 600 ordinary and extraordinary rays through three of the lens systems discussed in Chapter 4. The rays were arranged to simulate a 14° fwhm Gaussian beam and the analysis was carried out at 150 GHz.

We have assumed that the HDPE lens nearest the back-to-back array in the symmetric Cooke triplet lens and the symmetric single lens systems are birefringent. We set components of the crystal axis to (0.75,0.5,0.433) in all systems in accordance with [136]. The extraordinary index was set to 1.53 while the normal index of all HDPE elements was 1.52. The average displacement between the ordinary and extraordinary rays are shown in Table 7.8 along with the radius of curvature of the birefringent lens surface and the thickness of the birefringent lens.

Table 7.8: Displacements caused by birefringence in telecentric lens combiners.

Lens	Displacement (mm)	Radius of curvature (mm)	Thickness (mm)
Symmetric Cooke triplet	1.25	1319.28	20
Symmetric capped double Gauss	6.9	240	100
Symmetric single lens	5.15	1838.46	100

The results of Table 7.8 agree with the assumptions we arrived at from examining possible birefringence in QUaD. The symmetric Cooke triplet lens is least susceptible to large displacements caused by birefringence due to the narrowness of the lenses

[5]We remind ourselves that the radius of curvature is the reciprocal of the curvature.

and the large radii of curvature. This is highly advantageous because in Chapter 4 we showed that this system is also the best telecentric combiner and therefore should produce the best quality window function for QUBIC2.0 As we can see when examining the symmetric capped double Gauss lens the combination of a small radius of curvature combined with a thick lens leads to large displacements. This is precisely the behaviour we predicted upon the examination of the QUaD optical system.

Finally we have plotted the displacements of 30 rays on the patch of sky seen by various pixels. These rays have been displaced due to birefringence in one of the elements in the above QUBIC lens combiners. The birefringent conditions are equal to those used to calculate the values in Table 7.8. The nine pixels were located at the coordinates on the QUBIC detector plane shown in Table 7.9. The displacements on the sky are shown in Figures 7.21 - 7.23. Here all normally refracted rays are shown in blue while the extraordinary refracted rays are shown in green. As can be seen the displacements caused by the Cooke triplet are marginal while those caused by the double Gauss lens are almost as large as the beam itself.

Table 7.9: Coordinates of pixels in QUBIC detector plane.

(5,-5)	(5,0)	(5,5)
(-5,0)	(0,0)	(0,0)
(-5,-5)	(0,-5)	(5,-5)

7.7 Conclusions

We have arrived at a rather important conclusion at the end of this thesis. In several CMB polarimeters displacements between polarized beams have been recorded on the instruments focal plane[6]. It has been suggested that birefringence is a probable cause of these errors.

In the above chapter we used Zemax to model the displacement of rays on the sky due to birefringence in QUaD's dielectric components. We were able to create results that although not identical to those seen in QUaD do suggest that birefringence was

[6]Very recently the BICEP family of experiments has also reported such errors [140].

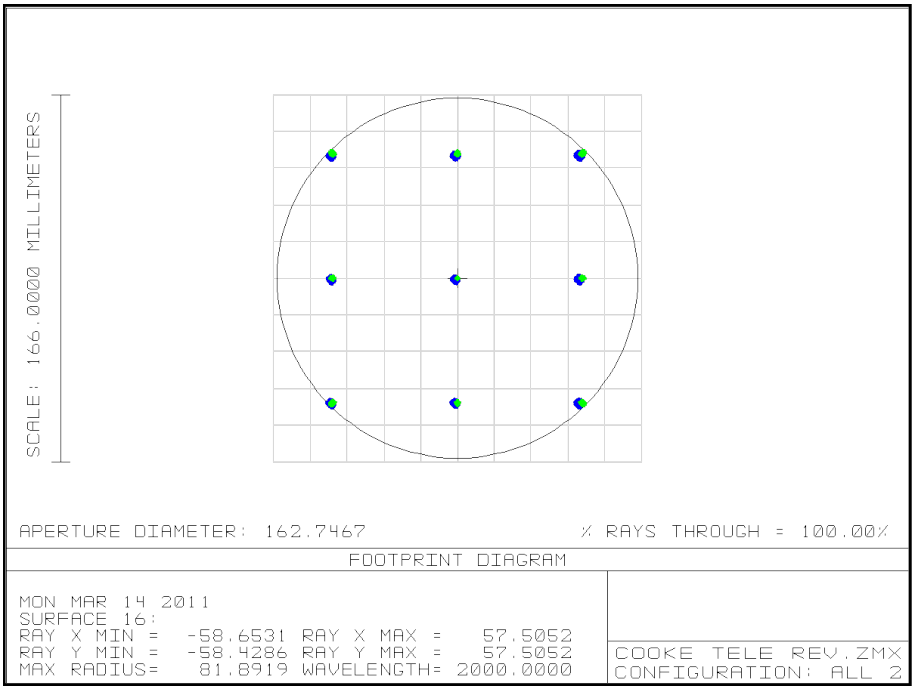

Figure 7.21: Displacement of rays on the sky from QUBIC caused by birefringence in the symmetric Cooke triplet lens.

a likely cause of the recorded displacements. We have used ordinary and extraordinary indexes from the literature, together with reasonable crystal axes directions to show that birefringence in one of QUaD's lenses was a likely cause of the recorded displacements.

Also we have performed a brief birefringent tolerance analysis of the lens systems designed for QUBIC2.0. We confirmed that the use of narrow lenses with large radii of curvatures will assist in reducing any possible birefringence in the lenses themselves.

We recall that limitations in our current abilities to multiplex bolometer detectors is severely reducing the size of any filled focal plane for CMB experiments. This in turn restricts the focal length of any implemented focusing system. Due to the limitations of reflecting systems at low focal lengths it is increasingly likely that more and more future CMB missions will implement lenses to focus an incident signal directly onto a detector array or at least help reduce the size of incident beams. Already a number of missions are reporting beam squint errors in currently implemented lens systems. As we have shown in the context of QUaD birefringence is a probable cause of these

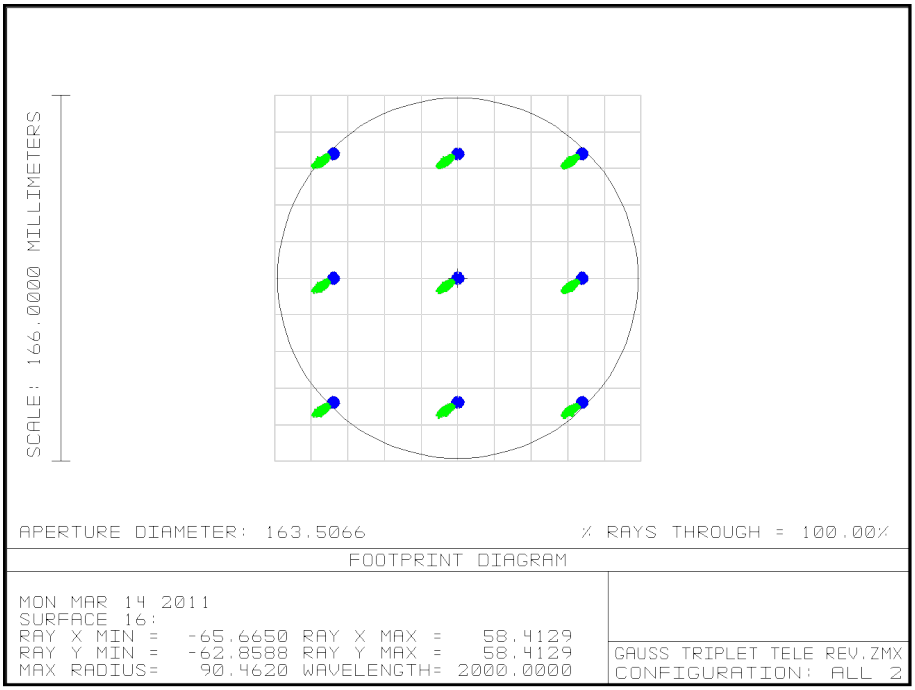

Figure 7.22: Displacement of rays on the sky from QUBIC caused by birefringence in the symmetric capped double Gauss lens.

errors. Fortunately our analysis of QUaD has enabled us to present ways of reducing such errors in future CMB missions by implementing thin lenses with large radii of curvatures.

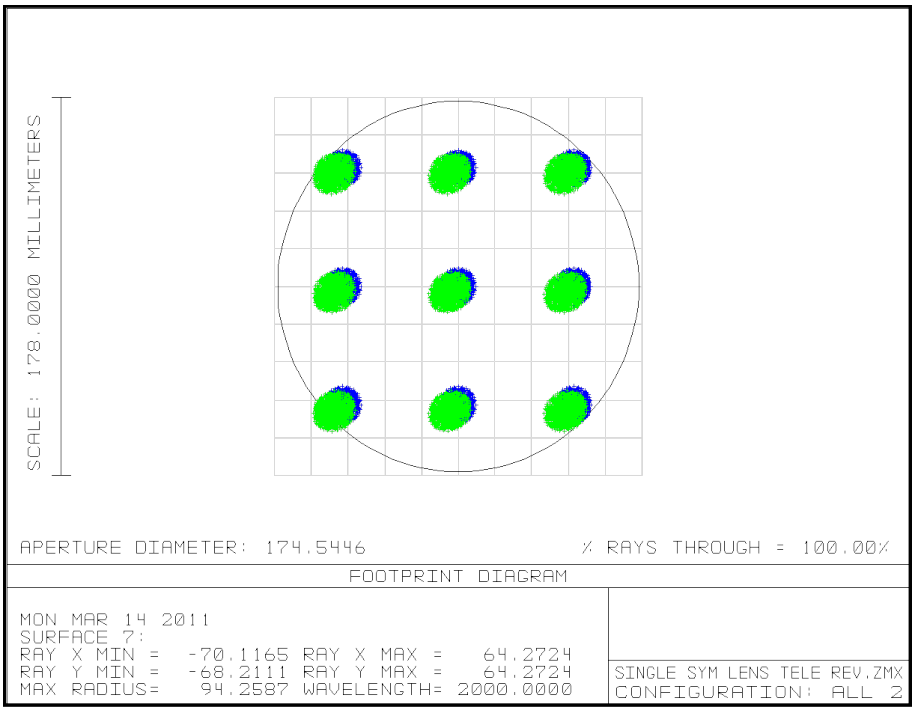

Figure 7.23: Displacement of rays on the sky from QUBIC caused by birefringence in the symmetric single lens.

8 Conclusions

In this thesis we have discussed the theory of the origins of the CMB, its temperature anisotropies and its polarization anisotropy modes. We have explained how observation of CMB B-mode polarization will help verify our current models of inflation and we have introduced QUBIC, a CMB telescope currently in design that will use a novel technique called bolometric interferometry to measure B-modes. We then discussed the evolution of QUBIC, an instrument that was originally intended to measure the visibilities of the Q and U components of CMB polarization, to QUBIC2.0 which will observe the Q and U power spectrum directly at discrete multipole intervals.

We presented in detail the author's direct contribution to both the QUBIC and QUBIC2.0 experiments: the design of a Fizeau quasi-optical combiner. The performance criteria of QUBIC and QUBIC2.0 placed extreme design specifications on the optical combiners for both instruments. Essentially, we need to design a CMB telescope for a 20×20 array of horns that is diffraction limited up to a 14° FOV with a focal length of 300 mm.

Of the dual reflector designs investigated the CATR was found to be the best performing, however geometrical restrictions meant that we cannot design one suitable for QUBIC. Of the possibilities for a short focal length design, a compensated Gregorian (CG) design was found which did fit the geometrical requirements of QUBIC and although it did produce aberrated fringes, these were found to reduce the sensitivity of the instrument by less than 10%; a performance considered acceptable by the collaboration. Fully refracting designs were also investigated but manufacturing and modeling considerations mean that as yet they are not favored for QUBIC. One particular drawback of lenses, the possibility of birefringence, was investigated using data from the QUaD experiment and it was found that birefringence was a candidate for the cause of the beam squint seen in the experiment.

In October 2010 a technical description of QUBIC was published in the ESO journal of *Astronomy and Astrophysics* [122][1] Based on this initial whitepaper the QUBIC collaboration received funding and support from the French National Research Agency (ANR) in 2011[2]. In the whitepaper the collaboration demonstrated that the CMB power spectrum could be observed by a bolometric interferometer with sufficient sensitivity to detect B-modes. The optical combiner used in the whitepaper simulations was the 300 mm focal length compensated Gregorian designed by the author[3].

Since the completion of this thesis there has been additional specifications placed on the QUBIC2.0 beam combiner. In particular the possibility of using bare bolometers (i.e bolometers not fed by directional horn antennas) has raised concerns about stray light entering the instrument. This has led to the collaboration considering the placement of a spatial filter (Lyot stop) in between the back-to-back horn array and the bolometer detectors. The most suitable position for such an aperture is the focal plane of the dual reflector combiner. As such QUBIC2.0 may now also require re-imaging optics to focus the beams traversing the Lyot stop onto the detector plane. The design and modeling of these re-imaging optics is currently underway at NUI Maynooth.

The first module of QUBIC2.0 is expected to undergo construction at the Franco-Italian Dome C Antarctic station in early 2014. The module will most likely use 400 back-to-back horns to observe the CMB at 150 GHz. Also a two-stage optical combiner, consisting of an off-axis dual reflector followed by re-imaging optics, will focus the sky signal from the back-to-back horn array onto the bolometer detectors. If successful the QUBIC team is hoping to report the definitive acquisition of CMB B-mode polarization within the first three season of observations.

[1]ESO, the European Southern Observatory, is an intergovernmental astronomy organization in Europe. It builds and operates some of the world's most advanced ground-based astronomical telescopes. For more information visit `http://www.eso.org/public/`.

[2]The French National Research Agency (ANR) is a research funding organization established by the French government in 2005. For more information visit `http://www.agence-nationale-recherche.fr/Intl`.

[3]This optical combiner was discussed in detail in chapter 4.

Bibliography

[1] A. Cho, "...While Planck Dusts the Skies For the Fingerprints of Inflation," *Science*, vol. 324, no. 5927, pp. 584–586, 2009.

[2] R. A. Alpher and R. C. Herman, "Remarks on the Evolution of the Expanding Universe," *Physical Review*, vol. 75, pp. 1089–1095, Apr. 1949.

[3] A. A. Penzias and R. W. Wilson, "A Measurement of Excess Antenna Temperature at 4080 Mc/s," *Astrophysical Journal*, vol. 142, pp. 419–421, 1965.

[4] R. H. Dicke, P. J. E. Peebles, P. G. Roll, and D. T. Wilkinson, "Cosmic Black-Body Radiation.," *Astrophysical Journal*, vol. 142, pp. 414–419, July 1965.

[5] G. F. Smoot, "COBE observations and results," *AIP Conf. Proc.*, vol. 476, pp. 1–10, 1999.

[6] D. J. Fixsen, E. S. Cheng, J. M. Gales, J. C. Mather, R. A. Shafer, and E. L. Wright, "The Cosmic Microwave Background Spectrum from the Full COBE FIRAS Data Set," *Astrophysical Journal*, vol. 473, pp. 576+, December 1996.

[7] C. L. Bennett, M. Halpern, G. Hinshaw, N. Jarosik, A. Kogut, M. Limon, S. S. Meyer, L. Page, D. N. Spergel, G. S. Tucker, E. Wollack, E. L. Wright, C. Barnes, M. R. Greason, R. S. Hill, E. Komatsu, M. R. Nolta, N. Odegard, H. V. Peiris, L. Verde, and J. L. Weiland, "First-year wilkinson microwave anisotropy probe (wmap) observations: Preliminary maps and basic results," *Astrophysical Journal Supplement Series*, vol. 148, no. 1, p. 1, 2003.

[8] E. Komatsu, K. M. Smith, J. Dunkley, C. L. Bennett, B. Gold, G. Hinshaw, N. Jarosik, D. Larson, M. R. Nolta, L. Page, D. N. Spergel, M. Halpern, R. S.

Hill, A. Kogut, M. Limon, S. S. Meyer, N. Odegard, G. S. Tucker, J. L. Weiland, E. Wollack, and E. L. Wright, "Seven-year Wilkinson Microwave Anisotropy Probe (WMAP) Observations: Cosmological Interpretation," *Astrophysical Journal*, vol. 192, p. 18, Feb. 2011.

[9] C. Bertout and T. Forveille, "Pre-launch status of the Planck mission," *Astronomy and Astrophysics*, vol. 520, Sept. 2010.

[10] U. Seljak and U. Zaldarriaga, "A Line-of-Sight Integration Approach to Cosmic Microwave Background Anisotropies," *Astrophysical Journal*, vol. 469, pp. 437+, Oct. 1996.

[11] J. M. Kovac, E. M. Leitch, C. Pryke, J. E. Carlstrom, N. W. Halverson, and W. L. Holzapfel, "Detection of polarization in the cosmic microwave background using DASI," *Nature*, vol. 420, pp. 772–787, Dec. 2002.

[12] R. Lambourne, *Relativity, Gravitation and Cosmology*. Relativity, Gravitation and Cosmology, Cambridge University Press, 2010.

[13] E. Komatsu, J. Dunkley, M. R. Nolta, C. L. Bennett, B. Gold, G. Hinshaw, N. Jarosik, D. Larson, M. Limon, L. Page, D. N. Spergel, M. Halpern, R. S. Hill, A. Kogut, S. S. Meyer, G. S. Tucker, J. L. Weiland, E. Wollack, and E. L. Wright, "Five-Year Wilkinson Microwave Anisotropy Probe Observations: Cosmological Interpretation," *Astrophysical Journal Supplement*, vol. 180, pp. 330–376, Feb. 2009.

[14] E. Hubble, "A Relation between Distance and Radial Velocity among Extra-Galactic Nebulae," *Proceedings of the National Academy of Science*, vol. 15, pp. 168–173, Mar. 1929.

[15] E. Kolb and M. Turner, *The early universe*. Frontiers in physics, Westview Press, 1993.

[16] P. J. E. Peebles, "The Black-Body Radiation Content of the Universe and the Formation of Galaxies.," *Astrophysical Journal*, vol. 142, pp. 1317+, Nov. 1965.

[17] Liddle, Andrew R. and Lyth, David H., *Cosmological Inflation and Large-Scale Structure*. Cambridge University Press, April 2000.

[18] D. Ruth, *The Cosmic Mircowave Background*. Cambridge University Press, 2008.

[19] W. Hu, "CMB temperature and polarization anisotropy fundamentals," *Ann. Phys.*, vol. 303, pp. 203–225, 2003.

[20] T. S. Pereira and L. R. Abramo, "Angular-planar CMB power spectrum," *Physical Review D*, vol. 80, pp. 063525+, Sept. 2009.

[21] R. Sachs, A. Wolfe, G. Ellis, J. Ehlers, and A. Krasiński, "Republication of: Perturbations of a cosmological model and angular variations of the microwave background (By R.K. Sachs and A.M. Wolfe)," *General Relativity and Gravitation*, vol. 39, pp. 1929–1961, November 2007.

[22] P. J. E. Peebles and J. T. Yu, "Primeval Adiabatic Perturbation in an Expanding Universe," *Astrophysical Journal*, vol. 162, pp. 815+, Dec. 1970.

[23] J. Silk, "Cosmic Black-Body Radiation and Galaxy Formation," *Astrophysical Journal*, vol. 151, pp. 459+, Feb. 1968.

[24] S. Dodelson and J. M. Jubas, "Microwave anisotropies in the light of the data from the COBE satellite," *Physical Review Letters*, vol. 70, pp. 2224–2227, Apr. 1993.

[25] M. Tegmark and E. F. Bunn, "A Brute Force Analysis of the COBE DMR Data," *Astrophysical Journal*, vol. 455, pp. 1+, Dec. 1995.

[26] M. Tegmark and A. de Oliveira-Costa, "How to measure CMB polarization power spectra without losing information," *Physical Review D*, vol. 64, pp. 063001+, Sept. 2001.

[27] A. Lewis, A. Challinor, and N. Turok, "Analysis of CMB polarization on an incomplete sky," *Physical Review D*, vol. 65, pp. 023505+, Jan. 2002.

[28] N. Aghanim, S. Majumdar, and J. Silk, "Secondary anisotropies of the CMB," *Rept. Prog. Phys.*, vol. 71, p. 066902, 2008.

[29] M. Zaldarriaga, "The Polarization of the Cosmic Microwave Background," *Measuring and Modeling the Universe*, pp. 309+, 2004.

[30] W. Hu and M. White, "A CMB polarization primer," *New Astronomy*, vol. 2, pp. 323–344, Oct. 1997.

[31] J. Kaplan, J. Delabrouille, P. Fosalba, and C. Rosset, "Cmb polarization as complementary information to anisotropies," Tech. Rep. astro-ph/0310650, Oct 2003.

[32] E. F. Bunn, "Detectability of Microwave Background Polarization," *Physical Review*, vol. D65, p. 043003, 2002.

[33] E. F. Bunn, M. Zaldarriaga, M. Tegmark, and A. de Oliveira-Costa, "E/B decomposition of finite pixelized CMB maps," *Physical Review D*, vol. 67, pp. 023501+, Jan. 2003.

[34] E. F. Bunn, "Separating E from B," *New Astronomy Reviews*, vol. 47, pp. 987–994, Dec. 2003.

[35] W. H. Kinney, "The energy scale of inflation: Is the hunt for the primordial B-mode a waste of time?," 2003.

[36] A. Lewis and A. Challinor, "Weak gravitational lensing of the CMB," *Physics Reports*, vol. 429, pp. 1–65, June 2006.

[37] W. H. Kinney, "Inflation After WMAP," *ArXiv Astrophysics e-prints*, June 2004.

[38] D. N. Spergel and M. Zaldarriaga, "CMB polarization as a direct test of inflation," *Physical Review Letters*, vol. 79, pp. 2180–2183, 1997.

[39] C. L. Reichardt, P. A. R. Ade, J. J. Bock, J. R. Bond, J. A. Brevik, C. R. Contaldi, M. D. Daub, J. T. Dempsey, J. H. Goldstein, W. L. Holzapfel, C. L. Kuo, A. E. Lange, M. Lueker, M. Newcomb, J. B. Peterson, J. Ruhl, M. C. Runyan, and Z. Staniszewski, "High-Resolution CMB Power Spectrum from the Complete ACBAR Data Set," *Astrophysical Journal*, vol. 694, pp. 1200–1219, Apr. 2009.

[40] A. Benoît, P. Ade, A. Amblard, R. Ansari, É. Aubourg, S. Bargot, J. G. Bartlett, J. Bernard, R. S. Bhatia, A. Blanchard, J. J. Bock, A. Boscaleri, F. R.

Bouchet, A. Bourrachot, P. Camus, F. Couchot, P. de Bernardis, J. Delabrouille, F. Désert, O. Doré, M. Douspis, L. Dumoulin, X. Dupac, P. Filliatre, P. Fosalba, K. Ganga, F. Gannaway, B. Gautier, M. Giard, Y. Giraud-Héraud, R. Gispert, L. Guglielmi, J. Hamilton, S. Hanany, S. Henrot-Versillé, J. Kaplan, G. Lagache, J. Lamarre, A. E. Lange, J. F. Macías-Pérez, K. Madet, B. Maffei, C. Magneville, D. P. Marrone, S. Masi, F. Mayet, A. Murphy, F. Naraghi, F. Nati, G. Patanchon, G. Perrin, M. Piat, N. Ponthieu, S. Prunet, J. Puget, C. Renault, C. Rosset, D. Santos, A. Starobinsky, I. Strukov, R. V. Sudiwala, R. Teyssier, M. Tristram, C. Tucker, J. Vanel, D. Vibert, E. Wakui, and D. Yvon, "First detection of polarization of the submillimetre diffuse galactic dust emission by Archeops," *Astronomy and Astrophysics*, vol. 424, pp. 571–582, Sept. 2004.

[41] B. G. Keating, P. A. R. Ade, J. J. Bock, E. Hivon, W. L. Holzapfel, A. E. Lange, H. Nguyen, and K. W. Yoon, "BICEP: a large angular scale CMB polarimeter," in *Society of Photo-Optical Instrumentation Engineers (SPIE) Conference Series* (S. Fineschi, ed.), vol. 4843 of *Presented at the Society of Photo-Optical Instrumentation Engineers (SPIE) Conference*, pp. 284–295, Feb. 2003.

[42] C. J. MacTavish, P. A. R. Ade, J. J. Bock, J. R. Bond, J. Borrill, A. Boscaleri, P. Cabella, C. R. Contaldi, B. P. Crill, P. de Bernardis, G. De Gasperis, A. de Oliveira-Costa, G. De Troia, G. di Stefano, E. Hivon, A. H. Jaffe, W. C. Jones, T. S. Kisner, A. E. Lange, A. M. Lewis, S. Masi, P. D. Mauskopf, A. Melchiorri, T. E. Montroy, P. Natoli, C. B. Netterfield, E. Pascale, F. Piacentini, D. Pogosyan, G. Polenta, S. Prunet, S. Ricciardi, G. Romeo, J. E. Ruhl, P. Santini, M. Tegmark, M. Veneziani, and N. Vittorio, "Cosmological Parameters from the 2003 Flight of BOOMERANG," *Astrophysical Journal*, vol. 647, pp. 799–812, Aug. 2006.

[43] D. Barkats, C. Bischoff, P. Farese, L. Fitzpatrick, T. Gaier, J. O. Gundersen, M. M. Hedman, L. Hyatt, J. J. McMahon, D. Samtleben, S. T. Staggs, K. Vanderlinde, and B. Winstein, "First Measurements of the Polarization of the Cosmic Microwave Background Radiation at Small Angular Scales from CAPMAP," *Astrophysical Journal*, vol. 619, pp. L127–L130, Feb. 2005.

[44] C. D. Sheehy, P. A. R. Ade, R. W. Aikin, M. Amiri, S. Benton, C. Bischoff, J. J. Bock, J. A. Bonetti, J. A. Brevik, B. Burger, C. D. Dowell, L. Duband, J. P. Filippini, S. R. Golwala, M. Halpern, M. Hasselfield, G. Hilton, V. V. Hristov, K. Irwin, J. P. Kaufman, B. G. Keating, J. M. Kovac, C. L. Kuo, A. E. Lange, E. M. Leitch, M. Lueker, C. B. Netterfield, H. T. Nguyen, R. W. O. IV, A. Orlando, C. L. Pryke, C. Reintsema, S. Richter, J. E. Ruhl, M. C. Runyan, Z. Staniszewski, S. Stokes, R. Sudiwala, G. Teply, K. L. Thompson, J. E. Tolan, A. D. Turner, P. Wilson, and C. L. Wong, "The keck array: a pulse tube cooled cmb polarimeter," vol. 7741, p. 77411R, SPIE, 2010.

[45] J. H. P. Wu, J. Zuntz, M. E. Abroe, P. A. R. Ade, J. Bock, J. Borrill, J. Collins, S. Hanany, A. H. Jaffe, B. R. Johnson, T. Jones, A. T. Lee, T. Matsumura, B. Rabii, T. Renbarger, P. L. Richards, G. F. Smoot, R. Stompor, H. T. Tran, and C. D. Winant, "MAXIPOL: Data Analysis and Results," *Astrophysical Journal*, vol. 665, pp. 55–66, Aug. 2007.

[46] G. S. Tucker, J. Kim, P. Timbie, S. Ali, L. Piccirillo, and C. Calderon, "Bolometric interferometry: the millimeter-wave bolometric interferometer," *New Astronomy Reviews*, vol. 47, no. 11-12, pp. 1173 – 1176, 2003. Proceedings of the Workshop on The Cosmic Microwave Background Radiation and its Polarization.

[47] K. Arnold, P. A. R. Ade, A. E. Anthony, F. Aubin, D. Boettger, J. Borrill, C. Cantalupo, M. A. Dobbs, J. Errard, D. Flanigan, A. Ghribi, N. Halverson, M. Hazumi, W. L. Holzapfel, J. Howard, P. Hyland, A. Jaffe, B. Keating, T. Kisner, Z. Kermish, A. T. Lee, E. Linder, M. Lungu, T. Matsumura, N. Miller, X. Meng, M. Myers, H. Nishino, R. O'Brient, D. O'Dea, C. Reichardt, I. Schanning, A. Shimizu, C. Shimmin, M. Shimon, H. Spieler, B. Steinbach, R. Stompor, A. Suzuki, T. Tomaru, H. T. Tran, C. Tucker, E. Quealy, P. L. Richards, and O. Zahn, "The POLARBEAR CMB polarization experiment," in *Society of Photo-Optical Instrumentation Engineers (SPIE) Conference Series*, vol. 7741 of *Presented at the Society of Photo-Optical Instrumentation Engineers (SPIE) Conference*, July 2010.

[48] M. L. Brown, P. Ade, J. Bock, M. Bowden, G. Cahill, P. G. Castro, S. Church, T. Culverhouse, R. B. Friedman, K. Ganga, W. K. Gear, S. Gupta, J. Hinderks,

J. Kovac, A. E. Lange, E. Leitch, S. J. Melhuish, Y. Memari, J. A. Murphy, A. Orlando, C. O'Sullivan, L. Piccirillo, C. Pryke, N. Rajguru, B. Rusholme, R. Schwarz, A. N. Taylor, K. L. Thompson, A. H. Turner, E. Y. S. Wu, M. Zemcov, and The QUa D collaboration, "Improved Measurements of the Temperature and Polarization of the Cosmic Microwave Background from QUaD," *Astrophysical Journal*, vol. 705, pp. 978–999, Nov. 2009.

[49] QUIET Collaboration, C. Bischoff, A. Brizius, I. Buder, Y. Chinone, K. Cleary, R. N. Dumoulin, A. Kusaka, R. Monsalve, S. K. Næss, L. B. Newburgh, R. Reeves, K. M. Smith, I. K. Wehus, J. A. Zuntz, J. T. L. Zwart, L. Bronfman, R. Bustos, S. E. Church, C. Dickinson, H. K. Eriksen, P. G. Ferreira, T. Gaier, J. O. Gundersen, M. Hasegawa, M. Hazumi, K. M. Huffenberger, M. E. Jones, P. Kangaslahti, D. J. Kapner, C. R. Lawrence, M. Limon, J. May, J. J. McMahon, A. D. Miller, H. Nguyen, G. W. Nixon, T. J. Pearson, L. Piccirillo, S. J. E. Radford, A. C. S. Readhead, J. L. Richards, D. Samtleben, M. Seiffert, M. C. Shepherd, S. T. Staggs, O. Tajima, K. L. Thompson, K. Vanderlinde, R. Williamson, and B. Winstein, "First Season QUIET Observations," *ArXiv e-prints*, Dec. 2010.

[50] Hamilton, J.-C. and Charlassier, R., "Qubic, a bolometric interferometer to measure the b-modes of the cmb," *EAS Publications Series*, vol. 40, pp. 399–404, 2010.

[51] Qubic Collaboration, E. Battistelli, A. Baú, D. Bennett, L. Bergé, J.-P. Bernard, P. de Bernardis, G. Bordier, A. Bounab, É. Bréelle, E. F. Bunn, M. Calvo, R. Charlassier, S. Collin, A. Coppolecchia, A. Cruciani, G. Curran, M. de Petris, L. Dumoulin, A. Gault, M. Gervasi, A. Ghribi, M. Giard, C. Giordano, Y. Giraud-Héraud, M. Gradziel, L. Guglielmi, J.-C. Hamilton, V. Haynes, J. Kaplan, A. Korotkov, J. Landé, B. Maffei, M. Maiello, S. Malu, S. Marnieros, J. Martino, S. Masi, A. Murphy, F. Nati, C. O'Sullivan, F. Pajot, A. Passerini, S. Peterzen, F. Piacentini, M. Piat, L. Piccirillo, G. Pisano, G. Polenta, D. Prêle, D. Romano, C. Rosset, M. Salatino, A. Schillaci, G. Sironi, R. Sordini, S. Spinelli, A. Tartari, P. Timbie, G. Tucker, L. Vibert, F. Voisin, R. A. Watson, M. Zannoni, and QUBIC Collaboration, "QUBIC: The QU bolometric interferometer for cosmology," *Astroparticle Physics*, vol. 34, pp. 705–716, Apr. 2011.

[52] W. Hu, "Structure Formation with Generalized Dark Matter," *Astrophysical Journal*, vol. 506, pp. 485–494, Oct. 1998.

[53] S. Winitzki and A. Kosowsky, "Minkowski functional description of microwave background Gaussianity," *New Astronomy*, vol. 3, pp. 75–100, Mar. 1998.

[54] D. N. Spergel, L. Verde, H. V. Peiris, E. Komatsu, M. R. Nolta, C. L. Bennett, M. Halpern, G. Hinshaw, N. Jarosik, A. Kogut, M. Limon, S. S. Meyer, L. Page, G. S. Tucker, J. L. Weiland, E. Wollack, and E. L. Wright, "First-year wilkinson microwave anisotropy probe (wmap) observations: Determination of cosmological parameters," *Astrophysical Journal Supplement Series*, vol. 148, no. 1, p. 175, 2003.

[55] P. de Bernardis, P. A. R. Ade, J. J. Bock, J. R. Bond, J. Borrill, A. Boscaleri, K. Coble, B. P. Crill, G. De Gasperis, P. C. Farese, P. G. Ferreira, K. Ganga, M. Giacometti, E. Hivon, V. V. Hristov, A. Iacoangeli, A. H. Jaffe, A. E. Lange, L. Martinis, S. Masi, P. V. Mason, P. D. Mauskopf, A. Melchiorri, L. Miglio, T. Montroy, C. B. Netterfield, E. Pascale, F. Piacentini, D. Pogosyan, S. Prunet, S. Rao, G. Romeo, J. E. Ruhl, F. Scaramuzzi, D. Sforna, and N. Vittorio, "A flat Universe from high-resolution maps of the cosmic microwave background radiation," *Nature*, vol. 404, pp. 955–959, Apr. 2000.

[56] J. P. Ostriker and P. J. Steinhardt, "Cosmic Concordance," *ArXiv Astrophysics e-prints*, May 1995.

[57] J. Kaplan and for the QUBIC collaboration, "QUBIC, a bolometric interferometer to measure the B modes of the CMB," *ArXiv e-prints*, Oct. 2009.

[58] J. Kaplan and for the QUBIC collaboration, "QUBIC, a bolometric interferometer to measure the B modes of the CMB," *ArXiv e-prints*, Oct. 2009.

[59] S. Masi, P. de Bernardis, C. Giordano, F. Nati, F. Piacentini, G. Polenta, M. Veneziani, M. Gervasi, G. Sironi, A. Tartari, M. Zannoni, S. Peterzen, J. Bartlett, Y. Giraud-Heraud, M. Piat, C. Rosset, M. Giard, R. Pons, B. Maffei, P. Ade, W. Gear, P. Mauskopf, L. Piccirillo, G. Pisano, and G. Savini, "Precision cmb polarization from dome-c: the brain experiment," *EAS Publications Series*, vol. 14, pp. 87–92, 2005.

[60] A. A. Michelson, "On the Application of Interference Methods to Astronomical Measurements," *Astrophysical Journal*, vol. 51, pp. 257+, June 1920.

[61] A. A. Michelson and F. G. Pease, "Measurement of the diameter of alpha Orionis with the interferometer.," *Astrophysical Journal*, vol. 53, pp. 249–259, May 1921.

[62] A. Wootten and A. R. Thompson, "The Atacama Large Millimeter/Submillimeter Array," *IEEE Proceedings*, vol. 97, pp. 1463–1471, Aug. 2009.

[63] T. Wilson, K. Rohlfs, and S. Hüttemeister, *Tools of radio astronomy*. Astronomy and astrophysics library, Springer, 2009.

[64] A. Thompson, J. Moran, and G. Swenson, *Interferometry and synthesis in radio astronomy*. Wiley, 2001.

[65] M. Yun, J. Bock, H. Leduc, P. Day, and M. J. Kim, "Fabrication of antenna-coupled transition edge polarization-sensitive bolometer arrays," *Nuclear Instruments and Methods in Physics Research Section A: Accelerators, Spectrometers, Detectors and Associated Equipment*, vol. 520, no. 1-3, pp. 487 – 489, 2004. Proceedings of the 10th International Workshop on Low Temperature Detectors.

[66] F. Roddier, "Pupil plane versus image plane in michelson stellar interferometry," *J. Opt. Soc. Am. A*, vol. 3, no. 12, pp. 2160–2166, 1986.

[67] S. Padin, J. K. Cartwright, B. S. Mason, T. J. Pearson, A. C. S. Readhead, M. C. Shepherd, J. Sievers, P. S. Udomprasert, W. L. Holzapfel, S. T. Myers, J. E. Carlstrom, E. M. Leitch, M. Joy, L. Bronfman, and J. May, "First Intrinsic Anisotropy Observations with the Cosmic Background Imager," *Astrophysical Journall*, vol. 549, pp. L1–L5, Mar. 2001.

[68] A. C. Taylor, A. Challinor, D. Goldie, K. Grainge, M. E. Jones, A. N. Lasenby, S. Withington, G. Yassin, W. K. Gear, L. Piccirillo, P. Ade, P. D. Mauskopf, B. Maffei, and G. Pisano, "CLOVER - A new instrument for measuring the B-mode polarization of the CMB," *ArXiv Astrophysics e-prints*, July 2004.

[69] J. Hamilton, R. Charlassier, C. Cressiot, J. Kaplan, M. Piat, and C. Rosset, "Sensitivity of a bolometric interferometer to the cosmic microwave backgroud power spectrum," *Astronomy and Astrophysics*, vol. 491, pp. 923–927, Dec. 2008.

[70] R. Charlassier, E. F. Bunn, J. Hamilton, J. Kaplan, and S. Malu, "Bandwidth in bolometric interferometry," *Astronomy and Astrophysics*, vol. 514, pp. A37+, May 2010.

[71] E. F. Bunn and M. White, "Mosaicking with Cosmic Microwave Background Interferometers," *Astrophysical Journal*, vol. 655, pp. 21–29, Jan. 2007.

[72] Prêle, D., Piat, M., Bréelle, E., Voisin, F., Geoffray, H., Marnieros, S., Dumoulin, L., Stanescu, D., Atik, Y., Evesque, C., Leriche, B., Pajot, F., and Bélier, B., "Superconducting niobium/silicon bolometer developments in the dcmb french collaboration," *EAS Publications Series*, vol. 37, pp. 107–117, 2009.

[73] G. Curran, M. Gradziel, C. O'Sullivan, J. Murphy, P. Hyland, A. Korotkov, S. Malu, L. Piccirillo, P. Timbie, and G. Tucker, "Quasi-optical design and analysis of the millimeter-wave bolometric interferometer (mbi)," in *Infrared and Millimeter Waves, 2007 and the 2007 15th International Conference on Terahertz Electronics. IRMMW-THz. Joint 32nd International Conference on*, pp. 188 –189, 2007.

[74] P. Hyland, B. Follin, and E. F. Bunn, "Phase shift sequences for an adding interferometer," *Monthly Notices of the Royal Astronomical Society*, vol. 393, pp. 531–537, Feb. 2009.

[75] R. Charlassier, J. Hamilton, É. Bréelle, A. Ghribi, Y. Giraud-Héraud, J. Kaplan, M. Piat, and D. Prêle, "An efficient phase-shifting scheme for bolometric additive interferometry," *Astronomy and Astrophysics*, vol. 497, pp. 963–971, Apr. 2009.

[76] C. O'Sullivan, E. Atad-Ettedgui, W. Duncan, D. Henry, W. Jellema, J. A. Murphy, N. Trappe, H. van de Stadt, S. Withington, and G. Yassin, "Far-infrared optics design and verification," *International Journal of Infrared and Millimeter Waves*, vol. 23, pp. 1029–1045, 2002. 10.1023/A:1019679102893.

[77] R. Wilson, *Reflecting Telescope Optics: Basic design theory and its historical development*. Astronomy and astrophysics library, Springer, 2004.

[78] J. Geary, *Introduction to lens design: with practical ZEMAX examples*. Willmann-Bell, 2002.

[79] L. Díaz and T. Milligan, *Antenna engineering using physical optics: practical CAD techniques and software*. No. v. 1 in Artech House antenna library, Artech House, 1996.

[80] P. Johansen, "Uniform physical theory of diffraction equivalent edge currents for truncated wedge strips," *Antennas and Propagation, IEEE Transactions on*, vol. 44, pp. 989 –995, July 1996.

[81] P. Goldsmith, *Quasioptics*. IEEE, 1994.

[82] A. Siegman, *Lasers*. University Science Books, 1986.

[83] C. O'Sullivan, J. A. Murphy, G. Cahill, M. L. Gradziel, N. Trappe, D. White, V. Yurchenko, S. Withington, and W. Jellema, "Developments in quasi-optical design for thz," vol. 5498, pp. 320–331, SPIE, 2004.

[84] M. L. Gradziel, D. White, J. A. Murphy, and S. Withington, "Improving the Efficiency of Quasi-optical Analysis and Design of Terahertz Systems," in *Fifteenth International Symposium on Space Terahertz Technology* (G. Narayanan, ed.), pp. 255+, 2004.

[85] M. Candotti, A. M. Baryshev, and N. Trappe, "Quasi-optical assessment of the alma band 9 front-end," *Infrared Physics & Technology*, vol. 52, no. 5, pp. 174 – 179, 2009.

[86] J. Goodman, *Introduction to Fourier optics*. McGraw-Hill physical and quantum electronics series, Roberts & Co., 2005.

[87] G. Reynolds and G. Parrent, *The New physical optics notebook: tutorials in Fourier optics*. Press Monograph Series, SPIE Optical Engineering Press, 1989.

[88] M. L. Gradziel, C. O'Sullivan, J. A. Murphy, G. Cahill, G. S. Curran, C. Pryke, W. Gear, and S. Church, "Modelling of the optical performance of millimeter-wave instruments in MODAL," in *Society of Photo-Optical Instrumentation Engineers (SPIE) Conference Series*, vol. 6472 of *Society of Photo-Optical Instrumentation Engineers (SPIE) Conference Series*, Feb. 2007.

[89] M. Kidger, *Fundamental optical design*. SPIE Monograph, SPIE Press, 2002.

[90] G. L. Pilbratt, J. R. Riedinger, T. Passvogel, G. Crone, D. Doyle, U. Gageur, A. M. Heras, C. Jewell, L. Metcalfe, S. Ott, and M. Schmidt, "Herschel Space Observatory. An ESA facility for far-infrared and submillimetre astronomy," *Astronomy and Astrophysics*, vol. 518, pp. L1+, July 2010.

[91] V. B. Yurchenko and A. Altintas, "Physical optics modeling of 2d dielectric lenses," *J. Opt. Soc. Am. A*, vol. 26, no. 2, pp. 305–312, 2009.

[92] S. Loiseau and S. Shaklan, "Optical design, modelling and tolerancing of a fizeau interferometer dedicated to astrometry," *Astron. Astrophys. Suppl. Ser.*, vol. 117, no. 1, pp. 167–178, 1996.

[93] W. B. Wetherell and M. P. Rimmer, "General analysis of aplanatic cassegrain, gregorian, and schwarzschild telescopes," *Appl. Opt.*, vol. 11, no. 12, pp. 2817–2832, 1972.

[94] D. Korsch, "Closed form solution for three-mirror telescopes, corrected for spherical aberration, coma, astigmatism, and field curvature," *Appl. Opt.*, vol. 11, no. 12, pp. 2986–2987, 1972.

[95] K. Nariai and H. Iwamoto, "A variation of schwarzschild telescope: Golden section solution with two concentric spheres and its extension to finite distance solutions," *Optical Review*, vol. 12, pp. 190–195, 2005. 10.1007/s10043-005-0190-z.

[96] C. Dragone, "A first-order treatment of aberrations in cassegrainian and gregorian antennas," *Antennas and Propagation, IEEE Transactions on*, vol. 30, pp. 331 – 339, May 1982.

[97] M. Lampton and M. Sholl, "Comparison of on-axis three-mirror-anastigmat telescopes," in *Society of Photo-Optical Instrumentation Engineers (SPIE) Conference Series*, vol. 6687 of *Presented at the Society of Photo-Optical Instrumentation Engineers (SPIE) Conference*, Sept. 2007.

[98] D. Korsch, "Design and optimization technique for three-mirror telescopes," *Appl. Opt.*, vol. 19, pp. 3640–3645, Nov 1980.

[99] W. Rusch, J. Prata, A., Y. Rahmat-Samii, and R. Shore, "Derivation and application of the equivalent paraboloid for classical offset cassegrain and gregorian antennas," *Antennas and Propagation, IEEE Transactions on*, vol. 38, pp. 1141 –1149, Aug. 1990.

[100] R. A. Shore, "A simple derivation of the basic design equation for offset dual reflector antennas with rotational symmetry and zero cross polarization," *IEEE Transactions on Antennas and Propagation*, vol. 33, pp. 114–116, Jan. 1985.

[101] S. Hanany and D. P. Marrone, "Comparison of designs of off-axis gregorian telescopes for millimeter-wave large focal-plane arrays," *Appl. Opt.*, vol. 41, no. 22, pp. 4666–4670, 2002.

[102] J. A. Murphy, "Distortion of a simple gaussian beam on reflection from off-axis ellipsoidal mirrors," *International Journal of Infrared and Millimeter Waves*, vol. 8, pp. 1165–1187, 1987. 10.1007/BF01010819.

[103] J. A. Murphy and S. Withington, "Perturbation analysis of gaussian-beam-mode scattering at off-axis ellipsoidal mirrors," *Infrared Physics & Technology*, vol. 37, no. 2, pp. 205 – 219, 1996.

[104] C. Dragone, "Unique reflector arrangement with very wide field of view for multibeam antennas," *Electronics Letters*, vol. 19, no. 25-26, pp. 1061–1062, 1983.

[105] F. Villa, M. Bersanelli, C. Burigana, R. C. Butler, N. Mandolesi, A. Mennella, G. Morgante, M. Sandri, L. Terenzi, and L. Valenziano, "The Planck Telescope," in *Experimental Cosmology at Millimetre Wavelengths* (M. de Petris & M. Gervasi, ed.), vol. 616 of *American Institute of Physics Conference Series*, pp. 224–228, May 2002.

[106] C. Granet, "Designing classical dragonian offset dual-reflector antennas from combinations of prescribed geometric parameters," *Antennas and Propagation Magazine, IEEE*, vol. 43, pp. 100 –107, Dec. 2001.

[107] S. Chang and J. Prata, A., "The design of classical offset dragonian reflector antennas with circular apertures," *Antennas and Propagation, IEEE Transactions on*, vol. 52, no. 1, pp. 12 – 19, 2004.

[108] S. Chang and J. Prata, A., "A design procedure for classical offset inverse cassegrain antennas with circular apertures," in *Antennas and Propagation Society International Symposium, 2001. IEEE*, 2001.

[109] S. Chang and J. Prata, A., "A design procedure for classical offset dragonian antennas with circular apertures," in *Antennas and Propagation Society International Symposium, 1999. IEEE*, vol. 2, pp. 1140 –1143 vol.2, Aug. 1999.

[110] R. J. Wylde, "Millimetre-wave Gaussian beam-mode optics and corrugated feed horns," *IEE Proceedings H: Microwaves Optics and Antennas*, vol. 131, pp. 258–262, Aug. 1984.

[111] M. Katz, *Introduction to geometrical optics*. World Scientific, 2002.

[112] H. Gross, F. Blechinger, and B. Achtner, *Handbook of Optical Systems, Survey of Optical Instruments*. Handbook of Optical Systems: Survey of Optical Instruments, Wiley-VCH, 2008.

[113] W. B. Joyce and B. C. DeLoach, "Alignment of gaussian beams," *Appl. Opt.*, vol. 23, pp. 4187–4196, Dec 1984.

[114] H. Kogelnik, "Coupling and Conversion Coefficients for Optical Modes," in *Quasi-Optics*, pp. 333+, June 1964.

[115] S. Withington and J. A. Murphy, "Analysis of diagonal horns through Gaussian-Hermite modes," *IEEE Transactions on Antennas and Propagation*, vol. 40, pp. 198–206, Feb. 1992.

[116] P. Goldsmith, "Quasi-optical techniques," *Proceedings of the IEEE*, vol. 80, pp. 1729 –1747, Nov. 1992.

[117] W. Smith, *Modern lens design*. McGraw-Hill professional engineering: Electronic engineering, McGraw-Hill, 2005.

[118] J. M. Sasian, "Design of a schwarzschild flat-field, anastigmatic, unobstructed, wide-field telescope," *Optical Engineering*, vol. 29, no. 1, pp. 1–5, 1990.

[119] G. Pisano, G. Savini, P. A. R. Ade, V. Haynes, and W. K. Gear, "Achromatic half-wave plate for submillimeter instruments in cosmic microwave background astronomy: experimental characterization," *Appl. Opt.*, vol. 45, pp. 6982–6989, Sep 2006.

[120] G. Savini, G. Pisano, and P. A. R. Ade, "Achromatic half-wave plate for submillimeter instruments in cosmic microwave background astronomy: modeling and simulation," *Appl. Opt.*, vol. 45, pp. 8907–8915, Dec 2006.

[121] G. Pisano, G. Savini, P. A. R. Ade, and V. Haynes, "Metal-mesh achromatic half-wave plate for use at submillimeter wavelengths," *Appl. Opt.*, vol. 47, pp. 6251–6256, Nov 2008.

[122] The QUBIC collaboration, E. Battistelli, A. Baù, D. Bennett, L. Bergé, J. Bernard, P. de Bernardis, A. Bounab, É. Bréelle, E. F. Bunn, M. Calvo, R. Charlassier, S. Collin, A. Cruciani, G. Curran, L. Dumoulin, A. Gault, M. Gervasi, A. Ghribi, M. Giard, C. Giordano, Y. Giraud-Héraud, M. Gradziel, L. Guglielmi, J. Hamilton, V. Haynes, J. Kaplan, A. Korotkov, J. Landé, B. Maffei, M. Maiello, S. Malu, S. Marnieros, S. Masi, A. Murphy, F. Nati, C. O'Sullivan, F. Pajot, A. Passerini, S. Peterzen, F. Piacentini, M. Piat, L. Piccirillo, G. Pisano, G. Polenta, D. Prêle, D. Romano, C. Rosset, M. Salatino, A. Schillacci, G. Sironi, R. Sordini, S. Spinelli, A. Tartari, P. Timbie, G. Tucker, L. Vibert, F. Voisin, R. A. Watson, and M. Zannoni, "QUBIC: The QU Bolometric Interferometer for Cosmology," *ArXiv e-prints*, Oct. 2010.

[123] A. Liu, M. Tegmark, S. Morrison, A. Lutomirski, and M. Zaldarriaga, "Precision calibration of radio interferometers using redundant baselines," *Monthly Notices of the Royal Astronomical Society*, vol. 408, pp. 1029–1050, Oct. 2010.

[124] E. F. Bunn, "Systematic Errors in Cosmic Microwave Background Interferometry," *Physical Review*, vol. D75, p. 083517, 2007.

[125] Prêle, D., Piat, M., Bréelle, E., Voisin, F., Geoffray, H., Marnieros, S., Dumoulin, L., Stanescu, D., Atik, Y., Evesque, C., Leriche, B., Pajot, F., and Bélier, B., "Superconducting niobium/silicon bolometer developments in the dcmb french collaboration," *EAS Publications Series*, vol. 37, pp. 107–117, 2009.

[126] A. Monfardini, L. J. Swenson, A. Benoit, A. Bideau, G. Bres, P. Camus, G. Garde, C. Hoffmann, J. Minet, H. Rodenas, and The Nika Collaboration, "Kinetic Inductance Detectors development for mm-wave Astronomy," in *EAS Publications Series* (P. Kern, ed.), vol. 37 of *EAS Publications Series*, pp. 95–99, 2009.

[127] R. W. Haas, "Further Development of MMW and SMMW Platelet Feed Horn Arrays," in *Multi-Feed Systems for Radio Telescopes* (D. T. Emerson & J. M. Payne, ed.), vol. 75 of *Astronomical Society of the Pacific Conference Series*, pp. 99–+, 1995.

[128] P. Clarricoats and A. Olver, *Corrugated horns for microwave antennas*. IEE electromagnetic waves series, P. Peregrinus on behalf of the Institution of Electrical Engineers, 1984.

[129] P. A. Ade, R. J. Wylde, and J. Zhang, "Ultra-Gaussian Horns for ClOVER - a B-Mode CMB Experiment," in *Twentieth International Symposium on Space Terahertz Technology* (E. Bryerton, A. Kerr, & A. Lichtenberger, ed.), pp. 128+, Apr. 2009.

[130] M. L. Brown, P. Ade, J. Bock, M. Bowden, G. Cahill, P. G. Castro, S. Church, T. Culverhouse, R. B. Friedman, K. Ganga, W. K. Gear, S. Gupta, J. Hinderks, J. Kovac, A. E. Lange, E. Leitch, S. J. Melhuish, Y. Memari, J. A. Murphy, A. Orlando, C. O'Sullivan, L. Piccirillo, C. Pryke, N. Rajguru, B. Rusholme, R. Schwarz, A. N. Taylor, K. L. Thompson, A. H. Turner, E. Y. S. Wu, M. Zemcov, and The QUa D collaboration, "Improved Measurements of the Temperature and Polarization of the Cosmic Microwave Background from QUaD," *Astrophysical Journal*, vol. 705, pp. 978–999, Nov. 2009.

[131] M. Bowden, A. N. Taylor, K. M. Ganga, P. A. Ade, J. J. Bock, G. A. Cahill, J. E. Carlstrom, S. E. Church, W. K. Gear, J. R. Hinderks, W. Hu, B. G. Keating, J. Kovac, A. E. Lange, E. M. Leitch, B. Maffei, O. Mallie, S. J. Melhuish, J. A. Murphy, G. Pisano, L. Piccirillo, C. Pryke, B. A. Rusholme, C. M. O'Sullivan, K. L. Thompson, and M. Zemcov, "Measuring the cosmic microwave background polarization with the QUaD experiment," in *Society of Photo-Optical Instrumentation Engineers (SPIE) Conference Series* (J. M. Oschmann Jr., ed.),

vol. 5489 of *Presented at the Society of Photo-Optical Instrumentation Engineers (SPIE) Conference*, pp. 84–94, Oct. 2004.

[132] C. O'Sullivan, G. Cahill, J. A. Murphy, W. K. Gear, J. Harris, P. A. R. Ade, S. E. Church, K. L. Thompson, C. Pryke, J. Bock, M. Bowden, M. L. Brown, J. E. Carlstrom, P. G. Castro, T. Culverhouse, R. B. Friedman, K. M. Ganga, V. Haynes, J. R. Hinderks, J. Kovak, A. E. Lange, E. M. Leitch, O. E. Mallie, S. J. Melhuish, A. Orlando, L. Piccirillo, G. Pisano, N. Rajguru, B. A. Rusholme, R. Schwarz, A. N. Taylor, E. Y. S. Wu, and M. Zemcov, "The quasi-optical design of the QUaD telescope," *Infrared Physics and Technology*, vol. 51, pp. 277–286, Mar. 2008.

[133] J. R. Hinderks, P. Ade, J. Bock, M. Bowden, M. L. Brown, G. Cahill, J. E. Carlstrom, P. G. Castro, S. Church, T. Culverhouse, R. Friedman, K. Ganga, W. K. Gear, S. Gupta, J. Harris, V. Haynes, B. G. Keating, J. Kovac, E. Kirby, A. E. Lange, E. Leitch, O. E. Mallie, S. Melhuish, Y. Memari, A. Murphy, A. Orlando, R. Schwarz, C. O. Sullivan, L. Piccirillo, C. Pryke, N. Rajguru, B. Rusholme, A. N. Taylor, K. L. Thompson, C. Tucker, A. H. Turner, E. Y. S. Wu, and M. Zemcov, "QUaD: A High-Resolution Cosmic Microwave Background Polarimeter," *The Astrophysical Journal*, vol. 692, pp. 1221–1246, Feb. 2009.

[134] M. Born, E. Wolf, A. Bhatia, P. Clemmow, D. Gabor, A. Stokes, A. Taylor, P. Wayman, and W. Wilcock, *Principles of Optics: Electromagnetic Theory of Propagation, Interference and Diffraction of Light*. Cambridge University Press, 2000.

[135] G. Beyerle and I. S. McDermid, "Ray-tracing formulas for refraction and internal reflection in uniaxial crystals," *Appl. Opt.*, vol. 37, pp. 7947–7953, Dec 1998.

[136] Q.-T. Liang, "Simple ray tracing formulas for uniaxial optical crystals," *Appl. Opt.*, vol. 29, pp. 1008–1010, Mar 1990.

[137] M. A. no Alejo, "Analysis of the refraction of the extraordinary ray in a plane-parallel uniaxial plate with an arbitrary orientation of the optical axis," *Opt. Express*, vol. 13, pp. 2549–2555, Apr 2005.

[138] M. Cho, J. Kim, H. Park, Y. Han, K. Moon, E. Jung, and H. Han, "Highly birefringent terahertz polarization maintaining plastic photonic crystal fibers," *Opt. Express*, vol. 16, pp. 7–12, Jan 2008.

[139] G. Ren, Y. Gong, P. Shum, X. Yu, J. Hu, G. Wang, M. O. L. Chuen, and V. Paulose, "Low-loss air-core polarization maintaining terahertz fiber," *Opt. Express*, vol. 16, pp. 13593–13598, Sep 2008.

[140] H. C. Chiang, P. A. R. Ade, D. Barkats, J. O. Battle, E. M. Bierman, J. J. Bock, C. D. Dowell, L. Duband, E. F. Hivon, W. L. Holzapfel, V. V. Hristov, W. C. Jones, B. G. Keating, J. M. Kovac, C. L. Kuo, A. E. Lange, E. M. Leitch, P. V. Mason, T. Matsumura, H. T. Nguyen, N. Ponthieu, C. Pryke, S. Richter, G. Rocha, C. Sheehy, Y. D. Takahashi, J. E. Tolan, and K. W. Yoon, "Measurement of Cosmic Microwave Background Polarization Power Spectra from Two Years of BICEP Data," *The Astrophysical Journal*, vol. 711, pp. 1123–1140, Mar. 2010.

Appendices

Zemax prescription data for the optimized telecentric dual reflectors

SYSTEM OPTIMIZED FROM COMPENSATED GREGORIAN (CG) COMBINER.

SURFACE DATA SUMMARY:

Surf	Type	Radius	Thickness	Glass	Diameter	Conic
OBJ	STANDARD	Infinity	350		300	0
STO	BICONICZ	-2289.206	0	MIRROR	600	-1
2	COORDBRK	-	0		-	-
3	STANDARD	Infinity	-700		20	0
4	STANDARD	Infinity	0		20	0
5	COORDBRK	-	0		-	-
6	BICONICZ	2002.531	543.0049	MIRROR	600	-1
7	COORDBRK	-	0		-	-
IMA	STANDARD	Infinity			240	0

SURFACE DATA DETAIL:

Surface OBJ : STANDARD
Surface STO : BICONICZ
Mirror Substrate : Curved, Thickness = 1.20000E+001

Tilt/Decenter	Decenter X	Decenter Y	Tilt X	Tilt Y
Before surface	0	0	36	0

Extrapolate? : 0
X Radius : -1595.5646
X Conic : -1
Max Zern Terms : 0
Norm Radius : 1
Term on X to 1: 0
Term on X to 2: 0.0002451155
Term on X to 3: 0
Term on X to 4: 8.35895e-012
Term on X to 5: 0
Term on X to 6: 2.409054e-016

Term on Y to 1: 0
Term on Y to 2: 0.0001831607
Term on Y to 3: 0
Term on Y to 4: -2.571919e-010
Term on Y to 5: 0
Term on Y to 6: -5.553662e-016

Aperture : Floating Aperture
Maximum Radius : 300
Surface 2 : COORDBRK

```
 Coordinate Return Solve: To Surface -1
 Decenter X     :                0
 Decenter Y     :                0
 Tilt About X   :               36
 Tilt About Y   :                0
 Tilt About Z   :                0
 Order          : Decenter then tilt
Surface   3     : STANDARD
Surface   4     : STANDARD
Surface   5     : COORDBRK
 Decenter X     :                0
 Decenter Y     :                0
 Tilt About X   :              -20
 Tilt About Y   :                0
 Tilt About Z   :                0
 Order          : Decenter then tilt
Surface   6     : BICONICZ
 Mirror Substrate : Curved, Thickness = 1.20000E+001
 Extrapolate?   : 0
 X Radius       :        1769.8581
 X Conic        :               -1
 Max Zern Terms : 0
 Norm Radius    :                1
 Term on X to  1:                0
 Term on X to  2:     0.0001053299
 Term on X to  3:                0
 Term on X to  4:    7.767219e-011
 Term on X to  5:                0
 Term on X to  6:    4.723829e-017
 Term on X to  7:                0
 Term on Y to  1:                0
 Term on Y to  2:    8.706052e-005
 Term on Y to  3:                0
 Term on Y to  4:   -3.751024e-011
 Term on Y to  5:                0
 Term on Y to  6:   -7.555746e-016

 Aperture       : Floating Aperture
 Maximum Radius :           300
Surface   7     : COORDBRK
 Decenter X     :                0
 Decenter Y     :        197.63762
 Tilt About X   :              -20
 Tilt About Y   :                0
 Tilt About Z   :                0
 Order          : Decenter then tilt
Surface IMA     : STANDARD



SYSTEM OPTIMIZED FROM A BACK-FED COMBINER.
```

SURFACE DATA SUMMARY:

Surf	Type	Radius	Thickness	Glass	Diameter	Conic
OBJ	STANDARD	Infinity	350		300	0
STO	BICONICZ	-2376.513	0	MIRROR	600	-1
2	COORDBRK	-	0		-	-
3	STANDARD	Infinity	-450		20	0
4	STANDARD	Infinity	0		20	0
5	COORDBRK	-	0		-	-
6	BICONICZ	2631.134	386.5111	MIRROR	600	-1
7	COORDBRK	-	0		-	-
IMA	STANDARD	Infinity			240	0

SURFACE DATA DETAIL:

Surface OBJ : STANDARD
Surface STO : BICONICZ
Mirror Substrate : Curved, Thickness = 1.20000E+001

Tilt/Decenter	Decenter X	Decenter Y	Tilt X	Tilt Y
Before surface	0	0	30	0

Extrapolate? : 0
X Radius : -1831.9728
X Conic : -1
Max Zern Terms : 0
Norm Radius : 1
Term on X to 1: 0
Term on X to 2: 5.5110845e-005
Term on X to 3: 0
Term on X to 4: -1.8999799e-010
Term on X to 5: 0
Term on X to 6: 5.3131916e-016
Term on X to 7: 0
Term on X to 8: 1.216302e-019
Term on X to 9: 0
Term on X to 10: -1.5095156e-024
Term on X to 11: 0
Term on X to 12: -1.4558443e-030
Term on X to 13: 0
Term on X to 14: 0
Term on X to 15: 0
Term on X to 16: 0
Term on Y to 1: 0
Term on Y to 2: 5.7387984e-005
Term on Y to 3: 0
Term on Y to 4: -1.6669951e-010
Term on Y to 5: 0
Term on Y to 6: -2.058256e-015
Term on Y to 7: 0
Term on Y to 8: 1.2290404e-019

```
 Term on Y to  9:                0
 Term on Y to 10:  -1.3400029e-024
 Term on Y to 11:                0
 Term on Y to 12:  -1.3136369e-033
 Term on Y to 13:                0
 Term on Y to 14:                0
 Term on Y to 15:                0
 Term on Y to 16:                0
 Aperture       : Floating Aperture
 Maximum Radius :           300
Surface   2     : COORDBRK
 Coordinate Return Solve: To Surface -1
 Decenter X     :                0
 Decenter Y     :                0
 Tilt About X   :               30
 Tilt About Y   :                0
 Tilt About Z   :                0
 Order          : Decenter then tilt
Surface   3     : STANDARD
Surface   4     : STANDARD
Surface   5     : COORDBRK
 Decenter X     :                0
 Decenter Y     :                0
 Tilt About X   :              -30
 Tilt About Y   :                0
 Tilt About Z   :                0
 Order          : Decenter then tilt
Surface   6     : BICONICZ
 Mirror Substrate : Curved, Thickness = 1.20000E+001
 Extrapolate?   : 0
 X Radius       :        1987.5233
 X Conic        :               -1
 Max Zern Terms : 0
 Norm Radius    :                1
 Term on X to  1:                0
 Term on X to  2:   5.3667053e-005
 Term on X to  3:                0
 Term on X to  4:   -8.978933e-011
 Term on X to  5:                0
 Term on X to  6:   -6.578054e-016
 Term on X to  7:                0
 Term on X to  8:   1.6716386e-020
 Term on X to  9:                0
 Term on X to 10:   4.1273453e-025
 Term on X to 11:                0
 Term on X to 12:   -1.440774e-030
 Term on X to 13:                0
 Term on X to 14:                0
 Term on X to 15:                0
 Term on X to 16:                0
 Term on Y to  1:                0
```

```
 Term on Y to  2:     2.44153e-005
 Term on Y to  3:                0
 Term on Y to  4:   8.9199333e-010
 Term on Y to  5:                0
 Term on Y to  6:  -1.2910979e-014
 Term on Y to  7:                0
 Term on Y to  8:   4.1750774e-020
 Term on Y to  9:                0
 Term on Y to 10:  -7.1821325e-026
 Term on Y to 11:                0
 Term on Y to 12:    2.049629e-033
 Term on Y to 13:                0
 Term on Y to 14:                0
 Term on Y to 15:                0
 Term on Y to 16:                0
 Aperture       : Floating Aperture
 Maximum Radius :           300
Surface   7     : COORDBRK
 Decenter X     :                0
 Decenter Y     :        223.15231
 Tilt About X   :              -30
 Tilt About Y   :                0
 Tilt About Z   :                0
 Order          : Decenter then tilt
Surface IMA     : STANDARD



OPTIMIZED CROSSED COMBINER



SURFACE DATA SUMMARY:

Surf     Type         Radius      Thickness                Glass      Diameter          Conic
 OBJ STANDARD       Infinity            500                           300               0
 STO BICONICZ      -3297.543              0               MIRROR       800              -1
   2 COORDBRK              -              0                              -               -
   3 STANDARD       Infinity           -350                           20               0
   4 STANDARD       Infinity              0                           20               0
   5 COORDBRK              -              0                              -               -
   6 BICONICZ       2192.367            550               MIRROR       800              -1
   7 COORDBRK              -              0                              -               -
 IMA STANDARD       Infinity                                         240               0

SURFACE DATA DETAIL:

Surface OBJ     : STANDARD
Surface STO     : BICONICZ
 Mirror Substrate : Curved, Thickness = 1.60000E+001
 Tilt/Decenter  :      Decenter X      Decenter Y          Tilt X          Tilt Y
```

```
 Before surface :               0              0             30              0
 Extrapolate?   : 0
 X Radius       :       -2393.7191
 X Conic        :               -1
 Max Zern Terms : 0
 Norm Radius    :                1
 Term on X to  1:                0
 Term on X to  2:   9.8169307e-005
 Term on X to  3:                0
 Term on X to  4:  -2.6859738e-011
 Term on X to  5:                0
 Term on X to  6:   1.9932569e-015
 Term on Y to  1:                0
 Term on Y to  2:   8.5093836e-005
 Term on Y to  3:                0
 Term on Y to  4:  -2.1178692e-010
 Term on Y to  5:                0
 Term on Y to  6:   5.8547372e-015

 Aperture       : Floating Aperture
 Maximum Radius :           400
Surface   2     : COORDBRK
 Coordinate Return Solve: To Surface -1
 Decenter X     :                0
 Decenter Y     :                0
 Tilt About X   :               30
 Tilt About Y   :                0
 Tilt About Z   :                0
 Order          : Decenter then tilt
Surface   3     : STANDARD
Surface   4     : STANDARD
Surface   5     : COORDBRK
 Decenter X     :                0
 Decenter Y     :                0
 Tilt About X   :               21
 Tilt About Y   :                0
 Tilt About Z   :                0
 Order          : Decenter then tilt
Surface   6     : BICONICZ
 Mirror Substrate : Curved, Thickness = 1.60000E+001
 Extrapolate?   : 0
 X Radius       :        1932.8741
 X Conic        :               -1
 Max Zern Terms : 0
 Norm Radius    :                1
 Term on X to  1:                0
 Term on X to  2:    0.00010882281
 Term on X to  3:                0
 Term on X to  4:  -1.2010784e-009
 Term on X to  5:                0
 Term on X to  6:   1.0445126e-014
```

```
 Term on Y to  1:                0
 Term on Y to  2:   8.0796807e-005
 Term on Y to  3:                0
 Term on Y to  4:  -1.8052189e-010
 Term on Y to  5:                0
 Term on Y to  6:   4.7998009e-015

 Aperture       : Floating Aperture
 Maximum Radius :           400
Surface   7     : COORDBRK
 Decenter X     :                0
 Decenter Y     :       -211.12522
 Tilt About X   :               21
 Tilt About Y   :                0
 Tilt About Z   :                0
 Order          : Decenter then tilt
Surface IMA     : STANDARD


OPTIMIZED OFF-AXIS PARABOLOID (OP)


SURFACE DATA SUMMARY:

Surf     Type         Radius      Thickness                Glass      Diameter          Conic
 OBJ STANDARD       Infinity            375                             240               0
 STO BICONICZ      -530.8796      -265.4398               MIRROR          1000      -0.133496
   2 COORDBRK              -       53.74271                                -               -
 IMA STANDARD       Infinity                                            150               0

SURFACE DATA DETAIL:

Surface OBJ     : STANDARD
Surface STO     : BICONICZ
 Mirror Substrate : Curved, Thickness = 2.00000E+001
 Tilt/Decenter  :      Decenter X      Decenter Y          Tilt X          Tilt Y
 Before surface :               0             260               0               0
 Extrapolate?   : 0
 X Radius       :       -523.88252
 X Conic        :      -0.65752244
 Max Zern Terms : 0
 Norm Radius    :                1
 Term on X to  1:                0
 Term on X to  2:   5.5531721e-005
 Term on X to  3:                0
 Term on X to  4:  -7.5994153e-009
 Term on X to  5:                0
 Term on X to  6:   2.7045578e-013
 Term on X to  7:                0
 Term on X to  8:  -3.4910281e-018
 Term on X to  1:                0
```

```
 Term on Y to  2:  -1.7758143e-005
 Term on Y to  3:                0
 Term on Y to  4:  -2.7772954e-010
 Term on Y to  5:                0
 Term on Y to  6:    8.791501e-015
 Term on Y to  7:                0
 Term on Y to  8:  -1.8758259e-020

 Aperture       : Floating Aperture
 Maximum Radius :           500
Surface   2     : COORDBRK
 Decenter X     :                0
 Decenter Y     :        30.188475
 Tilt About X   :        55.704183
 Tilt About Y   :                0
 Tilt About Z   :                0
 Order          : Decenter then tilt
Surface IMA     : STANDARD

COATING DEFINITIONS:
```

Zemax prescription data for the optimized telecentric lens combiners

SINGLE SYMMETRIC LENS SYSTEM.

SURFACE DATA SUMMARY:

Surf	Type	Radius	Thickness	Glass	Diameter	Conic
OBJ	STANDARD	Infinity	135.8488		240	0
STO	STANDARD	596.8197	100	UHMW_HDPE	400	-1
2	STANDARD	-389.4433	164.1425		400	-1
3	STANDARD	389.4433	100	UHMW_HDPE	400	-1
4	STANDARD	-596.8197	100.173		400	-1
IMA	STANDARD	Infinity			154.4689	0

DOUBLE SYMMETRIC LENS SYSTEM.

SURFACE DATA SUMMARY:

Surf	Type	Radius	Thickness	Glass	Diameter	Conic
OBJ	STANDARD	Infinity	102.8481		240	0
STO	STANDARD	-2848.622	60	UHMW_HDPE	400	-1
2	STANDARD	-455.6367	20		400	-1
3	STANDARD	362.8368	60	UHMW_HDPE	400	-1
4	STANDARD	2216.36	120.939		400	-1
5	STANDARD	-2216.36	60	UHMW_HDPE	400	-1
6	STANDARD	-362.8368	20		400	-1
7	STANDARD	455.6367	60	UHMW_HDPE	400	-1
8	STANDARD	2848.622	97.02038		400	-1
IMA	STANDARD	Infinity			156.1977	0

SYMMETRIC FRAUNHOFER FLINT LEADING CORRECTED DOUBLET LENS SYSTEM.

SURFACE DATA SUMMARY:

Surf	Type	Radius	Thickness	Glass	Diameter	Conic
OBJ	STANDARD	Infinity	Infinity		0	0
STO	STANDARD	Infinity	108.3046		240	0
2	STANDARD	362.1936	50	UHMW_HDPE	440	-5.251243
3	STANDARD	801.2649	20		440	-1
4	STANDARD	801.2649	100	UHMW_HDPE	440	-1
5	STANDARD	-687.4229	33.65379		440	1.983749
6	STANDARD	687.4229	100	UHMW_HDPE	440	1.983749
7	STANDARD	-801.2649	20		440	-1
8	STANDARD	-801.2649	50	UHMW_HDPE	440	-1
9	STANDARD	-362.1936	134.1285		440	-5.251243
10	STANDARD	Infinity	-1.312901		151.8245	0
IMA	STANDARD	Infinity			150.67	0

HIGHER ORDER SYMMETRIC TELECENTRIC DOUBLET LENS SYSTEM.

SURFACE DATA SUMMARY:

Surf	Type	Radius	Thickness	Glass	Diameter	Conic	Comment
OBJ	STANDARD	Infinity	102.8481		240	0	
STO	EVENASPH	-2848.622	60	UHMW_HDPE	400	-1	
2	EVENASPH	-455.6367	20		400	-1	
3	EVENASPH	362.8368	60	UHMW_HDPE	400	-1	
4	EVENASPH	2216.36	120.939		400	-1	
5	EVENASPH	-2216.36	60	UHMW_HDPE	400	-1	
6	EVENASPH	-362.8368	20		400	-1	

```
   7 EVENASPH       455.6367             60            UHMW_HDPE          400             -1
   8 EVENASPH       2848.622       97.02038                               400             -1
   9 STANDARD       Infinity             500                          152.2321             0
 IMA STANDARD       Infinity                                          546.9272             0

SURFACE DATA DETAIL:

Surface OBJ     : STANDARD
Surface STO     : EVENASPH
 Coeff on r  2  :    0.00036499645
 Coeff on r  4  :  -1.0874996e-008
 Coeff on r  6  :  -1.1633584e-013
 Coeff on r  8  :                0
 Coeff on r 10  :                0
 Coeff on r 12  :                0
 Coeff on r 14  :                0
 Coeff on r 16  :                0
 Aperture       : Floating Aperture
 Maximum Radius :           200
Surface   2     : EVENASPH
 Coeff on r  2  :    0.00030182625
 Coeff on r  4  :  -6.4506699e-009
 Coeff on r  6  :  -2.6600076e-013
 Coeff on r  8  :                0
 Coeff on r 10  :                0
 Coeff on r 12  :                0
 Coeff on r 14  :                0
 Coeff on r 16  :                0
 Aperture       : Floating Aperture
 Maximum Radius :           200
Surface   3     : EVENASPH
 Coeff on r  2  :   9.3148438e-005
 Coeff on r  4  :  -1.0409049e-008
 Coeff on r  6  :   3.0169982e-014
 Coeff on r  8  :                0
 Coeff on r 10  :                0
 Coeff on r 12  :                0
 Coeff on r 14  :                0
 Coeff on r 16  :                0
 Aperture       : Floating Aperture
 Maximum Radius :           200
Surface   4     : EVENASPH
 Coeff on r  2  :    5.107153e-005
 Coeff on r  4  :  -8.1248847e-009
 Coeff on r  6  :     7.48733e-014
 Coeff on r  8  :                0
 Coeff on r 10  :                0
 Coeff on r 12  :                0
 Coeff on r 14  :                0
 Coeff on r 16  :                0
 Aperture       : Floating Aperture
```

```
 Maximum Radius :           200
Surface   5     : EVENASPH
 Coeff on r  2  :   -5.107153e-005
 Coeff on r  4  :   8.1248847e-009
 Coeff on r  6  :    -7.48733e-014
 Coeff on r  8  :               0
 Coeff on r 10  :               0
 Coeff on r 12  :               0
 Coeff on r 14  :               0
 Coeff on r 16  :               0
 Aperture       : Floating Aperture
 Maximum Radius :           200
Surface   6     : EVENASPH
 Coeff on r  2  :  -9.3148438e-005
 Coeff on r  4  :   1.0409049e-008
 Coeff on r  6  :  -3.0169982e-014
 Coeff on r  8  :               0
 Coeff on r 10  :               0
 Coeff on r 12  :               0
 Coeff on r 14  :               0
 Coeff on r 16  :               0
 Aperture       : Floating Aperture
 Maximum Radius :           200
Surface   7     : EVENASPH
 Coeff on r  2  :   -0.00030182625
 Coeff on r  4  :   6.4506699e-009
 Coeff on r  6  :   2.6600076e-013
 Coeff on r  8  :               0
 Coeff on r 10  :               0
 Coeff on r 12  :               0
 Coeff on r 14  :               0
 Coeff on r 16  :               0
 Aperture       : Floating Aperture
 Maximum Radius :           200
Surface   8     : EVENASPH
 Coeff on r  2  :   -0.00036499645
 Coeff on r  4  :   1.0874996e-008
 Coeff on r  6  :   1.1633584e-013
 Coeff on r  8  :               0
 Coeff on r 10  :               0
 Coeff on r 12  :               0
 Coeff on r 14  :               0
 Coeff on r 16  :               0
 Aperture       : Floating Aperture
 Maximum Radius :           200
Surface   9     : STANDARD
Surface IMA     : STANDARD
```

CAPPED SYMMETRIC TELECENTRIC GAUSSIAN LENS SYSTEM.

SURFACE DATA SUMMARY:

Surf	Type	Radius	Thickness	Glass	Diameter	Conic	Comment
OBJ	STANDARD	Infinity	95.24772		240	0	
STO	STANDARD	-240.214	100	UHMW_HDPE	320	-1	
2	STANDARD	-297.949	20		360	-1	
3	STANDARD	682.9649	60	QUARTZS	440	-1	
4	STANDARD	-987.42	60		440	-1	
5	STANDARD	-283.4811	40	UHMW_HDPE	440	-1	
6	STANDARD	-1019.574	20		440	-1	
7	STANDARD	1019.574	40	UHMW_HDPE	440	-1	
8	STANDARD	283.4811	60		440	-1	
9	STANDARD	987.42	60	QUARTZS	440	-1	
10	STANDARD	-682.9649	20		440	-1	
11	STANDARD	297.949	100	UHMW_HDPE	320	-1	
12	STANDARD	240.214	100.0643		280	-1	
13	STANDARD	Infinity	-4.193809		155.9642	0	
14	STANDARD	Infinity	500		152.3626	0	
IMA	STANDARD	Infinity			581.7496	0	

A COOKE TRIPLET LENS SYSTEM.

SURFACE DATA SUMMARY:

Surf	Type	Radius	Thickness	Glass	Diameter	Conic	Comment
OBJ	STANDARD	Infinity	100.5509		240	0	
STO	STANDARD	342.9055	40	QUARTZS	340	-1	
2	STANDARD	574.8623	40.55782		320	-1	
3	STANDARD	-1319.28	20	UHMW_HDPE	320	-1	
4	STANDARD	1319.28	40.55782		340	-1	
5	STANDARD	-574.8623	40	QUARTZS	340	-1	
6	STANDARD	-342.9055	37.62469		340	-1	
7	STANDARD	342.9055	40	QUARTZS	320	-1	
8	STANDARD	574.8623	40.55782		320	-1	
9	STANDARD	-1319.28	20	UHMW_HDPE	320	-1	
10	STANDARD	1319.28	40.55782		320	-1	
11	STANDARD	-574.8623	40	QUARTZS	320	-1	
12	STANDARD	-342.9055	102.4751		320	-1	
13	STANDARD	Infinity	-2.215253		156.4355	0	
IMA	STANDARD	Infinity			154.5926	0	

SYMMETRIC DOUBLE CONVEX LENS ADJUSTED FOR FIELD CURVATURE.

SURFACE DATA SUMMARY:

Surf	Type	Radius	Thickness	Glass	Diameter	Conic	Comment
OBJ	STANDARD	Infinity	Infinity		0	0	
STO	STANDARD	Infinity	96.87538		240	0	
2	STANDARD	1838.459	100	UHMW_HDPE	400	-1	
3	STANDARD	-1742.845	24.3122		400	-1	
4	STANDARD	1838.459	100	UHMW_HDPE	400	-1	
5	STANDARD	-450.993	37.89073		400	-1	
6	STANDARD	450.993	100	UHMW_HDPE	400	-1	
7	STANDARD	-1838.459	24.3122		400	-1	
8	STANDARD	1742.845	100	UHMW_HDPE	400	-1	
9	STANDARD	-1838.459	90.42844		400	-1	
IMA	STANDARD	470.6007			200	0	

A COOKE TRIPLET OPTIMIZED TO PRODUCE IMAGES SUFFERING FROM LOW LEVELS OF ABERRATIONS.

SURFACE DATA SUMMARY:

Surf	Type	Radius	Thickness	Glass	Diameter	Conic	Comment
OBJ	STANDARD	Infinity	150		240	0	
STO	STANDARD	319.154	40	QUARTZS	360	-1	
2	STANDARD	504.2509	49.85229		360	-1	
3	STANDARD	-2350.241	20	UHMW_HDPE	360	-1	
4	STANDARD	2350.241	49.85229		360	-1	
5	STANDARD	-504.2509	40	QUARTZS	360	-1	
6	STANDARD	-319.154	55.29865		360	-1	
7	STANDARD	319.154	40	QUARTZS	300	-1	
8	STANDARD	504.2509	49.85229		300	-1	
9	STANDARD	-2350.241	20	UHMW_HDPE	300	-1	
10	STANDARD	2350.241	49.85229		300	-1	
11	STANDARD	-504.2509	40	QUARTZS	300	-1	
12	STANDARD	-319.154	45.44747		300	-1	
13	STANDARD	Infinity	-1.705322		150.9823	0	
14	STANDARD	Infinity	500		149.8883	0	
IMA	STANDARD	Infinity			470.6653	0	